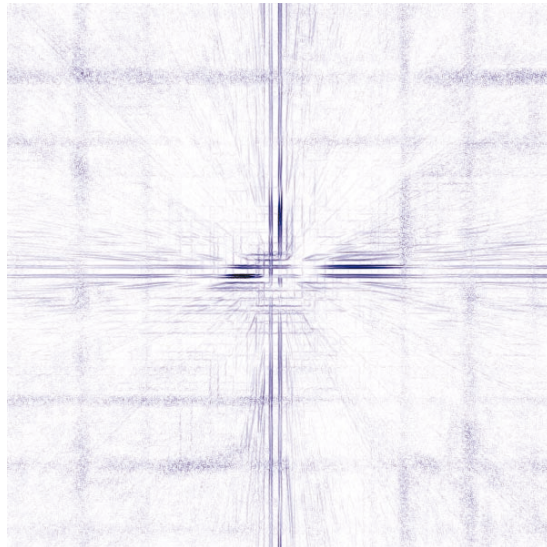


Dissertation zur Erlangung des Doktorgrades  
der Fakultät für Chemie und Pharmazie  
der Ludwig-Maximilians-Universität München

**Sorption isotherms of volatile molecules on micro- and meso-  
porous nanosized siliceous materials based on acoustic wave  
devices. Determination of corresponding isosteric heats of ad-  
sorption.**

von  
Alexander Darga  
aus Rosenheim  
Juni 2008



## **Erklärung**

Diese Dissertation wurde im Sinne von § 13 Abs. 3 bzw. 4 der Promotionsordnung vom 29. Januar 1998 von Herrn Professor Dr. Thomas Bein betreut.

## **Ehrenwörtliche Versicherung**

Diese Dissertation wurde selbständig, ohne unerlaubte Hilfe erarbeitet.

München, am 05.06.2008

A handwritten signature in black ink, appearing to read 'Alex Dep', written in a cursive style.

---

(Unterschrift des Autors)

Dissertation eingereicht am 05.06.2008

1. Gutachter: Prof. Dr. Thomas Bein
2. Gutachter: Prof. Dr. Knözinger

Mündliche Prüfung am 03.07.2008

## **Summary**

Microporous zeolites and mesoporous periodically silicious materials offer interesting features, like porosity in general, host-guest interactions and among others, sorption phenomena.

The application of addressable individual material pixels, pin-printed onto adequate pre-treated supporting surfaces for gas-sensor systems was evaluated. The contact pin-printing technique, well known in bio-science, was adopted and optimized. The successful deposition of colloidal suspensions of zeolite materials on Au-covered glass slides with chemically attached intermediate anchoring molecules was demonstrated on a 100  $\mu\text{m}$  scale (chapter 3).

In a collaboration with the physical department of the LMU Munich (Prof. Kotthaus) a gas sensor system, based on surface acoustic wave devices was developed. Thin layers of porous material in the sub-microgram range were applied, in order to record adsorption isotherms and to determine the released heat of adsorption of specific analyte gases. Related to very small sample amounts and short diffusion times the necessary experimental measurement time could be reduced down to several minutes (chapter 9).

An existing rudimentary quartz crystal microbalance (QCM) was enhanced and an automated intelligent equilibrium system was developed. Furthermore, the system was equipped with liquid mass controllers in order to measure the sorption properties together with vaporized liquid solvents (chapter 4). The developed QCM measurement setup was applied as advanced research tool in order to investigate sorption properties of various porous samples and to obtain the thermodynamic parameter, the isosteric heat of adsorption.

The incorporation of organic moieties into siliceous frameworks leads to a wide variety of adsorbate–adsorbent interactions including weak Van-der-Waals attractions as well as strong interactions such as Coulomb forces. Depending on the desired properties of such substituted highly porous matrix materials, optimized synthesis routes can be established to enhance the desired internal pore surface–affinity towards certain volatile compounds. Based on a fundamental knowledge of the host–guest system, sorption related applications may benefit from individually fine-tuned and modified sample materials. The sorption isotherms and isosteric heat of adsorption for non-modified, phenyl-

modified, cyano-modified, vinyl-modified and mercapto-functionalized mesoporous material for ethanol and 1-butanol sorption were determined. Additionally, nanosized zeolites, like ZSM-5, Sil-1 and zeolite beta were investigated (chapter 6).

Furthermore, sorption isotherms of vaporized toluene on non-modified and phenyl-functionalized mesoporous silica samples were determined using the gravimetric QCM technique at different temperatures. The mesoporous silica was modified by in situ via co-condensation and via post-synthesis grafting approaches, respectively. All samples were thoroughly characterized by several standard techniques and additionally with toluene sorption experiments on the automated QCM setup. The different heats of adsorption of toluene on the various modified silica surfaces obtained by the sorption data made it possible to gain additional information about the degree and type of surface functionalization. It is thus demonstrated that QCM studies can be a powerful and convenient tool for efficient investigations of functionalized mesoporous silica particles that yield valuable quantitative information on molecule-surface interactions (chapter 8).

**Table of content**

	Ehrenwörtliche Versicherung	<i>I</i>
	Summary	<i>II</i>
1	Introduction and motivation	<i>1</i>
1.1	Adsorption related applications	<i>2</i>
1.2	General description of adsorption	<i>3</i>
1.2.1	Classical isotherm types	<i>3</i>
1.2.2	Common adsorbents	<i>7</i>
1.2.3	Size selectivity of porous hosts	<i>8</i>
1.3	Sensor concepts for environmental monitoring	<i>9</i>
1.3.1	The need for chemical sensors	<i>9</i>
1.3.2	Economic aspects of chemical sensors	<i>10</i>
1.3.3	Established sensor technology	<i>11</i>
1.3.3.4	Trace metal sensors	<i>11</i>
1.3.3.5	Laser induced breakdown spectroscopy	<i>12</i>
1.3.3.6	Evanescant fiber-optic chemical sensor	<i>13</i>
1.3.3.7	Oxide metal gas sensors	<i>14</i>
1.3.3.7	Acoustic wave sensor arrays	<i>16</i>
2	Synthesis, characterisation, sample preparation and material properties	<i>22</i>
2.1	Mesoporous materials	<i>22</i>
2.1.1	Non-modified pure nanosized mesoporous material: QCM-E	<i>23</i>
2.1.1.1	Nitrogen sorption data	<i>24</i>
2.1.1.2	Dynamic light scattering measurement	<i>26</i>
2.1.1.3	Transmission electron micrographs	<i>26</i>
2.1.1.4	X-Ray scattering	<i>27</i>
2.1.2	Phenyl functionalized nanosized mesoporous material: QCM-Ph	<i>28</i>
2.1.2.1	Nitrogen sorption data	<i>28</i>

2.1.2.2	Dynamic light scattering measurement	30
2.1.2.3	Transmission electron micrograph	30
2.1.2.4	X-Ray scattering	31
2.1.2.5	Raman spectroscopy	32
2.1.2.6	Thermogravimetric analysis (TGA)	33
2.1.2.7	Scanning electron micrograph	34
2.1.3	Cyano functionalized material: QCM-CN	35
2.1.3.1	Nitrogen sorption data	36
2.1.3.2	Dynamic light scattering measurement	38
2.1.3.3	X-Ray scattering	38
2.1.3.4	Transmission electron micrograph	39
2.1.3.5	Raman spectroscopy	39
2.1.3.6	Thermogravimetric analysis	40
2.1.3.7	Scanning electron micrograph	41
2.1.4	Vinyl functionalized material: QCM-Vinyl	42
2.1.4.1	Nitrogen sorption data	42
2.1.4.2	Dynamic light scattering measurement	44
2.1.4.3	Raman spectroscopy	44
2.1.5	Mercapto functionalized material: QCM-SH	45
2.1.5.1	Nitrogen sorption data	46
2.1.5.2	Dynamic light scattering measurement	47
2.1.5.3	Raman spectroscopy	48
2.2	Microporous materials	49
2.2.1	Pure siliceous zeolite silicalite-1: Sil-1	50
2.2.1.1	X-Ray scattering	50
2.2.1.2	Dynamic light scattering	51
2.2.1.2	Scanning electron micrograph	52
2.2.2	Alumosilicate zeolite ZSM-5: ZSM-5	53
2.2.2.1	X-Ray scattering	53
2.2.2.2	Dynamic light scattering	54
2.2.2.3	Scanning electron micrograph	55
2.2.3	Zeolite beta: Zeo- $\beta$	55

2.2.3.1	X-Ray scattering	56
2.2.3.2	Scanning electron micrograph	57
3	Contact printing of colloidal silica nano-particles - Building a microarray	58
3.1	Leading industry standards in microarray printing technology: A brief overview	58
3.1.1	Microarray printing techniques	59
3.1.1.1	Non-contact microarray printing	60
3.1.1.2	Contact microarray printing	61
3.1.2	Pin-printing parameters	65
3.1.3	Experimental parameters of pin-printing colloidal silica nanoparticles	66
3.1.4	Formation of homogenous silica nanoparticle layers	71
3.2	Conclusion contact pin-printing	76
4	Acoustic wave sensors based on piezoelectricity	79
4.1	Classification of acoustic waves	80
4.1.1	Surface acoustic wave (SAW)	81
4.1.2	Acoustic plate mode (APM) sensors	81
4.1.3	Flexural plate wave (FPW) sensors	82
4.1.4	Shear mode (TSM) sensor	83
4.2	Influence of liquids on the resonance frequency	87
4.3	Influence of surface roughness on the resonance frequency of a QCM device	88
4.4	Experimental setup for QCM sorption experiments	89
4.4.1	Partial pressure control	94
4.4.2	Labview control program	96
4.4.2.1	Basic configuration panel	96
4.4.2.2	Flow control panel	98
4.4.2.3	Frequency counter panel	99
4.4.2.4	Flow step panel	100

4.4.2.5	Mean frequency determination panel	101
4.4.2.6	Temperature step panel	102
5	Heat of adsorption: Theoretical considerations	104
5.1	Commercial application I: The self cooling beer keg	104
5.2	Commercial application II: Drying of nourishments	105
5.3	Sensor related sorption applications based on piezoelectric devices	106
5.4	Relevance of the heat of adsorption for catalytic processes	107
5.5	Measurement methods acquiring the heat of adsorption	108
5.5.1	Calorimetric methods	109
5.5.2	Calculation from equilibrium data	111
6	QCM sorption experiments	116
6.1	Adsorption of ethanol	117
6.1.1	Sorption on non-modified mesoporous material: QCM-E	119
6.1.1.1	Heat of adsorption	122
6.1.2	Sorption on phenyl-functionalized mesoporous material: QCM-Ph	124
6.1.2.1	Heat of adsorption	127
6.1.3	Sorption on cyano-functionalized mesoporous material: QCM-CN	129
6.1.3.1	Heat of adsorption	130
6.1.4	Sorption on vinyl-functionalized mesoporous material: QCM-Vinyl	131
6.1.4.1	Heat of adsorption	133
6.1.5	Sorption on mercapto-functionalized mesoporous material: QCM-SH	134
6.1.5.1	Heat of adsorption	136
6.1.6	Conclusion mesoporous samples QCM-R	136
6.1.7	Sorption on zeolite ZSM-5: sample ZSM-5	139
6.1.7.1	Heat of adsorption of sample ZSM-5	140
6.1.8	Sorption on zeolite silicalite-1: sample Sil-1	142
6.1.8.1	Heat of adsorption of sample Sil-1	143
6.2	Sorption of 1-butanol	145



6.2.1	Sorption on non-modified mesoporous material: QCM-E	146
6.2.1.1	Heat of adsorption of sample QCM-E	147
6.2.2	Sorption on cyano-modified mesoporous material: QCM-CN	149
6.2.2.1	Heat of adsorption of sample QCM-CN	150
6.2.3	Sorption on phenyl-modified mesoporous material: QCM-Ph	151
6.2.3.1	Heat of adsorption of sample QCM-Ph	152
6.2.4	Sorption on vinyl-modified mesoporous material: QCM-Vinyl	153
6.2.4.1	Heat of adsorption of sample QCM-Vinyl	155
6.2.5	Sorption on mercapto-modified mesoporous material: QCM-SH	155
6.2.5.1	Heat of adsorption of sample QCM-SH	156
6.3	Conclusion mesoporous samples QCM-R	157
6.4	Sorption of n-butane on sample Sil-1	161
6.4.1	Heat of adsorption of sample Sil-1	163
7.	Special issue I: QCM measurements as advanced tool to investigate sorption and surface properties of porous materials	165
7.1	Probing the intrapore surface of phenyl-substituted nanoscale mesoporous silica	165
7.1.1	Introduction and motivation	166
7.1.2	Synthesis of mesoporous samples MSN	167
7.1.3	Characterization of mesoporous samples MSN	168
7.1.4	Dynamic light scattering	170
7.1.5	Nitrogen sorption characterisation	171
7.1.6	Thermogravimetric analysis	173
7.1.7	Solid state $^{29}\text{Si}$ -CP-MAS-NMR experiments	174
7.1.8	Raman spectroscopy	177
7.1.9	Toluene sorption experiments and determination of isosteric heats of adsorption	178
7.2	Conclusion phenyl-substituted nanoscaled mesoporous silica	184
8.	Special issue II: Direct-growth of $\text{Cu}_3(\text{BTC})_2(\text{H}_2\text{O})_3 \cdot x\text{H}_2\text{O}$ thin films on modified QCM-gold electrodes: Water vapor sorption measurements	

	and determination of the heat of adsorption	186
8.1	Introduction to metal organic frameworks and motivation of the study	186
8.2	Sample preparation	187
8.3	X-Ray analysis and TGA experiments	188
8.4	QCM sorption experiments with vaporized water	190
9.	Adsorption of organic vapors in thin films of nanosized microporous and mesoporous materials measured with surface acoustic waves	193
9.1	Generation of surface acoustic waves	193
9.2	SAW device and sample deposition	196
9.3	Measurement principle	198
9.4	Measurement chamber	199
9.5	Sorption of gaseous C <sub>4</sub> -hydrocarbons	204
9.5.1	Sorption of n-butane on sample Sil-1	204
9.5.2	Sorption of iso-butane on sample Sil-1	205
9.5.3	Signal answer time	207
9.5.4	Heat of adsorption	207
9.5.5	Sorption of n-butane and iso-butane on sample QCM-E	208
9.5.6	Sorption of 1-butene on sample Sil-1	209
9.5.7	Conclusion sorption of C <sub>4</sub> -alkanes	209
9.6	Sorption of gaseous C <sub>3</sub> -hydrocarbons	210
9.6.1	Sorption of propane on sample Sil-1	210
9.7	Conclusion of sorption experiments carried out with the developed SAW device	212
10.	Literature	214
11	Acknowledgement	224

12	Appendix	225
12.1	Labview controlling and regulation program	225
12.2	Calibration certificates of Bronkhorst mass flow controllers	232
12.3	Data sheet XA1600 QCM chip	239
12.4	Microarray program	240
12.5	Maple program for the determination of $V_{\text{real}}$	243
12.6	Linear regression plots of QCM sorption experiments	244
12.7	Supplementary toluene isotherms	249
12.8	Equipment used for SAW experiments	251
13	Curriculum Vitae	252

## 1 Introduction and motivation

In recent years during several conferences the governments of many nations pronounced the importance of environmental and climate protection. The participants of the Kyoto protocol, discussed in the Japanese City Kyoto and established in 1997, committed themselves to reduce the emission of CO<sub>2</sub> by 5.5% from the level in the year 1990 until 2012.

As a consequence, control mechanisms and analytical techniques had to be developed to succeed in the world wide struggle to reduce environmental pollution. In the '80s and '90s stationary analytical laboratories were mainly authorized to measure the contaminations. Well known techniques like gas chromatography, mass spectrometry, chemical detection reactions or spectrometric analyzers were used to determine the qualitative composition of the analyte as well as the quantitative aspect of the pollutant, for example. Those stationary analytical laboratories could not entirely fulfill the demands of quick analysis of the contaminating chemicals. As a consequence, portable and mobile analysis systems like handheld spectrometers, e.g. "Spectrosort"<sup>1</sup> or portable gas chromatographs have been developed. Parallel to traditional analysis methods the development of alternative systems was pushed particularly by the US government and the upcoming threat of chemical weapons. Leading manufacturers like *Triton Systems, Inc.*<sup>2</sup> are sensor systems suppliers of the US Army to detect toxic biological or chemical materials, so called war-fare agents. Recently, *Triton Systems* were awarded a grant by the US Army Research Office for the development of sensitive coatings for surface acoustic wave (SAW) sensors.<sup>[1]</sup> Those advanced analytical miniaturized system are based on the adsorption of volatile compounds onto the sensing surface of the sensor chip surface.

In the following chapters, the basic principles of adsorption shall be presented, emphasizing the description of sorption isotherms. Additionally, a brief introduction to common adsorbents and their characteristics is given. As the focus of the thesis is not the synthesis of "intelligent" sensor materials itself but the combination of functional materials and the applied measurement technique, particularly some main aspects of sorbent systems are highlighted.

---

<sup>1</sup> SPECTRO Analytical Instruments GmbH & Co. KG, Boschstr. 10, 47533 Kleve, Germany.

<sup>2</sup> Triton Systems, Inc., 200 Turnpike Road, Chelmsford, MA 01824, USA.

### 1.1 Adsorption related applications

Applications taking advantage of adsorption phenomena have expanded rapidly because of sharply rising environmental or quality requirements. Likewise, advances in adsorbent technology have made it possible to meet industrial quality standards, which imply purity of the adsorbent, uniform size and shape of individual species of the material and long-life cycles. Ongoing sorption performance improvements resulting from intense researches are furthermore based on a better understanding of the adsorption mechanisms taking place at the materials internal or external surface. Powerful and more accurate simulations<sup>[37]</sup> of the sorption process supported the rapid development of highly porous, cheap and stable materials.<sup>[2]</sup>

The most popular applications of adsorption can be categorized as purification of polluted material, e.g. effluent water treatment to remove traces of pollutants, as well as potentially toxic taste or odor. Another widespread application of adsorption is the recovery of very pure para-xylene from mixed isomers in the so called Parex® process, offered by UOP<sup>3</sup>. Being aware that there are thousands of different applications of adsorption phenomena, this topic intends to point on the diversity of operations. The industrial used applications have all in common that they require high adsorption capacity, coupled with high selectivity. In many cases, the adsorption rate and pressure drop are also important. Hence, particle size is important. As a general rule, sorption related commercial processes rely on approved and well known materials and particle sizes, in order to avoid any unexpected results, for example toxicity of certain nano-sized particles.<sup>[3]</sup> In this context, it is not crucial if the particle size is in the nanometer or micrometer region or even millimeter sized. As long as the commercial application takes no advantage of nanosized particles, no changes in the material selection are made. For example, many commercial sorption related application would benefit from nanosized particles due to shorter diffusion paths or higher surface areas.<sup>[4]</sup>

Nearly every different application has a different set of additional priorities. For example, the most important qualification for effluent water purification is low cost. In this special case, activated carbon offers both low cost and high effectiveness and is therefore prioritized as adsorbent and purification material. In other sorption driven applications like catalysis the material choice could fall on a siliceous highly porous zeolite, as for example for cracking heavy oil.<sup>[5]</sup>

---

<sup>3</sup> UOP LLC, 25 East Algonquin Road, Des Plaines, IL 60017-5017, USA.

## 1.2 General description of adsorption

The most important attributes of an applied adsorbent for any sorption related application are: capacity, selectivity, regenerability, kinetics and compatibility. With increasing material amounts in the region of hundreds of kilogram or even tons, the cost is another major criterion in choosing the right adsorbent. To evaluate material specific parameters a number of different approaches are available, whereas this work focuses on the evaluation of capacity and selectivity.

The adsorption capacity (loading, degree of coverage) is the most important characteristic of an adsorbent. Sorption capacity is defined as the amount of adsorbate molecules taken up by the adsorbent per unit mass, volume or unit cell of the adsorbent. Commonly accepted is the fact, that the degree of coverage strongly depends on the gas-phase concentration, temperature, and other conditions (especially the initial condition of the adsorbent). Typically, adsorption capacity data is gathered at constant temperature and various adsorbate concentrations or partial pressures for a vapor or gas. The data is usually plotted as isotherm ( $T=\text{constant}$ ) with degree of coverage versus relative partial pressure  $p/p_0$  at constant temperature. The relative partial pressure  $p/p_0$  is the partial pressure of the gas or vaporized liquid apparent inside the experimental container divided by its temperature dependent vapor pressure. The nomenclature  $p/p_0$  allows the direct comparison of isotherms.

### 1.2.1 Classical isotherm types

Concerning the majority of possible shapes of isotherms, they can be divided into six types shown in figure 1 according to IUPAC. At sufficiently low surface coverage most of the isotherms can be reduced to a linear form, which is best described with the so called *Henry's law* region. Type I isotherms are reversible and asymptotically approach the maximum sorption capacity at  $p/p_0 = 1$ . They are typical for microporous solids. Type I isotherm materials have all in common relatively low external surfaces, e.g. zeolites (molecular sieves), porous oxides and certain kinds of activated carbons with high internal surface areas. Usually, the uptake volume is limited by the accessible micropore volume. The International Union of Pure and Applied Chemistry (IUPAC)

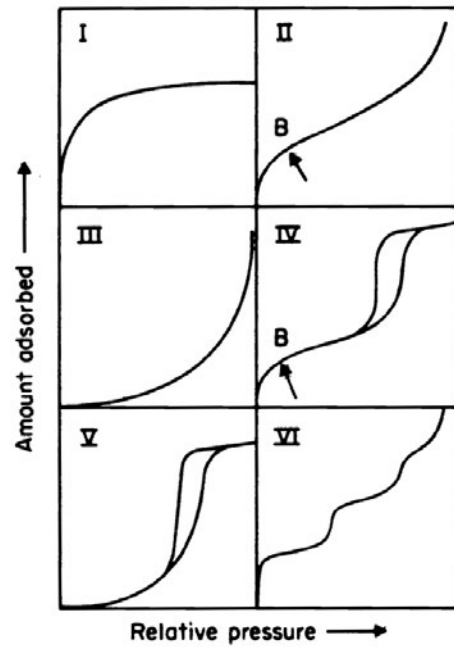


Fig. 1: IUPAC classified isotherms

classified porous materials into three main groups:

1. Micropores with pores  $< 2$  nm
2. Mesopores with pores between 2 nm and 50 nm
3. Macropores with pore sizes  $> 50$  nm

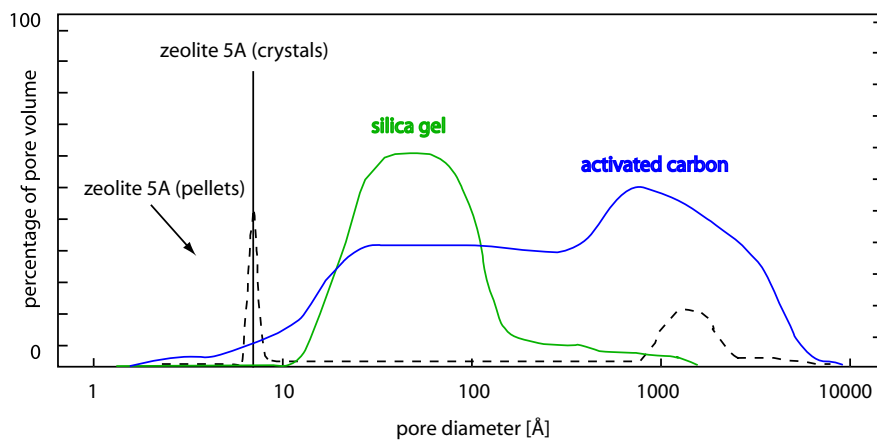


Fig. 2: Pore size distribution of common adsorbents

The correlation between pore size, maximum sorption capacity and kinetics of the sorption process are evident but not always unambiguous. In figure 2 the pore size distributions of well known molecular sieves and adsorbents are compared. As illustrated, the pore size distribution is quite narrow for zeolites, e.g. zeolite 5A but is slightly increased as soon as the microporous zeolite is used in the form of pellets. This behavior is related to intraparticle volumes, which can also be observed with activated carbon. Zeolite 5A can be described as LTA type zeolite<sup>[6]</sup> with a three dimensional channel system and pore entrances of 4.3 Å in diameter. The molecular composition is  $[\text{Na}_{12}(\text{H}_2\text{O})_{27}]_8[\text{Al}_{12}\text{Si}_{12}\text{O}_{48}]_8$ .

In figure 3 the framework of LTA type zeolite material is shown as ball and stick model, whereas each corner represents either silicon or aluminum atoms connected to each other *via* oxygen bridging atoms (Si/Al-O-Si/Al). Blue areas emphasize the 3D-channel system. Green colored volumes demonstrate the void volume inside the sodalite cages (eight 6-membered rings connected via quadrangular intersections). Returning

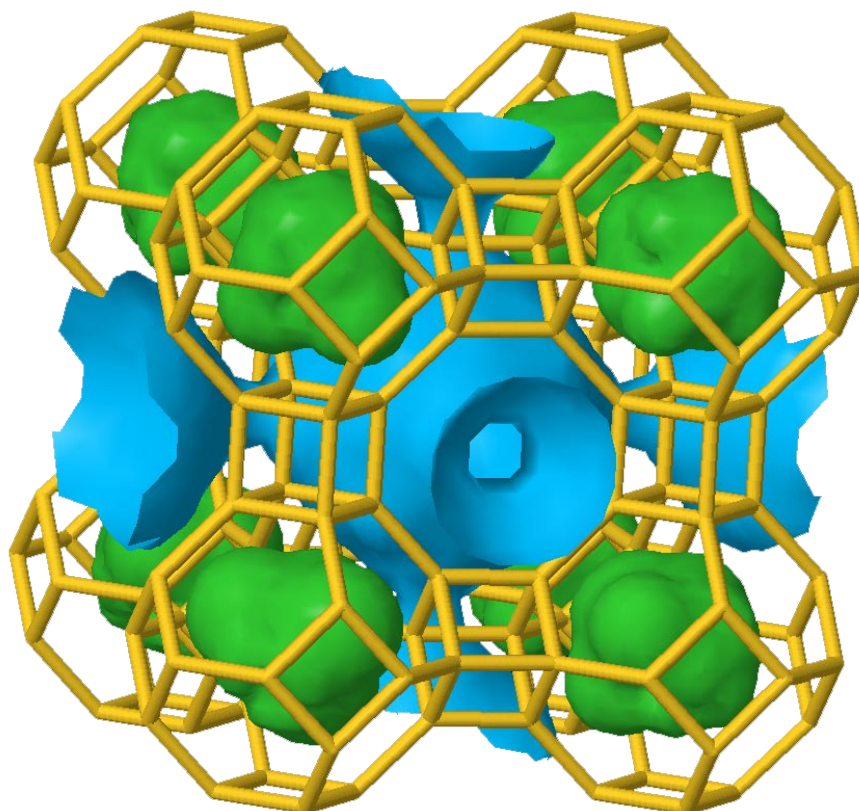


Fig. 3: Ball and stick model of LTA type zeolite<sup>[6]</sup>



to the applications of porous materials, zeolite 5A is a well known molecular sieve which is commonly applied in petrochemical hydrocarbon processing, air separation and dehumidification processes.

Type II isotherms are observed with macroporous or non-porous adsorbents. The isotherm exhibits single layer to multilayer adsorption, which is reflected in the open shaped isotherm.

The very uncommon type III isotherm is convex to the axis of the partial pressure  $p/p_0$  and there are no restrictions concerning multilayer adsorption. The absence of a distinctive point where monolayer coverage merges into multilayer adsorption is remarkable.

Type IV isotherms are observed during nitrogen adsorption in mesoporous materials, for example. Characteristic of that isotherm type is the double S shape and sometimes a hysteresis loop at higher partial pressures, related to capillary condensation inside existing mesopores and the subsequent desorption at lower partial pressures. Those kind of adsorption phenomena show a plateau (pore filling) at high partial pressures.

Type V isotherms are usually not observed with typical porous adsorbents and not common. They are sometimes observed with the adsorption of polar molecules on hydrophobic surfaces. The type V isotherms is usually the analog to type III isotherm observed with porous adsorbents. Nevertheless, type V isotherms are dominated by weak interaction between adsorbate and adsorbent. At higher partial pressure, strong adsorbate - adsorbate interactions are observed.

Type VI isotherms represent stepwise monolayer-multilayer adsorption on non-porous adsorbents. The step height is related to the monolayer capacity and remains constant for 2-3 layers, roughly. A famous example for type VI isotherms is the adsorption of argon or krypton on carbon at the temperature of liquid nitrogen.<sup>[7], [8]</sup>

As the focus of this work is the sorption of vaporized organic solvents and light alkanes on porous siliceous sorbents, the hysteresis phenomena in general as observed for example during nitrogen sorption on mesoporous silica particles will be not explained in detail.

Furthermore, the origin of the hysteresis is not fully understood<sup>[9]</sup> and it is supposed to be even more challenging in the context of specific sorption processes of vaporized liquids on chemically modified mesoporous silica nanoparticles.

### 1.2.2 Common adsorbents

In industrial application, several tailored adsorbents are indispensable in order to fulfill the customers demands.

Table 1 summarizes some important adsorbents applied in commercial or industrial applications. As evident, the key features of an adsorbent are selectivity in separation related processes, either in the gas or liquid phase, or in terms of purification applications an extensive sorption capacity paired with low production cost, e.g. for activated carbon. This goal is archived due to very high surface areas, between  $500 \text{ m}^2 \text{ g}^{-1}$  up to  $1500 \text{ m}^2 \text{ g}^{-1}$  being readily achievable. For comparison, a soccer field has an area of about  $7500 \text{ m}^2$ . Carbon aerogels while more expensive, have even higher surface areas and are used in special applications. As for example, market researches estimate the annual consumption for activated carbon for the US market to 225.000.000 kg, valued

adsorption process	adsorbent material
gas separation $\text{N}_2/\text{O}_2$	zeolite/carbon molecular sieves
gas separation $\text{NH}_3/\text{H}_2$	activated carbon
gas separation $\text{H}_2\text{S}/\text{CS}_2$	activated carbon
liquid separation $\text{H}_2\text{O}/\text{EtOH}$	zeolite
$\text{H}_2$ removal from industrial exhausts	activated carbon/molecular sieves
respirator filter	activated carbon
exhaust hood	activated carbon zeolite
solvent regeneration	activated carbon
$\text{SO}_2$ removal	activated carbon/ $\text{Al}_2\text{O}_3$
drying of natural gas	$\text{SiO}_2/\text{Al}_2\text{O}_3/\text{zeolites}$
drying of air	$\text{SiO}_2$
purification of drinking water	activated carbon
removal of phenols from industrial effluents	activated carbon
heavy oil cracking	zeolites

Tab. 1: Common adsorbents and their related industrial process

at 315.000.000 US \$.<sup>[10]</sup> Growth rates currently are between 3 and 5%.

### 1.2.3 *Size selectivity of porous hosts*

Activated carbon is not capable to selectively adsorb molecules dependent on their shape and size. This option requires another class of materials, e.g. zeolites.

Zeolites exhibit microporosity in molecular dimensions, hence offering shape and size selective properties available during sorption. Very popular applications taking benefit of porous hosts are listed in table 1.

Figure 4 schematically displays the basic principle of size selectivity which is very important in catalysis. The phenomena can be divided into three classes.

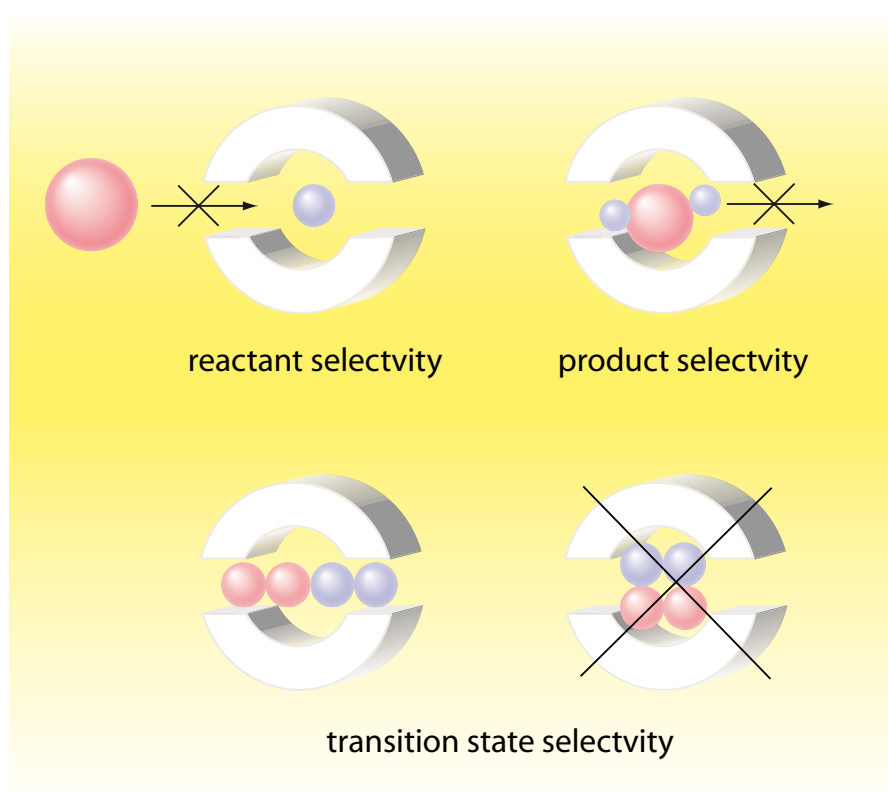


Fig. 4: Basic principle of molecular sieves

Reactants with a bigger molecular size compared to the entrance to the internal framework of zeolites are blocked and further reactions inside the siliceous material are prevented. This exclusion is called *reactant selectivity*.

*Product selectivity* comes into play when reactants have already entered the pores and cages of the porous material. Chemical potentially catalytic driven reactions may produce unwanted products. Those unwanted side-products may also be the kinetically determined products. Due to the narrowed “exit” pathway of the pore system only the thermodynamic determined desired product is able to penetrate the barrier and escape from the host system. Thus, reactions that conventionally yield merely the wanted product can be influenced and forced to yield the desired products in excess.

The third class of size selectivity is called *transition state selectivity*. During chemical reactions intermediate products open alternative reaction pathways. Usually, exclusively one single product is desired to prevent subsequent time consuming and expensive separation procedures of product mixtures. Related to size limitations and/or internal surface modifications, unwanted transition states are either not possible or metastable. In consequence, the suitable and sterically feasible transition state leads to the desired product.

## 1.3 Sensor concepts for environmental monitoring

### 1.3.1 *The need for chemical sensors*

Modern and intelligent sensor approaches attempt to mimic biological systems by incorporating several sensor elements into one single device.<sup>[27]</sup> So called artificial noses are nowadays in the focus of research and development and are commercially available, as for example the artificial nose Artinos® from Sysca AG<sup>4</sup>.

A condensed overview about state-of-art chemical sensor arrays can be found in reference [11].

Chemical sensors detect the presence of specific chemicals or classes of chemicals. Examples include oxygen sensors, also known as lambda sensors usually applied in catalyst in automotive vehicles, ion-selective electrodes, pH glass electrodes, and redox electrodes. Furthermore, a carbon monoxide detector is a chemical sensor often

---

<sup>4</sup> SYSCA AG, Im Köbler 2, D-75438 Knittlingen, Germany.

used in the home. These detectors continually sample air and will alert the homeowner if the amount of toxic carbon monoxide exceeds a certain level. Carbon monoxide concentrations between 70 and 100 ppm (exposition over several hours) cause symptoms like rhinorrhea, head ache, conjunctivitis and shortness of breath. Above an intoxication with 200 ppm CO exposed over several hours vertigo, abnormal fatigue and vomitus are observed. Brain damage, unconsciousness and in the worst case existus above 400 ppm are possible. Due to a 300 times higher affinity to hemoglobin, vital oxygen is replaced by carbon monoxide. The hazardousness of CO gas is related to the lack of human senses for the odorless, colorless and tasteless gas. In order to prevent those described threats, chemical or physical sensors are necessary to rapidly detect increasing CO concentrations.

In manufacturing or industrial plants, chemical sensors are used to manage process control, quality assurance, and safety for the employees.

The engine management and control systems of automobiles process information from sensors and adjust engine parameters to achieve the best balance of fuel economy, performance and emissions. Oxygen sensors have been used in automobiles since the late 70's. In many countries, automobiles have to pass an emissions test annually, in order to get the permission to be used. The test equipment also uses chemical sensors to check the exhaust emissions.

Amongst others, chemical sensors have been developed to detect threats from explosives, chemical and biological weapons or drugs.<sup>[12]</sup> For example, airport security utilizes chemical sensors to detect explosives and even drugs.<sup>5, 6</sup> Chemical sensors are also being developed to detect illnesses of people.<sup>[13], [14]</sup>

### *1.3.2 Economic aspects of chemical sensors*

Referring to reference [15] US companies generated \$213 billion in environmental industry revenue in 2001 with a annual growth rate of 2.1%. Instrument technology is a \$3.8 billion dollar industry. The growth rate in 2001 is cited with 4%, which is quite high in industrial technology markets. The U.S. water industry's revenue of \$80 billion dollar is divided into water utilities (38% of the total amount), wastewater

---

<sup>5</sup> Advanced Aviation Technology Ltd., The Old Post Office, The Street, Compton, England.

<sup>6</sup> Sionex Corporation, 300 Second Avenue, Waltham, MA 02451, USA.

treatment (35%), and water equipment including chemical additives accounts for 27% of the water industry revenue in 2001. Furthermore solid waste management, air pollution detection (gas sensors) and control equipment count for \$69.1 billion dollars. It is worth to mention, that until 2010 overall growth rates between 19% up to 250% are projected in the fields of energy and water industry. New background support is expected from ongoing worldwide discussions and conferences concerning climate protection. Recently, on the G8 conference in Germany in 2007 the governments recognized the importance of intense and target-oriented reduction of the annual output of CO<sub>2</sub>, well known as greenhouse gas. Individual solutions, including the promotion of new technologies to reduce and produce energy or problematic atomic energy plants were discussed.

In this context, it can be anticipated that sensor surveillance systems are necessary to track pollution which exceed agreed maximum values.

### *1.3.3 Established sensor technology*

For years, several sensor concepts were developed to monitor environmental pollution. In the following chapter, some of the most important sensor technologies are summarized in short.

#### *1.3.3.1 Trace metal sensors*

A common concept to trace metal ions is the nano-electrode system, which takes advantage of traces of metal ion induced current and tension variations within a homogeneously applied electromagnetic field. The sensor signal is a function of the redox potential of the analyte and usually plotted as cyclic voltammetric response. A very good overview of nanoelectrodes, nanoelectrode arrays and their applications can be found in reference.<sup>[16]</sup> The big advantage of the nanoelectrode arises from the huge amount of up to 150000 individual electrodes on 1 cm<sup>2</sup> of adequate substrate material. This miniaturization is achieved by applying modern techniques like lithography and chemical

vapor deposition (CVD). The design of the nano-electrode sensor integrates additional reference electrodes eliminating the need for external buffer solutions. Compared to standard electrode sensing devices a  $10^3$  higher signal to noise ratio (SNR) can be achieved which enables the operator to measure traces of metal ions.

### 1.3.3.2 *Laser induced breakdown spectroscopy*

The laser induced spectroscopy (LIBS) is based on the thermal sublimation of solid or liquid sample material. The generated plasma is spectroscopically analyzed. The LIBS method is suitable for almost every element, especially for toxic metals and inorganic compounds. Due to the analyzed radiation, specific elements within a chemical substance are detected very accurately by their “fingerprint” signals. Recent developments offer fiber optic systems providing the ability to measure on locations where usually no measurements can be performed, for example remote measurements under hazardous environmental conditions.<sup>[17]</sup>

Figure 5 schematically depicts the basic function principle of a laser induced breakdown spectroscopy. A conventional LIBS system consist of a pulsed laser, and subsequent optics to focus the laser light onto the solid or liquid sample surface. An ad-

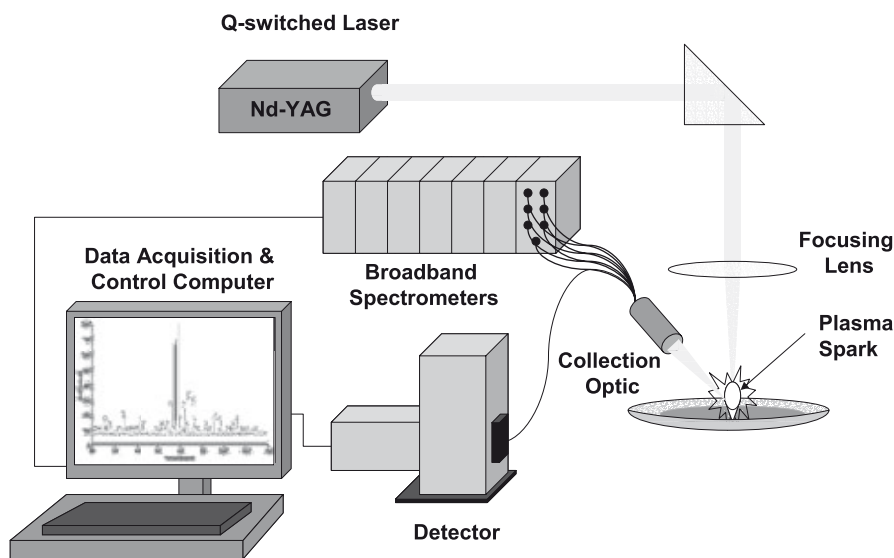


Fig. 5: Schematic principle of a LIBS system<sup>[18]</sup>

ditional optical system collects the emitted light during relaxation into the energetic ground state of the plasma atoms and a connected spectrometer analyzes the emitted light in the range from 200 nm to 980 nm. All chemical elements in the excited state emit a characteristic radiation which in consequence allows to specify the accurate elemental qualitative and quantitative composition of the sample. The data collecting process is personal computer controlled which ensures the ability to collect and analyze almost in real-time. A very detailed introduction to LIBS sensor systems with literature references according environmental monitoring can be found in reference [18]. A prototype man-portable mobile LIBS sensor systems was used to detect and discriminate landmines from different countries and manufacturers.<sup>[19]</sup>

### 1.3.3.3 *Evanescent fiber-optic chemical sensor*

An extensive evaluation of an evanescent fiber-optic chemical sensor to monitor chemical volatile compounds like mono, di-, tri- and tetra-chlorinated short chain-hydrocarbons and toluene can be found in reference [20]. Those kinds of pollutants are very harmful and monitoring in drinking water reservoirs is mandatory.

The principle of an evanescent fiber-optic chemical sensor is based on the phenomena of light travelling through media of different refractive indices. Equation (1) describes the basic physical law of total internal reflection. Total reflection occurs when light traveling in a medium with refractive index  $n_1$  strikes the boundary to a medium with a relatively low refractive index  $n_2$ . As long as the critical angle  $\theta_c$  is slightly decreased in appropriate manner, a small amount of energy penetrates into the media with the lower refractive index, schematically illustrated in figure 6. Volatile compounds at the boundary will interact with the evanescent wave and will cause a specific increase or decrease of intensity which is recorded as the measurement sensor signal. Both quantitative and qualitative information about species in aqueous media can be obtained.

$$\theta_c = \sin^{-1} \left( \frac{n_2}{n_1} \right) \quad (1)$$



## 1.3.3.4 Oxide metal gas sensors

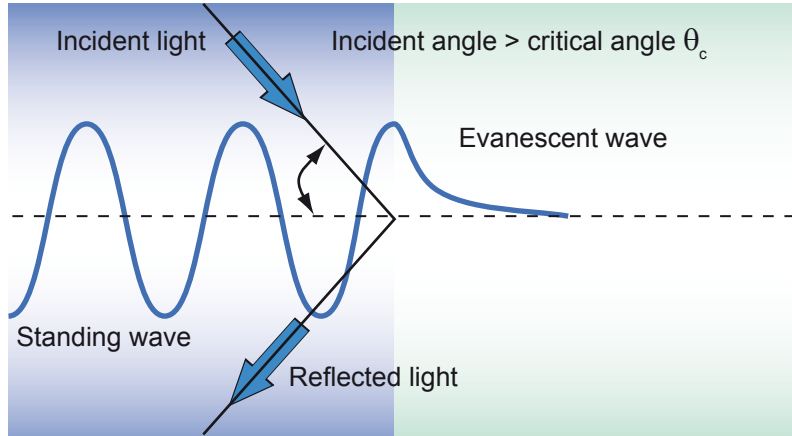


Fig. 6: Illustration of evanescent wave

The development of metal oxide gas sensors is connected to the development of micro fabrication silicon process technology. The metalloid silicon is very often chosen as substrate material due to its excellent ability to integrate sensing and signal processing electronics into the same substrates. The required techniques are readily available

Materials reported for gas-sensing applications	Gaseous species	Operating temperature range (°C)	Physical state & form of the material	Processing compatibility for integrated sensor development	Reference
Metal oxide semiconductors	General	N.A.	Thin films (Resistive type)	Not possible	28, 31–33
n-Type metal oxides	General	N.A.	—	Not possible	34
SnO <sub>2</sub> , ZnO, TiO <sub>2</sub> , Ga <sub>2</sub> O <sub>3</sub>	General	N.A.	Thin films	Not possible	33
Semiconductor metal oxides	General	300 to 350	Thin films	?	35
Semiconducting metal oxides	O <sub>2</sub>	250 to 1000	Thin and thick films	?	36
Semiconducting metal oxides	Hydrocarbons	200 to 400	Thick film paste	Hybrid microcircuits	37
Non-stoichiometric perovskite materials	General	490	Thin films	?	38
Different oxides	Hydrocarbons	250 to 300	Chip form	?	9
Porous glass	NO <sub>2</sub>	−196 (LN <sub>2</sub> )	Thick sheets	Not possible	39
Pt, Au, Ni, Mo Thin films with SnO <sub>2</sub> coating	CO	20 to 280	Sandwich structures	Silicon processing	40
Composite metal structures on MIS devices	NO <sub>x</sub>				
	General	25 to 200	M-I-S devices	Silicon processing	41

LN<sub>2</sub>—Liquid Nitrogen; N.A.—Not available.

Tab. 2: General classification of metal oxide sensors<sup>[21]</sup>

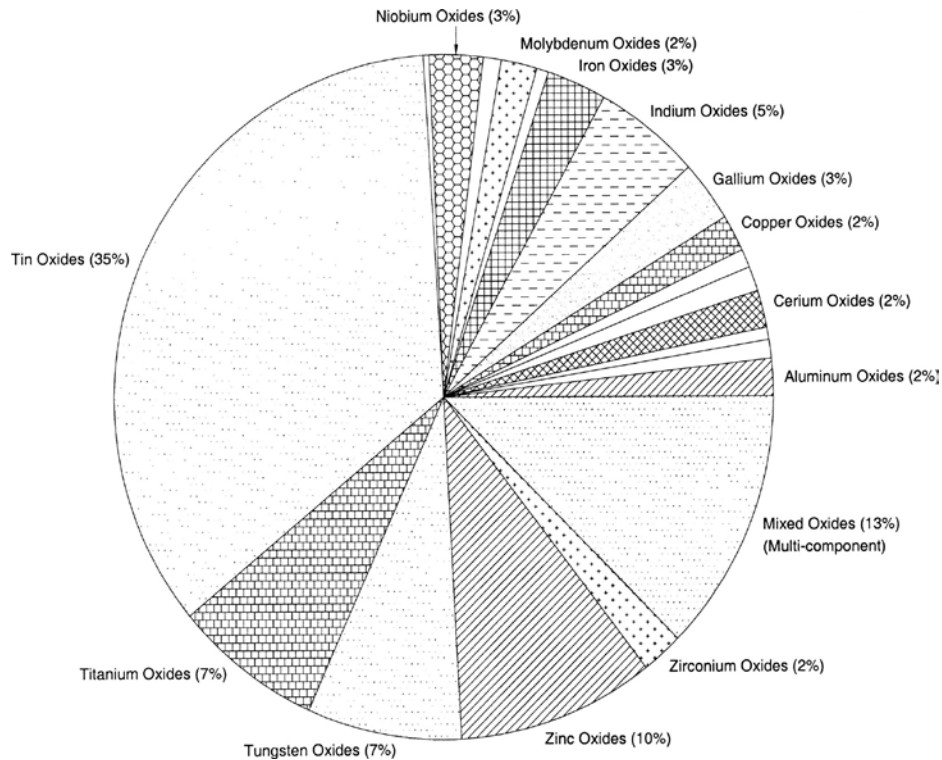


Fig. 7: Relative quota of metal oxides subject of sensor related research from the past to 2004<sup>[21]</sup>

because of rapid progress of lithographic patterning and miniaturization techniques developed in the last years for microchip industries. Recent research reports have confirmed the benefits of nano-engineering on sensor performance. *Rella et al.*<sup>[22]</sup> demonstrated good response to  $\text{NO}_2$  and  $\text{CO}$  when the  $\text{SnO}_2$  grain size (metal oxide sensor material) was below 10 nm.

The demand of suitable sensor systems or arrays determines that not only one metal oxide coated sensor system can be used to detect or monitor volatile organic compounds (VOC). A huge variety of different materials have been developed in order to satisfy the requirements of increasing gas sensitivity and improvement of their selectivity, reduction of electric power consumption by resistive heater of gas sensors and decreasing response and recovery times.<sup>[23]</sup> As given in table 2, taken from reference [21], metal oxide sensors can be categorized into several groups. It is remarkable, that most metal oxide sensors operate at relatively high temperatures above 200 °C.

The sensing principle of resistive sensors is based on changes of the resistance of a semi-conducting metal oxide thin film caused by adsorption of gas molecules. The

gas-solid interactions influence the density of electronic species in the film, hence the resistance of the film. Sometimes metal oxide sensors are also called chemiresistors. A detailed recommended overview about metal oxide sensor is presented by *Eranna et al.*<sup>[21]</sup> As listed in figure 7 taken from reference [21], a variety of different metal oxide sensor is necessary to cover various VOCs, whereas the focus of research still is SnO<sub>2</sub>. The data has been collected from the authors up to year 2004 and represents the relative ratio of publications based on different oxides.

### 1.3.3.5 *Acoustic wave sensor arrays*

As the focus of this work is the monitoring of concentration variations of VOCs a review about existing applications based on acoustic wave sensors shall be given. Due to enormous interest in the field of acoustic sensors, either applied for gaseous species or as biosensor in liquid media, only an incomplete overview can be given. The operating mode of acoustic wave sensor systems is explained starting on page 79.

A closer look on the relevance of acoustic wave sensors, performed by literature search<sup>7</sup>,

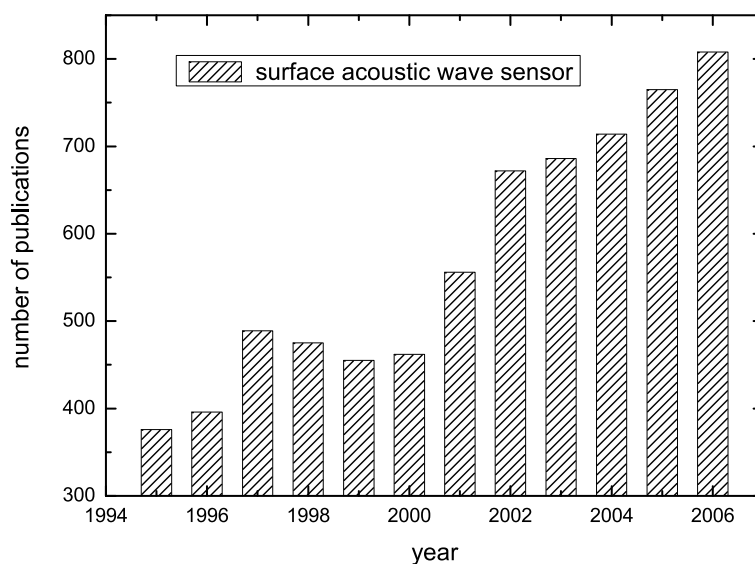


Fig. 8: Publications related to surface acoustic wave sensors

reveals the renaissance of those kinds of sensors in the recent years. The search term “*acoustic wave sensor*” was used. Figure 8 displays the increasing tendency of publications engaging with surface acoustic wave sensors. The interest in SAW sensors even decreased from 1997 till 2000 but dramatically increased from year 2000. Huge groups like the \$78 billion revenue (in 2006) strong Lockheed Martin<sup>8</sup> compete in the battle for intelligent and efficient sensor systems<sup>[24]</sup>, motivated by million of dollar programs of the US defense department.<sup>9</sup>

Analogous tendencies are observed with the number of publications dealing with quartz crystal micro balance sensors (QCM, in details explained on page 83). According to figure 9 from 2001 on a strong interest in QCM based sensors is observed which might also be connected to the terrorist attack in 2001 in New York. The data was collected with the online database search engine SciFinder 2006.

Early publications report the successful application of acoustic wave techniques as chemical detector systems, e.g. detection of 1,3-butadiene at low ppm concentrations with a ligand coated surface<sup>[25]</sup> or one of the first gas sensing systems based on surface acoustic waves, reported by *D’Amico*<sup>[26]</sup> in 1982. Recent developments in the field of

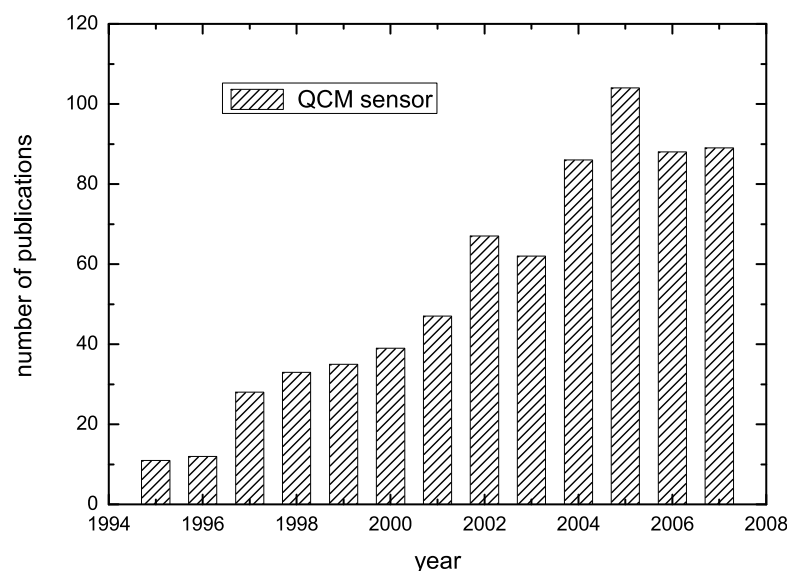


Fig. 9: Publications related to quartz crystal balance sensors until 2007/07.

<sup>7</sup> SciFinder Scholar 2006

<sup>8</sup> Lockheed Martin Corporation, 6801 Rockledge Drive, Bethesda, MD 20817, USA.

<sup>9</sup> US Naval Research Lab, 4555 Overlook Ave., SW, Washington, DC 20375, USA.

acoustic wave sensor investigate various polymer coatings as active sensing elements on a single substrate.<sup>[27]</sup>

The authors applied the following polymer coatings in order to detect and classify chemical warfare agents: polyisobutylene (PIB), polyepichlorohydrin (PECH), polydimethylsiloxane (PDMS), polybutadiene (PPD) and polyisoprene (PIP).

Figure 10 displays the results for the analyte  $\text{CH}_2\text{Cl}_2$ . As evident, the researchers could hardly distinguish and discriminate the injected agent with the polymer coatings, except the higher frequency shift with PIP coated sensor device.

Furthermore, increasing concentrations did not cause a proportional response: from 1 ppm to 3 ppm no signal change (frequency shift) was observed. A quite slight increase of a frequency shift is detectable starting with concentrations  $> 4$  ppm  $\text{CH}_2\text{Cl}_2$ .

Hence, the reported sensor system is thereby not able to work in parallel mode with multi-coatings and to gain information about the analyte via cognitive recognition.

*Penza et al.*<sup>[28]</sup> presented in 1999 a surface acoustic wave sensor device which monitors humidity with polyvinyl-alcohol coated sensor delay lines. Cross signals due to

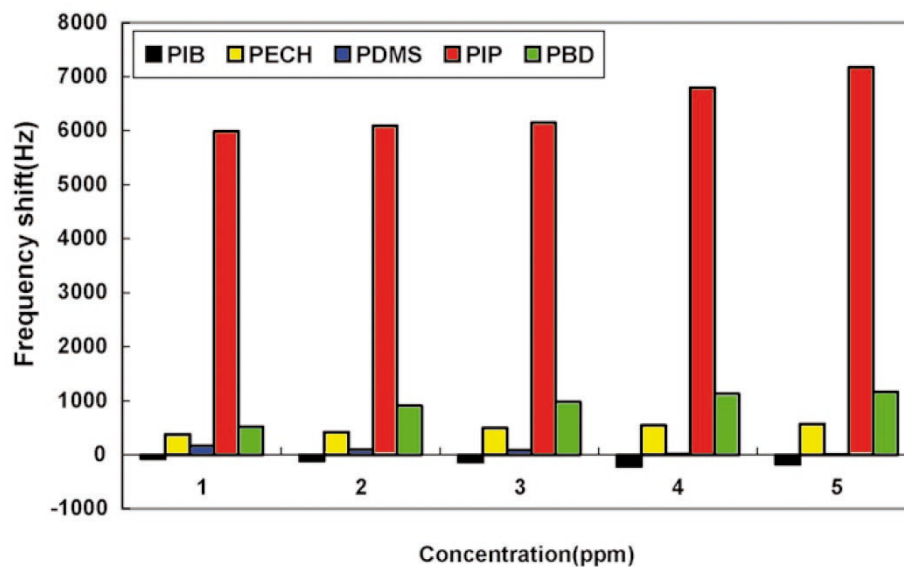


Fig. 10: Sensor response of polyisobutylene (black), polychlorohydrin (yellow), polydimethylsiloxane (blue), polybutadiene (red) and polyisoprene (green) exposed to vaporized methylenedichloride<sup>[27]</sup>

alcohol vapor are not negligible (see figure 11) and are one of the limitations of the presented sensor approach.

A more sophisticated approach integrating several miniaturized acoustic wave gas sensor elements onto one single sensor device was presented by *Plöttner et al*<sup>[29]</sup>. on a IEEE conference in 2001. On a sensing delay line the conductivity dependency of a copper phthalocyanine (Cu-Pc) exposed to oxidizing or reducing gases was investigated. It turned out that a high sensor sensitivity was achieved during monitoring NO<sub>2</sub> (0.2 ppm) whereas ambient humidity as extrinsic factor heavily disturbed the quality

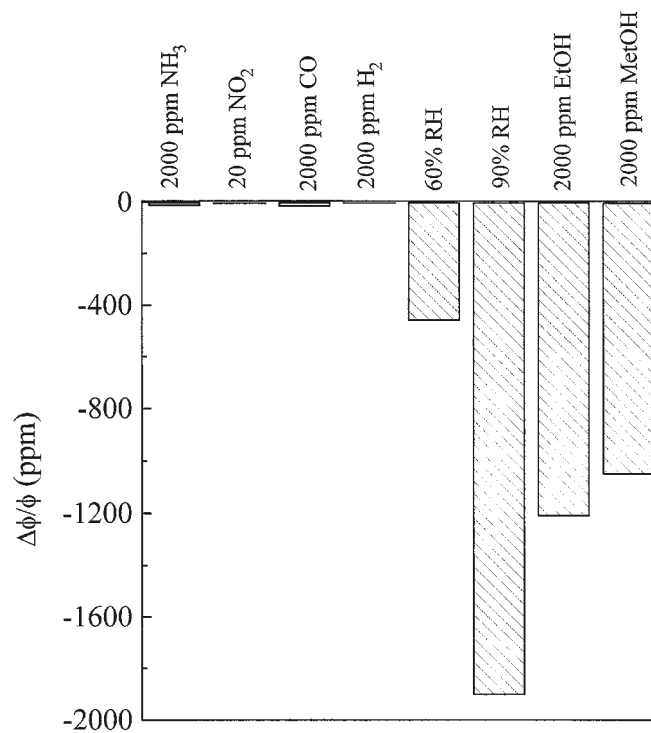


Fig. 11: Frequency shift (sensor signal) caused by various vapors

of the measurements. The authors strongly recommend an additional humidity sensor to calibrate the Cu-Pc sensor system.

Motivated by the reported successful approaches, one of the aims of this work was to

evaluate the possibility of building a sensor or sensor array based on siliceous size selective materials, e.g. zeolites and functionalized mesoporous silica materials. Inspired by the publication of *Cho et al.*<sup>[30]</sup> in 2002 who applied the so called pin-printing approach (in details explained on page 61) to build an integrated chemical sensor array platform the described contact-printing approach was evaluated in order to pattern siliceous porous materials. *Cho et al.* demonstrated a 100 sensor array panel by preparing up to 100 discrete O<sub>2</sub>-responsive sensor elements on the face of a single light emitting diode (LED). The sensor elements were printed onto a specially treated LED surface and one single sensor element consist of the oxygen sensitive Tris(4,7-diphenyl-1,10-phenanthroline) ruthenium(II) chloride pentahydrate ([Ru(dpp)<sub>3</sub>]Cl<sub>2</sub>).

The luminescence signal was collected with a microscope and detected with a CCD. Figure 12 shows a scanning electron micrograph image of the developed sensor array surface.

In this present work siliceous highly porous materials were chosen due to high thermal stability, the ability to chemically anchor particles onto appropriate substrates (acoustic wave active materials, e.g. LiNbO<sub>3</sub> or quartz) and to potentially functionalize the nanoscaled crystal surfaces in order to increase selectivity.

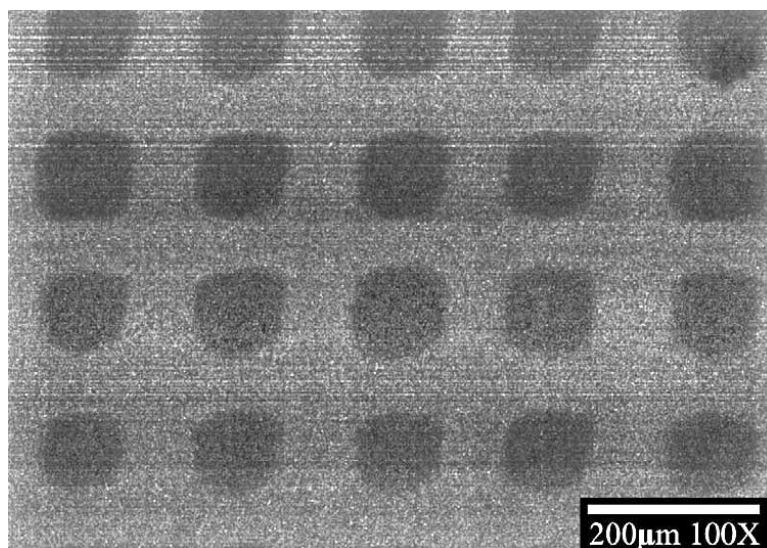


Fig. 12: Scanning electron micrograph image of a LED sensor surface

In a first approach, it was evaluated if the pin-printing technique is an appropriate tool to pattern silica materials at the micrometer scale followed by the results of applying the quartz crystal micro balance technique to gain information about the affinity of various gases and vaporized liquids towards different porous materials.

The surface acoustic wave technique was applied to demonstrate the proof of concept with solid state material sensors on a piezoelectric material. The principle of localized addressing of single sensor elements on a sensor device was demonstrated and published.<sup>[31]</sup>



## 2 Synthesis, characterisation, sample preparation and material properties

### 2.1 Mesoporous materials

Colloidal suspensions of all mesoporous and microporous samples were spin-coated onto the cleaned and dried QCM chip after the determination of its individual resonance frequency (see on page 92) and subsequently calcined at appropriate temperature with respect to potentially introduced chemical functionality -R. In order to remove organic template molecules the porous samples were either template extracted or calcined in air. To prove the existence of embedded species -R several techniques were employed before and after the post synthesis treatments.

The general synthesis route is based on the description of reference [32]. The materials

sample ID	material	synthesis info
QCM-E	non-functionalized mesoporous silica	synthesized according to reference [32]
QCM-Ph	phenyl-functionalized mesoporous silica	synthesized according to reference [32]
QCM-CN	cyano-functionalized mesoporous silica	synthesized according to reference [32]
QCM-Vinyl	vinyl-functionalized mesoporous silica	synthesized according to reference [32]
QCM-SH	thiol-functionalized mesoporous silica	synthesized according to reference [32]
Sil-1	nanosized zeolite silicalte-1	synthesized according to reference [32]
ZSM-5	nanosized zeolite ZSM-5	synthesized according to reference [32]
Zeo- $\beta$	nanosized zeolite beta	synthesized according to reference [32]
MSN-I	non-functionalized mesoporous silica	synthesized by <i>J. Kecht</i> <sup>[33]</sup> according to reference [32]
MSN-II	phenyl-functionalized mesoporous silica (grafted moiety)	synthesized by <i>J. Kecht</i> <sup>[33]</sup> according to reference [32]
MSN-III	phenyl-functionalized mesoporous silica (co-condensed moiety)	synthesized by <i>J. Kecht</i> <sup>[33]</sup> according to reference [32]
Cu <sub>3</sub> BTC <sub>2</sub>	porous copper 1,3,5-benzotricarboxylate metal organic framework	synthesized by <i>E. Biemmi</i> <sup>[134]</sup>

Tab. 3: Sample ID codes and synthesis information

were characterized with different analytical methods. In some cases the characterisation results are referred to reference [32] due to identical batch and post synthesis treatments.

The colloidal mesoporous particles were synthesized in aqueous solution purified with a Millipore Milli-Q Academic A10 system<sup>10</sup> to remove potentially remaining organic molecules from the reaction solvent. Unfunctionalized mesoporous sample materials were synthesized with pure tetraethoxysilane (TEOS) as silica source whereas the synthesis of functionalized species was performed with an additional amount of modified silanes (RTES). The process of forming mesoporous structures is a template based approach which utilizes hexadecyltrimethylammoniumchloride (CTAC) as structure directing agent. The co-reactant triethanolamine (TEAH) acts as a basic and complexing catalyst. Table 3 summarizes the prepared samples with corresponding sample code and additionally lists the person who synthesized the samples.

#### 2.1.1 Non-modified pure nanosized mesoporous material: QCM-E

The non-modified sample QCM-E was synthesized as follows;

1 ml (5 mmol) TEOS is combined with 7.3 g (48 mmol) triethanolamine (TEAH) and heated for 25 minutes at 90 °C without stirring. Meanwhile, an aqueous CTAC solution is prepared with 1.3 g (1.1 mmol) 25 %wt CTAC solution diluted with 12.2 ml (0.68 mmol) water and gently heated up 60 °C. Those two warm solutions are combined and stirred 3 h at room temperature. The same volume of ethanol is added and centrifuged for 30 minutes at 19000 rpm. Extraction of the organic template CTAC is performed by heating under reflux at 95 °C for 30 minutes in a solution of 2 g ammonium nitrate in 100 ml ethanol. The nanosized particles are washed with ethanol and subsequently

TEOS	TEAH	CTAC	H <sub>2</sub> O
1	9.6	0.22	140

Tab. 4: Molar ratio of nanosized sample QCM-E

<sup>10</sup> Millipore, 290 Concord Road, Billerica, MA 01821, USA.

centrifuged after each of three extraction steps, resulting in a clear colloidal ethanolic suspension. The molar ratio of the synthesis is listed in table 4.

The colloidal suspensions were spincoated at 3000 rpm onto acoustic wave devices, either QCM or SAW devices.

The spincoated QCM chip is calcined at 350 °C for 360 minutes with a temperature ramp of 0.5 °C per minute. Characterisation of sample QCM-E is either performed with dried bulk material or in colloidal solution (dynamic light scattering measurements).

### 2.1.1.1 Nitrogen sorption data

Nitrogen sorption measurements were performed on the Quantachrome NOVA 4000e sorption measurement system at the temperature of liquid nitrogen (77.35 K). To determine porosity and pore sizes the BJH equilibrium model (Barrett, Joyner, Halenda)<sup>[34]</sup> embedded in the Quantachrome software Autosorb V1.52<sup>11</sup> is used. The BJH model is known to underestimate pore size of mesoporous materials.<sup>[35], [36]</sup> This explains the observed difference in calculated pore diameter between the BJH and DFT methods of

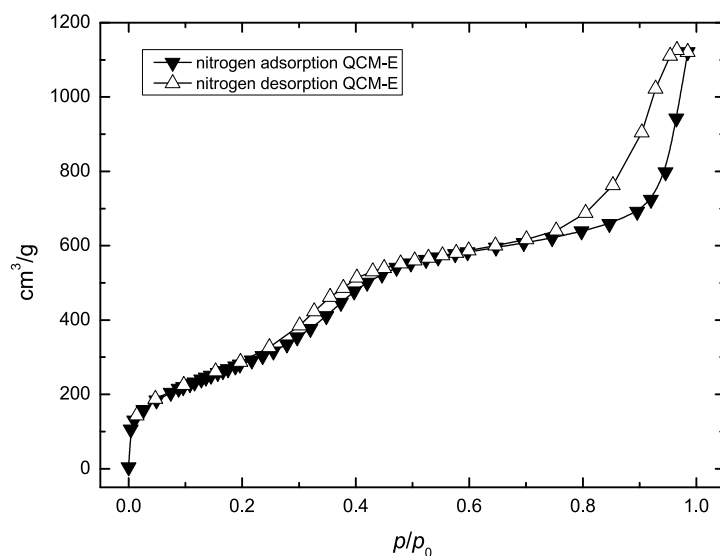


Fig. 13: Nitrogen sorption isotherm for QCM-E at 77 K

<sup>11</sup> Quantachrome GmbH, Rudolf-Diesel-Str. 12, D-85235 Odelzhausen, Germany.

pore size analysis.

Calculations of the surface area are made according to the BET model (Brunauer, Emmett, Teller).<sup>[37]</sup>

In figure 13 the nitrogen sorption isotherm of QCM-E is illustrated. It exhibits a classical type IV isotherm according to the IUPAC classification. The step into capillary condensation at  $p/p_0 \approx 0.3$  is not that sharp and prominent as for example pronounced from Maddox *et al.*<sup>[38]</sup> The authors give a comprehensive description of heterogeneity effects in the pore system and concluding results obtained with Monte-Carlo simulations which predict the nitrogen sorption behavior on the MCM type material.

The experimental nitrogen isotherm data shows explicit hysteresis which is related to the condensation of nitrogen inside the mesopores. The surface area of  $1020 \text{ m}^2 \text{ g}^{-1}$  is calculated referring to the BET theory and data sets below  $p/p_0 < 0.3$ .

The pore size distribution of sample QCM-E can be found in figure 14. Sample QCM-E possesses a comparably narrow pore size distribution and the majority of the pores exhibit a dimension of approximately 3.5 nm, calculated according to the BJH model.

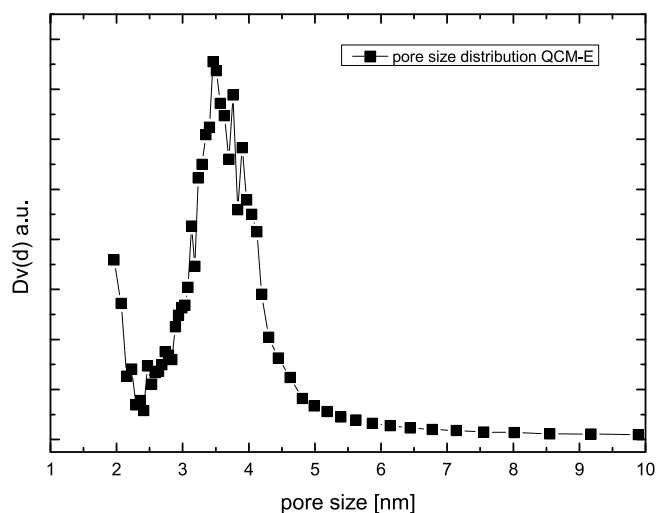


Fig. 14: Pore size distribution of QCM-E

### 2.1.1.2 *Dynamic light scattering measurement*

The results from dynamic light scattering measurements (DLS) are given in figure 15. The unweighted particle size distribution reveals an average particle diameter of 110 to 180 nm (log scale) demonstrating the existence of nanosized species.

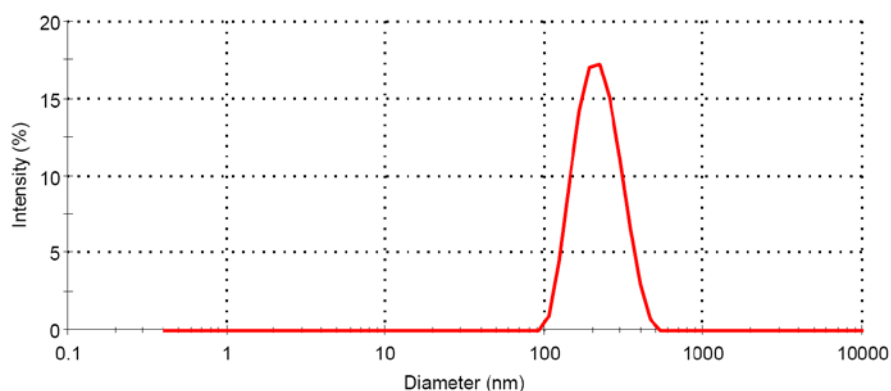


Fig. 15: Particle size distribution of sample QCM-E

### 2.1.1.3 *Transmission electron micrographs*

Transmission electron microscope (TEM) images were taken using a JEOL JEM 2011 microscope operating at 200 kV.

In figure 16 the TEM image of sample QCM-E is presented emphasizing uniform size (90 - 110 nm) and shape of the mesoporous particles. The wormlike irregular structure of the mesoporous material is visible. In contrast to the DSL measurement, TEM investigations do not represent an average particle size but point out randomly chosen particles. Moreover, the significantly higher DLS value for the particle size may also be related to some agglomerates present in the ethanolic solution.

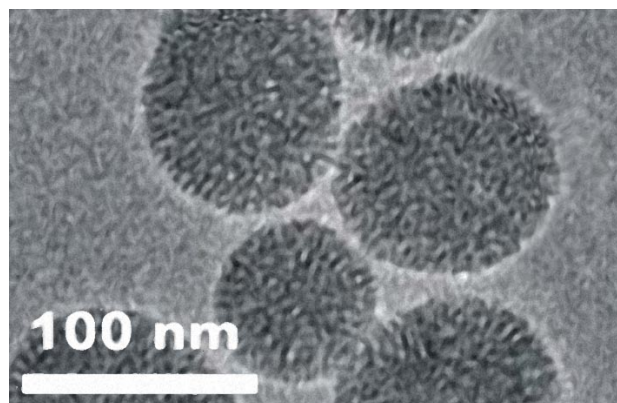


Fig. 16: TEM image of sample QCM-E

#### 2.1.1.4 X-Ray scattering

X-Ray diffractograms were taken on a Scintag XDS 2000 with monochromatic X-Rays ( $\text{Cu-K}_\alpha$ ). The pre-dried powder was measured as thin layer in a polymethylacrylat (PMMA) holder between the theta values  $2\theta = 1 - 10^\circ$  with a step size of  $0.02^\circ \text{ s}^{-1}$ . Figure 17 compares the experimental obtained data for sample QCM-E with reflexes for hexagonal ordered MCM-41 type material.<sup>[39]</sup> In context with data from TEM investigations, it can be concluded that a wormlike structure is present with randomly oriented pores and channels. The obtained X-ray pattern is in good agreement with literature data, discussing explicit wormlike mesoporous silica material KIT-1.<sup>[40]</sup>

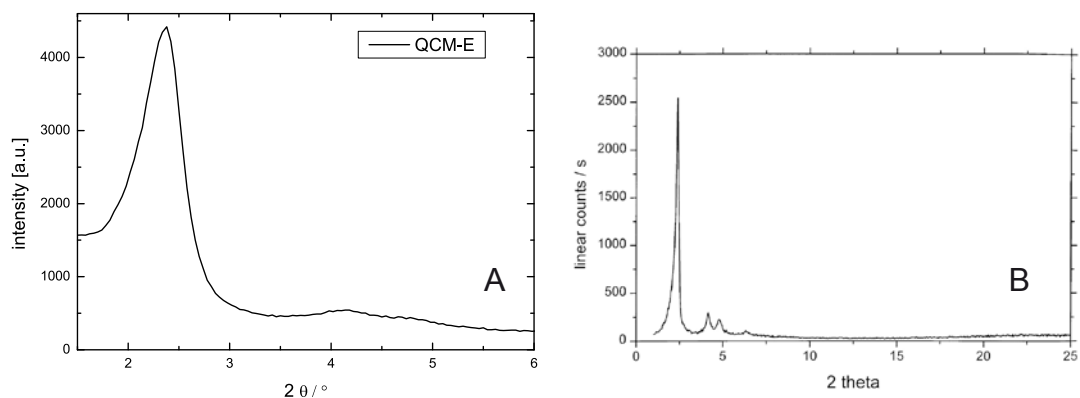


Fig. 17: X-Ray scattering: QCM-E experimental data (A) and hexagonal oriented MCM-41 material from literature data (B)<sup>[39]</sup>

### 2.1.2 Phenyl functionalized nanosized mesoporous material: QCM-Ph

The phenyl functionality is introduced into the silica framework in situ during a co-condensing synthesis process, adding an appropriate portion of phenyltriethoxysilane (Ph-TES) to the batch from the synthesis of QCM-E. The total molar amount of the silica source is furthermore held constant. Analogous treatment and purification steps lead to an ethanolic colloidal suspension. The molar ratio of synthesis reactants is listed in table 5.

TEOS	Ph-TES	TEAH	CTAC	H <sub>2</sub> O
0.9	0.1	9.6	0.22	140

Tab. 5: Molar ratio of nanosized sample QCM-Ph

#### 2.1.2.1 Nitrogen sorption data

The nitrogen sorption isotherm of sample QCM-Ph is presented in figure 18. Compared to the pure siliceous material QCM-E sample QCM-Ph reveals no significant difference in sorption behavior except the overall lower BET surface of 963 m<sup>2</sup> g<sup>-1</sup>.

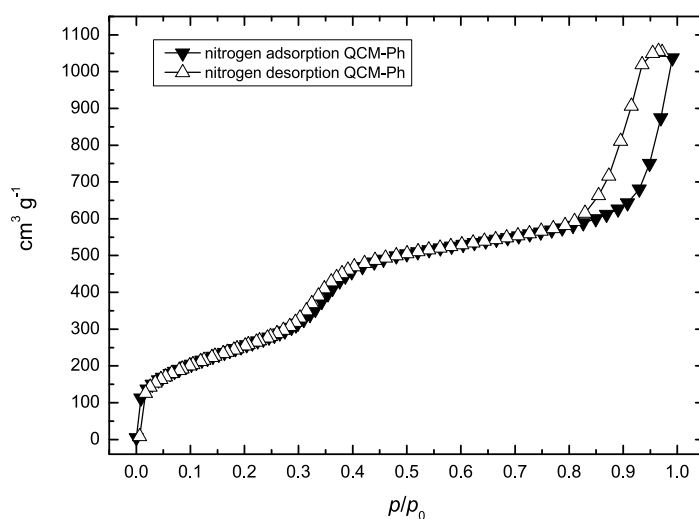


Fig. 18: Nitrogen sorption isotherm for sample QCM-Ph at 77 K

Concerning the decrease from 1020 to 963 m<sup>2</sup> g<sup>-1</sup> one is obliged to judge whether the modification is the reason for the decreased surface area or not. Among several reasons, minor unavoidable synthesis parameter variations or slight differences in ambient conditions (humidity, temperature) in the synthesis route may lead to the decrease of 5.6 %, respectively 57 m<sup>2</sup> g<sup>-1</sup>.

However, the introduction of the phenyl functionality is not negligible. The determination of the pore size distribution results in a distinguishable situation: The introduction of phenyl groups occurs in situ, thus implementing the functionality into the silicon-oxygen framework which implies some phenyl rings extending into the pores of the channel. As a result, a decreasing pore size of approximately 0.3 nm is observed representing the overall Van-der-Waals diameter 0.28 nm of a native phenyl ring. The internal surface property of a phenyl modified mesoporous sample materials is generally discussed in more details involving solid state <sup>29</sup>Si-NMR data starting on page 165.

The pore size distribution of QCM-Ph is displayed in figure 19. A maximum in the distribution is reached at a pore size of 3.2 nm. A negligible fraction of the sample reveals a pore size around 7 nm.

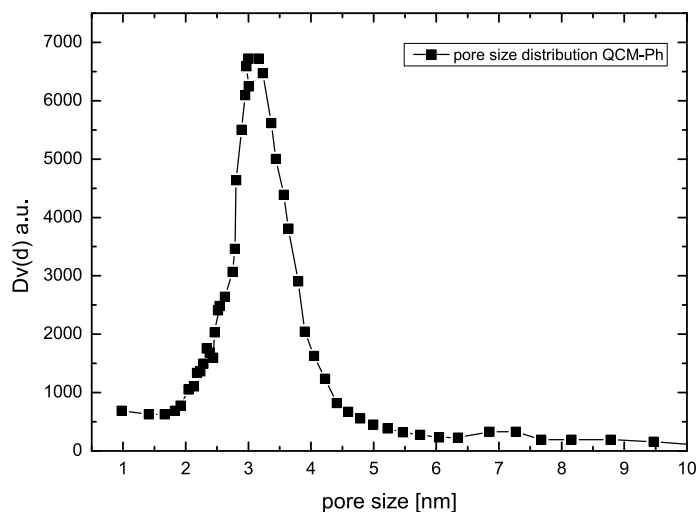


Fig. 19: Pore size distribution of sample QCM-Ph



### 2.1.2.2 *Dynamic light scattering measurement*

The DLS data of sample QCM-Ph show no significant deviation from the expected result, namely an identical particle size distribution as the QCM-E sample (see figure 20). The DLS analysis method is not sensitive enough to determine incremental changes in size due to its averaging nature and model calculation character.

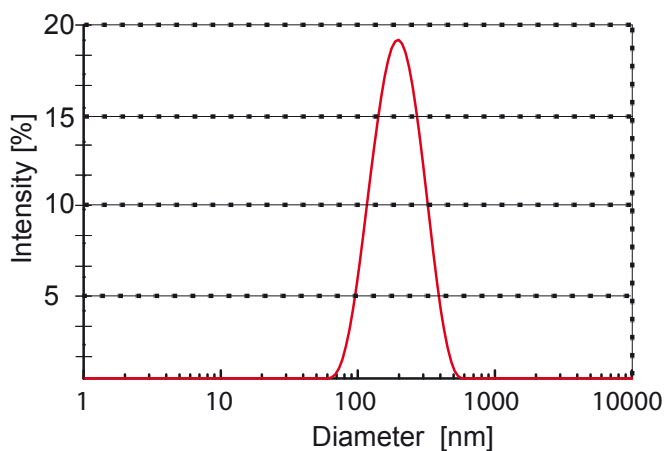


Fig. 20: Particle size distribution of sample QCM-E

### 2.1.2.3 *Transmission electron micrograph*

Although the general morphology of the mesoporous particles of sample QCM-Ph is not dramatically influenced by the Ph-TES additive, an elongation of the spheres is detectable which is displayed in figure 21. An explanation of that phenomenon might be the inter micelle attraction during the synthesis evoked by phenyl - micelle interactions of the Ph-TES silica source. Further information about morphologies of phenyl modified silica species can be found in reference [32].

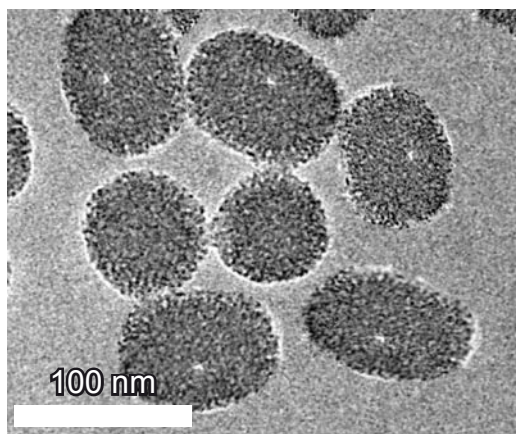


Fig. 21: TEM image of sample QCM-Ph

#### 2.1.2.4 X-Ray scattering

The X-Ray scattering of sample QCM-Ph exhibits no noticeable variance in the position and width of the reflexes, which is in accordance to the non critical introduction of a small (0.28 diameter) organic functionality. Furthermore, the applied equipment (Scintag XDS 2000) is not the appropriate tool to distinguish between a modified and a non modified sample. In figure 22 the data for QCM-Ph is presented, indicating a wormlike structure and morphology.

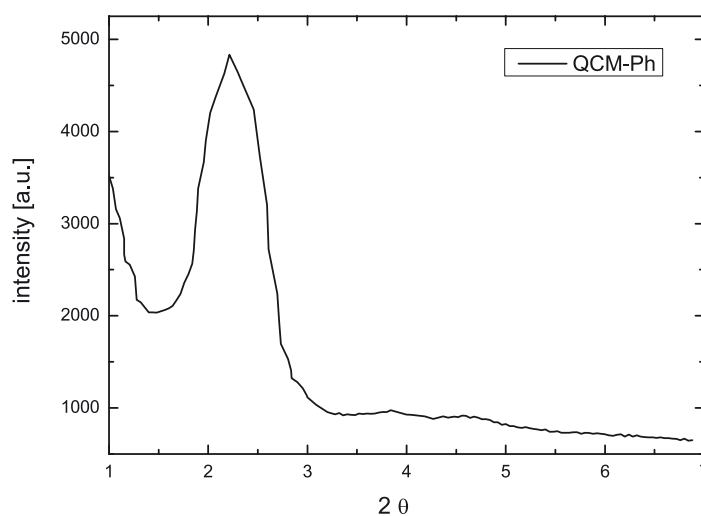


Fig. 22: X-Ray scattering of sample QCM-Ph

### 2.1.2.5 Raman spectroscopy

To prove the successful introduction of organic functional groups (in this case a phenyl group) into the silica network, Raman spectra of the porous thin films on the QCM substrates were collected on a Yvon Horiba HR800 UV Raman microscope using a 632.81 nm Laser.

In figure 23 the direct comparison of both spectra QCM-E (black line) and QCM-Ph (red line) are plotted. As clearly visible, the QCM-Ph sample shows extra bands related to the anchored phenyl ring:

The band at  $\tilde{\nu} = 628 \text{ cm}^{-1}$  is related to an aromatic ring in plane deformation, at  $\tilde{\nu} = 1007 \text{ cm}^{-1}$  to the C-H vibration of a mono substituted phenyl ring (bonded to a silicon atom). At around  $\tilde{\nu} = 1165 \text{ cm}^{-1}$  the aromatic ring =C- deformation vibration is detectable and at  $\tilde{\nu} = 1603 \text{ cm}^{-1}$  the -C=C- vibrations. The aromatic =C-H- vibrations are observed at  $\tilde{\nu} = 3060 \text{ cm}^{-1}$ . The presence of -C-H- stretching vibrations is validated by peaks at  $\tilde{\nu} = 2800 - 3000 \text{ cm}^{-1}$ . The initial Raman spectra is taken after the intense washing process, still offering carbon - hydrogen bond related vibrations. These strong Raman -C-H- stretching vibrations, related to the template molecule hexadecyltrimethylam-

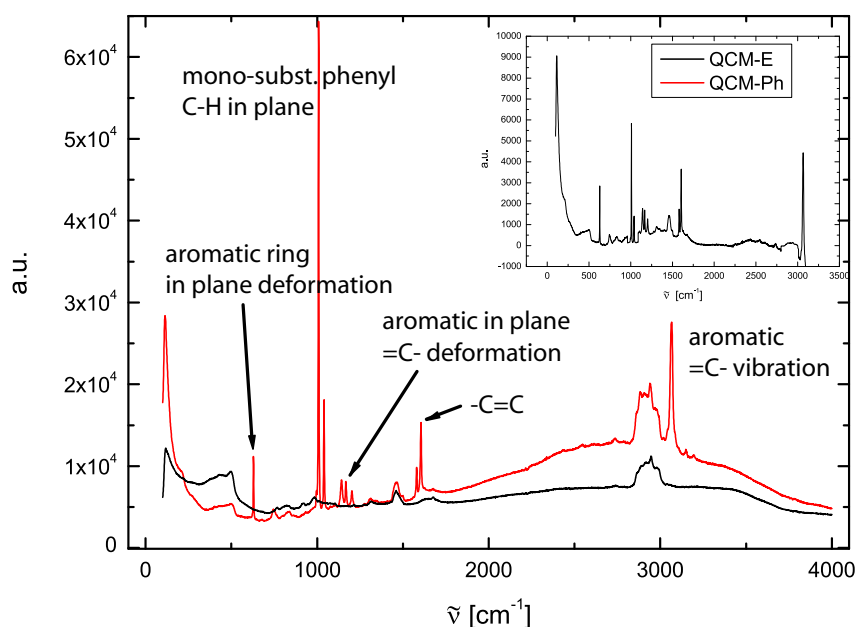


Fig. 23: Raman spectra of sample QCM-E (black) and QCM-Ph (red)  
The inset shows the spectra of QCM-Ph after calcination

moniumchloride, are more or less present in every mesoporous sample investigated in this work. However, the Raman spectroscopic method employed in this work is not to be intended quantitative. It is more likely that a few hydrocarbon fragments could not be totally extracted during the washing step of the final extraction of template molecules. Additionally, the spin-coated samples were spectroscopically investigated after the extraction procedure or calcination process (calcination only performed with sample QCM-E and QCM-Ph) at 350 °C. The small inset in figure 23 demonstrates the Raman bands of sample QCM-Ph after calcination as thin film on the QCM chip. While Raman peaks related to the phenyl ring ( $-C=C-$ ,  $=C-H$  and aromatic  $-C-H$  in plane deformation vibrations) are still present, signals related to C-H hydrocarbon vibrations are almost vanishing.

#### 2.1.2.6 Thermogravimetric analysis (TGA)

The thermogravimetric behavior of modified samples was investigated on a Netzsch STA 440 C TG/DSC at a heating rate of 10 K min<sup>-1</sup> in synthetic air (25 ml min<sup>-1</sup>). In figure 24 the result for sample QCM-Ph is displayed. As clearly visible, the phenyl

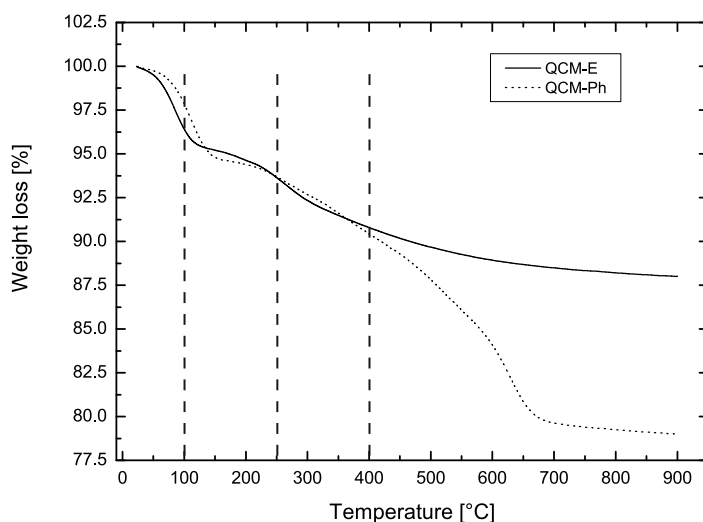


Fig. 24: Thermogravimetric data of QCM-Ph (dotted line) and QCM-E (straight line)

modified sample “survives” the high temperature treatment in air up to 350 °C which is consistent with literature data.<sup>[41], [42]</sup>

Up to 100 °C physisorbed water is removed. From about 100 °C to 250 °C template combustion occurs and above approximately 400 °C the decomposition of phenyl groups is traceable.

A detailed description and interpretation of TGA data of modified mesoporous silica particles can be found in reference [42].

#### 2.1.2.7 Scanning electron micrograph

Due to limitations of *Sauerbrey's* law (details on page 86 and following) important factors regarding gravimetric sorption measurements based on acoustic wave techniques are smoothness and overall thickness of the additional mass density deposited onto the QCM plate. The following SEM results are identical for both sample types, the non-modified sample QCM-E and the chemically modified materials QCM-Ph, QCM-

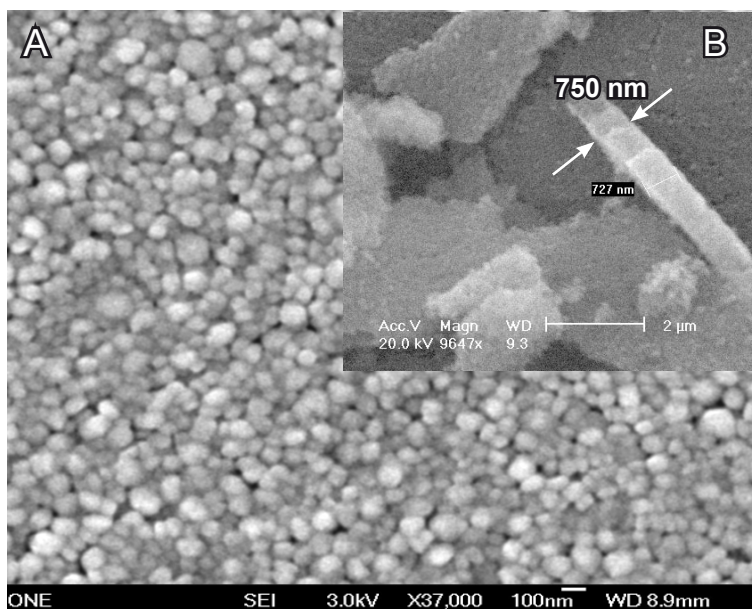


Fig. 25: SEM image of QCM-E (A) and QCM-Ph (B) deposited on a QCM chip

CN, QCM-Vinyl and QCM-SH. This result is not surprising because of analogous and identical synthesis conditions and molar ratios. Furthermore, the molar amount of the RTES (triethoxysilane with a functional group R) added to the reaction mixtures equals only 10 % of the total amount of the silica source tetra-ethoxy-silane (compare table 5).

Scanning electron micrographs (SEM) images were taken on a JEOL JSM 6500F and Philips FEI SEM XL-40 microscope. In figure 25, the evidence for the overall size of the mesoporous particles in the range of 100 nm is confirmed. The spin-coated deposited particle layer exhibits a smooth and homogenous surface morphology (shown for sample QCM-E). The thickness was investigated by scratching the surface layer and measuring the dimensions of the resulting flakes. The layer thickness of sample QCM-Ph is approximately 750 nm (inset B of figure 25) which is within the range of the preconditions of the validity of *Sauerbrey's* law (details on page 84).

### 2.1.3 Cyano functionalized material: QCM-CN

The cyano functionality ( $\text{—C}\equiv\text{N}$ ) was introduced into the silica framework in situ via co-condensation co-condensing process, adding an appropriate portion of cyano-propyltriethoxysilane (CN-TEOS) to the batch from the synthesis of QCM-E. The total amount of the silica source, the silane is furthermore held constant. Identical treatment steps and purification procedures lead to an ethanolic colloidal suspension.

The synthesis conditions and molar ratios are adopted from reference [32]. The molar ratios of the synthesis are given in table 6. In contrast to sample QCM-Ph, the removal of template molecules was performed by a three times repeated extraction with an acidic mixture of 15 ml concentrated HCl and 150 ml EtOH for 24 h at 60 °C.<sup>[167]</sup> Finally the sample was washed three times with ethanol resulting in a colloidal suspen-

TEOS	CN-TEOS	TEAH	CTAC	H <sub>2</sub> O
0.9	0.1	9.6	0.22	140

Tab. 6: Molar ratio of nanosized sample QCM-CN

sion of mesoporous silica particles.

### 2.1.3.1 Nitrogen sorption data

As expected from previous experiments, the nitrogen sorption isotherm does not differ remarkably from the phenyl or non-modified samples, as plotted in figure 26. The isotherm is best described with an IUPAC classified type IV isotherm, well known for mesoporous materials with pore condensation. The calculated surface area according to the BET model is 904 m<sup>2</sup>.

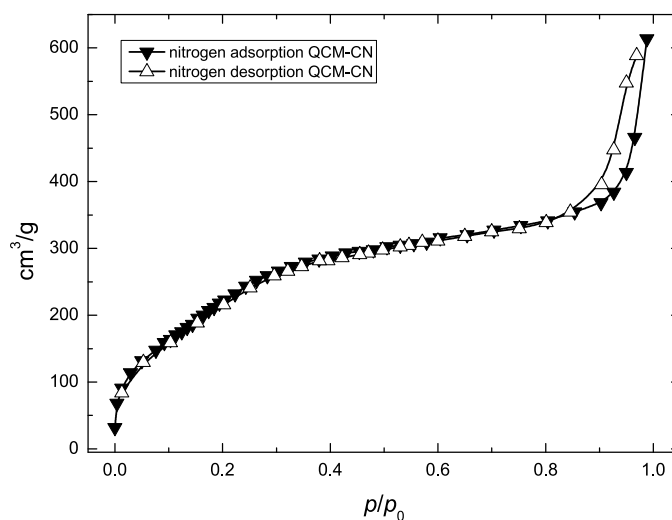


Fig. 26: Nitrogen sorption isotherm for QCM-CN at 77 K

Calculations concerning pore size distribution are processed with the Quantachrome software package according to the BJH model. Results are plotted in figure 27, indicating that the pore size distribution is comparable to sample QCM-Ph. A maximum value is determined at 2.5 nm, whereas the mean value between 1 and 4 nm is 2.2 nm. This implies a decreased pore size from the non-modified sample QCM-E to the cyano

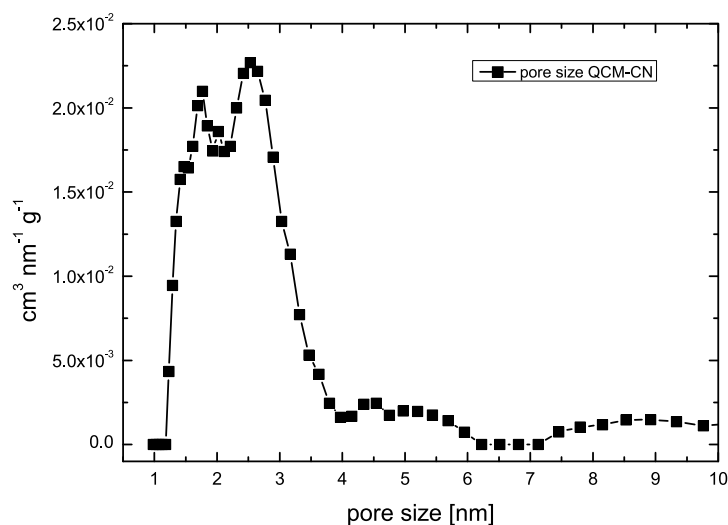


Fig. 27: Pore size distribution of sample QCM-CN

modified sample QCM-CN of about 1.0 nm. The cyanopropyl-functionality is relatively compact with a calculated maximum dimension of 6.4 Å<sup>[88]</sup> (measured from the anchoring Si-atom to the nitrile group). If two cyanopropyl-fragments would face each other attached to the internal wall of a single pore, this value may be doubled, resulting in a maximum decrease of 12.4 Å. The actual decrease of 1.0 nm compared to the non-functionalized sample QCM-E could indicate tilted cyano-propyl chains.

Related to reference [35] there is always a discrepancy between BJH and DFT simulations. Therefore only calculated values obtained from similar simulation methods can be compared to each others.

For example, *Köhn et al.*<sup>[43]</sup> investigated the sorption properties of typical probe molecules (nitrogen, argon and krypton) on mesoporous MCM-48 type material. Depending on the chosen model, either BJH or DFT, and the sorbent gas, discrepancies in pore size arise in the range from 2.05 to 3.04 nm. The authors conclude that additional work is needed to totally understand sorption phenomena inside mesopores.

*Ravikovitch et al.*<sup>[35]</sup> recently investigated the sorption properties of nitrogen and toluene adsorbing on hexagonal ordered MCM-41 type material and plugged hexagonal templated silica (PHTS).<sup>[44]</sup> The authors compared experimental results with simulation data and were confronted with the inhomogeneity of the mesoporous material. Therefore, simulation calculation parameters, like surface heterogeneity or pertuba-



tion energy in the order of 20% of the solid - fluid energy had to be adjusted to match experimental data. In simulations, the authors claim to be able to calculate pore size distributions with the adsorbent toluene in good agreement with data obtained from nitrogen sorption experiments.

### 2.1.3.2 *Dynamic light scattering measurement*

DLS data is available in figure 28. The particle size distribution ranges from 120 - 170 nm. Compared to sample QCM-E, no significant difference is observed.

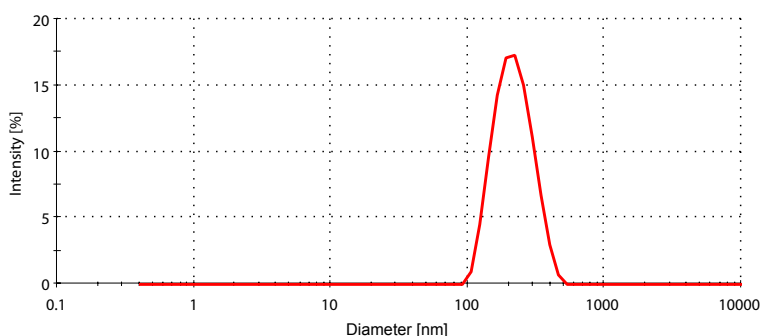


Fig. 28: Particle size distribution of sample QCM-CN

### 2.1.3.3 *X-Ray scattering*

The nature of the mesoporous particles in terms of their structural order is not influenced by adding the cyanopropyltriethoxysilane moiety at the described molar amounts. Controlling measurements reveal reflexes at identical positions with minor variations in intensity which can not be validated quantitatively: The particles are randomly oriented on the X-Ray measurement plate and it can not be guaranteed that an identical sample amount is placed under the X-Ray beam and it is very unlikely to produce exactly identical sample surface in terms of smoothness and height.

The X-ray scattering is identical to figure 22 and valid also for any of the following

functionalized mesoporous material introduced in this chapter.

#### 2.1.3.4 Transmission electron micrograph

As expected, the TEM image of sample QCM-CN (see figure 29) reveals no significant difference compared to the other samples discussed so far. The particle size is determined to be between 100 and 130 nm. Individual particles reveal a wormlike pore structure.<sup>[40]</sup>

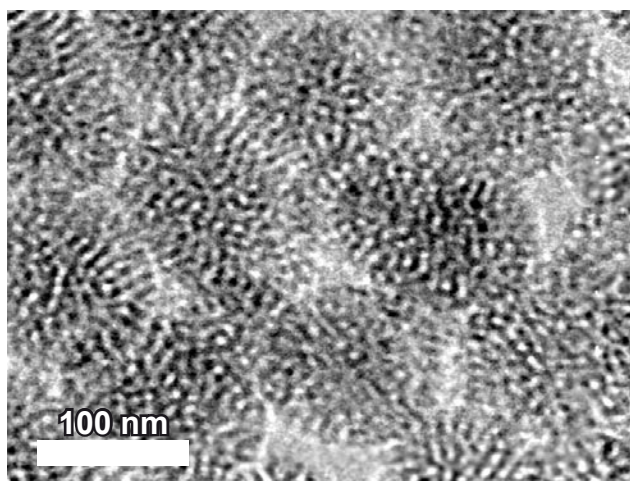


Fig. 29: TEM image of sample QCM-CN

#### 2.1.3.5 Raman spectroscopy

Raman spectroscopic analysis reveals the successful introduction of the nitrile group into the co-condensed material (see figure 30). In the Raman spectra of the cyano-functionalized sample the peak at  $\tilde{\nu}=2256\text{ cm}^{-1}$  can be attributed to the characteristic stretching mode of the nitrile group.<sup>[45]</sup> Other bands are related to the silicon - oxygen network of the mesostructure and to the hydrocarbon vibrational modes of the template molecule at  $\tilde{\nu}=2800 - 3000\text{ cm}^{-1}$ , which disappear almost completely after template

removal by extraction (shifted blue spectra in figure 30).

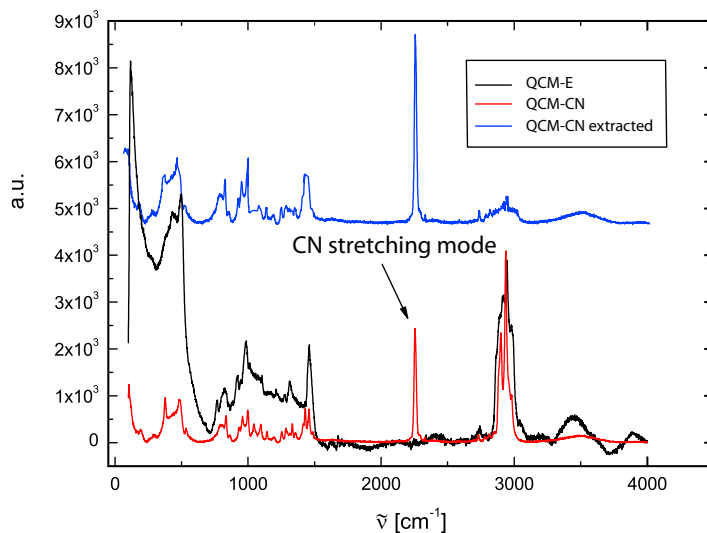


Fig. 30: Raman spectra of sample QCM-E (black), QCM-CN (red) and extracted sample QCM-CN (blue)

#### 2.1.3.6 Thermogravimetric analysis

Thermogravimetric analysis data for sample QCM-CN is shown in figure 31. In contrast to sample QCM-E and QCM-Ph the sample QCM-CN was initially pre-dried at 110 °C for 24 h under a nitrogen flow of 2000 ml min<sup>-1</sup> inside the QCM measurement cell, in order to evaluate the water loss during the TGA experiment. As demonstrated, no remarkable water loss can be observed with the pretreated mesoporous sample. Drawing the conclusion for the QCM measurement itself, the chosen temperature at 100 - 110 °C is sufficient to successfully remove adherent water molecules. Furthermore, the temperature is held constant until frequency stability is reached (see on page 92), ensuring that in any case water molecules are supposed not to be present during sorption experiments. Between 200 °C and 400 °C the combustion of the organic compound is observed and at temperatures above 450 °C the decomposition of the mesoporous network itself is initialized.

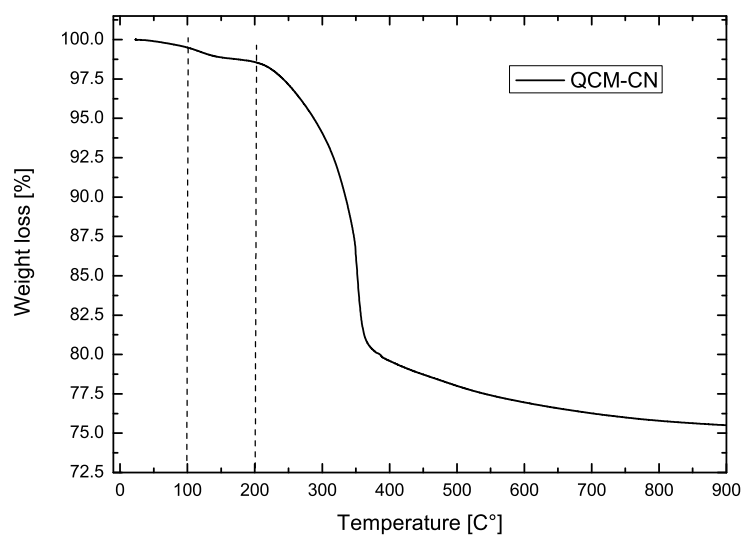


Fig. 31: TGA data obtained from sample QCM-CN

#### 2.1.3.7 Scanning electron micrograph

Figure 32 presents the results of surface and thickness investigations on sample QCM-

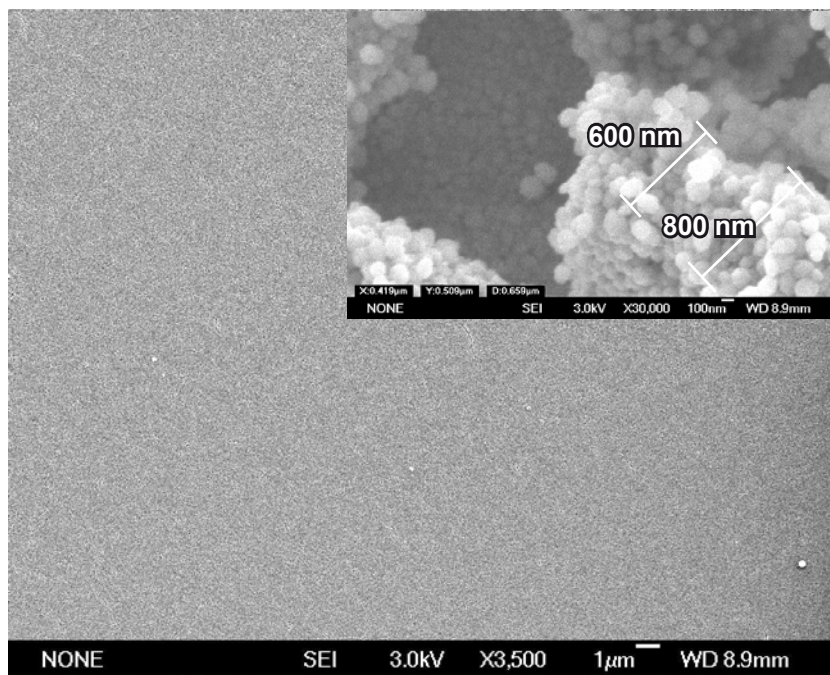


Fig. 32: SEM image of sample QCM-CN

CN spincoated onto a QCM device.

The surface is smooth over the whole Au patterned electrode area (scale bar is 1  $\mu\text{m}$ ) and the overall thickness ranges from 600 - 800 nm (see inset of figure 32). The thickness of the layer was determined by scratching the surface and measuring the thickness of single flakes. The individual size of the round shaped particles is about 100 -130 nm as expected from the results of sample QCM-E and QCM-Ph.

#### 2.1.4 Vinyl functionalized material: QCM-Vinyl

The vinyl functionality ( $-\underset{\text{H}}{\text{C}}=\text{CH}_2$ ) is introduced into the silica framework in situ during a co-condensation process, adding an appropriate portion of vinyltriethoxysilane (Vinyl-TEOS) to the batch from the synthesis of QCM-E. The total amount of the silica source, the silane, is furthermore held constant. Identical treatment steps and purification procedures lead to an ethanolic colloidal suspension.

The synthesis conditions and molar ratio are adopted from reference [32]. The molar ratio of the synthesis is given in table 7.

TEOS	Vinyl-TEOS	TEAH	CTAC	H <sub>2</sub> O
0.9	0.1	9.6	0.22	140

Tab. 7: Molar ratio of nanosized sample QCM-Vinyl

##### 2.1.4.1 Nitrogen sorption data

The recorded isotherm of nitrogen at the temperature of liquid nitrogen is given in figure 33. The evaluation of the surface area according to the BET model reveal a value of 1073  $\text{m}^2 \text{g}^{-1}$  and the shape is classified as type IV isotherm.

Pore size distribution investigations (BJH model) show a narrow distribution with a maximum value for the pore size of 2.6 nm (figure 34). Compared to the non-modified sample QCM-E, the vinyl group functionalized sample exhibits a decrease in pore size

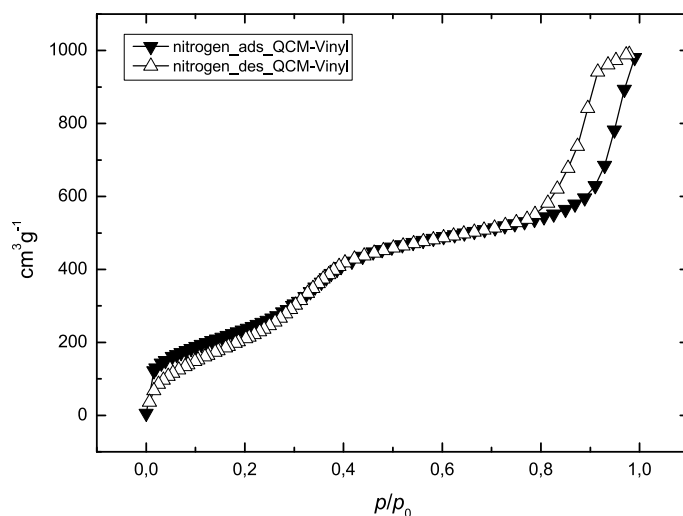


Fig. 33: Nitrogen sorption isotherm for QCM-Vinyl at 77 K

of 0.9 nm. Investigations of the vinyl group itself reveal a maximum molecule dimension of 2.8 Å from the terminal CH<sub>2</sub>-group to the anchoring silicon atom. At a first glance, two vinyl fragments anchored on the pore wall and facing each other would result in a decrease of approximately 0.6 nm leaving a gap between BJH calculations and the simple model of fragment dimensions.

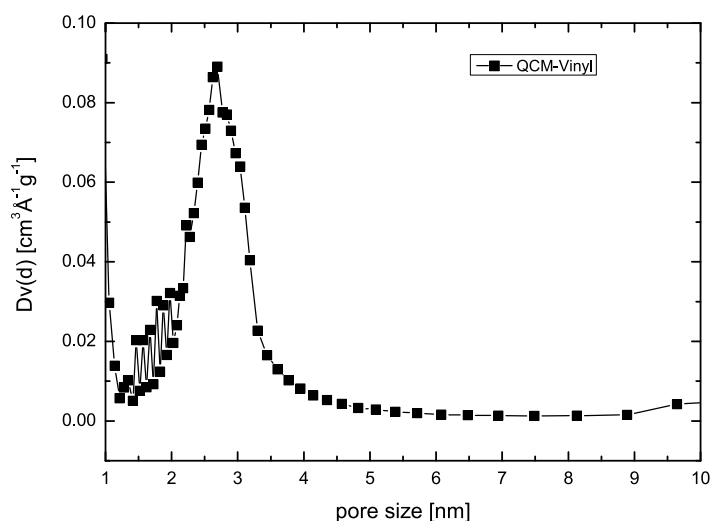


Fig. 34: Pore size distribution of sample QCM-Vinyl (BJH model)

#### 2.1.4.2 Dynamic light scattering measurement

As illustrated in figure 35 the DLS data implies no significant change in particle sizes caused by the introduction of the organic vinyl moiety. Approximately, the particle size ranges from 100 - 200 nm, which is similar to the non-modified sample QCM-E.

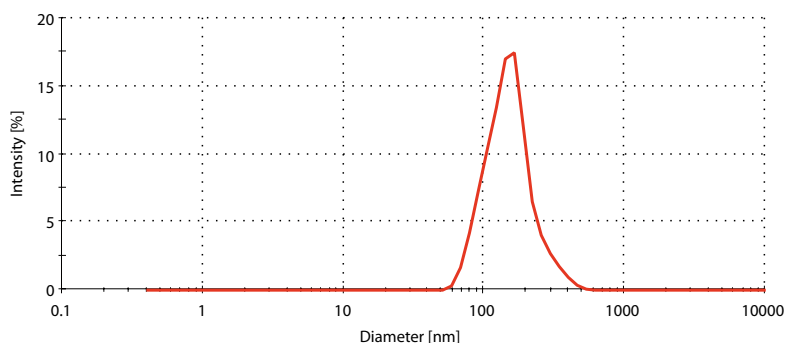


Fig. 35: Particle size distribution of sample QCM-Vinyl

#### 2.1.4.3 Raman spectroscopy

Raman spectroscopic analysis reveals the successful introduction of the vinyl group into the co-condensed matter (see figure 36). The peak at  $\tilde{\nu}=3072\text{ cm}^{-1}$  is related to the terminal  $=\text{CH}_2$  olefinic C-H stretching vibrations of the organic vinyl fragment.<sup>[46]</sup> At  $\tilde{\nu}=1607\text{ cm}^{-1}$  the C=C stretching bond is observed and at  $\tilde{\nu}=1415\text{ cm}^{-1}$  characteristic C-H alkene bending motions are evoked.<sup>[46]</sup> Clear evidence of the existence of a vinyl group is thereby ensured. After template extraction the vinyl functional group remains anchored to the siliceous network (see figure 37). The region from  $\tilde{\nu}=2900$  to  $3050\text{ cm}^{-1}$  is usually related to C-H stretching modes originating from alkanes but in this case overlapped by olefinic hydrogens. As already mentioned, the Raman spectra data are not quantitative due to the analysis of a specific small region on the coated QCM chip as well as other reasons, hence no qualification or judgement on the residual amount can be given.

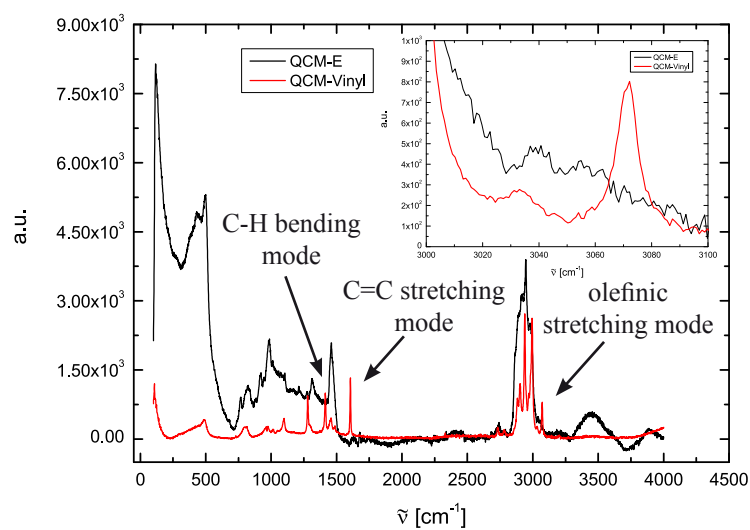


Fig. 36: Raman spectra of sample QCM-E (black) and QCM-Vinyl (red)

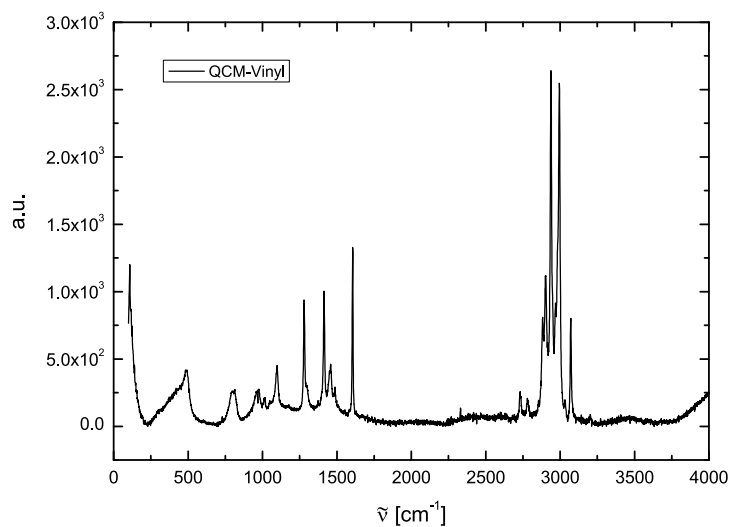


Fig. 37: Raman spectra of extracted sample QCM-Vinyl

### 2.1.5 Mercapto functionalized material: QCM-SH

The mercapto functionality ( $\text{—SH}$ ) is embedded into the silica framework according to the described method in situ during synthesis. Table 8 displays the molar ratios of the reaction mixture. To introduce the mercapto group, 10 % of the originally included



silica source TEOS is exchanged with mercaptopropyltriethoxysilane (SH-TES). Other synthesis parameters, in details listed on page 23, are held constant to maintain the inter-comparability of the mesoporous sample materials.

Finally, the ethanolic colloidal suspension is spin-coated onto a QCM chip.

TEOS	SH-TES	TEAH	CTAC	H <sub>2</sub> O
0.9	0.1	9.6	0.22	140

Tab. 8: Molar ratio of nanosized sample QCM-SH

### 2.1.5.1 Nitrogen sorption data

The nitrogen sorption isotherm, acquired at the temperature of liquid nitrogen, is shown in figure 38 implying evidence of a highly porous material having mesopores. According to the IUPAC classification system, the isotherm can be classified as type IV. Surface area calculations regarding the BET model exhibit a maximum surface area of 946 m<sup>2</sup> g<sup>-1</sup>. Pore size evaluations using the BJH model reveal a pore distribution given in figure 39. At the maximum of the graph the pore size is determined to 2.1 nm.

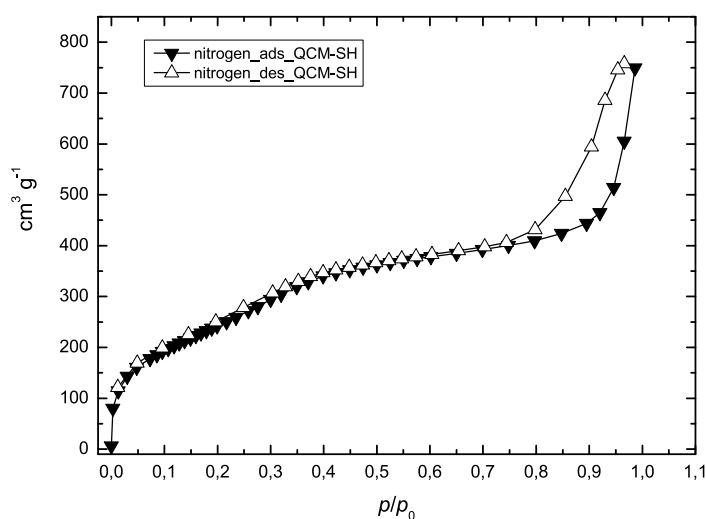


Fig. 38: Nitrogen sorption isotherm of sample QCM-SH

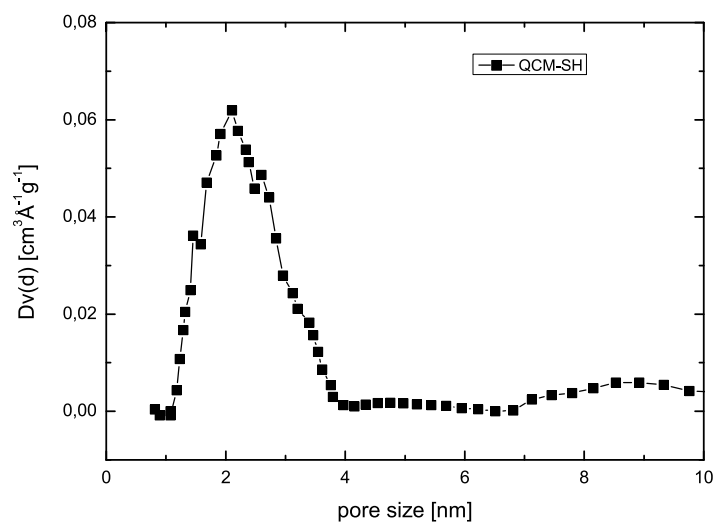


Fig. 39: Pore size distribution sample QCM-SH

#### 2.1.5.2 Dynamic light scattering measurement

The particle size distribution is displayed in figure 40 revealing dimensions ranging from 90 - 130 nm. This result is consistent with the previously investigated samples. Extensive investigations of particle size and morphology on mercapto functionalized colloidal mesoporous silica particles are found in the recent literature.<sup>[47]</sup>

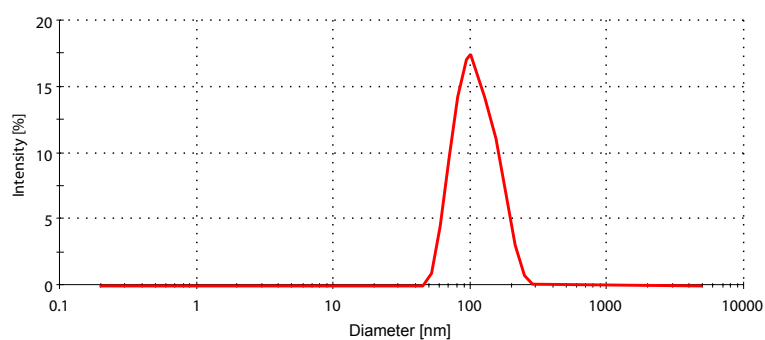


Fig. 40: Particle size distribution of sample QCM-SH

### 2.1.5.3 Raman spectroscopy

Raman spectroscopic investigations prove the embedding of organic moieties, in this case a mercaptopropyl, into the siliceous framework.

In figure 41 the characteristic Raman bands are marked and assigned as follows:

At  $2582\text{ cm}^{-1}$  the S-H stretching mode is observed.<sup>[46]</sup> At the wave number of  $\tilde{\nu}=656\text{ cm}^{-1}$  the characteristic C-S stretching vibration is present.

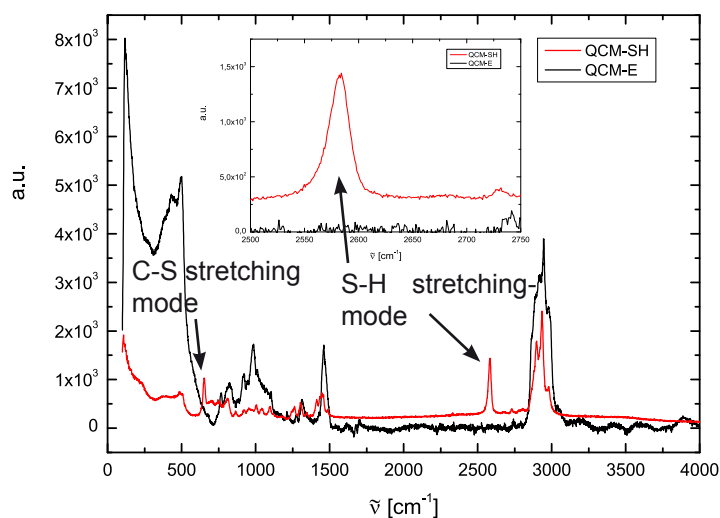


Fig. 41: Raman spectra of sample QCM-SH (red) and QCM-E (black)

Comparable results arise after the post synthesis extraction treatment (figure 42). The significant identifying modes at  $\tilde{\nu}=656\text{ cm}^{-1}$  and  $2582\text{ cm}^{-1}$  are still detectable. In contrast, the ratio between the strong Raman band at  $\tilde{\nu}=2582\text{ cm}^{-1}$  and the C-H stretching modes related to template fragments ( $\tilde{\nu}=2800 - 2950\text{ cm}^{-1}$ ) is shifted due to a decreased intensity of template related C-H vibrational modes.

Hence, it is important to mention that still few alkyl chain fragments are observed in the Raman spectra. Nevertheless, the spectroscopic analysis can not be regarded as a quantitative method due to different samples investigated: the as synthesized material is measured as dried powder and the extracted sample is investigated as spincoated

layer on the QCM chip. To take into account different samples and focal distances varying Raman laser focus spot sizes were adjusted to obtain optimized spectroscopic measurement results in general.

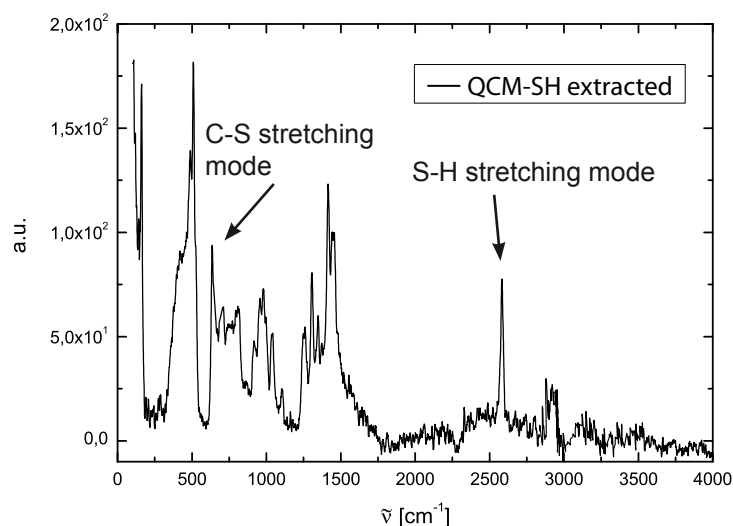


Fig. 42: Raman spectra of sample QCM-SH after template extraction

## 2.2 Microporous materials

Microporous materials, mainly zeolites of different kinds, were synthesized according to available literature synthesis parameters (cited individually) or obtained from co-workers in the group of Prof. Bein. If a microporous material has been synthesized by co-workers it is listed in table 3.

TEOS	EtOH	H <sub>2</sub> O	Na <sub>2</sub> O	TPAOH
25	100	420	0.13	9

Tab. 9: Molar ratio of nanosized sample Sil-1

### 2.2.1 Pure siliceous zeolite silicalite-1: Sil-1

The zeolite silicalite-1 is synthesized according to reference 48. The molar ratio of the synthesis of silicalite-1 is given in table 9.

20 g (96 mmol) silica source TEOS, 35.0 g (172 mmol) of a 1 molar tetrapropylammoniumhydroxide (TPAOH) solution, 30.9 mg (0.50 mmol) sodiumoxide ( $\text{Na}_2\text{O}$ ), 5.91 ml (0.33 mmol) double distilled (dd) and cleaned (Millipore cleaning system) water and 22.4 ml (384 mmol) ethanol are mixed together and stirred at room temperature for 2 h. Subsequently, the reaction mixture is heated for 2 h at 90 °C. After cooling down again to room temperature the colloidal suspension is centrifuged for 1 h at 19000 rpm. The residual solid is redispersed in water and treated in an ultrasonic bath for 15 minutes. The procedure centrifugation - redispersion is repeated 3 times, finally ending up with an aqueous colloidal suspension of silicalite-1 crystals. This suspension is spincoated onto a freshly cleaned surface of an acoustic device (either SAW chip or QCM chip) followed by a calcination step of the coated chip at 350 °C for 12 h at a heating ramp of 0.5 °C min<sup>-1</sup>.

#### 2.2.1.1 X-Ray scattering

Crystalline materials, such as zeolites are preferentially identified by their significant X-Ray scattering reflexes. In figure 43 the X-Ray pattern of sample Sil-1 as synthesized, a commercially available silicalite-1 zeolite bulk material<sup>12</sup> and a simulated powder pattern<sup>[6]</sup> are compared. The strongest and most significant reflexes are marked with an asterisk.

---

<sup>12</sup> Union Carbide Corporation, 171 River Rd. Piscataway, New Jersey 08854, USA.

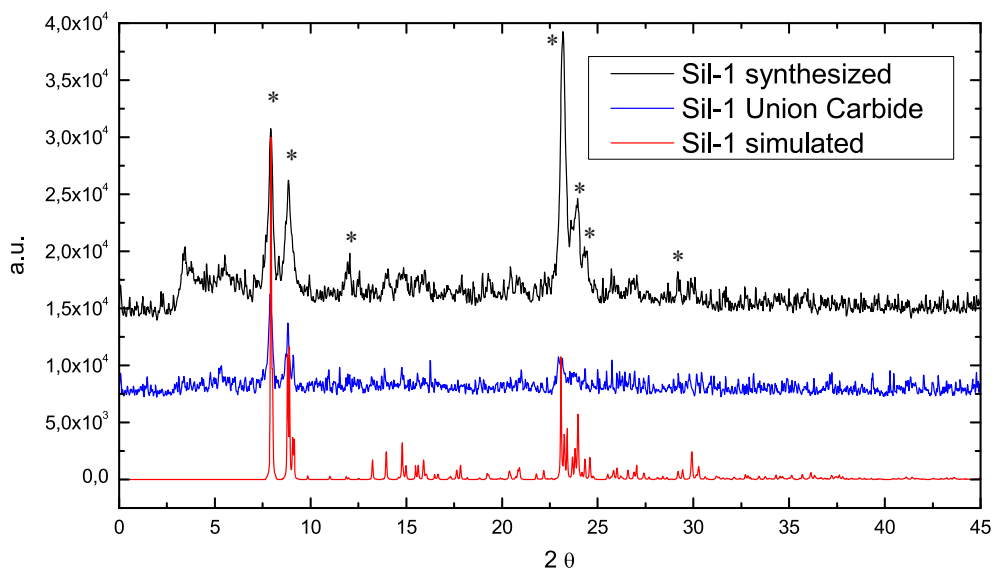


Fig. 43: X-Ray pattern of sample Sil-1 as synthesized (black), Union Carbide (blue) and simulated (red)

### 2.2.1.2 Dynamic light scattering

In order to check the particle size just right after the synthesis, DLS measurements were executed. The recorded graph in figure 44 emphasizes the relatively narrow particle size distribution and the overall estimated diameter of about 80 - 200 nm. The size

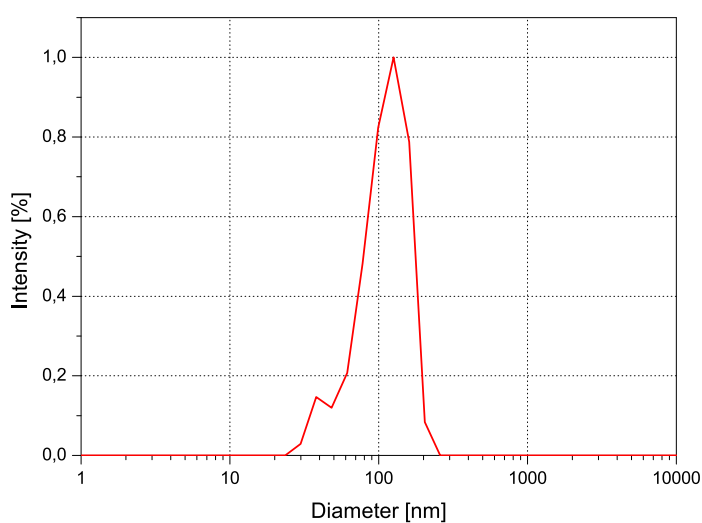


Fig. 44: Particle size distribution of sample Sil-1

is confirmed with SEM investigations.

### 2.2.1.3 Scanning electron micrograph

In figure 45 the SEM image of sample Sil-1 is shown. The aqueous colloidal suspension has been spincoated at 3000 rpm onto an acoustic wave device (details see on page 92). The overall thickness of the zeolite layer is evaluated by scratching the surface and investigations of blistering flakes.

Exemplarily shown on the presented area of  $25 \mu\text{m}^2$ , the layer is smooth and homogeneous. As displayed in the inset the nanoparticle layer is estimated to be 650 nm thick. In good agreement to the DLS experiment, the particle diameter is around 100 nm and the size distribution is quite narrow.

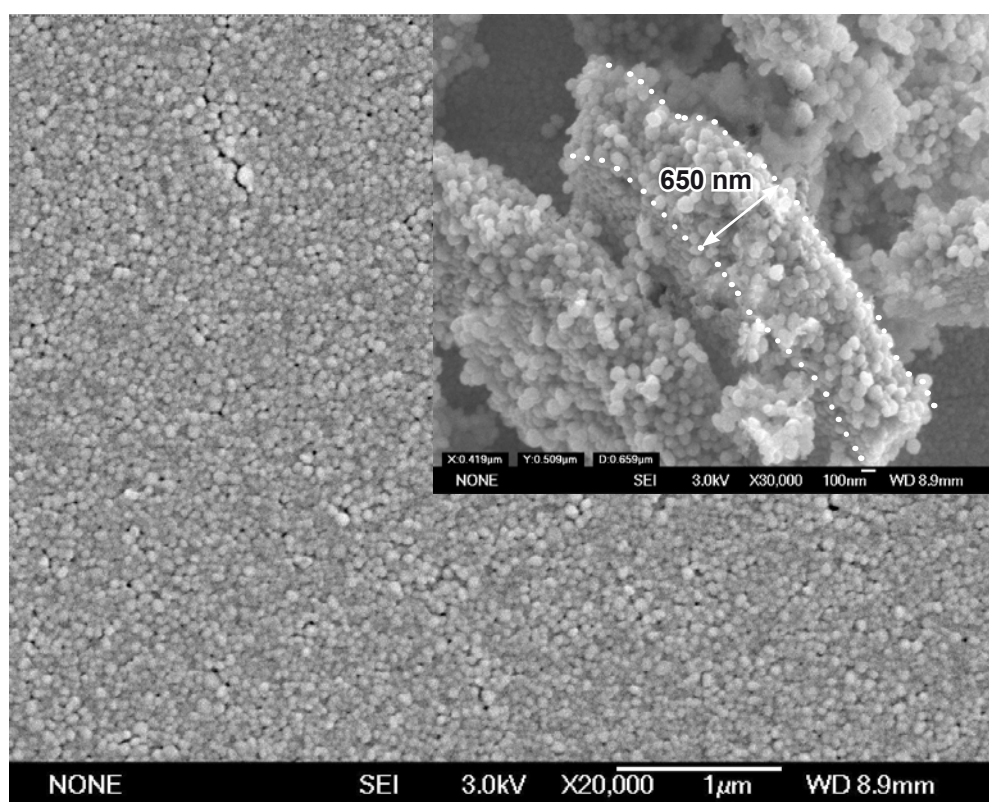


Fig. 45: SEM image of spincoated silicalite-1 layer

### 2.2.2 Alumosilicate zeolite ZSM-5: ZSM-5

The synthesis of nanosized ZSM-5 ( $\text{Na}_n^+ (\text{H}_2\text{O})_{16} [\text{Al}_n \text{Si}_{96-n} \text{O}_{192}]$ ) zeolite was performed in a two step reaction. Initially sol I was prepared as follows:

14.6 g of a solution of tetrapropylammoniumhydroxide (TPAOH) obtained from Fluka as 1 molar solution of TPAOH and 4.8 g freeze dried  $\text{SiO}_2$  (LUDOX SM-30, Aldrich) is combined and stirred for 24 hours until a clear solution is obtained.

Sol II contains 14.6 g TPAOH and 0.3 g  $\text{Al}[\text{OCH}(\text{CH}_3)_2]_3$  (Aluminum isopropoxide,  $\geq 98\%$ , Aldrich) and is also vigorously stirred for 24 hours until a clear solution appears.

$\text{SiO}_2$	$\text{H}_2\text{O}$	$\text{Al}_2\text{O}_3$	TPAOH
25	600	0.25	9

Tab. 10: Molar composition of nanosized sample ZSM-5

The molar composition is listed in table 10.

Both solutions are combined and stirred for 1 hour until the clouding disappears.

Subsequent aging (12 hours) of the final solution results in a cloudy gel.

At hydrothermal conditions the gel is treated for 6 days at  $90^\circ\text{C}$ . The resulting colloidal solution is purified by centrifugation at 19000 rpm (1 hour) and redispersed in double distilled water in an ultrasonic bath.

The purification procedure of centrifugation and redispersion is repeated three times, finally obtaining a white powder of nanosized zeolite ZSM-5 crystals.

#### 2.2.2.1 X-Ray scattering

Experimentally obtained X-ray patterns of freshly synthesized and not calcined sample ZSM-5 (black) is compared (figure 46) with a calcined sample (red) and a simulated



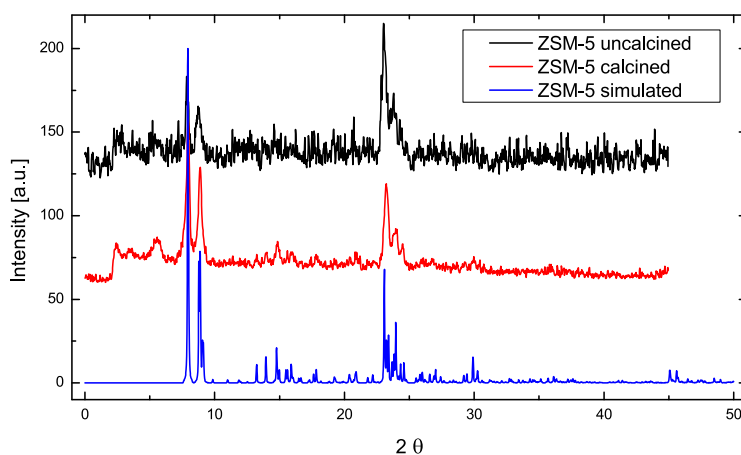


Fig. 46: X-Ray pattern of sample ZSM-5 as synthesized (black), calcined (red) and simulated (blue)

powder pattern (blue).<sup>[6]</sup> As proven, the ZSM-5 zeolite could be successfully synthesized.

#### 2.2.2.2 *Dynamic light scattering*

Figure 47 on page 55 depicts the recorded dynamic light scattering data obtained from a colloidal aqueous solution of sample ZSM-5. As evident, the particle size distribution is quite narrow with an averaged maximum at about 100 nm in diameter.

#### 2.2.2.3 *Scanning electron micrograph*

Particle sizes were confirmed by SEM investigations on sample ZSM-5. As evident from figure 48 the particle size distribution is narrow with an averaged value of approximately 100 nm in diameter.

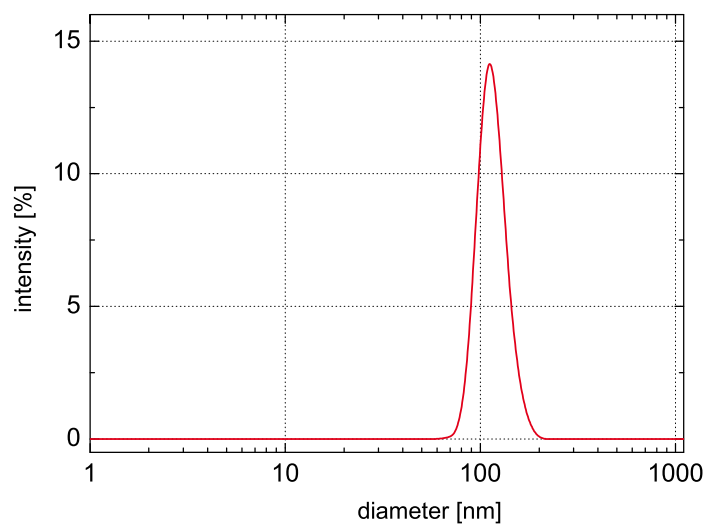


Fig. 47: Particle size distribution of sample ZSM-5

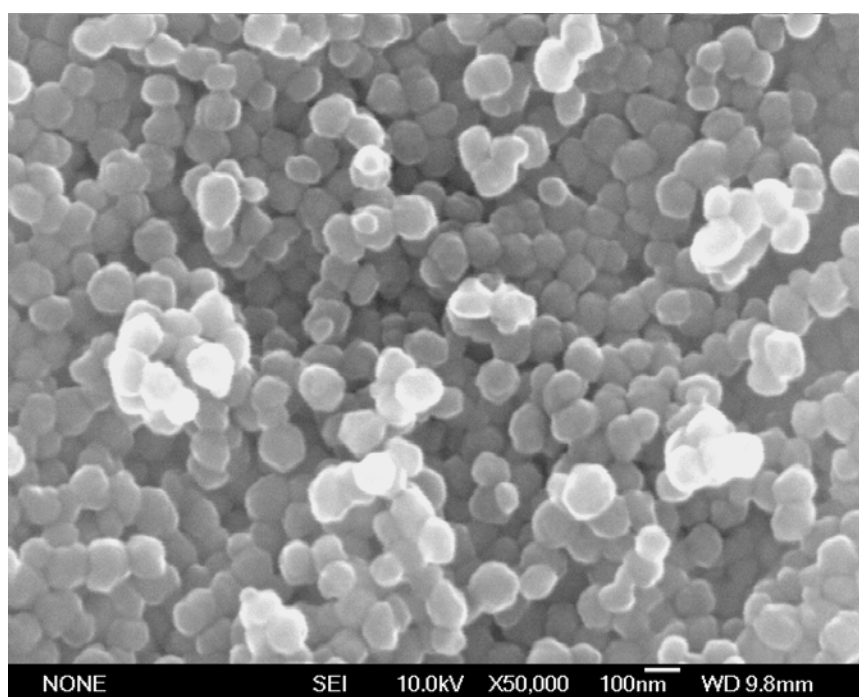


Fig. 48: SEM image of freshly synthesized sample ZSM-5

### 2.2.3 Zeolite beta: Zeo- $\beta$

The molar ratios of the synthesis of sample Zeo- $\beta$  are listed in table 11.

Al <sub>2</sub> O <sub>3</sub>	H <sub>2</sub> O	TEOS	TEAOH
0.25	390	25	9

Tab. 11: Molar ratios of nanosized sample Zeo- $\beta$

255 mg (2.50 mmol) Al<sub>2</sub>O<sub>3</sub> is stirred with 45.7 ml double distilled and purified water (Millipore Milli-Q system) for 1 hour in a polypropylene beaker. A second reaction mixture containing 55.8 ml (250 mmol) tetraethoxyorthosilicate (TEOS) and 37.0 ml (90 mmol) tetraethylammoniumhydroxide (35 %wt aqueous solution) is likewise stirred. Subsequently, the two solution are combined and continuously stirred for one hour. The clear solution is heated at 105 °C for seven days and after precipitation centrifuged at 19000 rpm for one hour obtaining a white powder of nanosized zeolite beta crystals. The powder is washed twice with double distilled and purified water and redispersed in ethanol in ultrasonic bath for 25 minutes. This cleaning procedure is repeated three times.

#### 2.2.3.1 X-Ray scattering

In figure 49 the X-Ray patterns of sample Zeo- $\beta$  (black) and data obtained from the IZA structure database<sup>[6]</sup> (blue) are given, identifying the zeolite beta with BEA structure. It has to be mentioned that the investigated sample Zeo- $\beta$  is nanosized, thus some peak broadening is expected.

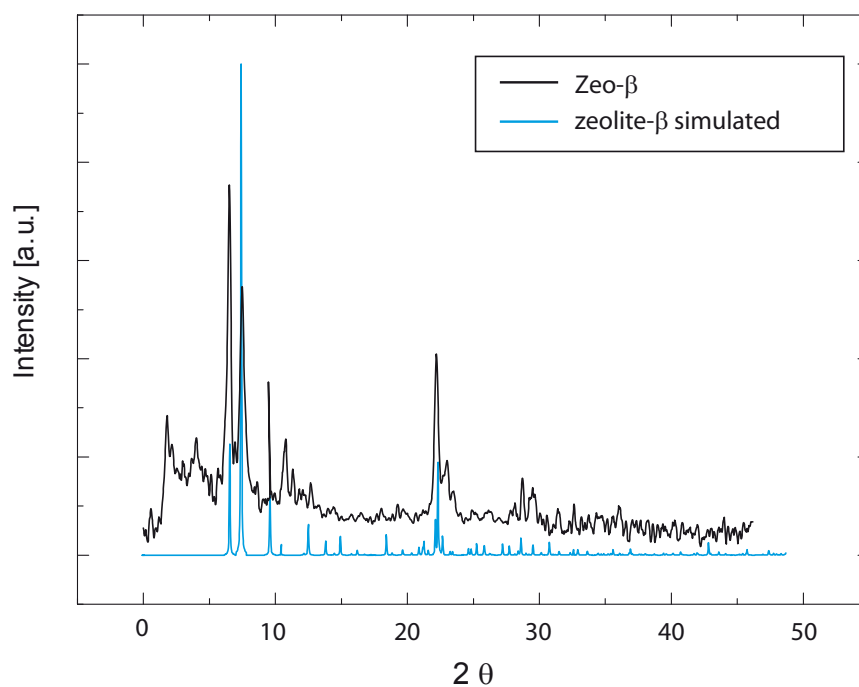


Fig. 49: X-Ray pattern of sample Zeo- $\beta$  (black) and simulated data (blue)<sup>[6]</sup>

### 2.2.3.2 Scanning electron micrograph

Sample Zeo- $\beta$  was preferentially applied in the pin-printing approach to separately deposit porous nanoparticles onto appropriate surfaces. Therefore the morphology and dimensions of the nanosized sample are discussed in details starting on page 66. Especially, figure 67 on page 76 demonstrates the nanosized dimensions of sample Zeo- $\beta$  and the external morphology of individual crystals.

### **3 Contact printing of colloidal silica nano-particles - Building a micro-array**

One of the demanding requirements of an intelligent sensor system is the ability to discriminate between different substances. Several approaches, including high performance liquid chromatography (HPLC) or gas chromatography (GC) are capable to distinguish between different materials related to different sorption behaviors of analyte molecules towards the stationary phase of the columns.<sup>[49]</sup>

In order to mimic such important analytical instruments with conventional acoustic surface wave devices, it is necessary to apply sensing materials which are capable to discriminate substances during the sorption process either by shape or chemical/physical selectivity. Simultaneously, high sorption capacities and appropriate adsorption enthalpies are additional important requirements to be sensitive in the low or even sub-ppm range.

In the following chapter, a promising approach to deposit nanoporous silica particles as potential sensor materials is presented. The procedure is based on a micro-arranging technology, which is well known in life- and bio-science, for example fluorescence genome analysis.<sup>[50], [51]</sup> A commercially available subsystem has been equipped with essential pin-printing pins in order to apply very small sample amounts of colloidal silica particles onto gold coated supporting surfaces, like Au coated microscope slides or surface acoustic wave devices with a gold coated sensing area.

#### **3.1 Leading industry standards in microarray printing technology: A brief overview**

From the very first days of the discovery of DNA (Desoxyribonucleicacid), the factor “time” played an important role during genome decoding due to the manual analysis procedure and the delicate sample material. Beside this problem, scientist had to overcome the problem of locating the countless genes on the DNA. Human DNA contains about 24.800 genes and about  $3 \cdot 10^9$  base pairs.<sup>[52]</sup> In 1990 the human genome project<sup>[53]</sup> was initialized to decrypt the entire human genome, which succeeded in the year 2004

with a certain accuracy.

Based on this research, numerous gene defects and their macroscopic effects - genetic diseases - could be identified and in addition, quantified with supplementary experiments, very often carried out with microarray techniques.

A research group at Stanford University<sup>[54], [55]</sup> used a variety of printing approaches, whereby tweezers, split pins, micro spotting pins or ink-jets printers were tested to deposit pre-synthesized oligonucleotides or PCR (polymerase chain reaction) products onto solid substrates such as chemically-pretreated microscope slides. After printing, the microarrays were processed to remove unbound DNA and probed with a fluorescent sample.

In figure 50 a typical example of pin printed fluorescent spots on a microscope slide is presented. The pattern was created with a triple arrangement of Chipmaker™ 3 pins producing spots with diameters of about 125  $\mu\text{m}$  and a spacing in between each spot of about 20  $\mu\text{m}$ .<sup>[56]</sup>

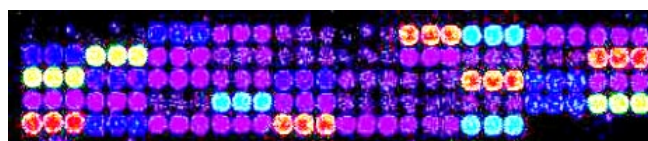


Fig. 50: Printed and hybridized microarray fluorescent spots printed with Chipmaker™ 3 pins<sup>[56]</sup>

### 3.1.1 Microarray printing techniques

The making of microarrays requires the deposition of very small sample volumes. The volume delivered onto a surface is typically in the range of  $10^{-9}$  -  $10^{-12}$  liters per drop. Conventional liquid handling systems, like syringes, are usually not capable of delivering these very small sample amounts. As a consequence, new technologies such as the microspotting approach emerged and offered the opportunity of handling small volumes, thus enabling the parallel analysis of hundreds of printed DNA samples or protein interactions on one single microscope slide, e.g. the one presented in figure 50.

The microspotting technology can be divided into two distinct categories, the non-contact dispensing and contact dispensing systems. Non-contact printing devices are mostly modified ink-jet printers<sup>13</sup> and eject tiny sample volumes out of a reservoir onto a substrate material by means of special modified printheads.

Direct contact printing in contrast involves the contact of a liquid loaded pin with the solid support surface. The pin-printing technique includes solid pins, either made of metallic or non-metallic materials, capillary tubes, tweezers, split pins and micro-spotting pins or ink stamps. These direct contact printing devices have all in common the direct delivery of droplets onto the surface.

### 3.1.1.1 *Non-contact microarray printing*

As the focus of this topic lies on the direct pin-printing approach, the non-contact techniques will be explained only in short.

Ink-jet printing dispensers work similar to ink-jet printers. The “ink” (e.g. protein or DNA buffered solutions) is initially loaded into the printer device’s fluid reservoir via small vacuum pumps or direct injection into the printer head. Two basic concepts feature the dosing of small volumes as tiny drops onto the supporting surface.

A piezoelectric head dispenser which is controlled by a piezoelectric crystal (more

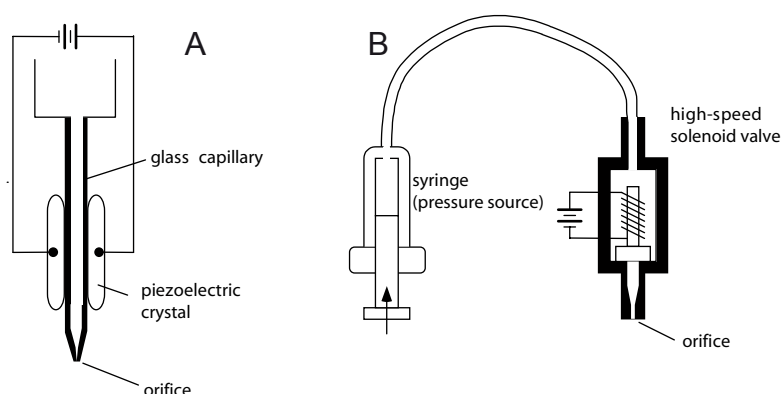


Fig. 51: Piezoelectric dispensing system (A) and solenoid syringe dispenser (B)<sup>[56]</sup>

<sup>13</sup> Arrayjet Limited, Unit 5, McSense Business Enterprise Park, 32 Sycamore Road, Mayfield, Dalkeith EH22 5STA, Scotland, UK.

information on piezoelectricity is available on page 79) squeezes a capillary thus ejecting small sample volumes out of the nozzle. The piezoelectric approach allows a quite rapid producing of microarrays due to high-speed dispensing of several thousands of droplets onto the support.<sup>[57]</sup> Disadvantages arise from the possibility of inclusion of small air bubbles into the droplets, thus reducing the reliability of the system. Furthermore, the deposition of relatively large sample amounts and the time consuming sample change and device cleaning procedure are not advantageous. Overall, the piezoelectric microspotting approach has not reached a commonly accepted reputation of generating reproducible microarrays.

Figure 51 schematically illustrates the piezoelectric spotting device (A) and another non-contact printing approach, namely the solenoid syringe device (B). As the name indicates, a modified syringe containing the liquid sample material introduces a defined pressure onto a micro-solenoid valve which ejects small droplets in the range of  $5 \cdot 10^{-9}$  liters on demand. A commercial system is available from Innovadyne Technologies, Inc.<sup>14</sup>, for example.

### 3.1.1.2 Contact microarray printing

Figure 52 schematically illustrates three different commercially available contact

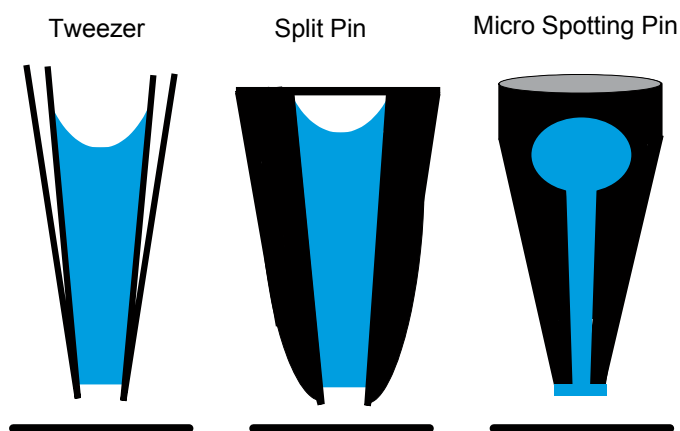


Fig. 52: Commercially available contact pin dispenser systems<sup>[56]</sup>

<sup>14</sup> Innovadyne Technologies, Inc., 2835 Duke Court, P.O. Box 7329, Santa Rosa, CA, USA.



printing dispenser devices to produce microarrays.

The tweezer system, e.g. available from *Parallel Synthesis Technologies, Inc.*<sup>15</sup> (figure 53) offers easy handling, moderate pricing and in addition, mechanical durability and chemical resistance.

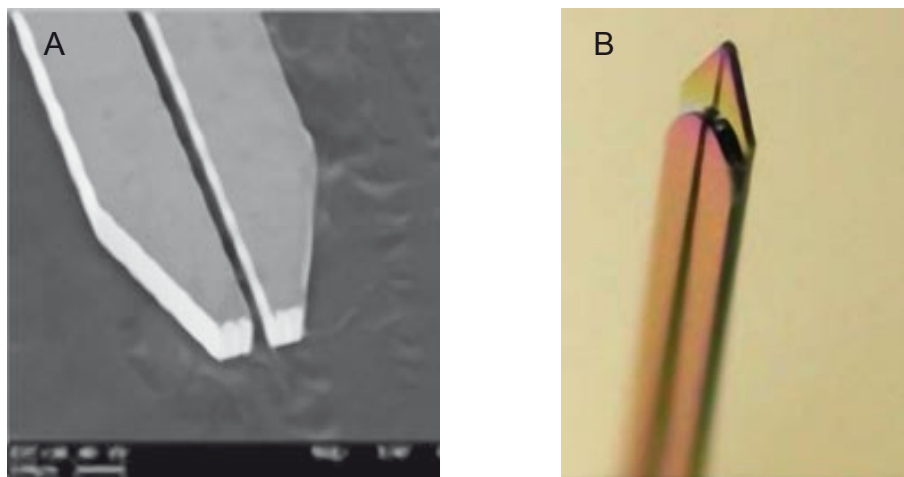


Fig. 53: SEM picture of a silicon pin tip, with a pin tip area of  $200 \times 200 \mu\text{m}$  (A) and a photomicrograph of a Si pin with a tip size of  $100 \times 100 \mu\text{m}$  (B) available from *Parallel Synthesis Technologies, Inc.*

Split pins can be obtained from *Point Technologies, Inc.*<sup>16</sup>, for example. Those split pins are available in stainless steel quality or various alloys or pure metals (e.g. tung-



Fig. 54: Split pin from *Point Technologies™, Inc.*

<sup>15</sup> *Parallel Synthesis Technologies, Inc.*, 3054 Lawrence Expressway, Santa Clara, CA 95051, USA.

<sup>16</sup> *Point Technologies, Inc.*, 1966 13th Street, Suite 270 Boulder, CO 80302, USA.

sten) for special applications. In figure 54 a magnified image of a split pin from *Point Technologies, Inc.* is shown. In principle, split pins work like tweezers that contact the surface to deliver the liquid stored inside the small capillary slit.

A very popular representative of the microspotting pin design is TeleChems™ ArrayIt® technology<sup>17</sup>. This work focuses on the implementation of TeleChems Chipmaker™ pins into the silica particle printing process. The SEM image in figure 55 (A) depicts

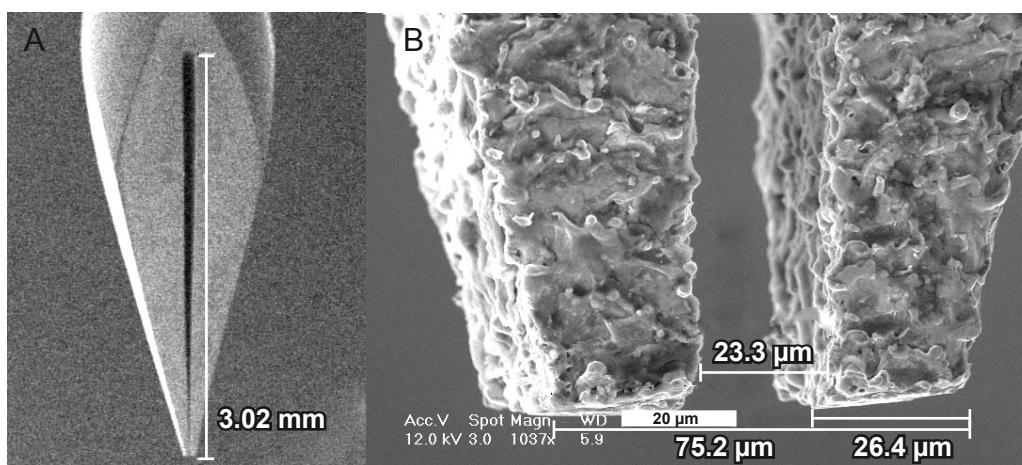


Fig. 55: SEM image of a ChipMaker™ 3 micro-spotting pin head (A) and tip (B)

one applied high precision manufactured stainless steel Chipmaker™ 3 pin with an overall length of about 45 mm and a capillary slit of 3 mm height. On figure 55 (B) the essential feature of the micro spotting pin is emphasized: The tip of the pin exhibits only an overall width of 75 μm and the opening of the capillary is limited to 23.3 μm. In contrast to split pins or tweezer systems, the Chipmaker™ pin works in a three step ink-stamping process, illustrated in figure 56.

The three basic steps in the microspotting process are:

- A Cleaning and loading of the pin, approaching the surface
- B Direct contact printing onto the surface
- C Lift-off the surface

In the first step A the pin has to be cleaned in an appropriate solution (water, ethanol

<sup>17</sup> TeleChem International, Inc., ArrayIt® Division, 524 East Weddell Drive, Sunnyvale, CA 94089, USA.

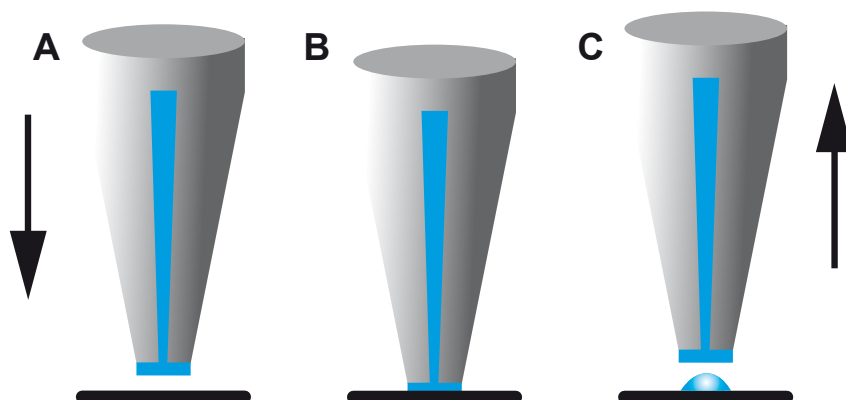


Fig. 56: Three step microspotting process with ChipMaker™ pins

or special detergent) dependent on the liquid or suspension printed. The pin is loaded with the solution or organic fluid by dipping into the solution, whereas it is important to dip only one third of the slit into the solution in maximum. Capillary forces are responsible for the slit filling with fluidic media.

In the next step B, the fluid is printed onto the potentially chemical modified surface. The contact pin-printing technology is capable of dispensing single spot volumes in the high picoliter up to low nanoliter range. According to the approaching speed and the z-axis movement dimensions (centimeter vs. millimeter) the contact time between surface and pin can be adjusted. The longer the contact time, the more liquid is released onto the surface. Depending on the nature of the surface (hydrophobic or hydrophilic) a specific contact angle (for definition see figure 57) between surface and liquid is accomplished.

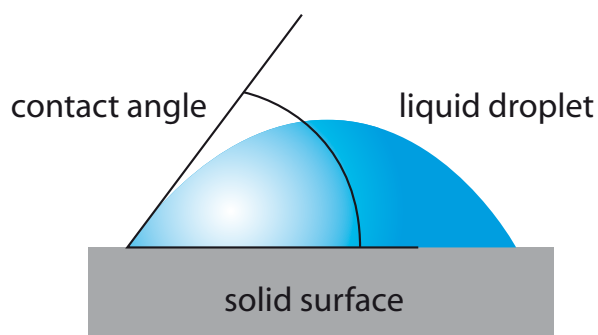


Fig. 57: Contact angle between deposited droplet and solid surface

This specific contact angle is a key aspect during the subsequent drying process of the deposited droplet. Size and shape of the liquid droplet are among the main criteria to influence shape, smoothness and size of the dried product - the spotted material pixel. In this context, the capillary width of the pin has a major impact on the size of the deposited droplet.

Beside the dimensions of the droplet and the contact angle, additional parameters, like temperature, ambient humidity and physical or chemical forces/bonds influence the drying process of the droplet and in consequence the size, degree of coverage and the quality of the printed spot.

### 3.1.2 *Pin-printing parameters*

In table 12 the relevant performance parameters of all three previously introduced contact printing techniques are summarized.<sup>[56]</sup> The most important parameters which usually lead to the decision either to introduce or decline one of the three printing systems, are the density of printed spots per microscope slide (spots cm<sup>-1</sup>), the spots printed per second, simplicity, robustness and costs per spot. In this work, the contact pin-printing technique was chosen because of the relatively simple mechanically driven design, the robustness of the metal pins and the moderate cost per spot. Parameters like spot size are strongly dependent on the characteristics of the colloidal suspension that is delivered onto the surface. Furthermore, the potentially chemically pre-treated surface itself plays an important role in the development of the liquid deposited droplet. Silicon pins could not be used due to expected strong adhering forces between nanosized silica particles and the chemically similar silicon surface of this exclusive pin design.

The collected tabular data compare the mentioned contact printing systems in general and emphasize their individual advantages and disadvantages.

parameters	printing technology		
	piezoelectric	syringe-solenoid	micro spotting pin
minimum sample volume <sup>a</sup> [ $\mu\text{l}$ ]	20 - 50	20 - 50	5
loading volume <sup>b</sup> [ $\mu\text{l}$ ]	5 - 10	5 - 10	0.2 - 1.0
print volume [nl]	0.05 - 10	4 - 100	0.5 - 2.5
spot size [ $\mu\text{m}$ ]	125 - 175	250 - 500	75 - 360
spot density [spots $\text{cm}^{-2}$ ]	500 - 2500	200 - 400	400 - 10.000
programmable volume	✓	✓	–
number of nozzles or pins	4 - 8	8 - 16	1 - 64
delivery speed [spots $\text{sec}^{-1}$ ]	100 - 500	10 - 50	64
simplicity	x	xx	xxx
robustness	x	xx	xxx
costs per spot	high	average	low

a volume of sample in a 384-well plate  
b sample volume loaded by dispensing system

Tab. 12: Parameters of commercially available contact printing systems

### 3.1.3 *Experimental parameters of pin-printing colloidal silica nanoparticles*

The specific parameters for the Chipmaker3™ pin (CMP3), which was used in the microarray spotting process of porous siliceous nano-particles are listed in table 13. A single TeleChems® Chipmaker3™ pin was inserted into a provided pin-holder head (see figure 58, picture taken from <http://www.arrayit.com>). The pin-holder head itself is connected to a BioDot® micro-dispensing robot<sup>18</sup> (model Cartesian Technologies PS 7500) equipped with a three dimensional motion control system with a positioning accuracy of  $\pm 2\text{-}5 \mu\text{m}$ . In order to gain more control over the rapid drying process of the deposited small volumes in the range of 1 nl, the BioDot® robot is equipped with a housing and an inlet for water vapor at the desired relative humidity, generated by ul-

<sup>18</sup> BioDot, Inc, 17781 Sky Park Circle, Irvine, CA 92614, USA.

Chipmaker3™ pin	
uptake volume [ $\mu\text{l}$ ]	0.25
print volume [nl]	0.7
spot diameter minimum [ $\mu\text{m}$ ]	100
minimum center to center spacing [ $\mu\text{m}$ ]	120

Tab. 13: Chipmaker™ 3 pin specific characteristics

trasonic induced evaporation of double distilled water. Relative humidity values were adjusted according to the uptake fluid (aqueous or ethanolic) and to the concentration

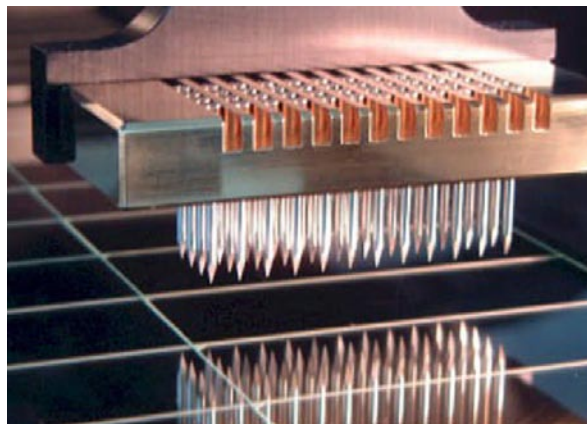


Fig. 58: Pin-holder head

of the colloidal suspensions. A similar pin-printing approach of dispensing sol-gel solutions of light emitting ruthenium complexes is described in reference [30].

In order to control the deposition of droplets a simple positioning program including xyz-parameters was written (for details see appendix), which is constructed as follows:

- A Defining the absolute position of the 3x3 matrix pixels in the xy-plane

- B Setup of z-axis parameters
- C Loop programming of  $n$  times 3x3 (optional)

Potential impurities on supporting surfaces were removed by three times washing with double distilled water, followed by three times treatment with acetone.

#### *Step A*

The absolute positions of the deposited pixels are illustrated in the SEM picture given in figure 59. The distance between each single pixel in x- and y-direction is 120  $\mu\text{m}$ . One spot consists of deposited nanocrystalline zeolite beta (sample Zeo- $\beta$ ). As clearly

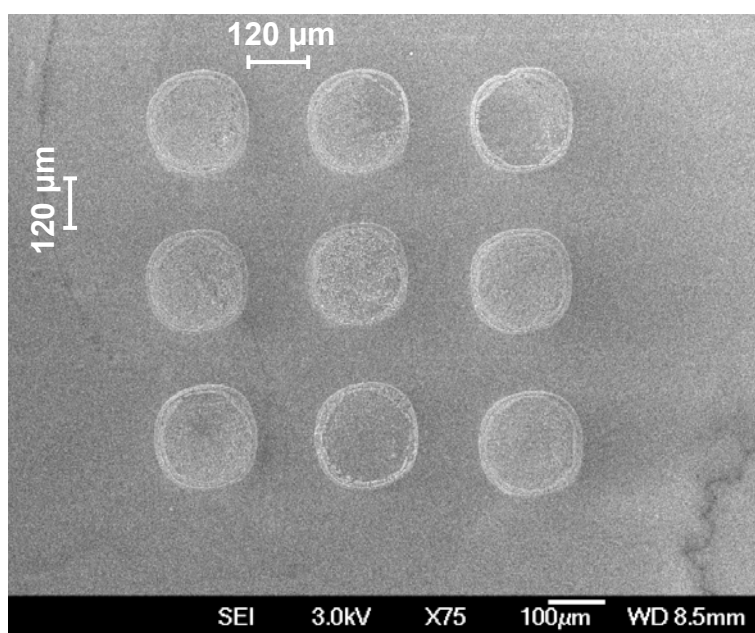


Fig. 59: SEM image of zeolite beta 3x3 array

visible, the shape is almost perfect circular, which is related to previous delivering of circular droplets of the ethanolic colloidal suspension.

#### *Step B*

The approaching speed of the pin-holder head with one single Chipmaker<sup>®</sup> 3 pin inserted was 2.5 cm s<sup>-1</sup>. The delay time between the first touch down of the liquid loaded

pin on the surface and the lift-off was adjusted to 250 - 300 ms, thus dispensing relatively small sample volumes onto the non-modified but thoroughly cleaned microscope slide.

### Step C

As soon as one single 3x3 matrix was printed correctly, the program could be optionally extended to an  $n$  times 3x3 matrix by sequentially increasing absolute position values and grouping them into subprogram loops. An sophisticated example can be seen in figure 60 where a four times 3x3 microarray was printed (left) and for demonstration purposes the word “LMU” (Ludwig-Maximilians-University, right). The printing process was started at position 1 of 3x3 field (A) and continued on position 2, successively completing the 3x3 array (A). Microspotting continued without any pause on position 1 of 3x3 matrix field (B). Labeling for arrays (B), (C) and (D) are not inserted into figure 60 for clarity purposes. The poor quality of printed spots, especially from 3x3 field (D) on and the “LMU” logo, is related to running short of liquid

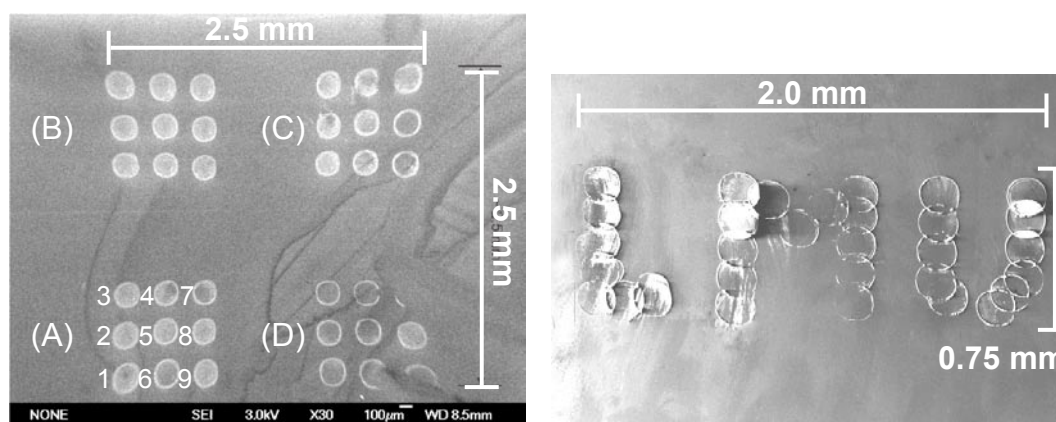


Fig. 60: SEM image of a four times 3x3 microarray of zeolite beta nanocrystals (left) and the word “LMU” (right) printed on a bare glass microscope slide

reservoir and relatively weak adhesion forces between the bare glass surface and the zeolite beta nano-particles in general (Van-der-Waals forces are assumed).

A closer look at figure 60 reveals circularly shaped spots with a distinctive mass concentration building at the outer rim (“donut” shape).



This behavior can be explained by the inhomogeneous drying process of nanoliter droplets. Figure 61 demonstrates schematically the different volume element dispersion (black straight arrows) within the drop (A) and the flow inside a dispensed droplet (B). The colloidal suspension concentration at the initial state of the dispensed droplet is supposed to be homogeneous. As soon as the evaporation starts, the concentration at the peripheral regions of the drop increases at a higher degree compared to the central positions. At a constant evaporation rate the ratios between volume and concentrations

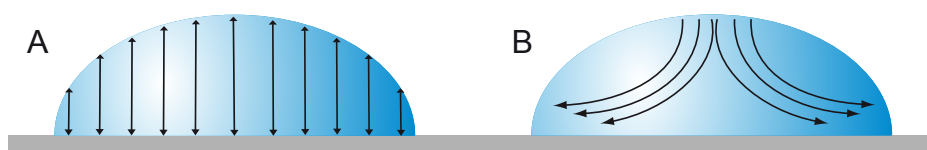


Fig. 61: Volume elements of a drop located on a solid surface support (A) and liquid - mass flow convection vectors inside a drying drop (B)

decrease more rapidly at the peripheral regions compared to the central positions. A non-preferential evaporation rate is assumed. The concentration compensation routes to a volume mass flow from the inner area to the external regions of the drop. A simultaneously occurring total vaporization process is responsible for exceeding the supersaturation concentration for the colloid and subsequently to the “precipitation” of the dispersed solid particles. Consequently, the liquid flow from the central region of the drop deposits more and more material at the edges, building the already mentioned “donut” shaped crust of matter.

Recently, *R. Duggal et al.*<sup>[58]</sup> investigated the formation of layers of single walled carbon nanotubes by drying single drops of aqueous carbon nanotube suspensions which were dispensed on glass slides. They conclude that the driving force of the formation of ring like morphology dried spots are capillary flows as discussed and schematically illustrated in figure 61. A very detailed investigation of capillary flows in evaporating sessile drops can be found in reference [59].

In order to prevent such inhomogeneous ring-like solid structures related to the explained drying mechanism, it is necessary to decelerate the drying process itself and to introduce supporting physical or chemical forces in order to build a uniform layer of deposited nanoparticles. Uniform and homogenous layers in terms of preventing local-

ized mass agglomerations are essential when gas detection with surface acoustic wave techniques is targeted. Agglomerations of matter provoke unwanted damping and energy dissipation of the propagating acoustic wave thus leading to severe measurement difficulties or in the worst case to erroneous results.

### 3.1.4 Formation of homogenous silica nanoparticle layers

The goal of forming homogenous siliceous particle layers could be reached by the implementation of intermediate “gluing” layers between the supporting surface and the nanosized zeolite particles.

As schematically illustrated in figure 62, an electrostatic approach<sup>[60]</sup> with a positively charged polymer (Berocell 6100<sup>®</sup>, molecular weight approximately 50000, Akzo Nobel) as binding layer was chosen to attach negatively charged silica particles onto a gold surface. The gold surface was covered with mercaptopropyltrimethoxysilane

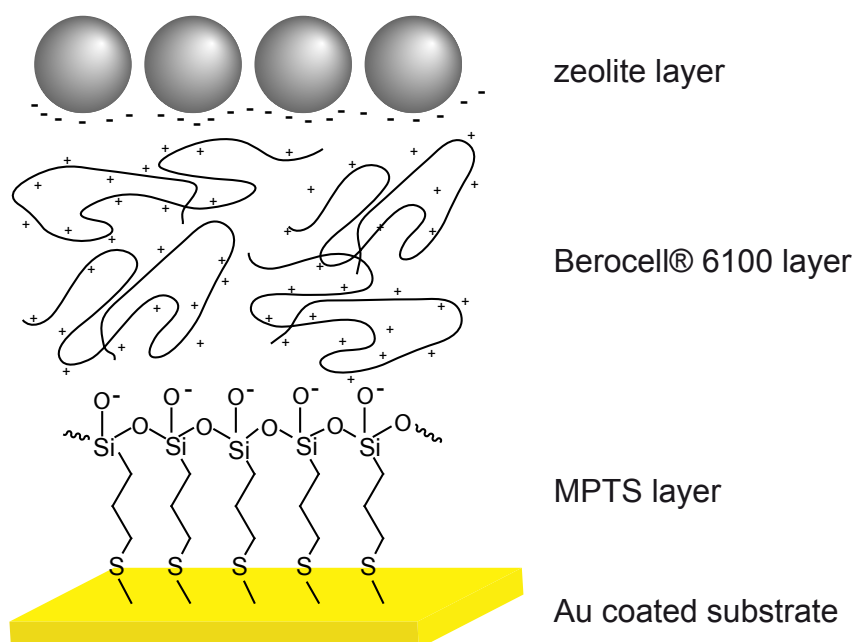


Fig. 62: MPTS layer on gold substrate with intermediate Berocell polymer layer and electrostatically attached zeolite crystals

(MPTS), which offers strong gold-mercapto bonds and - after hydrolysis - a negatively charged silicate interface.

The gold coated microscope slides were obtained from Advalytix AG<sup>19</sup> and manufactured with a 1 nm sub layer of titanium increasing adhering forces and a gold layer thickness of about 10 nm. Prior to the treatment with MPTS the slides were washed with double distilled and purified water (Millipore Milli-Q Academic A10 system). Subsequently, the slides were repetitively cleaned with acetone. The cleaned and dried gold coated microscope slides were treated with a 1 %wt Berocell<sup>®</sup> 6100 - toluene solution for ten hours in a closed nitrogen atmosphere without stirring to prevent moisture induced hydrolysis of the silane groups. The mercapto modified gold substrates were rinsed twice with double distilled water to remove polymer excess and the hydrolysis of the silanol groups was supported by a three times treatment with a 0.1 molar ammonia solution.

Subsequently, the negatively charged slides were transferred into the BioDot<sup>®</sup> housing. The humidity inside the housing was set to 60 % relative humidity at 24 °C room temperature.

Every pin used during the pin printing process was “run-in” without any fluid according to the manufacturers’ manual for about 1000 times to optimize the contact area of the pin tip (figure 55) with the substrate.

A colloidal 3 %wt ethanolic suspension of sample Zeo- $\beta$  nano-particles was applied onto the pin’s tip with a plastic syringe: A drop was ejected onto the slit just contacting the metal. Responsible capillary forces sucked the liquid into the empty slit of the pin followed by 30 - 50 printing cycles to get rid of adherent outer liquid film.

The printing process of the 3x3 microarray itself was initialized as soon as the automatic printing program (see appendix on page 240) was started. The absolute contact time between pin and surface could not be exactly measured but was estimated to 200 - 300 ms and adjusted to obtain optimal results in terms of discrete and homogeneous silica pixels. Consequently after the sequential dispensing, the used pin was thoroughly rinsed with double distilled water to remove the colloidal suspension within the slit thus avoiding clogging. Additionally, the pin was treated for at least 30 minutes in ultrasonic bath to get rid of remaining nanoparticles.

Figure 63 displays a printed 3x3 microarray of zeolite beta nano-crystals. The printed dots are labeled from 1 - 9 in the order of printing sequence.

In order to test the mechanical durability of adhering nanocrystals with the intermedi-

---

<sup>19</sup> Advalytix AG, Sauerbruchstraße 50, 81377 Munich, Germany.

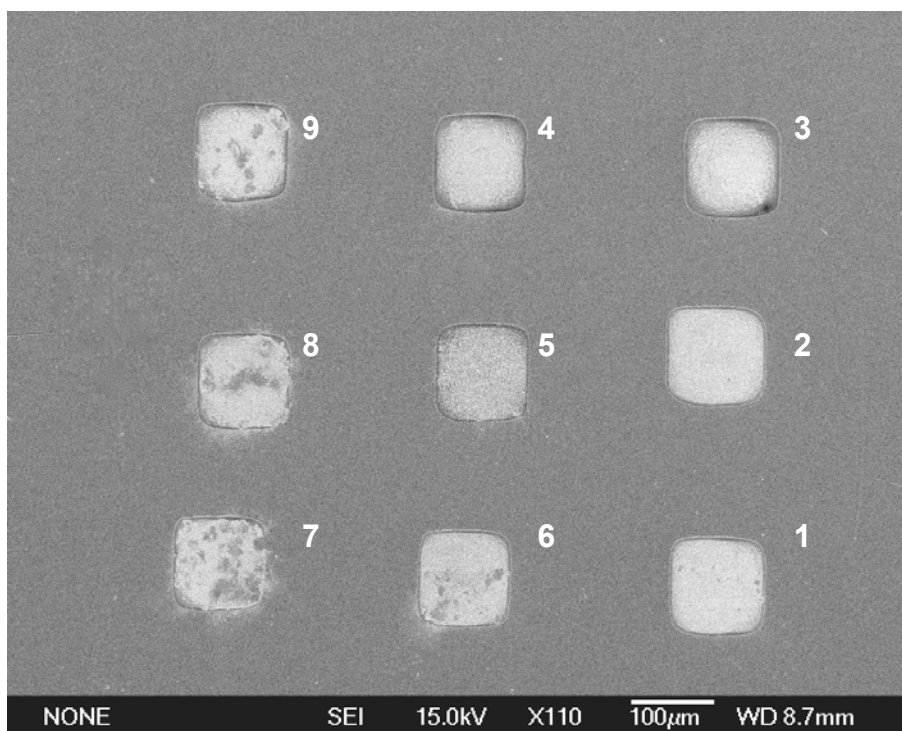


Fig. 63: SEM image of pin-printed 3x3 microarray of zeolite beta nanocrystals, treated 10 minutes in aqueous ultrasonic bath

ate Berocell 6100<sup>®</sup> layer, the microscope slide was treated for 10 minutes in an aqueous ultrasonic bath. During this treatment loosely attached crystals at the surface and borderline of each square pixel were reliably removed. As confirmed from the SEM image the printed pixels are approximately quadratic which is related to the shape of the tip of the pin and the contact printing process itself. The microspotting process was started at position 1 and continued on position 2, 3, 4 and so on. Beginning from position 7, a decreasing quality of printed squares is observed which is related to small agglomerates of zeolite crystal at the printing area of the tip (compare figure 55) cumulating at each single printing step.

To confirm the successful attachment of MPTS and the cationic polymer Berocell 6100<sup>®</sup> a similar gold coated sample slide was prepared without any chemical linker chemistry for comparison. As proven in figure 64 the SEM image shows a distinctive circular appearance of the printed pixels. In this context, it is important to emphasize the fact that without the chemical pretreatment with MPTS and Berocell 6100<sup>®</sup> the contact angle between the deposited drop differs vastly from the one with the linker

chemistry. Without any anchoring intermediate elements the contact angle is observed

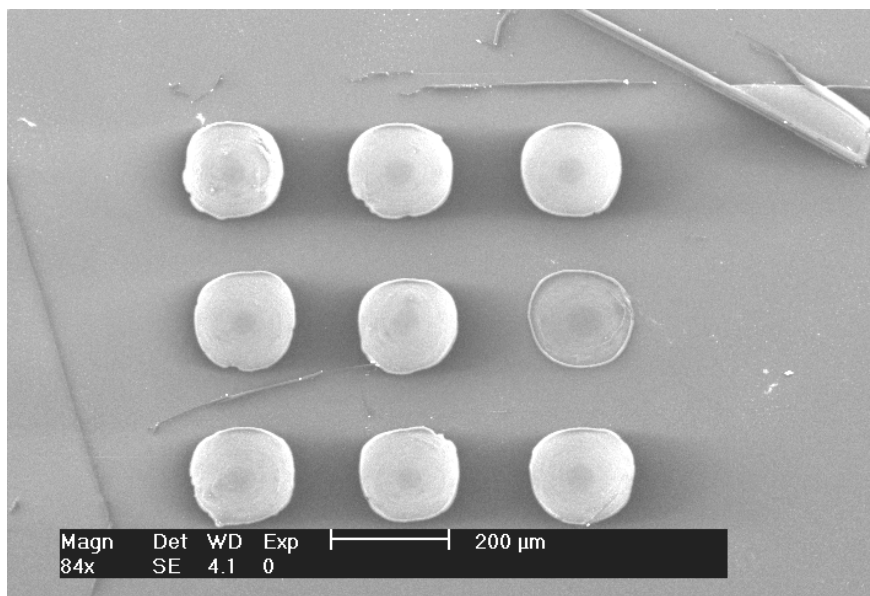


Fig. 64: SEM image of deposited zeolite beta nanocrystals without an intermediate linking chemistry

to be relatively high indicating a quite low tendency of the dispensed ethanolic colloidal suspension to adhere to the golden surface.

A comparison of the pixels' individual shape supports the importance of linker chem-

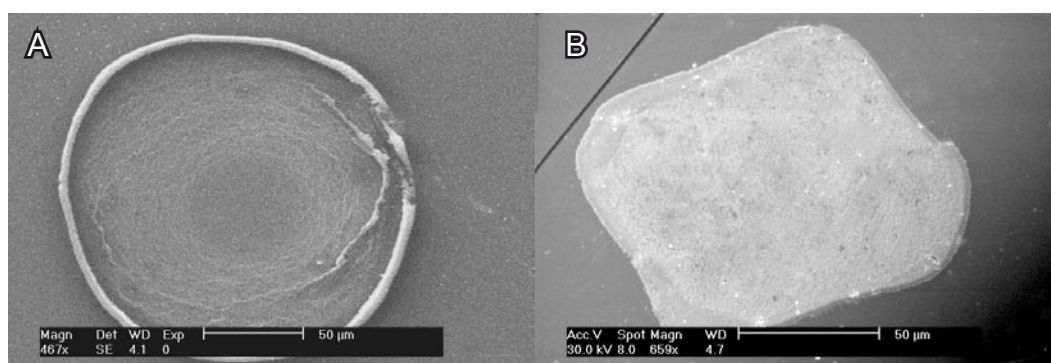


Fig. 65: SEM image of single dispensed spots of zeolite beta without linking chemistry (A) and anchoring chemistry based on MPTS and Berocell® 6100 (B)

istry to dispense a colloidal suspension in order to form uniform, well defined and homogeneously covered areas of nanocrystals. In figure 65 one circular pixel printed without linker chemistry (A) and one square pixel with basic chemical linkers (B) are compared to each other. As clearly visible, the non-modified surface entails the described “donut” shape, which includes material agglomerations at the outer rim of the printed dot and a barely covered inner area. In comparison, the surface with the electrostatically attached nanocrystals exhibits a homogeneously covered spotted surface. The pin printed spot shows furthermore a less prominent outer rim and less material

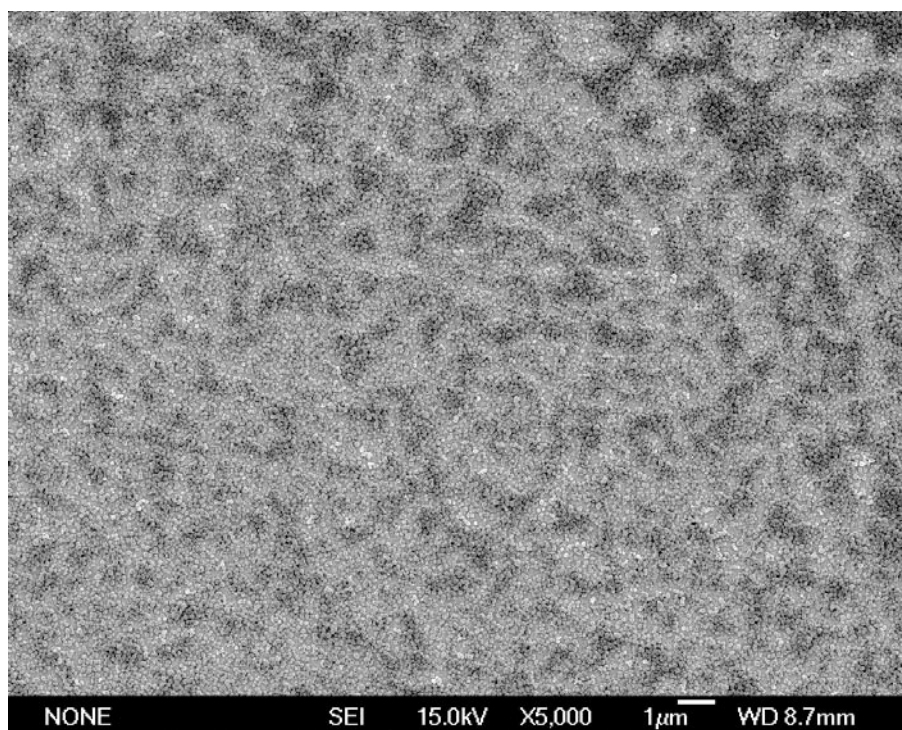


Fig. 66: Magnified SEM image of central locations of micro spotted and chemically linked zeolite beta nanocrystals

agglomerations. A close up of the central locations of the spot (figure 66) demonstrates the densely packed nanosized zeolite beta crystals.

A detailed SEM image, displayed in figure 67, emphasizes the attachment of a up to four layers in maximum of zeolite crystals. The degree of coverage over the entire spot

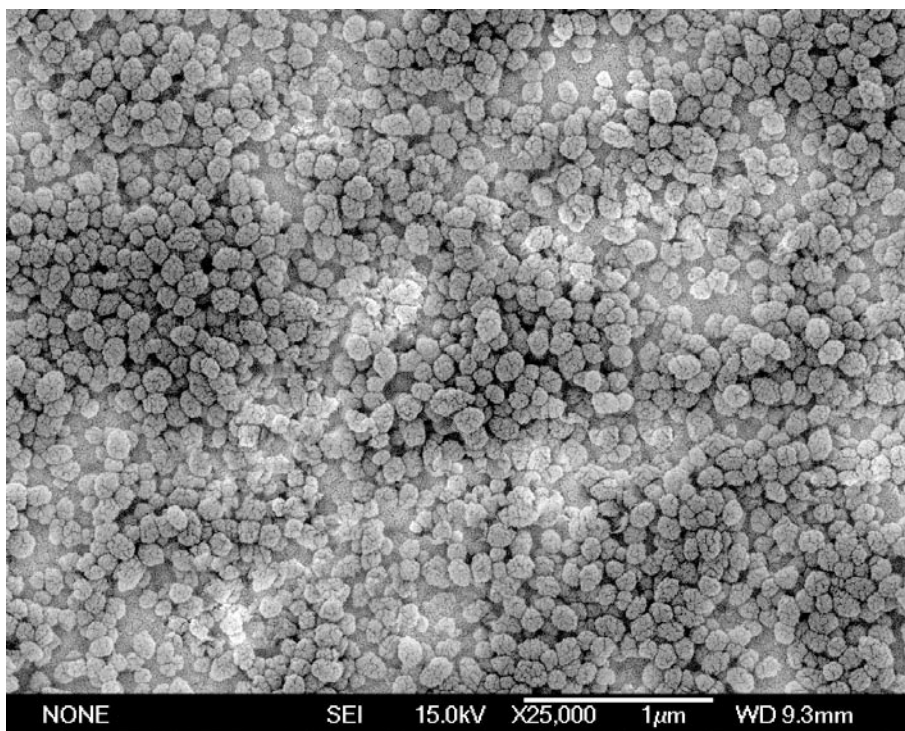


Fig. 67: SEM magnification of pin printed zeolite beta nanocrystals

is estimated to be at least 95%. The sharp and defined border of the printed spot can be seen in figure 68. Due to the already explained drying mechanism inside liquid drops on surfaces a slightly higher packing density at the outer rims of the pixel is observed. The scanning electron image of the inset in figure 68 was taken on a different position of the pixel not shown on the main image. Bright grey colors represent the gold covered microscope slide whereas dark grey areas are attributed to layers of about 6 - 8 deposited and stacked nanocrystal layers (estimated from the SEM picture). The requirement of sharp boundaries of each single matrix pixel element is also fulfilled.

### 3.2 Conclusion contact pin-printing

In a final analysis, the contact pin-printing approach is capable of dispensing small sample volumes of colloidal silica nanoparticles onto glass or gold coated surfaces.

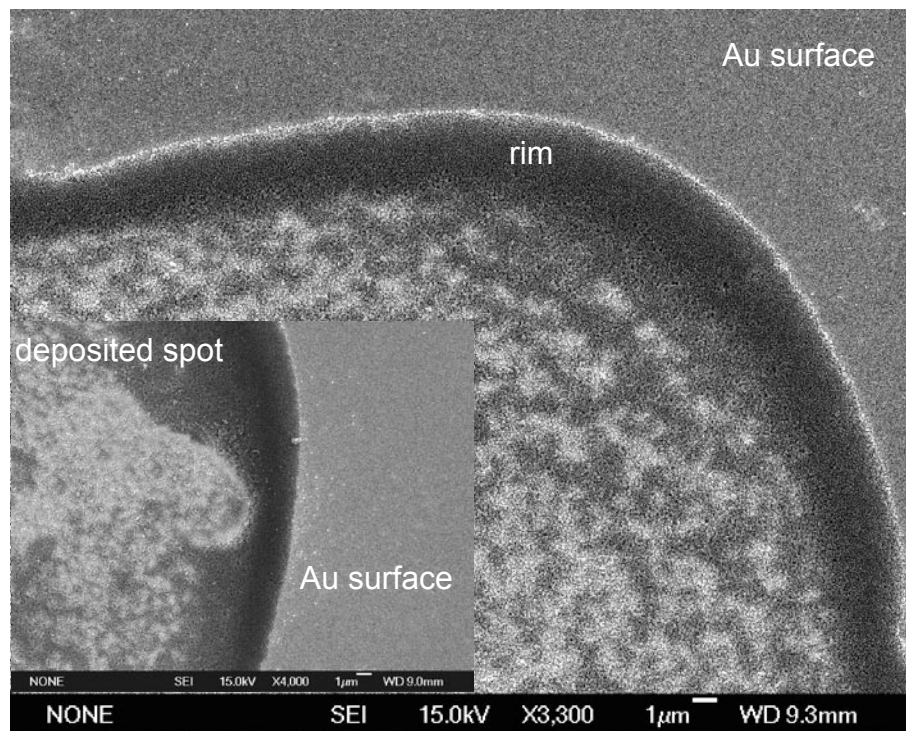


Fig. 68: SEM image of pin printed zeolite beta focused on the outer rim of the spot

Small stainless steel microspotting pins, usually involved in the process of establishing microarrays of biological materials (protein sequencing, DNA analysis) have been used to print pixels of few layers of zeolite beta nanocrystals.

Without any intermediate chemical linker chemistry, only barely covered and circularly shaped spots are produced. Material agglomerations at the utmost rim of spots prevent the use as potential sensing material in acoustic surface devices due to expected frequency damping effects. Irregularly shaped spots may not contribute to a per pixel addressing as desired in a sensor array built of nanoporous particles. Furthermore, the reproducibility in terms of size, shape and mass distribution of series of pixels is not guaranteed without an intermediate linker chemistry.

It could be demonstrated that the application of MPTS as intermediate linking layer and the positively charged polymer Berocell® 6100 lead to rectangularly formed pixels with a homogenous particle distribution over the whole printed area as well as moderate mass accumulations at the rim. The process hence requires a gold covered surface to anchor mercapto bearing molecule fragments.

Very important parameters influencing the overall size and appearance of printed spots



may also not be neglected. A rapid drying process of deposited nanoliter droplets has a negative impact on the desired uniform shape thus parameters such as relative humidity and surface wetting must be tracked and optimized during the printing procedure. In order to prevent clogging of the pins' capillary, an intense cleaning process is necessary before and after the printing procedure.

#### 4 Acoustic wave sensors based on piezoelectricity

Quartz resonators are used as extremely accurate measurement instruments in modern industry products for more than 40 years. Quartz resonators are applied in communication electronics, watches, force sensors and filters, for example. The material quartz exists in 2 technically important modifications: From room temperature up to 573 °C the trigonal  $\alpha$ -quartz is the stable phase that transforms reversibly into the high temperature modification  $\beta$ -quartz which is stable up to 867 °C.

The basic principle of quartz resonators is the so called piezoelectric effect. Piezoelectricity is qualified as the generation of electric charges on surfaces of solid state materials by means of traction, torsion or pressure. This phenomenon was systematically described for the first time in 1880 by *Pierre and Jacques Curie*.

In figure 69 the direct piezoelectric effect of quartz is schematically demonstrated. The deformation of a piezoelectric material evokes microscopic dipoles within the unit cell. The displacement of the charge centers  $S^-$  and  $S^+$  from the common center induces a microscopic electrical tension. Subsequently, the summation over the unit cells in the crystal induces a macroscopic detectable tension.

The piezoelectric effect can only be observed on crystals without a center of symmetry. Quartz crystals are not centro-symmetric: Every silicon atom is located in the centre of a tetrahedron formed by 4 oxygen atoms. A force, either mechanical deformation, stress or strain in the direction base - apex (crystallographic direction [111]) deforms

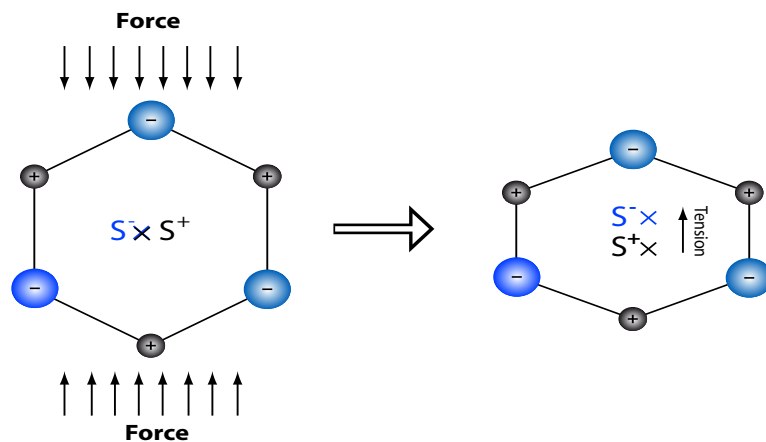


Fig. 69: Piezoelectric effect of quartz

those tetrahedrons, so that the squeezed tetrahedrons are polarized. Electricity is produced on the surfaces of the crystal in the direction [111].

By applying an electric field on the piezoelectric crystal, an induction of mechanical deformation or stress is detectable and hence called inverse piezoelectric effect.

Commercially available quartz crystal resonators offer high chemical resistivity, mechanical durability and high frequency stability concerning temperature changes. The general frequency stability  $\Delta f/f = 10^{-8}$  of quartz resonators leads to many applications, especially in electronic devices. Beside quartz, several piezoelectric resonator materials like lithium-niobate ( $\text{LiNbO}_3$ ) or barium-titanate ( $\text{BaTiO}_3$ ) are nowadays employed in band pass filters used in high frequency applications, for example: mobile phones, digital audio and video broadcasting and pressure sensors rely on the dependability on these tiny devices.

In the year 1959 *Sauerbrey*<sup>[61]</sup> demonstrated the physical relationship between additional mass loading on quartz plates and frequency changes. This fundamental work initiated numerous studies based on quartz crystal micro balances (QCM). The sensitivity of this gravimetric measurement method is in the range of nanograms and therefore a factor of approximately 100 times more sensitive compared to commercially available electro-mechanical balances.

Recent developments allow to manufacture acoustic sensors to detect very small quantities of analyte molecules in life and bio-science.<sup>[62]</sup>

#### 4.1 Classification of acoustic waves

A periodically oscillating electric field causes the piezoelectric material to contract and expand which introduces a whole bunch of different frequencies. In resonance conditions acoustic waves propagate either on the surface or through the material.

In the literature numerous modes of acoustic waves are known and divided into the following classes:

#### 4.1.1 Surface acoustic wave (SAW)

Surface acoustic waves are propagating along the surface of the material and are reflected on obstacles (e.g. inhomogeneous mass agglomerations on the surface) and edges of the used piezoelectric material. The velocity of the SAW is strongly dependent on external parameters, like temperature, pressure and surrounding dielectric. In the case of a mass sensor, the additional mass on the surface of the SAW device strongly influences the velocity of the propagating wave.

The SAW is excited with electroplated interdigital transducers (IDT). Surface acoustic wave devices have several disadvantages in sensor applications, for example the limitation not to be applicable in liquid medium due to energy dissipation into the liquid phase. On the other hand they are very sensitive.

In figure 70 a SAW device with IDT and the surface wave itself is schematically outlined. Usually, the surface penetration is around one wavelength of the SAW.

A sensor device based on surface acoustic waves is described in detail starting on page 196.

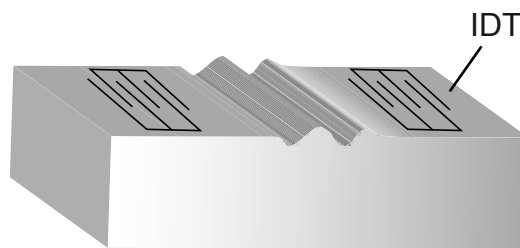


Fig. 70: Scheme of a surface acoustic wave device

#### 4.1.2 Acoustic plate mode (APM) sensors

Acoustic plate mode sensors benefit from reflections of the generated acoustic wave at the borderlines of the piezoelectric material. Interdigital transducers at the bottom side of the acoustic plate mode device excite an acoustic wave which propagates at the rear side parallel to the surface by means of total reflection at the boundary layer of the

sensor. The experimentally recorded signal detects the alteration of the velocity of the acoustic wave in case of an additional mass density on the surface, for example. Unlike SAW sensors, APM sensors are suitable for measurements in liquids. In figure 71 (A) an APM mode with corresponding wave propagation directions is schematically demonstrated. Part (B) shows a typical device with electrodes.

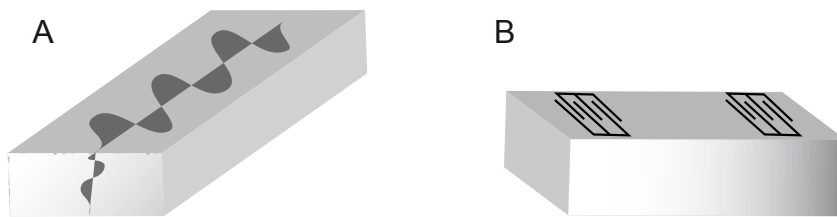


Fig. 71: Scheme of an acoustic plate mode propagation direction (A) and the corresponding device with lithographically applied IDT (B)

#### 4.1.3 *Flexural plate wave (FPW) sensors*

For flexural plate wave resonators very thin silicon nitride membranes are enclosed in silicon frames. Interdigital transducers are responsible for the excitation of the acoustic wave. Those kinds of waves exhibit amplitudes in the range of 100 nm, so that they may be used to maneuver fluids and small particles. Due to lower fundamental frequencies  $<10$  MHz, less expensive electric circuits are necessary to run these devices. Figure 72 (B) schematically displays a FPM device and in part (B) the direction of the propagating FPW-waves are outlined.

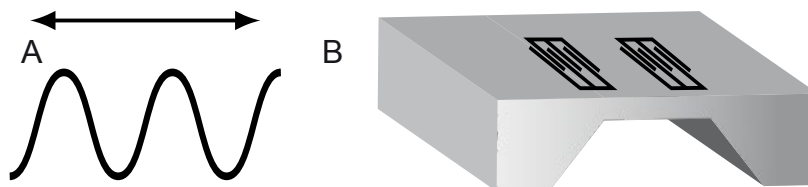


Fig. 72: Scheme of flexural plate wave device (B) and propagation direction (A)

#### 4.1.4 Shear mode (TSM) sensor

One of the three main topics of the work is based on the quartz crystal micro balance technique. Synonyms for thickness shear mode (TSM) sensors are bulk acoustic wave (BAW) resonators or quartz crystal micro balance (QCM) sensors.

QCM sensors consist of a piezoelectric quartz plate. For the excitation of the thickness shear mode two important requirements must be fulfilled:

- 1) Essential electrodes on the upper side and underside convert the applied external electric field into mechanical energy and vice versa. For this purpose, usually thin Au-electrodes deposited under vacuum conditions are used.
- 2) Only special cuts of the quartz crystal show the desired TSM vibrations (see figure 73). In order to minimize the influence of temperature on the resonance frequency, an AT-cut quartz is used in common practice. The approximate temperature dependence of an AT-cut quartz plate is  $1 \text{ Hz K}^{-1}$ .<sup>[63]</sup> The cut of  $35,25^\circ$  in terms of the optical axis of quartz ensures the highest possible sensitivity concerning mass density increases during adsorption experiments.

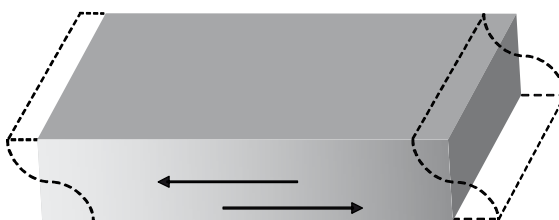


Fig. 73: Scheme of a shear thickness mode wave

Figure 74 (A) displays the AT-cut quartz crystal and TSM mode of a QCM chip (B), schematically. The yellow circular area represents the Au electrodes on both sides of

the chip. Under the precondition that any adsorbed mass on the surface of a QCM device behaves analogous to the piezoelectric substrate and the percentage of gained mass is low, any measured frequency shift is proportional to the adsorbed mass. In the literature a linear correlation between additional deposited mass and frequency changes up to a 2 % decrease of the fundamental frequency of the quartz resonator is found.<sup>[166]</sup> In case of a 10 MHz QCM device the linearity can be assumed for frequency changes up to 20.000 Hz.

This causal relationship between mass changes and frequency shifts was described for the first time by *Sauerbrey* in 1959.<sup>[61]</sup>

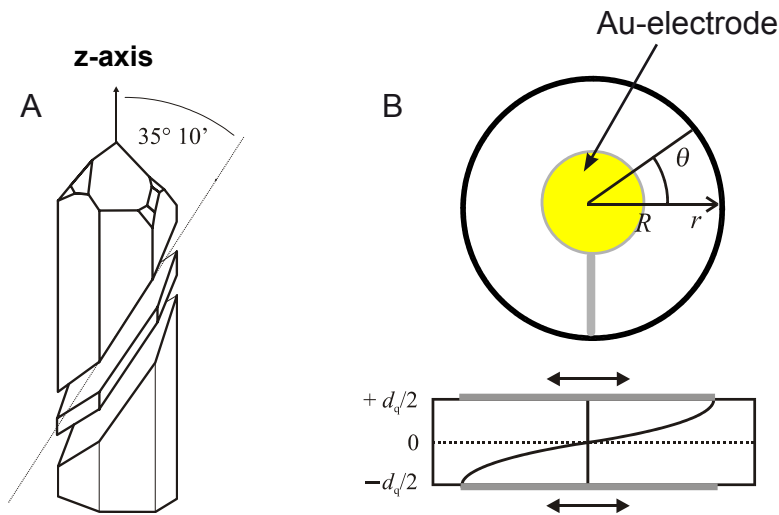


Fig. 74: AT-cut of quartz (A) and TSM mode of a QCM-chip (B)

Resonant acoustic waves are observed if the thickness of the quartz plate  $d_Q$  is half the size of the induced transversal wavelength  $\lambda_Q$  within the quartz crystal (equation (2)). Inside the quartz material the speed of sound is constant ( $v_Q = 3340 \text{ m s}^{-1}$ ) and depen-

$$d_Q = \frac{\lambda_Q}{2} \quad (2)$$

dent only on the wavelength  $\lambda_Q$  and the frequency  $f_Q$  of the acoustic wave (equation (3)).

$$v_Q = \lambda_Q f_Q \quad (3)$$

As a consequence the thickness  $d_Q$  and resonance frequency  $f_Q$  are changing in a constant ratio, due to the constant value of  $v_Q$  (equation (4)).

$$\frac{\Delta d_Q}{d_Q} = -\frac{\Delta f_Q}{f_Q} \quad (4)$$

*Sauerbrey* defined the additional mass density  $M_F$  of the top layer as the product of  $d_F$  times the density  $\rho_F$  (equation (5)). Analogous relationships are valid for the QCM chip itself.

$$M_F = d_F \rho_F \quad (5)$$

According to equation (5) the proportional change in frequency  $\Delta f_Q$  of the QCM sensor is described by the additional mass density  $\Delta M_F$  (see equation (6)).

$$\Delta f_Q = -f_Q \frac{\Delta M_F}{M_Q} \quad (6)$$



The commonly accepted *Sauerbrey* equation (7) is obtained by combining equation (2) - (5) resulting in expression equation (6).

$$\Delta f_Q = -2f_Q^2 \frac{\Delta M_F}{\rho_Q \nu_Q} \quad (7)$$

From the *Sauerbrey* equation it is obvious that the sensitivity of a QCM sensor is proportional to the squared basic oscillation frequency. The fundamental mode is connected to the overall thickness of the chip via equation (2), hence the higher  $f_Q$  the thinner the thickness of the quartz plates must be.

For example, a QCM chip running at 10 MHz exhibits a thickness of 166.7  $\mu\text{m}$ .

Boundary conditions of the corresponding wave equation lead to the recognition that besides the fundamental oscillation of 10 MHz ( $n=1$ ) exclusively odd overtones can be excited (e.g. 20 MHz,  $n=2$ ; 50 MHz,  $n=5$ ).

Considering the fundamental vibration of a QCM chip, the amplitude of the TSM is in maximum for  $r=0$  (center of the Au electrode; compare figure 74) and decreases to nearly zero at  $r=R$  at the edges of the Au electrode. The radial sensitivity (figure 75) is in maximum at the center of the Au electrode and decreases towards the edges. This behavior is usually described with a *Gauss* distribution.<sup>[64]</sup>

Regarding a commonly used 10 MHz QCM chip, the following sensitivity (table 14)

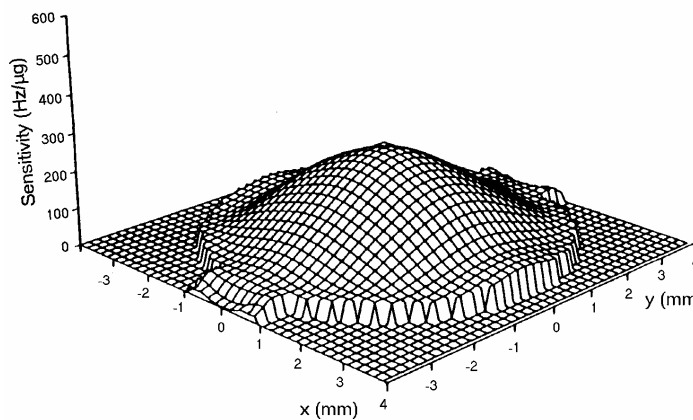


Fig. 75: Radial sensitivity distribution of a TSM oscillation

is set for granted in this work, whereas the parameters of quartz, the density  $\rho_Q = 2.648 \text{ g cm}^{-3}$  and the shear modulus  $\mu_Q = 2.947 \cdot 10^{11} \text{ g cm}^{-1} \text{ s}^{-2}$  were inserted into equation (8) to calculate the sensitivity.

$$\Delta m = \frac{A\sqrt{\mu_Q\rho_Q}}{-2f_0^2} \Delta f \quad (8)$$

By increasing the fundamental frequency the sensitivity increases but due to limitations of a significant higher fragility at decreased thickness ( $\cong$  higher  $f_Q$ ) and the higher complexity of the required electronic circuits, commercially available QCM devices<sup>20,21</sup> operate usually at 5 or 10 MHz.

Nowadays, QCM sensor systems are preferentially applied in bio-science, especially for investigations in liquids. In fluidic medium one has to be aware of visco-elastic effects of the surrounding liquid and thus energy loss through dissipation phenomena.

$f_Q$ [MHz]	$S_Q$ [ $10^{-9} \text{ g Hz}^{-1} \text{ cm}^{-2}$ ]
10	4.42

Tab. 14: Sensitivity of a 10 MHz QCM-chip

## 4.2 Influence of liquids on the resonance frequency

This work is focused on solid state sensitive layers, as for example microporous zeolites and mesoporous silica materials. Therefore, only a short introduction to QCM techniques in liquid environment shall be given. Besides important parameters like temperature and additional mass density the high viscosity or density of liquid medium compared to air has a dramatic influence on the resonance frequency.

*Gordon et al*<sup>[65]</sup> investigated the effects of density  $\rho_{li}$  and viscosity  $\eta_{li}$  of fluidic media on the correlation between frequency shifts and additional mass. Equation (9) describes the relationship between frequency changes and fundamental frequency.

<sup>20</sup> Q-Sense AB, Redegatan 13, 42677 Västra Frölunda, Sweden.

<sup>21</sup> KSV Instruments Ltd., Höyläämötie 7, 00380 Helsinki, Finland.

Applications of QCM-sensors in liquids have to cope with the fact that not only temperature fluctuations directly influence the resonance frequency itself, but temperature also influences the viscosity and density of the surrounding liquid. As a consequence, temperature stability is a high priority during QCM measurement and experiments in liquids.<sup>[66]</sup>

$$\Delta f = f_0^{3/2} \sqrt{\frac{\eta_{li}\rho_{li}}{\pi\mu_Q\rho_Q}} \quad (9)$$

The temperature coefficient of a 10 MHz quartz in liquids is settled around 15 Hz per Kelvin in the temperature range from 30 to 50 °C. Detailed information about quartz resonators in liquids can be found elsewhere.<sup>[67],[68]</sup>

#### 4.3 Influence of surface roughness on the resonance frequency of a QCM device

*Yin et al.*<sup>[69]</sup> investigated the influence of solid film morphology on the damping behavior of QCM devices. In conjunction with frequency shifts due to additional adsorbed mass density, the amplitude of the crystal quartz oscillator is influenced in the form of damping. This damping is explained by energy dissipation into the solid state film layered on the surface of the chip. The most important factors which have an impact on the damping are the mechanical properties of the overlying film and the slippage between the thin solid layer and the flat quartz surface.<sup>[70],[71]</sup>

The empirical relationship, expressed in equation (10), was found where  $A$  is the amplitude of the covered piezoelectric crystal,  $A_0$  the original amplitude of the uncovered quartz crystal,  $c$  an empirical parameter of the layered material,  $\Delta m$  the additional

$$\frac{\Delta A}{A_0} = -c \frac{\Delta m}{m_Q} \quad (10)$$

mass deposited on the QCM plate and  $m_0$  the original weight of the QCM chip. The explanation for decreasing amplitudes is energy transfer into the rigid or flexible surface covering layer. The authors extend the concept of damping onto the morphology of the surface layer: damping is related to energy dissipation which occurs in the liquid phase adsorbed in the pores of the substrate as well as the interference between the surface of the quartz crystal and the deposited film itself.

#### 4.4 Experimental setup for QCM sorption experiments

A quartz crystal micro balance (QCM) equipped with a fully automatic carrier and analyte flow system (see figure 76) was used to record the frequency changes of a vibrating QCM quartz chip<sup>22</sup> with a fundamental frequency of 10 MHz. Figure 77 depicts the used 10 MHz QCM Chip together with a 1 Euro coin for size comparison.

The central unit is the mixer and the controlled evaporation mixer element (CEM). In that unit the liquid analyte and the carrier gas (evaporated liquid nitrogen) are mixed and heated to the specific boiling point of the liquid to ensure an entirely homogeneous mixture of both components and gaseous phases. The partial pressure is adjusted by digital mass flow controllers (MFC)<sup>23</sup>, which control the mass flow of the analyte. In case of liquids, mass flows are converted into volumetric flows by certain assumptions

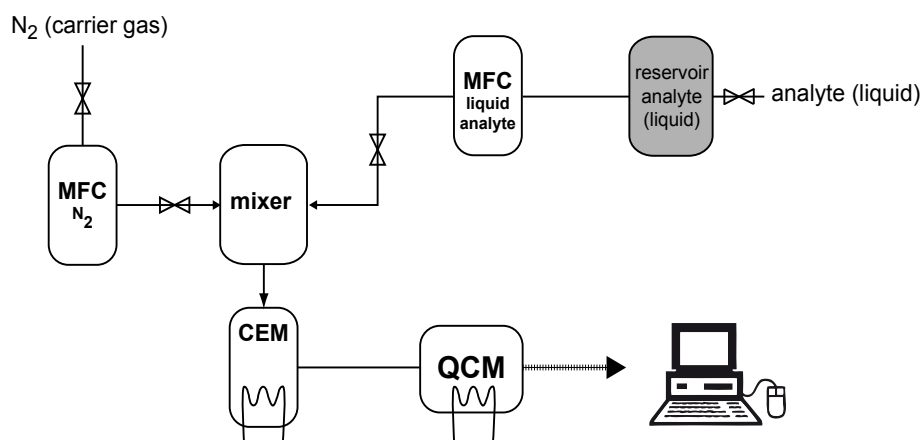


Fig. 76: Experimental setup

<sup>22</sup> model XA 1600, AT-cut; KVG Quartz Crystal Technology, 74924 Neckarbischofsheim, Germany.

<sup>23</sup> model W-101A-110-P and F-201C, Bronkhorst High-Tech, BV Nijverheidsstraat 1A, 7261 AK Ruurlo, Netherland.

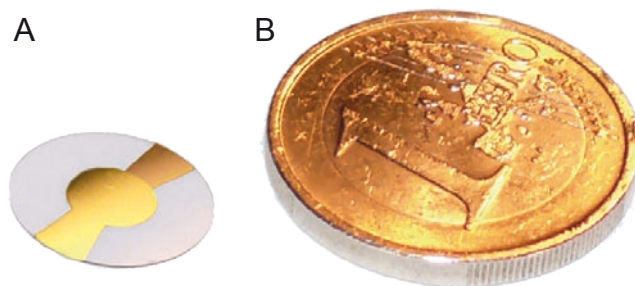


Fig. 77: QCM-chip (A) and Euro coin (B)

described in detail on page 95.

Frequency changes are automatically recorded by a PC supported measurement system. The automation was performed by a computer program written in the object oriented language LabView from National Instruments<sup>24</sup> which can be found in details in the appendix.

The challenge was to develop an automated data recording system which ensures the data point acquisition explicitly at equilibrated conditions. In the case of a QCM experiment, equilibrium conditions are represented by frequency stability over a specific time period.

As previously mentioned, additional adsorbed mass is responsible for frequency shifts of the QCM chip. As long as the adsorption and desorption processes are kinetically not hindered, equilibrium conditions are indicated by a “flat” evolution of data points (see figure 79 on page 92). In figure 78 a typical run of a temperature step (isotherms are commonly recorded at 4 different temperatures) is illustrated.

---

<sup>24</sup> National Instruments, 11500 N Mopac Expwy, Austin, TX 78759-3504, USA.

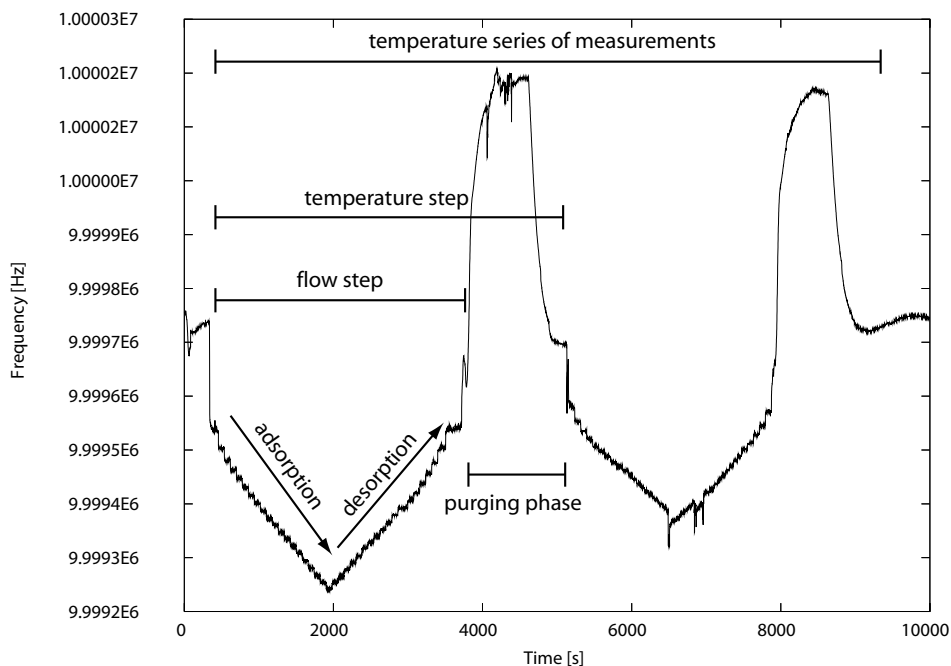


Fig. 78: Typical measurement raw data with two temperature steps

The QCM experiment is divided into 5 parts.

- part I: Evaluation of the fundamental frequency of each chip
- part II: Spin coating with the porous sorbent matrix
- part III: Drying of the sorbent material
- part IV: Recording of frequency changes - flow step phase
- part V: Purging phase

### *Part I*

Each QCM chip is thoroughly cleaned with double distilled water and acetone. After inserting the quartz chip into the QCM measurement cell, the temperature is raised to 140 °C with a nitrogen purge flow of 2000 ml min<sup>-1</sup> and held constant until the resonance frequency is stable ( $\pm 2-4$  Hz) within a time period of 1 hour.

The individual fundamental frequency of a single QCM chip is recorded at ambient room temperature and a nitrogen flow of 2000 ml min<sup>-1</sup>.

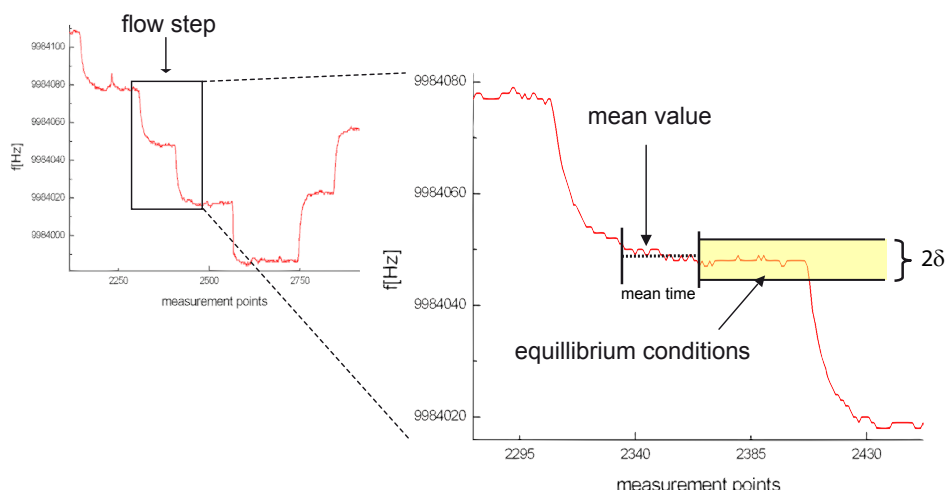


Fig. 79: Schematic evaluation of equilibrium conditions

### Part II

The dried and in part I defined quartz crystal is covered by spincoating with a colloidal suspension of the material of interest. The rotation speed is set to 3000 rpm to ensure homogenous distribution of the nanocrystals on the sensitive gold electrode.

The thickness of the porous film is adjusted by single or multiple casting procedures with respect to the preconditions of the *Sauerbrey* equation in order to achieve a reasonable frequency response to partial pressure changes. It turned out that an optimal result is obtained for additional mass loadings between 5 and 15  $\mu\text{g}$ , resulting in 1150 and 3500 Hz frequency shifts, respectively. The coated QCM chip is calcined in air below the critical combustion temperature of potentially introduced functional groups and in case of microporous or non-modified samples below temperatures from which on destruction of the siliceous framework occurs. The corresponding temperature and treatment conditions are given in the individual material synthesis and characterization sections starting on page 22.

### Part III

A well known feature of highly porous materials is their impressive sorption potential. To get rid of intermediately adsorbed molecules, mainly water and other unspecified volatile organic molecules, the spin coated QCM chip is heated up to 125  $^{\circ}\text{C}$  under nitrogen flow (2000  $\text{ml min}^{-1}$ ) inside the measurement cell. The temperature and the

purge flow is held constant until no significant frequency change is observed.

#### Part IV

Once the desired experimental temperature is reached, the flow step phase is initialized. Mass changes of the sensitive layer due to additional adsorbed mass, result in a slight decrease of the resonance frequency. The small adsorbed additional masses in the range of approximately 20 nanograms in minimum are precisely detectable by applying the *Sauerbrey* equation.

According to table 14, a frequency change of 1 Hz correspond to  $4.42 \cdot 10^{-9}$  g cm<sup>-2</sup> additional adsorbed mass. The amount of adsorbed analyte vapor in mmol g<sup>-1</sup> is calculated according to equation (11).

$$\theta \left[ \frac{\text{mmol}}{\text{g}} \right] = \frac{f_{0_{eq.}}^* - f_{eq.}^i}{f_0 - f_0^*} \cdot \frac{4.42 \cdot 10^{-9} \frac{\text{g}}{\text{Hz}}}{M_{mol}} \quad (11)$$

$f_0$  is the individual fundamental frequency of the QCM chip at room temperature (295 K),  $f_0^*$  the fundamental frequency with an additional sensing layer,  $f_0 - f_0^*$  the frequency shift between the empty and coated chip,  $f_{0_{eq.}}^*$  the fundamental frequency at the given temperature and nitrogen carrier gas flow,  $f_{eq.}^i$  the frequency at equilibrium conditions at a specific partial pressure,  $f_{0_{eq.}}^* - f_{eq.}^i$  the uptake of volatile molecules expressed as frequency changes in  $\Delta\text{Hz cm}^{-2}$ .

To ensure equilibrium conditions while increasing or decreasing the partial pressure of the analyte gases or vaporized liquids, frequency fluctuations are monitored. In figure 79 one flow step is magnified. Adsorbed molecules don't remain on the originally occupied adsorption sites but desorb and adsorb again or are moving along the surface (dynamic equilibrium conditions). As long as the partial pressure increases, the amount of adsorbed molecules increases as well. The graph illustrates this adsorption behavior with a typical adsorption curve (decreasing frequency) approaching a constant mean value. Regarding different self diffusion values of sorbate molecules, their chemical nature (hydrophobic - hydrophilic), size and shape as well as experimental temperature and partial pressure, the duration of reaching a constant mean value has to



be individually determined. Once this condition is fulfilled, the mean value is acquired by recording the frequency over a specified time period (see figure 79) and subsequently averaged followed by the evaluation of real equilibrium conditions. An individual adjustment of the time period and the frequency variance factor  $\Delta f$  ensures that correct equilibrium conditions are present and thus equilibrated frequency values are recorded. The next flow step initializes increased partial pressure of the adsorptive and analogous subsequent steps are performed to gather the complete isotherm indicated by the end of the flow step phase in figure 78. The following purging and recalibrating period accomplishes the entire removal of volatile compounds. As mentioned, frequency stability indicates the successful removal of volatile molecules and temperature permanence. In consequence, the whole temperature step at a certain temperature is finished and the recorded frequency values in conjunction with partial pressures are saved as a txt-file (ASCII data) and may be optionally sent via e-mail to an arbitrary recipient. Additional temperature steps complete a series of measurements at usually 4 different temperatures.

#### 4.4.1 *Partial pressure control*

The general definition of partial pressure of a gas is the pressure that it would exert if it would occupy the container alone. In the case of ideal gases the ideal gas law according to *Dalton* can be expressed by establishing the concept of molar fraction  $x_i$  whereas  $x_i = n_i/n_{total}$ . The pressure of one component  $p_i$  is expressed by equation (12).

$$p_i = x_i p_{total} \quad (12)$$

The relative partial pressure  $p/p_0$  of vaporized liquids is calculated according to equation (13), whereas  $p$  is the partial pressure of the analyte,  $p_0$  its vapor pressure at a specific temperature,  $p_{atm.}$  the ambient pressure in Pascal,  $\psi_i$  the valve opening of MFC<sub>*i*</sub>

(liquid) in percent,  $\kappa$  a proportionality factor of  $MFC_l$  regarding a standard liquid (1 g water per hour),  $\psi_g$  the valve opening of the  $MFC_g$  (carrier gas) and  $\lambda_g$  a proportional factor of  $MFC_g$ . The calculated partial pressures are based on ideal gas behavior assumptions ( $V_{mol} = 24.464 \text{ l mol}^{-1}$ ,  $T = 298.15 \text{ K}$ ).

$$\frac{p}{p_0} = \frac{p_{atm.}}{p_0} \frac{\Psi_l \kappa_l \frac{V_{mol}}{M}}{\Psi_g \lambda_g + \Psi_l \kappa_l \frac{V_{mol}}{M}} \quad (13)$$

Partial pressures were additionally calculated assuming Van-der-Waals behavior (equation (14)) to take into account repulsive and attractive molecular interactions and the non-zero volume taken up by the molecules themselves.

$$\left(p + a \frac{n^2}{V^2}\right)(V - nb) = nRT \quad (14)$$

The characteristic parameters  $a$  and  $b$  in the Van-der-Waals equation were taken from reference [72].

In order to obtain a volumetric flow from the evaporated liquid the molar volume according to equation (15) was evaluated with a short mathematical program (details can be found in the appendix) written with the help of the mathematical software Maple<sup>25</sup>.

$$pV^3 - (pnb + nRT)V^2 + an^2V + an^3 = 0 \quad (15)$$

The cubic equation possesses three possible complex solutions ( $V_{real,i}$ ) for the real gas state volume  $V_{real}$ . The minimum value  $|V_{real,i} - V_{ideal}|$  was determined, thus discovering the correct solution for  $V_{real}$ . The obtained real gas state volume  $V_{real}$  was inserted

---

<sup>25</sup> Maplesoft, 615 Kumpf Drive, Waterloo, Ontario, Canada.

into equation (13) to calculate the relative partial pressure  $p/p_0$ . Plotting the adsorbed amount in  $\text{mmol g}^{-1}$  versus  $p/p_0$  results in the isotherm of the investigated gas or vaporized liquid.

#### 4.4.2 Labview control program

##### 4.4.2.1 Basic configuration panel

The experimental QCM setup was basically constructed at Purdue University in 1997. In the original state the frequency counter was controlled by a simple Labview program in version 5.xx). Neither the automatic recording of equilibrium frequencies nor the temperature control and liquid flow system were present.

Figure 80 displays the developed basic setup panel front end. The following fields are related to the temperature controller<sup>26</sup> and are default values which should not be altered: “Controller No”, “Zone No” and “Port for omega”.

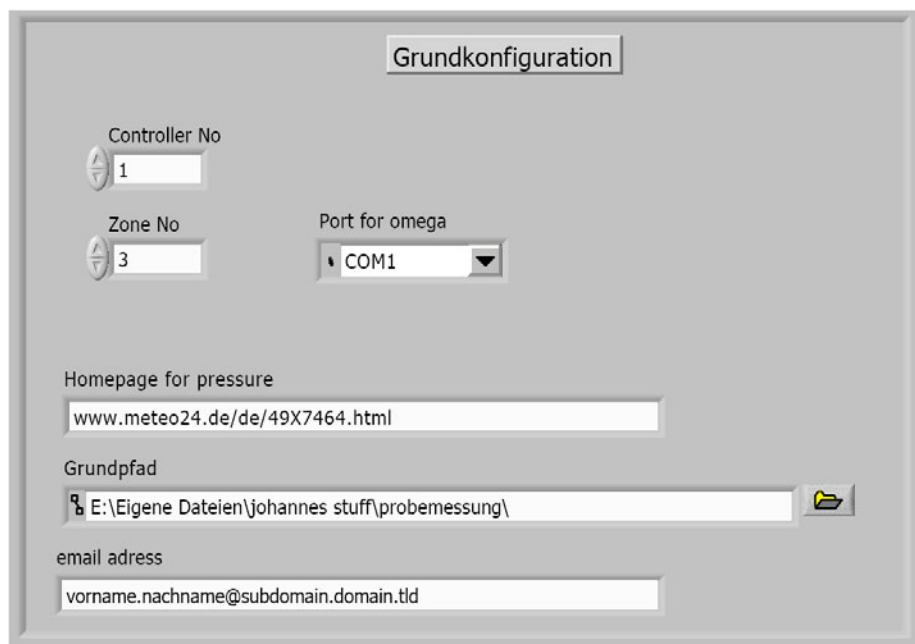


Fig. 80: Basic setup panel

<sup>26</sup> Omega CN3402, OMEGA Engineering Limited, Manchester M44 5BD, UK

Measured and recorded data sets are saved to hard disk or a network drive in a default location which is accessible via the field “Grundpfad”. Saved data may also be sent to an e-mail address specified in field “email address”. Referring to equation (13), the atmospheric pressure is essential for the correct partial pressure determination.

Due to the ability to remotely control the measurement PC via remote desktop protocol (RDP) the atmospheric pressure in the laboratory in Munich at 560 meters height above sea level is preferentially determined by semi empirical calculations. Starting with the sea level pressure obtained from an official meteorologic web site (“Homepage for pressure”) e.g. <http://www.meteo24.de> the absolute pressure in the laboratory is calculated according to the barometric formula (see table 15 for explanation of parameters), expressed in equation (16) and recommended by the German weather forecast organization Deutscher Wetterdienst (DWD)<sup>27</sup>.

$$p_0 = p(h)e^x \quad x = \frac{g_0}{R(T(h) + ChE + a \frac{h}{2})} h \quad (16)$$

$p_0$	pressure at sea level
$p(h)$	pressure at level
$h$	level
$g_0$	9.80665 m <sup>2</sup> s <sup>-1</sup>
$R$	287.05 m <sup>2</sup> s <sup>-2</sup> K <sup>-1</sup> , gas constant of dry air
$a$	0.65 K m <sup>-1</sup> , vertical temperature gradient
$E$	vapor pressure of water content
$Ch$	0.12 K E <sup>-1</sup> , additional parameter to E; takes into account the change of vapor pressure while increasing height
$t(h) > 9.1$ °C	$E = 18.2194 \cdot (1.0463 - e^{-0.0666 \cdot t(h)})$

Tab. 15: Parameters of barometric formula

<sup>27</sup> Deutscher Wetterdienst, Kaiserleistraße 29, 3563067 Offenbach am Main, Germany.

In order to validate the obtained semi empirical pressure values several controlling measurements with a barometer were performed. Deviations in the range of 50 - 100 Pascal were present which is acceptable in either case due to the minor influence on the 3rd decimal place in the final  $p/p_0$  value.

#### 4.4.2.2 *Flow control panel*

The flow panel controls 6 MFCs simultaneously. In the upper part of the flow panel the vapor flows in percent of the maximum valve opening are visually tracked. The

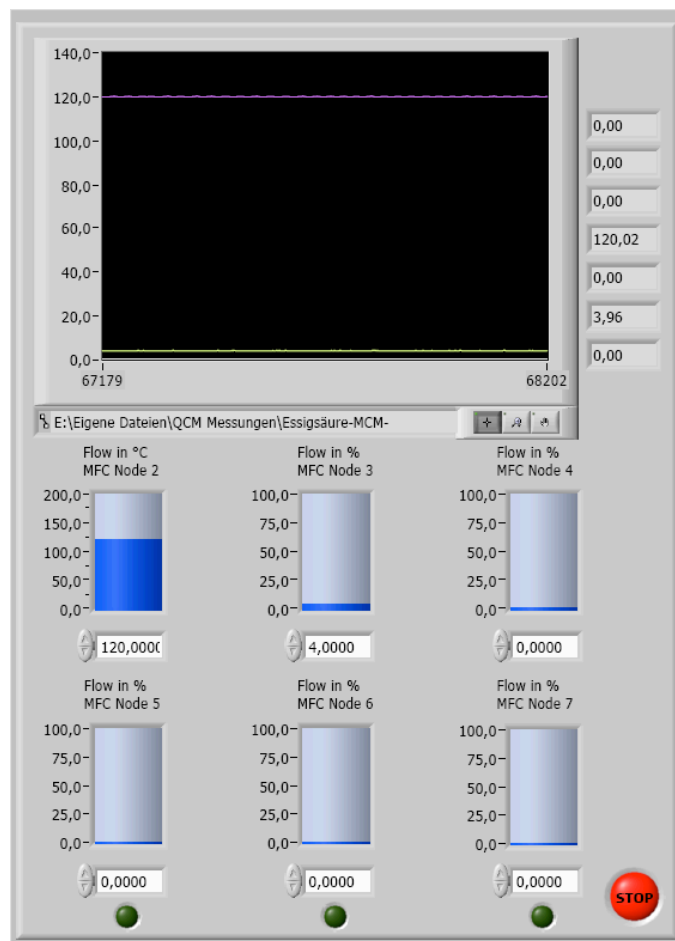


Fig. 81: Flow control panel

temperature of the controlled evaporating mixer (CEM) is directly printed in °C. Colored lines represent each MFC which are adjusted manually by inserting a numeric value into the corresponding field. For example, in figure 81 the temperature of the CEM is set to 120 °C and the nitrogen carrier flow to 4% valve opening, respectively 80 ml min<sup>-1</sup>. Green selectable highlighted buttons indicate whether a specific MFC is embedded in the automatic measurement process or not. Each MFC node is addressed individually by a unique numeric serial number thus providing the ability to connect any sorbent to the MFC. In table 16 the node numbers, their corresponding colored lines and observables are listed. Depending on the quantity of MFCs connected to the system the node numbers and corresponding colored lines in the display could vary.

node No.	color	observable
2	purple	temperature
3	green	liquid flow
5	yellow	N <sub>2</sub> flow

Tab. 16: Default node numbers and their representing colors

#### 4.4.2.3 Frequency counter panel

The basic frequency counter program is shown in figure 82. On the left part of the panel two QCM chip frequencies are counted and simultaneously displayed in red (QCM1) and blue (QCM2) in real-time. In the right part of the panel information about the mean values, standard deviation and the default saving location are given for the measured frequency distributed over the entire measurement duration (upper field). Equilibrium mean frequencies are saved to different files (QCM1\_mean.txt and QCM2\_mean.txt). The “file description QCM” field was added to the original panel to provide a user dependent input mask for additional and optional stored information, e.g. sample name, id and comments. Furthermore, the default saving paths were embedded in the panel.

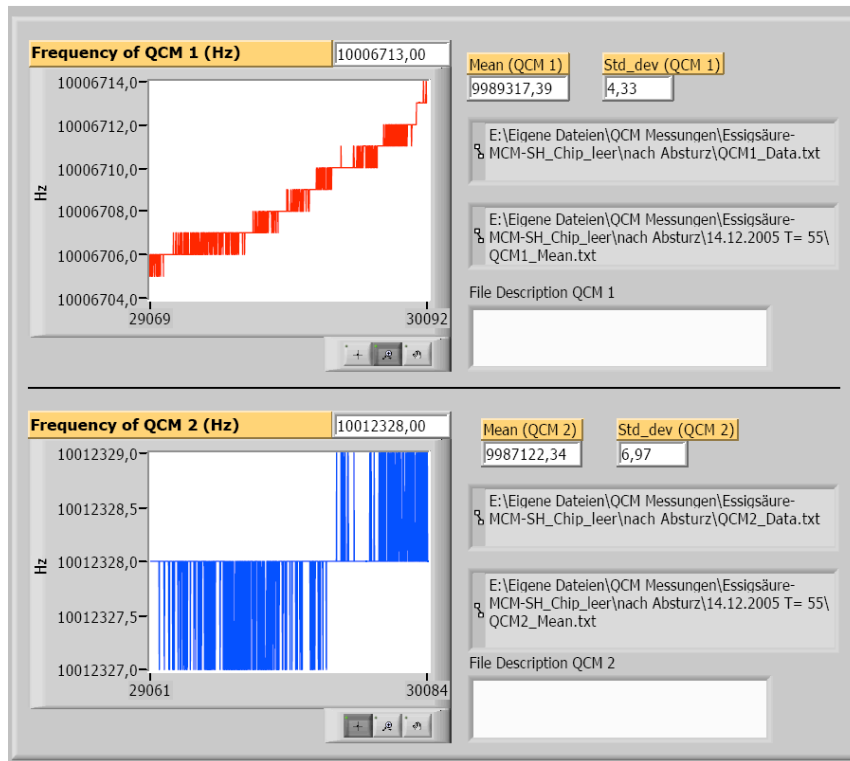


Fig. 82: Frequency counter panel

#### 4.4.2.4 Flow step panel

Most effort was focused on the development of an automated detection of frequency stability at a certain relative partial pressure, thus to be able to record exclusively frequency values at or close to equilibrium. At the flow step panel (figure 83) individual parameters can be adjusted. The two signals “Mittelwert #1” and “Mittelwert #2” display the actual averaged values in Hz. Both mean values are determined over a time period which has to be entered at the field “mean in s” in seconds. The duration of the



Fig. 83: Flow-step panel

accumulation of data points is dependent on the chemical nature of the adsorptive, the temperature set point for the experiment and the carrier flow conditions and has to be evaluated and optimized once a experiment is started.

As soon as the valid averaged value is identified, the algorithm checks if the deviation from the mean value is situated within the border condition “delta #1 in Hz” (QCM1) or “delta #2 in Hz” (QCM2) to take into account different sorption potentials of porous materials on the piezoelectric chips and the behavior of the investigated vapors. Hence, the frequency must be constant within the boundary conditions (set as delta Hz) over the specified “Stabilitätsbedingungen in s” period of time in seconds. Subject to the condition that the  $\Delta\text{Hz}$  value residues within the specified range, the program initializes the next flow step with increased partial pressure. In the field “Schrittgröße” the step size in percent of maximum valve opening of the MFC can be adjusted (see figure 83), The actual valid value for the MFC is visible in field “Aktueller Wert”.

If the sine qua non condition -  $\Delta\text{Hz}$  stability over a defined period of time - is not valid, the algorithm loop restarts from the evaluation of the average frequency value determination “Mittelwert #1” and “Mittelwert #2”. This loop evaluation will be performed unless the preset stability requirements are fulfilled. Once the next sequential partial pressure step is initialized, the adsorption (or desorption) process requires sufficient time to reach equilibrium conditions (static frequency). This important parameter is adjusted in the input box “Pause in s” as time delay in seconds. This delay has to be determined with awareness of its high impact on the quality of the recorded isotherms and the subsequent calculation of isosteric heats of adsorption, respectively.

#### 4.4.2.5 Mean frequency determination panel

As explained previously, the determination of the frequency mean value is the key step in recording data sets which represent equilibrium conditions. For this reason, the average frequencies  $f_0$  and  $f_0^*$  (see page 93) are similarly acquired. In figure 84 the mean frequency evaluation panel is shown. The duration of acquiring the meantime can be set manually, whereas a value of at least 80 - 100 s is recommended. Clicking the green button “Start mean measurement” activates the determination. The results



are separately displayed in “Mittelwert #2” (QCM1) and “Mittelwert #2” (QCM2).



Fig. 84: Mean frequency determination panel

#### 4.4.2.6 Temperature step panel

Beside the frequency stability sequence algorithm, an adequate temperature control and feedback mechanism (see figure 85) was developed to be able to measure frequency shifts fully automated at different temperatures. At the panel “Konfiguration Temp-Step” the necessary preferences are entered in the box “Setpoint in °C”. As an

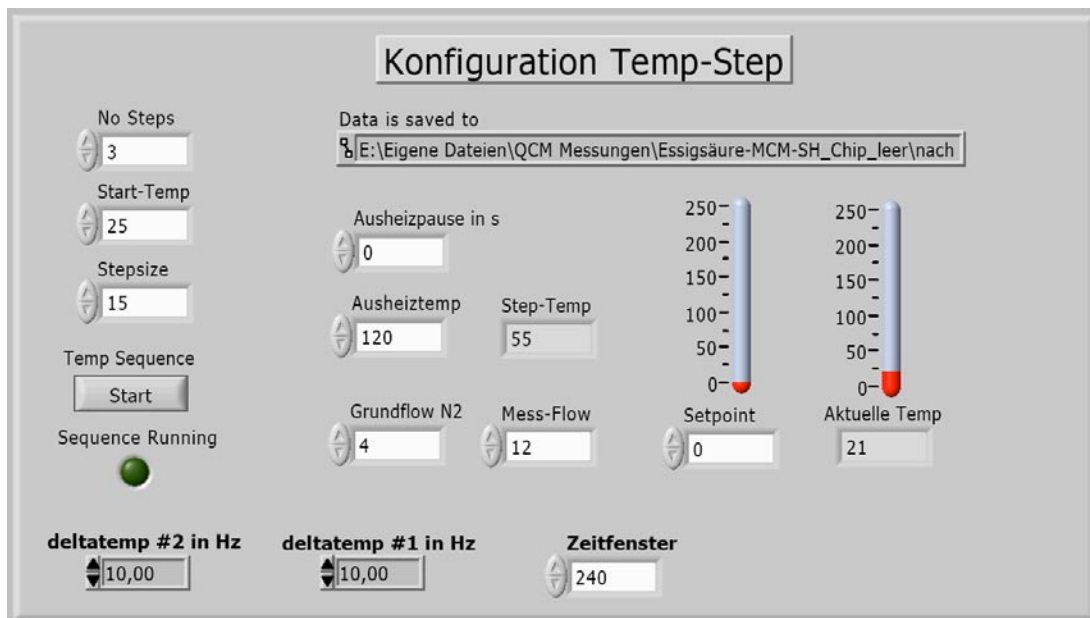


Fig. 85: Temperature step panel

option, the temperature during the QCM experiment can be manually altered at any time. The greyed field “Data is saved to” is write protected and displays the default saving location, defined in the basic setup panel (see figure 80). The input boxes “No Steps”, “Start-Temp” and “Stepsize” are related to the temperature step phase. According to figure 85 three temperature steps (“No. Steps”) are planned, for example:

- 1st step from the starting temperature “Start-Temp” of 25 °C up to 40 °C
- 2nd step from 40 ° to 55 °C
- 3rd step from 55 °C to 70 °C

The step size is defined in the input field “Stepsize”. Actual temperatures are displayed in the read only field “Step-Temp” and “Aktuelle Temp”

In between each temperature step, the QCM chips are purged with nitrogen at increased temperature. Purge flow (“Grundflow N2”) and bake out temperature (box “Ausheiztemp”) are adjustable. The temperature is held constant during the purging phase for a defined time period in seconds, set at the field “Ausheizpause in s” Due to demonstrating purpose the actual value is 0 seconds (see figure 85). As soon as the purging process is finished, the algorithm systems checks if the frequency is stable within the boundary conditions “deltatemp #1 in Hz” and “deltatemp #2 in Hz” within the time period “Zeitfenster” (in seconds). In the example settings, the time window is set to 240 seconds and the boundary conditions are  $\pm 10$  Hz for the QCM chips, each. The nitrogen carrier flow rate as an important parameter for the relative partial pressure calculations is adjustable at the input box “Mess-Flow” as percentage of maximum valve opening.

To start the preset temperature measurement the “Start” button must be pressed before the QCM-Labview program itself is continuously running. The green button “Sequence Running” is highlighted as soon as the measurement is started.

Summarizing the instructions to run a complete temperature step measurement, it is very important to manually evaluate the necessary settings in advance in order to optimize measurement duration, time delays and the quality of recorded frequency shift data.

## 5 Heat of adsorption: Theoretical considerations

In this chapter general applications of adsorption phenomena are described in short. The relevance of adsorption phenomena applied in sensor systems is presented, whereas a short introduction into recent fields of research shall be given.

Starting with commercial applications, more basic academic results of sorption experiments are presented in the second part of this chapter.

### 5.1 Commercial application I: The self cooling beer keg

An astonishing and fancy but useful application of sorption of molecules on porous material is the self cooling system of a beer keg.<sup>28</sup>

Figure 86 illustrates the basic cooling principle. The beer barrel itself contains the liq-



Fig. 86: Self cooling beer keg  
 English translations:  
 Ventilbetätigung= valve opening  
 Zeolith= zeolite, Bier= beer,  
 Ventil= valve, Verdampfer= liquid  
 water to be vaporized

uid beer to be cooled surrounded by water. The outer cladding contains the dried and anhydrous hydrophilic zeolite. By opening the valve between the liquid and the zeolite the sorption process is initialized. The water in the evaporator evaporates rapidly and thereby cools the beer. The evaporation energy is independent of the ambient pressure due to isobaric conditions but dependent on the ambient temperature. In table 17 evaporation enthalpies are exemplarily listed.<sup>[74]</sup>

From thermodynamics, it is well known that the evaporation energy at a certain temperature at isobaric conditions is equivalent to the heat of adsorption whereas the evaporation enthalpy is endothermic and the adsorption enthalpy exothermic. The released heat of adsorption inside the pores of the zeolite is spread into the metal outer rim of the keg and dissipated into the environment.

From the vaporization energies listed in table 17 it is apparent that the vaporisation energy decreases slightly with increasing temperature. As the manufacturer promises, at temperatures between room temperature and 60 °C the beer keg can be cooled to more refreshing temperatures of approximately 8 - 12 °C.

T [°C]	$\Delta H_{\text{vap.}}$ kJ mol <sup>-1</sup>
0	45.054
25	43.990
40	43.350
60	42.482
80	41.585
100	40.657
120	39.684
140	38.643
160	37.518
180	36.304

Tab. 17: Evaporation enthalpy of water<sup>[72]</sup>

## 5.2 Commercial application II: Drying of nourishments

From the same manufacturer a sophisticated conceptual approach exists to desiccate luxury foodstuffs, like aqueous coffee essences, with zeolites. The *Zeo-Tech* company emphasizes that their drying procedure with extremely hydrophilic zeolite ensures the removal of humidity but prevents the unwanted extraction of aromatic components.

Conventional freeze drying processes extract water and the aromatic compounds which flavor the coffee itself, for example. To exclusively remove only water molecules, *Zeo-Tech* rely on a shape and size selective zeolite material.

The released heat during the adsorption respectively the drying process is used to pre-dry the humid coffee powder. Thus, it is possible to abandon a water condenser which dehumidifies the coffee samples. From an energetic point of view, the process of drying food with zeolites is more efficient compared to conventional techniques. The necessary energy to evaporate the moisture is taken from the adsorption process on the zeolite via a hot dry air stream. The amount of energy consumed in the whole drying process is limited to the regeneration of the water loaded zeolite.

The total energy consumption depends naturally on the degree of pre drought of the coffee powder. An amount of 1000 kg with a water content of approximately 40%wt can be dried with an energy consumption of around 600 kWh.

In comparison, a freeze drying process with a mechanical refrigeration plant producing freeze dried coffee in the range of 550 - 600 kg h<sup>-1</sup> consumes around 1200 - 1400 kWh electrical power.<sup>29</sup> Normalized to 1000 kg, the power consumption is approximately 2400 up to 2800 kWh t<sup>-1</sup>. This amount covers the energy consumption in the factory process from the reception of the coffee extract to discharge of freeze dried coffee.

As a conclusion, the zeolite supported drying process is around 4 -5 time more efficient in terms of energy consumption.

### 5.3 Sensor related sorption applications based on piezoelectric devices

During the last decades many efforts have been made to develop gas sensing systems based on piezoelectric devices. Usually, the sensor signal of these analytical devices is either related to mass changes upon adsorption<sup>[75]</sup> or the electrical behavior of semiconductor components.<sup>[21]</sup> *Saitoh et al.*<sup>[76]</sup> developed a new sensor approach. They combined the response upon mass change and released heat of adsorption upon adsorption to a sensor signal. So far, this is the first approach to use the information from the released adsorption heat and the adsorbed mass to discriminate volatile molecules. The authors used an AT-cut quartz QCM together with a Y-cut QCM. The AT-cut QCM shows a nearly zero temperature coefficient at room temperature whereas the Y-cut QCM exhibits a large temperature coefficient (1000 ppm K<sup>-1</sup>). To demonstrate the effectiveness of such a sensor system the sensor response to some volatile organic solvents, such as benzene, toluene, cyclohexane or ethylbenzene was demonstrated. The response on the AT-cut QCM was not specific whereas the Y-cut QCM part showed a

---

<sup>29</sup> Niro A/S, Gladsaxevej 305, DK-2860 Soeborg, Denmark.

distinctive response upon each single evaporated solvent by detecting different isosteric heats of adsorption. Therefore the authors conclude that their combination of both AT and Y-cut QCM devices offers a new possibility to discriminate gas mixtures.

#### 5.4 Relevance of the heat of adsorption for catalytic processes

The knowledge of the quantitative amount of the heat of adsorption plays an important role in gas separation and catalytic chemical processes.

In a catalyzed reaction, a catalyst opens an alternative reaction pathway with a lowered activation energy. The molar ratio of the involved reactants and products in the state of equilibrium is however not affected. The catalyst influences exclusively the velocity of reaching the equilibrium of the reaction.

In heterogeneous catalysis the initial step is the physisorption of the reactants onto the solid surface. The exothermal sorption process releases a specific heat which represents the affinity of the gaseous species towards the solid surface and may allow a preliminary judgement on the efficiency of the catalytic reaction.

In case of porous matrix materials an adsorption occurs on available free adsorption sites. It has been demonstrated<sup>[77], [78]</sup> that the heat of adsorption affects the behavior and efficiency of hydrocarbon cracking reactions at catalytic active sites. *Bokhoven et al.*<sup>[79]</sup> investigated the activity properties of light alkane conversion and the important influence of the heat of sorption. The authors propose that the enhanced conversion rate of alkanes on H-MOR zeolite including additional alumina Lewis sites ( $Al^{3+}$ ) is related to increased heat of adsorption thus leading to a higher concentration of reactants.

In several studies, it was discovered that longer alkane chains produce a higher heat of adsorption resulting in lower apparent activation energies necessary for the catalytic mono molecular cracking reaction.<sup>[80], [81], [155]</sup>

*Denayer et al.*<sup>[156]</sup> concluded that differences in hydrosiomerization activities for alkanes with varying chain length are explained by their different heat of adsorption.

*Van de Runstraat et al.*<sup>[157]</sup> demonstrated that distinguishable heats of adsorption can explain the varying activities for n-hexane conversion over various zeolites.

Both authors came to the conclusion that the popular theory of different strengths of Lewis acidic sites inside the pores of porous materials is not the sole explanation. Higher isomerization rates of alkanes are moreover related to a increased cumulative population of reactants within the pores which is strongly dependent on the amount of released heat of adsorption.

The influence of the sorption heat on conversion activities of hydrocarbons was not only observed at microporous materials but also discovered with mesoporous siliceous materials. *Vinh-Thang et al.*<sup>[158]</sup> investigated the relationship between the sorption properties of toluene and n-heptane on SBA-15, a typical mesoporous material. According to variations in pore sizes of four SBA-15 samples, the maximum in adsorption capacity for the investigated hydrocarbons is presented, ranging from 3.5 to 7.5 mmol g<sup>-1</sup> for toluene. The authors focus on the effect of capillarity condensation occurring inside mesopores. The higher the pore volume of the mesoporous sample the higher the sorption capacity of the material. The determined heat of adsorption is reciprocally proportional to the pore sizes, thus concluding that the sample with a narrow pore opening evokes the maximum heat and vice versa. The authors summarize that the synthesized mesoporous SBA-15 samples preferentially adsorb the  $\pi$ -electron rich hydrocarbon toluene thus providing potential separation properties for cyclic and long chain hydrocarbons.

Basic description mechanisms of sorption initialized catalytic processes are based on the assumption that molecules in the gas phase collide with already adsorbed molecules on the catalyst surface. Some extended concepts take into account that adsorbed molecules or atoms may react with each other on the surface of the catalyst.

All theorems have in common that the knowledge of the specific sorption properties of the gaseous species is mandatory. Together with the insight to the catalyst's surface a prediction of catalytic activity can be given and the catalytic process may be further industrially applied.

In the previous prefacing topic the importance of the isosteric heat of adsorption was highlighted and the following chapter gives an overview of measurement techniques for the acquisition of this information.

## 5.5 Measurement methods acquiring the heat of adsorption

Three main concepts are well established to determine heats of adsorption. Commonly accepted empirical approaches are direct methods which measure the temperature increase during sorption or evaluate isosteric sorption data. With indirect methods the heat of adsorption is calculated from previously obtained adsorption isotherms.

There are essentially three methods known to experimentally determine the heat of adsorption:

- 1) Calorimetric measurement.
- 2) Calculation from adsorption equilibrium data
- 3) Calculation from desorption kinetics data

In this chapter an introduction to the basic measurement techniques for the popular experimental concepts 1) and 2) shall be given.

### 5.5.1 Calorimetric methods

In a calorimeter, schematically illustrated in figure 87, the investigated substance is separated and thermally insulated from the environment. The chemical reaction or in this case the physisorption takes place in the calorimeter bomb. The released heat is transferred into the surrounding medium, usually water. Temperature changes are precisely monitored with a thermometer. Taking into account well known parameters, like

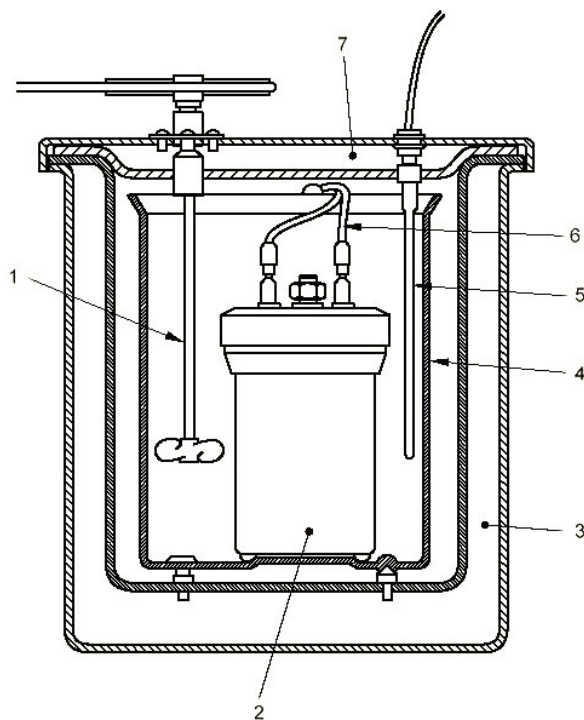


Fig. 87: Bomb calorimeter  
 1) Stirrer      2) Calorimeter bomb  
 3) Jacket  
 4) Calorimeter vessel  
 5) Thermometer  
 6) Inlet  
 7) Jacket lid



calorimeter dimensions, volume and the specific heat capacity of water, the enthalpy of the reaction can be determined. Calorimetry can be divided into two classes in general:

1) Constant volume calorimetry

Constant volume calorimetry involves the use of a constant volume calorimeter. As a consequence, no work is performed in constant volume calorimetry, so the heat measured equals the change in internal energy of the system. The fundamental correlation describing constant volume calorimetry is given in equation (17).

$$q = c_v dT = \Delta U \quad (17)$$

2) Constant pressure calorimetry

Constant pressure calorimetry is performed at constant pressure conditions. As a consequence, the measured heat equals the internal energy minus the work  $w$  performed. The enthalpy of the process under investigation is expressed in equation (18)

$$q = \Delta U - w = \Delta H \quad (18)$$

The mentioned thermodynamic equations describe the basic principle of calorimetry but do not take into account the sorption of molecules on the surface or internal surface of the matrix material, respectively partial pressure changes. In order to record sorption isotherms and calorimetric data, an extended approach is usually applied (see figure 88), which represents exemplarily a widely used measurement system. Commercially available systems may vary in some details but the principal functionality is identical.

The calorimetric approach to determine the heat of integration is a sophisticated experimental method. Several assumptions based on the experimental setup are made which lead to variety of equations describing the calorimetric approach. The experimental setup is quite demanding in terms of temperature stability, precision in volumetric and barometric measurements and last but not least technical skills of the operator. Additionally, in a typical experiment several milligrams of sample material are required to be able to record temperature changes due to the sorption heat. On the other hand, the

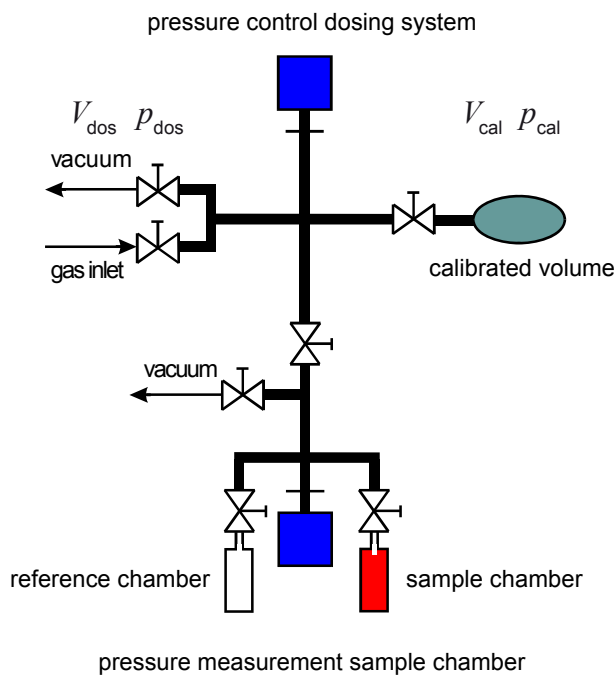


Fig. 88: Adsorption calorimetry dosing system

calorimetric method provides high accuracy of the obtained experimental data and in respect to many different scientific questions<sup>[82]</sup> the calorimeter designs can be adapted to the experimental requirements or are commercially available.<sup>30</sup>

### 5.5.2 Calculation from equilibrium data

The acquisition of the heat of adsorption based on recorded isotherm data is an indirect method. In order to obtain the desired value at isosteric conditions (identical degree of coverage) several isotherms of the investigated system sorptive - sorbent at different temperatures are evaluated.

*Benoit Clapeyron* developed the so called *Clapeyron* equation in 1834. The equation describes the slope  $a$  of phase boundary in a phase diagram.

At a boundary of a phase, respectively a system, described by means of temperature  $T$  and pressure  $p$ , two distinguishable phases  $\alpha$  and  $\beta$  coexist in a state of equilibrium. In consequence, the two phases exhibit identical chemical potentials and the system can be described with equation (19).

To determine the slope of the phase borderline, it's necessary to evaluate the expression  $\frac{dp}{dT}$ . At the whole phase boundary, equation (19) is valid in case of infinitesimal

<sup>30</sup> SETARAM France, 7, rue de l'Oratoire, 69300 Caluire, France.

$$\mu_{\alpha}(p, T) = \mu_{\beta}(p, T) \quad (19)$$

changes of  $p$  or  $T$ . This leads to the constraint that the changes of the potentials  $\mu_{\alpha}$  and  $\mu_{\beta}$  are similar and equation (20) can be proclaimed.

$$d\mu_{\alpha} = d\mu_{\beta} \quad (20)$$

Based on the fundamental thermodynamic equations, equation (21) can be written.  $S_m$  and  $V_m$  are molar variables.

$$d\mu = -S_m dT + V_m dp \quad (21)$$

Equation (22) follows from inserting equation (21) into equation (20).

$$-S_{\alpha,m} dT + V_{\alpha,m} dp = -S_{\beta,m} dT + V_{\beta,m} dp \quad (22)$$

The *Clapeyron* equation (23) is obtained from equation (22) by combining  $\Delta S_m = S_{\beta,m} - S_{\alpha,m}$ , respectively  $\Delta V_m = V_{\beta,m} - V_{\alpha,m}$ . The *Clapeyron* equation is valid for every possible phase equilibrium, e.g. the coexistence of a two solid phases of a pure chemical substance.

$$\frac{dp}{dT} = \frac{\Delta S_m}{\Delta V_m} \quad (23)$$

In case of reversible processes the entropy of the phase change can be calculated from the released heat  $q_{rev}$  which matches at isobaric conditions the change in molar entropy (24).

$$\Delta S_m = \frac{q_{rev}}{T} = \frac{\Delta H}{T} \quad (24)$$

In case of a phase transition between a liquid and a solid phase the *Clausius-Clapeyron* equation is expressed as equation (25).

$$\frac{dp}{dT} = \frac{\frac{\Delta H_{vap}}{T}}{\Delta V_m} = \frac{\Delta H_{vap}}{T(\Delta V_g - V_l)} \quad (25)$$

The following approximation transforms equation (25) into equation (26), which allows the direct determination of the heat of vaporization  $\Delta H_{vap}$ .

- 1) The molar volume of the liquid is negligible ( $V_l \ll V_g$ )
- 2) Ideal gas behavior is assumed for  $V_g$

$$\frac{dp}{dT} = -\frac{\Delta H_{vap}}{TV_{gas}} = -\frac{\Delta H_{vap}}{\frac{RT^2}{p}} \quad (26)$$

The above relationship may also be written as equation (27).

$$\frac{dp}{dT} \frac{T^2}{p} = \frac{\Delta H_{vap}}{R} \quad (27)$$

With  $\frac{dp}{p} = d(\ln p)$  and  $\frac{dT}{T^2} = -d\left(\frac{1}{T}\right)$  equation (27) can be expressed as equation (28), the commonly used *Clausius-Clapeyron* equation to calculate the heat of vaporization.

$$\frac{d(\ln p)}{d(1/T)} = \frac{\Delta H_{vap}}{R} \quad (28)$$

As mentioned on page 105, the heat of vaporization (endothermic) is equivalent to the heat of adsorption (exothermic), thus in equation (28)  $\Delta H_{vap}$  may be replaced by the isosteric heat of adsorption  $\Delta H_{ads}$  with a leading negative sign.

From a more practical point of view the following steps are performed to determine the isosteric heat of adsorption of the system under investigation.

- 1) Recording of isotherms at different temperatures
- 2) Plotting the obtained isotherms into one figure
- 3) The partial pressures of each single isotherm are determined in the region of the isotherm where sufficiently recorded data points are available<sup>31</sup>
- 4) In the final step  $\ln p$  versus  $1/T$  is plotted and the slope  $-\frac{\Delta H_{\text{vap}}}{R}$  is determined

In figure 89 (A) isotherms of ethanol on a mesoporous material at 4 temperatures ( $T = 296 \text{ K}$ ,  $308 \text{ K}$ ,  $323 \text{ K}$  and  $343 \text{ K}$ ) are exemplarily plotted into one figure. As an example, at a coverage of  $\theta = 2.0 \text{ mmol}$  the corresponding partial pressures are marked with dotted blue lines.

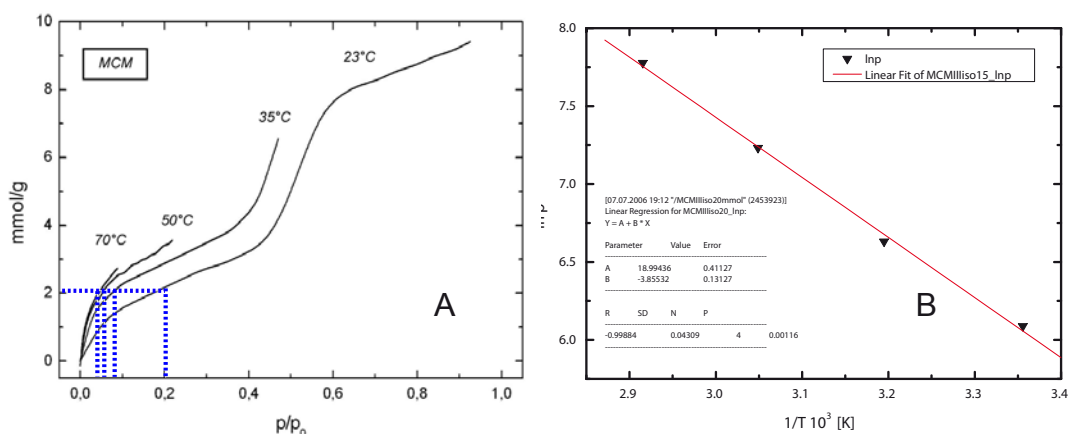


Fig. 89: Example of 4 isotherms of ethanol on QCM-E (A) and  $\ln p$  plotted versus  $1/T$  (B)

In table 18 the relevant extracted data to determine  $\Delta H_{\text{ads}}$  is listed. The first two yellow columns represent the measured data, respectively the recorded isotherm, the following green column is the vapor pressure  $p_0$  of the liquid, if an evaporated liquid is to be adsorbed on the material of interest. The listed vapor pressures  $p_{\text{vap}}$  are taken from a specialized database.<sup>[83]</sup> The first blue column is recursively calculated according to  $p/p_0$ . The plotted values  $\ln p$  and  $1/T$  are calculated from the column  $p$  (first blue column), respectively  $T$  (first yellow column).

In figure 89 (B) an example plot of  $\ln p$  vs.  $1/T \cdot 10^3$  is displayed. By linear regression (red line) the linear equation of the corresponding graph is assigned. From the slope

<sup>31</sup> The coverage  $\theta$  is given for the determination of the isosteric heat of adsorption for every single sample and analyte.

of the linear equation the value  $-\frac{\Delta H_{ads}}{R}$  is acquired and hence the heat of adsorption  $\Delta H_{ads}$  in  $\text{kJ mol}^{-1}$  for the analyte substance adsorbing on the matrix material is obtained. Additionally, the error of the fitting can be extracted from the linear regression calculation.

$T$ [K]	$p/p_0$	$p_{vap}$ [Pa]	$p$ [Pa]	$\ln p$	$1/T \cdot 10^3$
296	0.22	6751	796	6.68	3.38
313	0.080	13290	870	6.82	3.19
328	0.069	28610	1046	6.95	3.04
343	0.049	70630	1343	7.20	2.92

Tab. 18: Example of relevant data to determine  $\Delta H_{ads}$

## 6 QCM sorption experiments

Sorption and diffusion of volatile compounds in porous silica materials has been the subject of numerous studies. [43], [84], [85], [86], [87]

Surprisingly, very few data are available about the heat of adsorption of volatile organic molecules adsorbing on nano-particles of siliceous mesoporous materials, e.g. mesoporous MCM-41 type silica.

As mentioned on page 107, knowledge of the specific sorption behavior is very important for several potential applications. In this chapter the recorded isotherms of various organic vapors and gases adsorbing on nanosized mesoporous wormlike structured siliceous materials as well as their isosteric heat of adsorption are presented. One has to be aware of the small sample amounts between 5 and 70  $\mu\text{g}$  coated on QCM chips and the small overall particle dimensions of 75 - 150 nm resulting in a rapid heat flux and relatively short total data acquisition time of 4 - 6 hours.

The interpretation of obtained sorption results is based on experimentally gained data and some model calculations. Simulations of molecule dimensions and dipole moments of the relevant anchored molecular fragments were performed with standard “as given” options within numerous software preferences of the applied software Chem3D from CambridgeSoft<sup>[88]</sup>. The simulation data assist in the evaluation of the experimentally obtained sorption results.

The chapter “QCM sorption experiments” is divided into several sub-chapters each describing the sorption characteristics of different adsorptives adsorbing on various micro- or mesoporous samples.

The sub-chapters start with a short introduction of sorption relevant physical properties of vaporized or gaseous adsorptives and continue with a detailed presentation of recorded analyte isotherms. In intermediate paragraphs, the investigated samples are compared regarding their sorption features including conventionally obtained nitrogen sorption data. Furthermore, the isosteric heat of adsorption is presented for each individual material and adsorptive.

## 6.1 Adsorption of ethanol

Ethanol is a polar solvent with a dipole moment of  $1.69 \pm 0.03$  Debye.<sup>[72]</sup>

In figure 90 a labeled ball and stick model of ethanol is illustrated. The inter-atomic distances are listed in table 19, which were calculated with the computational program Cambridgesoft Chem3D Ultra<sup>[88]</sup>, using Van-der-Waals radii as basic parameters. The dimension of ethanol does not exceed 4.1 Å in maximum (center to center spacing)

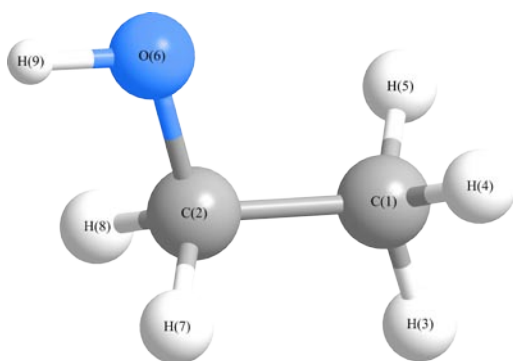


Fig. 90: Ball and stick model of ethanol

atom	distance [Å]
O(6)-H(9)	0.9605
C(2)-O(6)	1.4134
C(2)-H(7)	1.1131
C(2)-H(8)	1.1131
C(1)-H(5)	1.1142
C(1)-H(4)	1.1142
C(1)-H(3)	1.1143
C(1)-C(2)	1.5228
C(1)-O(6)	2.3987
H(9)-H(3)	4.1049

Tab. 19 : Inter-atomic distances of ethanol

which allows ethanol to diffuse into the mesoporous network without any size related limitations: the mesopore openings are at least more than five times bigger than the ethanol molecule itself. Inter-atomic distances obtained from crystal structures at 87 K are shown in figure 91.<sup>[73]</sup> Although the crystal structure values were determined at 87 K the values are in good agreement with model calculations at room temperature (compare table 19). As a result, in further discussions the values from model calculations at room temperature were applied.

The most important physical data for the calculation of isotherms and the relevant Van-



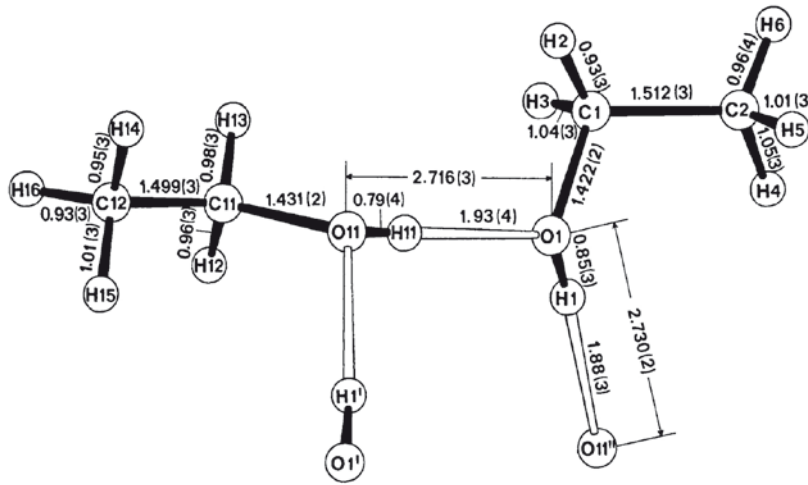


Fig. 91: Inter-atomic distances of EtOH at 87 K obtained from crystal structure<sup>[73]</sup>

der-Waals parameters are taken from reference [72] and listed in table 20. These specific parameters are used to calculate the molar liquid flow, respectively the volumetric flow (assuming real gas behavior) in the partial pressure calculation step explained on page 94.

physical data of ethanol				
molar mass [g mol <sup>-1</sup> ]	46.07			
density [g cm <sup>-3</sup> ] (at 293.15 K)	804.9			
vapor pressure [Pa]	295 K	308 K	323 K	343 K
	5645	13180	28410	70190
heat of vaporization [kJ mol <sup>-1</sup> ] (at 295 K)	43.07			
boiling point [K]	351.5			
Van-der-Waals parameters				
a	12.56			
b	0.0871			

Tab. 20: Physical data and Van-der-Waals parameters of ethanol

6.1.1 Sorption on non-modified mesoporous material: QCM-E

The isotherms of ethanol adsorbing on non-modified mesoporous material QCM-E at four different temperatures (295 K, 313 K, 328 K and 343 K) are presented in figure 92. In general and valid for all presented isotherms in this work is the following nomenclature: closed triangles represent the adsorption branch and open triangles the desorption of the volatile vapor or gas.

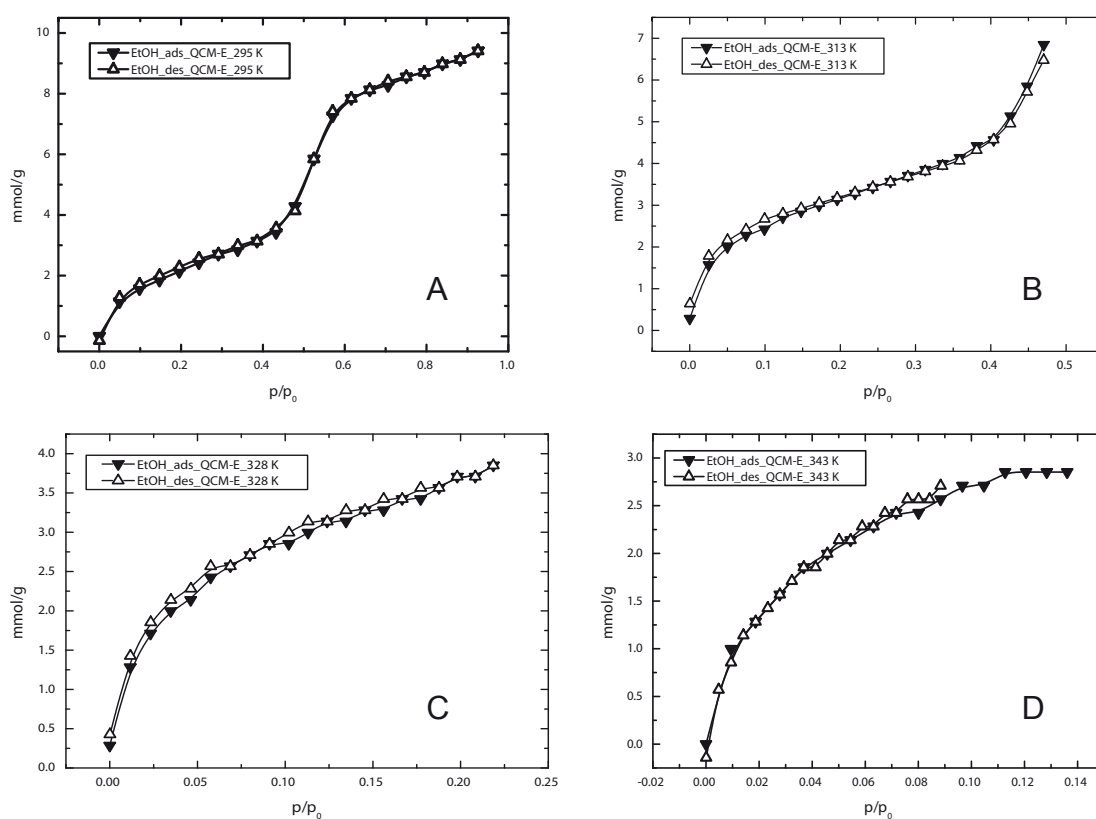


Fig. 92: Isotherms of ethanol adsorbing on sample QCM-E at 295 K (A), 313 K (B), 328 K (C) and 343 K (D)

As clearly visible, the room temperature isotherm follows a IUPAC classified type IV isotherm, typical for mesoporous materials with intra pore condensation. At  $p/p_0 \approx 0.1$  it can be assumed that all mesopores are occupied with at least one monolayer of

ethanol molecules and above that value multi-layer adsorption and furthermore pore condensation is occurring which correlates with reference [86]. The maximum sorption capacity for sample QCM-E is around  $10 \text{ mmol g}^{-1}$  at  $p/p_0 = 0.92$ .

*Nguyen et al.*<sup>[86]</sup> investigated the sorption properties of benzene and ethanol on four MCM-41 type material samples. In figure 93 the isotherm of ethanol and benzene adsorbing on one of their samples is given. Comparable to this work, the averaged maxi-

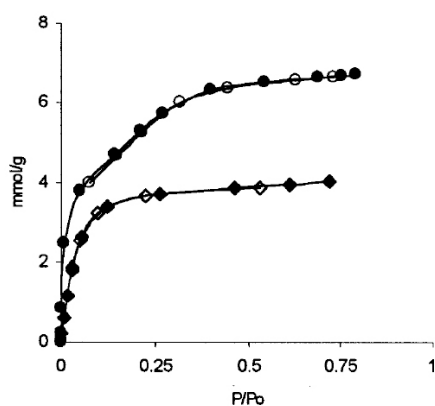


Fig. 93: Isotherm of ethanol (circles) and benzene (squares) on MCM-41<sup>[86]</sup>

sample ID	$\theta_{\max} [\text{mmol g}^{-1}]^a$
MCM-41-1	7
MCM-41-2	not available
MCM-41-3	16
MCM-41-4	14

<sup>a</sup> Estimated from plotted graphs

Tab. 21: Maximum degree of coverage for MCM-41 samples<sup>[86]</sup>

imum amount (see table 21) adsorbed is approximately  $12 \text{ mmol g}^{-1}$  with big variations. The difference in the maximum sorption capacity of around  $2 \text{ mmol g}^{-1}$  may be attributed to structure differences and individual sample surface variations of the MCM-41 material and the QCM-E sample: MCM-41 is a hexagonally ordered material, whereas the QCM-E sample is worm-like structured. Additionally, the samples of *Nguyen et al.* were synthesized with different chain lengths of the organic template molecule (14 - 16 carbon atoms).

Controlling experiments reveal a minor dependence on the mesoporous samples itself. In several experiments with samples synthesized under identical conditions only a non remarkable difference of  $\Delta\theta_{\max} = 0.5 - 0.7 \text{ mmol g}^{-1}$  between individual samples was observed.

During ethanol sorption experiments no hysteresis loop is present which is in good

agreement with investigations made by *Nguyen* and co-workers. Small gaps between the adsorption and desorption branch, especially in the isotherm recorded at 328 K, are due to temperature fluctuations of approximately  $\pm 0.5$  K caused by the temperature controller.

In figure 94 the frequency evolution of one of the QCM measurements is illustrated. Obviously, the temperature instability causes a periodic frequency oscillation of 15 Hz (see inset). Due to the averaging algorithm mechanism, in detail explained on page 93, the influence of temperature deviations is not that critical. In further experiments, this intense oscillation behavior is eliminated by extensive calibration steps of the temperature controller thus minimizing the temperature controller dependent oscillations down to less than 3 Hz (313 K - 328 K) and 7 - 10 Hz ( $T \geq 343$  K).

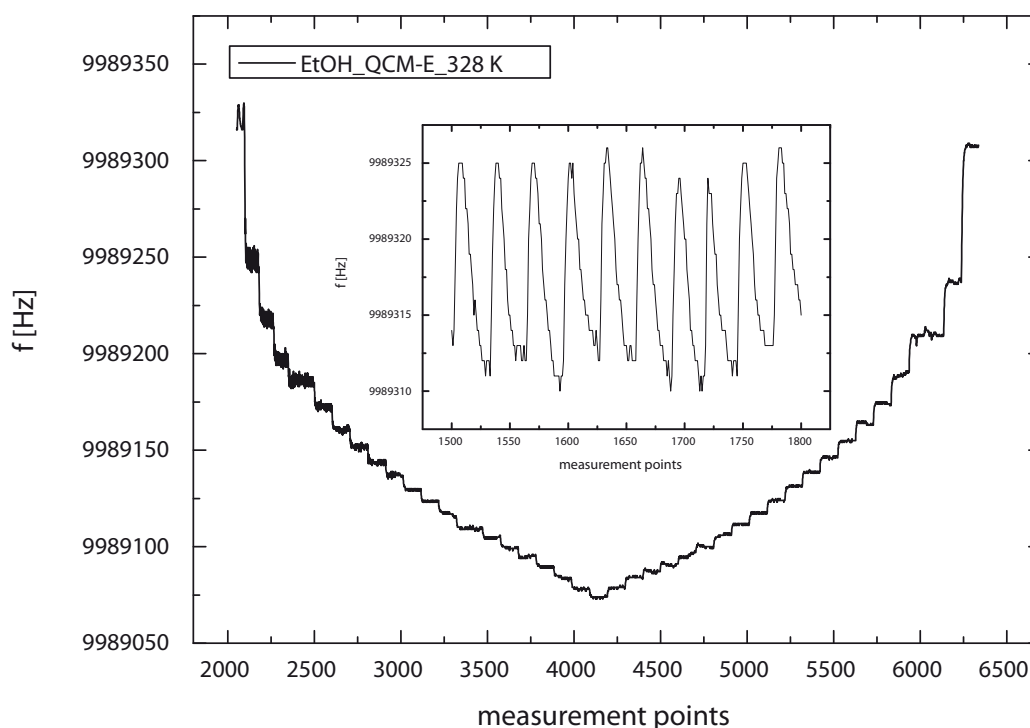


Fig. 94: Frequency changes caused by additional adsorbed/desorbed ethanol vapor and temperature fluctuations during the sorption experiment at 328 K (inset)

At 343 Kelvin, close to the boiling temperature of ethanol (350.8 K) at ambient pressure conditions of 95800 Pa, frequency fluctuations due to the relative high sample cell temperature are apparent but do not disturb the measurement itself. The impact on the characteristics of the isotherm is the attrition of some data points in the desorption branch from  $p/p_0 = 0.14$  to  $p/p_0 = 0.09$ . There is no influence on the final determination of the released sorption heat.

Beside temperature controller related frequency fluctuations, figure 94 demonstrates the reversibility of the sorption experiment as well as the rapid signal response to partial pressure changes. Usually, within 2 - 5 seconds the signal response, visible as a frequency decrease, is observed (figure 95). Equilibrium conditions are clearly detectable as frequency steps that are parallel to the x-axis. During the time period of 300 seconds the frequency is stable within  $\pm 10$  Hz.

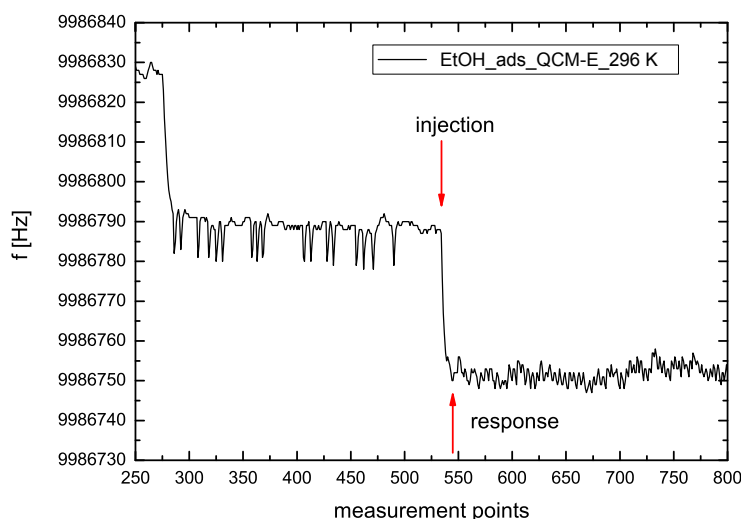


Fig. 95: Magnified RAW data obtained from sorption of ethanol on sample QCM-E (each point  $\cong 1.4$  seconds)

### 6.1.1.1 Heat of adsorption

According to the *Clausius-Clapeyron* method, the heat of adsorption is determined from the isotherms at different temperatures at isosteric conditions ( $\theta = \text{constant}$ ). Table 22 and figure 96 ( $\ln p$  versus  $T^{-1}$ ) display the relevant data used for the determina-

EtOH@QCM-E / $\theta = 2.5 \text{ mmol g}^{-1}$					
$T$ [K]	$p/p_0$	$p_{vap.}$ [Pa]	$p$ [Pa]	$\ln p$	$T^{-1} \cdot 10^3$
295	0.243	6306	1605	7.38	3.38
313	0.113	17800	2011	7.61	3.19
328	0.065	36050	2343	7.76	3.05
343	0.060	70190	4211	8.34	2.91

Tab. 22: Relative pressures of ethanol at various temperatures adsorbing on sample QCM-E

tion of the isosteric heat of adsorption at the isosteric coverage of  $2.5 \text{ mmol g}^{-1}$ , as examples. The vapor pressures at the corresponding temperatures are listed in column  $p_{vap.}$  and the related specific partial pressures are listed in column  $p$ .

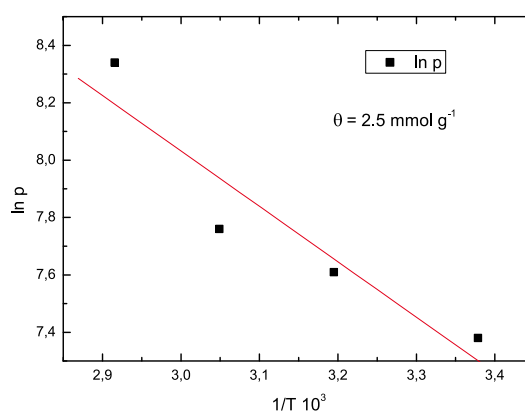


Fig. 96: Plot of  $\ln p$  versus  $T^{-1} \cdot 10^3$  at  $\theta = 2.5 \text{ mmol g}^{-1}$

Table 23 exhibits the calculated heat of adsorption for three different loadings of  $1.75 \text{ mmol g}^{-1}$ ,  $2.0 \text{ mmol g}^{-1}$  and  $2.5 \text{ mmol g}^{-1}$ . The average value of the isosteric heat of adsorption of ethanol adsorbed at the investigated QCM-E sample is  $-17.4 \pm 5.6 \text{ kJ mol}^{-1}$ . So far, in the literature no reliable data for the heat of adsorption of vaporized ethanol on siliceous mesoporous worm like structured material is known. To put this into perspective, *He et al.*<sup>[89]</sup> recently investigated the heats of adsorption of methane,

EtOH@QCM-E	
$\theta$ [mmol g <sup>-1</sup> ]	$-\Delta H_{\text{ads.}}$ [kJ mol <sup>-1</sup> ]
1.75 <sup>32</sup>	17.0 ± 8.6
2.0	13.4 ± 1.7
2.5	21.7 ± 6.5

Tab. 23: Heat of adsorption of ethanol sorbing on sample on QCM-E

ethane and carbon dioxide on MCM-41 like material. The values are given as 11 - 16 kJ mol<sup>-1</sup> for methane, 21 - 23 kJ mol<sup>-1</sup> for ethane and 23 - 25 kJ mol<sup>-1</sup> for carbon dioxide (all exothermic reactions). Compared to the enthalpy (heat) of vaporization  $\Delta H_{\text{vap.}}$  of ethanol (42.32 kJ mol<sup>-1</sup>), which is defined as the change of enthalpy in the conversion of one mole of liquid into the gaseous state at constant temperature, the value of ca. 13 - 22 kJ mol<sup>-1</sup> for the non-modified sample QCM-E is surprisingly low. It can be assumed that the high calcination temperature of 360 °C for the films studied here leads to substantial dehydroxylation of the silanols. This could lead to a hydrophobic siloxane surface with low heat of adsorption for ethanol.

*Caputo et al.*<sup>[90]</sup> recently investigated the sorption characteristics of ethanol vapor on zeolitized tuff from Campania (Southern Italy) and determined the heat of adsorption for ethanol. The value  $\Delta H_{\text{ads.}}$  is cited to be -25 kJ mol<sup>-1</sup>. This material could be considered as related to mesoporous silica, although the investigated tuff material is not mesoporous but microporous and crystalline.

### 6.1.2 Sorption on phenyl-functionalized mesoporous material: QCM-Ph

As demonstrated on page 28 a partial batch of sample QCM-E is co-condensed during synthesis *in situ* with phenyltriethoxysilane to obtain a mesoporous siliceous material functionalized with phenyl groups. This additional phenyl group dramatically changes the internal surface behavior. The phenyl group itself exhibits a dipole moment of nearly 0 Debye<sup>[72]</sup>, which emphasizes the non-polar character of that chemical frag-

<sup>32</sup> Disregarding the isotherm at 328 K, the value for  $\Delta H_{\text{ads.}}$  is  $-20.5 \pm 4.5$  kJ mol<sup>-1</sup>. The quality factor of the fit rises up  $R=0.91$  (including the isotherm at 328 K, the quality factor of the fit is  $R=0.49$ )

ment. The second effect influencing the sorption behavior of ethanol is the decrease of about 0.3 nm in pore size from the non modified material (3.8 nm) to the modified substance (3.5 nm). The decrease in pore size is reflected in the molecular dimension of the phenyl ring of about 0.3 nm in diameter. The Van-der Waals diameter was estimated with the software Chem3D<sup>[88]</sup>. Phenyl groups opposing each other inside the inner pore wall are not very likely because this situation would result in a decrease of approximately 0.6 nm if the introduced phenyl groups are not tilted. This approximation leads to the conclusion that the concentration of introduced phenyl groups is low enough to maintain the sorption capacity of the QCM-Ph sample which is reflected in a relative high surface area of 963 m<sup>2</sup> g<sup>-1</sup>.

In figure 97 the four isotherms of ethanol on the functionalized sample QCM-Ph are displayed. As expected, the shape of the room temperature isotherm is described with a type IV IUPAC classified model, indicating a mesoporous material with internal

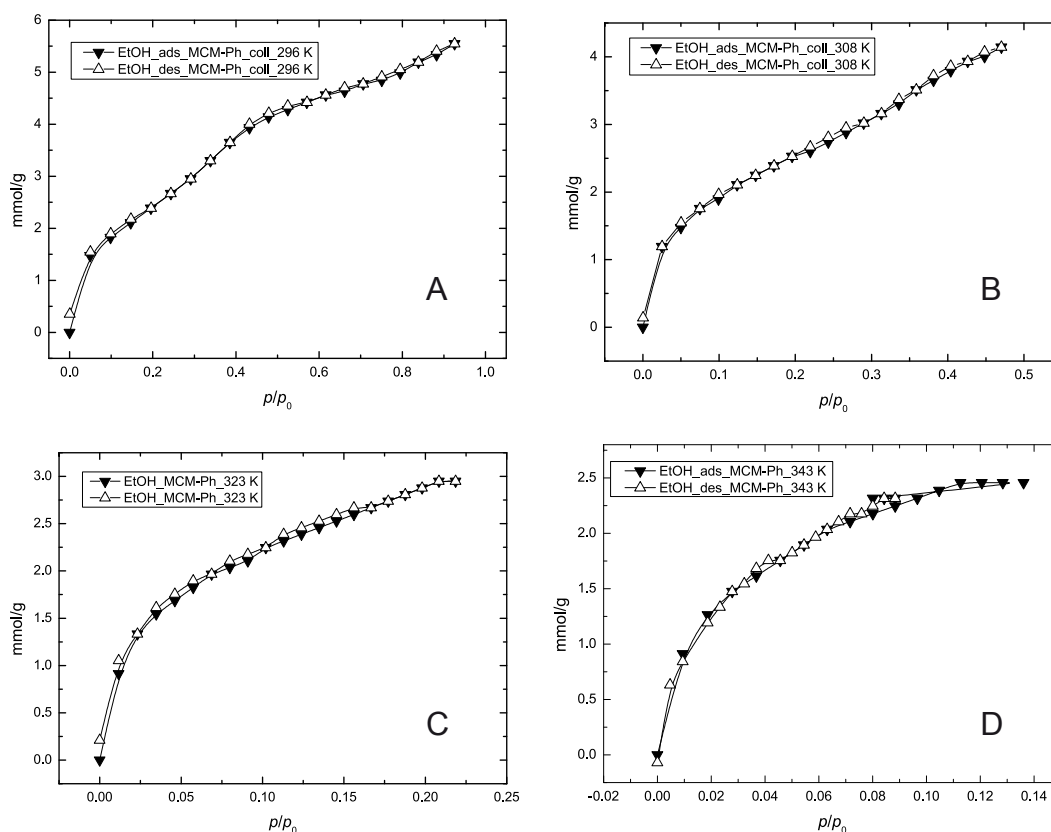


Fig. 97: Sorption isotherms of EtOH on phenyl functionalized sample QCM-Ph at 296 K (A), 308 K (B), 323 K (C) and 343 K (D)



pore condensation below  $p/p_0 = 1$ . A noticeable hysteresis is not observed. The very last desorption step back to  $p/p_0 = 0$  is kinetically hindered and the amount  $\theta$  does not decrease to the initial value of  $0 \text{ mmol g}^{-1}$ . In control experiments with extended desorption delay times, resonance frequencies representing a degree of coverage of  $0 \text{ mmol g}^{-1}$  were reached within 1 - 2 hours. An explanation might be pore blocking effects of some phenyl groups at the entrance to the internal pore system. The apparent limits do not influence any further investigations or calculations and are accepted as a desorption branch related systematic error in that specific sorption experiment. Exclusively, the isotherms' adsorption branches are utilized to determine the isosteric heat of adsorption.<sup>[91], [92], [93]</sup> Proof of equilibrium conditions during sorption experiments is given in figure 98. Over a time period of 4300 seconds the resonance fre-

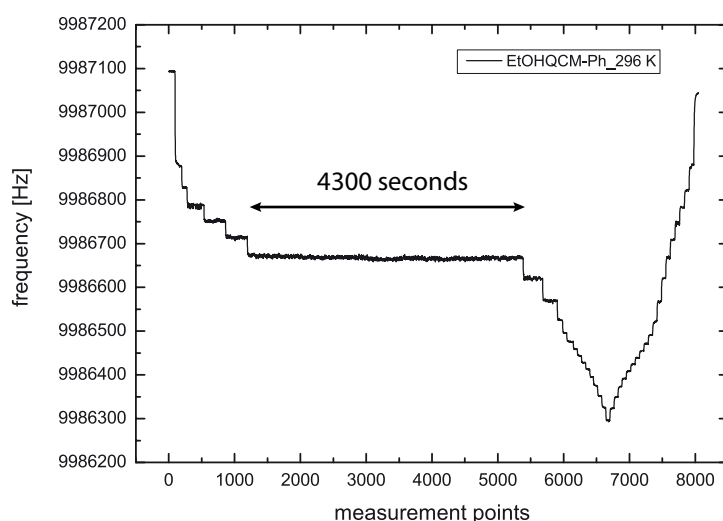


Fig. 98: Raw data of ethanol adsorbing on sample QCM-Ph at 296 K

quency fluctuates only  $\pm 7 \text{ Hz}$ , respectively  $28 \text{ ng}$ . In contrast, an increase of partial pressures, i.e. higher ethanol concentrations evoke spontaneous decreases in frequency with a specific time delay. This time delay of the frequency signal is related to the mass transport from the CEM (see on page 89) to the measurement cell which takes approximately  $0.5 - 1.0 \text{ s}$  at a nitrogen carrier flow of  $240 \text{ ml min}^{-1}$ . In order to compare the samples QCM-E and QCM-Ph based on pure sorption data, the two corresponding

room temperature isotherms are plotted into separated graphs (see figure 99) in terms of molar sorption capacity (A) in  $\text{mmol g}^{-1}$  and surface area (B) in  $\text{mmol m}^{-2}$ . From this experiment alone, the obviously different surface properties are distinguishable and thus further investigations in terms of determination of the isosteric heat of adsorption were performed.

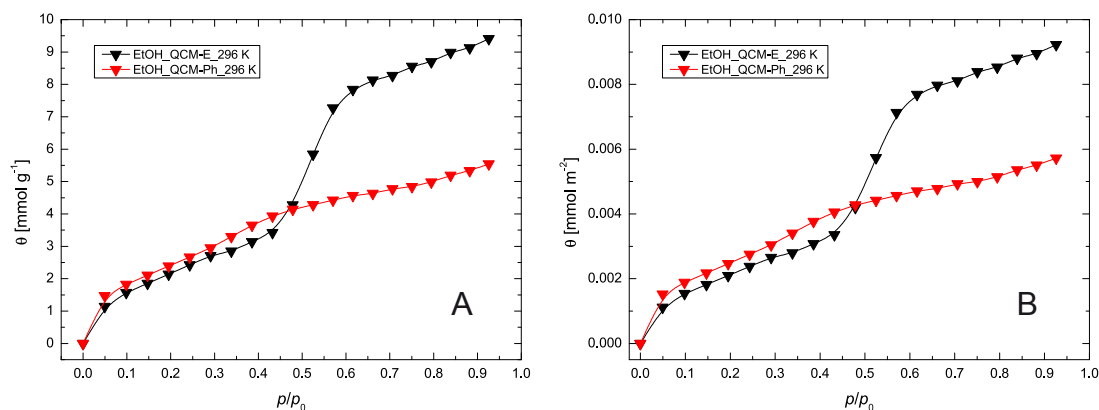


Fig. 99: Adsorption isotherms of ethanol on QCM-E (black) and QCM-Ph (red), plotted as a function of  $\text{mmol g}^{-1}$  (A) and  $\text{mmol m}^{-2}$  (B)

### 6.1.2.1 Heat of adsorption

In table 24 the isosteric heats of adsorption for ethanol adsorbing on sample QCM-Ph are reported. The averaged value is  $-27.7 \pm 4.5 \text{ kJ mol}^{-1}$ .

In principle, the calculation of isosteric sorption heat can be performed at any degree

EtOH@QCM-Ph	
$\theta$ [ $\text{mmol g}^{-1}$ ]	$-\Delta H_{\text{ads}}$ [ $\text{kJ mol}^{-1}$ ]
1.5	$25.4 \pm 5.0$
2.0	$26.3 \pm 4.0$
2.5	$31.3 \pm 4.5$

Tab. 24: Heat of adsorption of ethanol adsorbing on sample QCM-Ph

of coverage but it is strongly recommended to take into account increasing adsorptive adsorbate interactions above a critical point - the formation of monolayer and multilayer adsorption. Above that regime one would expect to obtain more or less the sorption enthalpy of adsorptive on adsorptive, in this case ethanol molecules adsorbing on a layer of ethanol already adsorbed on the modified silica surface. To evaluate that critical point the space filling of an analyte molecule in terms of its molecular dimension is estimated from model calculations (COSMO module included in the MoPac package of reference [88]) assuming a single molecule lying parallel to the surface and occupying the maximum in surface area. The solvent ethanol molecule exhibits a molecular surface of  $87.1 \text{ \AA}^2$ . In combination with the specific surface area of  $963 \text{ m}^2 \text{ g}^{-1}$  one can assume a monolayer appearing beyond a coverage of about  $1.8 \text{ mmol g}^{-1}$ . Figure 100 combines the acquired isotherms of ethanol at four different experimental temperatures. Up to  $2.5 \text{ mmol g}^{-1}$  one can assume that at room temperature the forming of multilayers or even pore filling is not present.

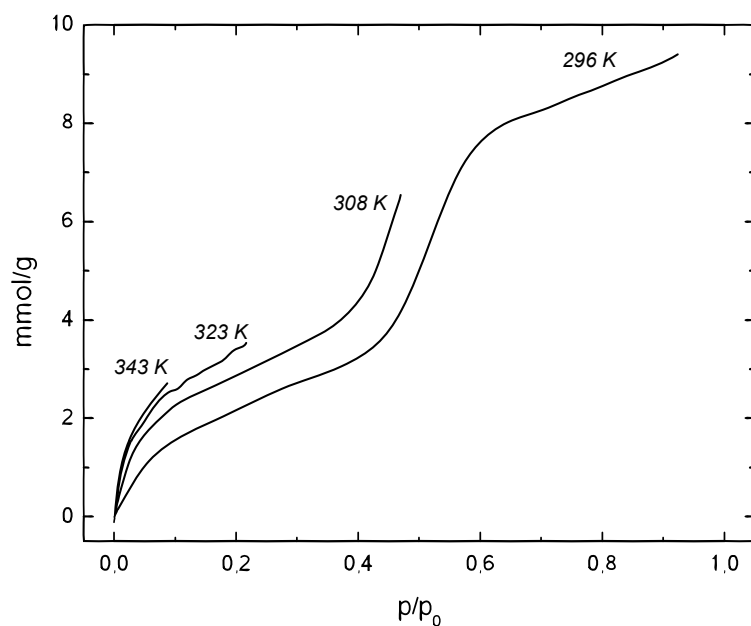


Fig. 100: Isotherms of ethanol on QCM-Ph at 296 K, 308 K, 323 K and 343 K

6.1.3 Sorption on cyano-functionalized mesoporous material: QCM-CN

The sorption data obtained from ethanol vapor adsorbing on the cyano-modified sample QCM-CN at 296 K, 308 K, 323 K and 343 K are available in figure 101.

The isotherm at room temperature is classified as type IV according to the IUPAC convention. Obviously, no hysteresis phenomena are observed. At certain data points, especially at final desorption steps at  $p/p_0 < 0.01$  some discrepancies of adsorption and desorption coverage values are detectable but do not interfere with further investigations of the sorption heat. These minor differences might occur due to the automated measurement system which stops the equilibria loop detection algorithm after a certain time in order not to unnecessarily delay succeeding temperature steps.

The shape of the room temperature isotherm is similar to the one of sample QCM-Ph and the maximum sorption capacity of sample QCM-CN (ca. 10 mmol g<sup>-1</sup>) even ex-

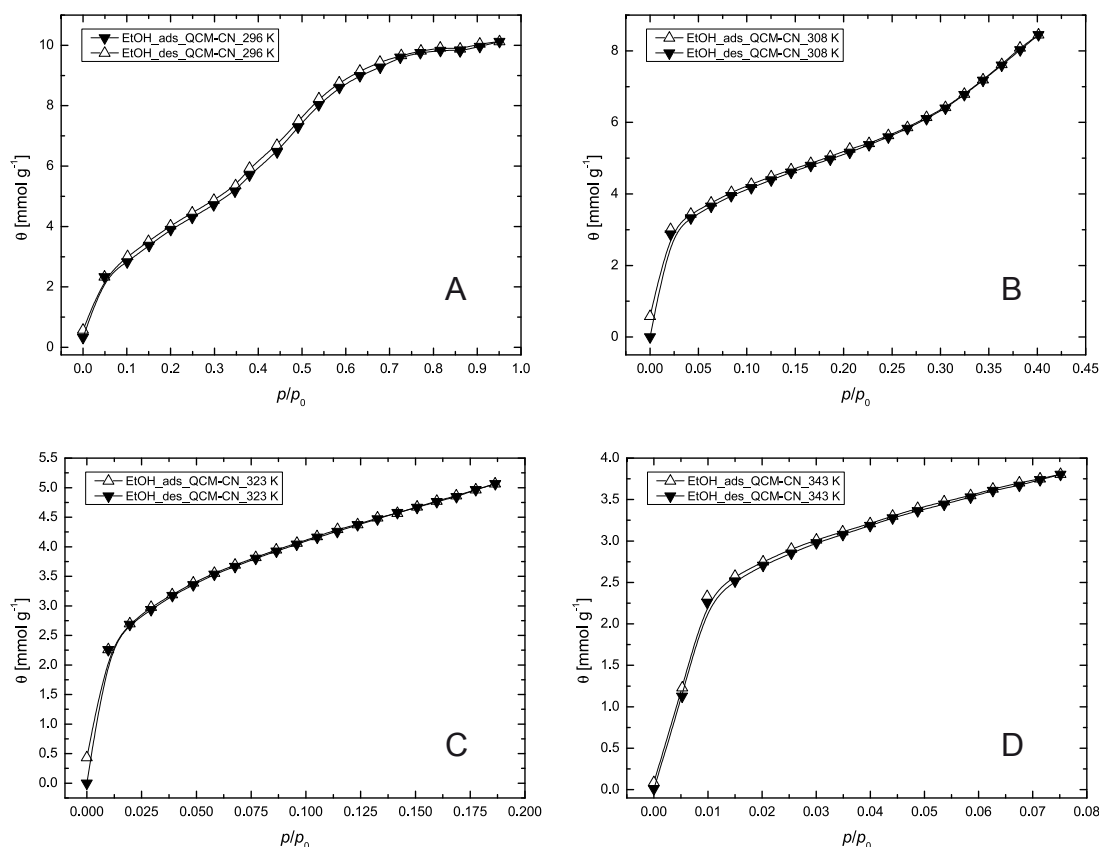


Fig. 101: Sorption isotherms of ethanol on QCM-CN at 296 K (A) 308 K (B), 323 K (C) and 343 K (D)

ceeds the one from QCM-Ph (ca. 5.5 mmol g<sup>-1</sup>). A possible explanation might be the reduced size of the organic substitutional molecule, in this case a decrease in size from a phenyl ring (approximated 0.3 nm in diameter) to the cyano group (estimated 0.1 nm). From characterisation data it is known that the surface area of QCM-CN is 904 m<sup>2</sup> g<sup>-1</sup> which is even lower compared to sample QCM-Ph with a surface area of 963 m<sup>2</sup> g<sup>-1</sup>.

In figure 102 the room temperature isotherms of QCM-CN (blue) together with already discussed samples QCM-E (black) and QCM-Ph (red) are plotted, whereas graph A shows the usually applied standard normalized degree of coverage in mmol g<sup>-1</sup> and graph B the coverage normalized to the BET surface areas of every individual material in mmol m<sup>-2</sup>.

Very important in this case is the fact that the room temperature isotherm of ethanol sorbing on sample QCM-CN was recorded at 295 K. One Kelvin temperature difference results in a slight shift of relative partial pressure  $p/p_0$  values due to a 385 Pa lower vapor pressure at that specific sample.

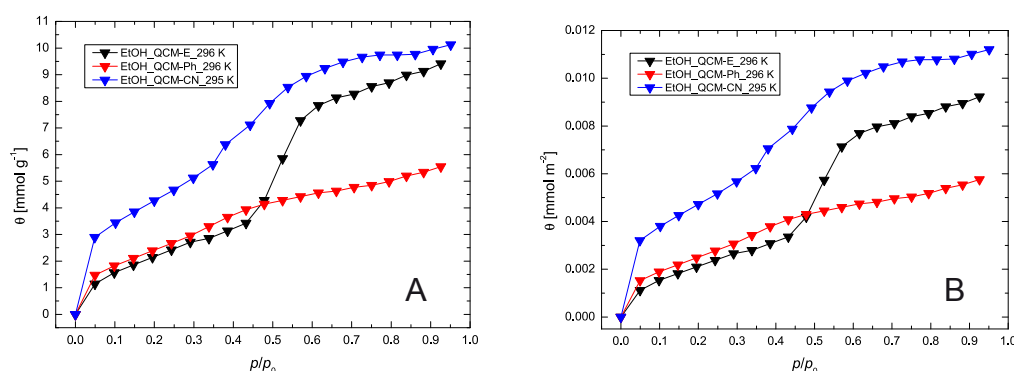


Fig. 102: Adsorption isotherm of ethanol on QCM-E (black), QCM-Ph (red) and QCM-CN (blue) plotted as a function of mmol g<sup>-1</sup> (A) and mmol m<sup>-2</sup> (B)

### 6.1.3.1 Heat of adsorption

To evaluate the recorded isotherms in terms of affinity of ethanol towards a specific surface the heat of adsorption was determined (table 25). The average value of  $-22.8 \pm 6.2$  kJ is about 5 kJ mol<sup>-1</sup> lower compared to the phenyl functionalized sample and

around  $5.5 \text{ kJ mol}^{-1}$  higher compared to the value of the non-modified sample. Therefore, it can be concluded that the cyano group with a dipole moment of ca. 1.7 Debye<sup>[88]</sup> presents a surface of moderate polarity for ethanol molecules.

EtOH@QCM-CN	
$\theta$ [mmol g <sup>-1</sup> ]	$-\Delta H_{\text{ads}}$ [kJ mol <sup>-1</sup> ]
3.0	$18.3 \pm 9.1$
3.5	$23.5 \pm 5.6$
3.75	$26.7 \pm 3.9$

Tab. 25: Heat of adsorption of ethanol adsorbing on QCM-CN

#### 6.1.4 Sorption on vinyl-functionalized mesoporous material: QCM-Vinyl

The modification of silanol groups of mesoporous silica with vinyl groups results in ethanol sorption isotherms illustrated in figure 103. The sorption data were obtained with a spin-coated amounts of sample ranging from  $6.3 - 9.4 \mu\text{g cm}^{-2}$  on the QCM chip. At high partial pressures above  $p/p_0 = 0.75$  there might be a controller problem indicated by a slight negative slope in the adsorption isotherm at 295 K (marked with an arrow). Very likely, this behavior is caused by fluctuations in the liquid mass flow controller system because two observations were made during the measurement:

First, in the desorption branch such a “strange” behavior is not present and second, in the recorded liquid MFC graph very small fluctuations of  $\pm 0.8 \%$  were observed during the this very specific flow step. The maximum mass flow of liquid ethanol in the performed sorption experiments was  $28.8 \text{ mg min}^{-1}$  and the mentioned  $0.8 \%$  deviation represents  $230.4 \mu\text{g min}^{-1}$  in maximum.

In general, the shape of the room temperature isotherm does not vastly differ from the ones obtained with sample QCM-Ph or QCM-CN and can be described with an IUPAC classified type IV isotherm. The maximum sorption capacity of roughly  $7 \text{ mmol g}^{-1}$  ranges between the samples QCM-E and QCM-CN (both approximately  $10 \text{ mmol}$

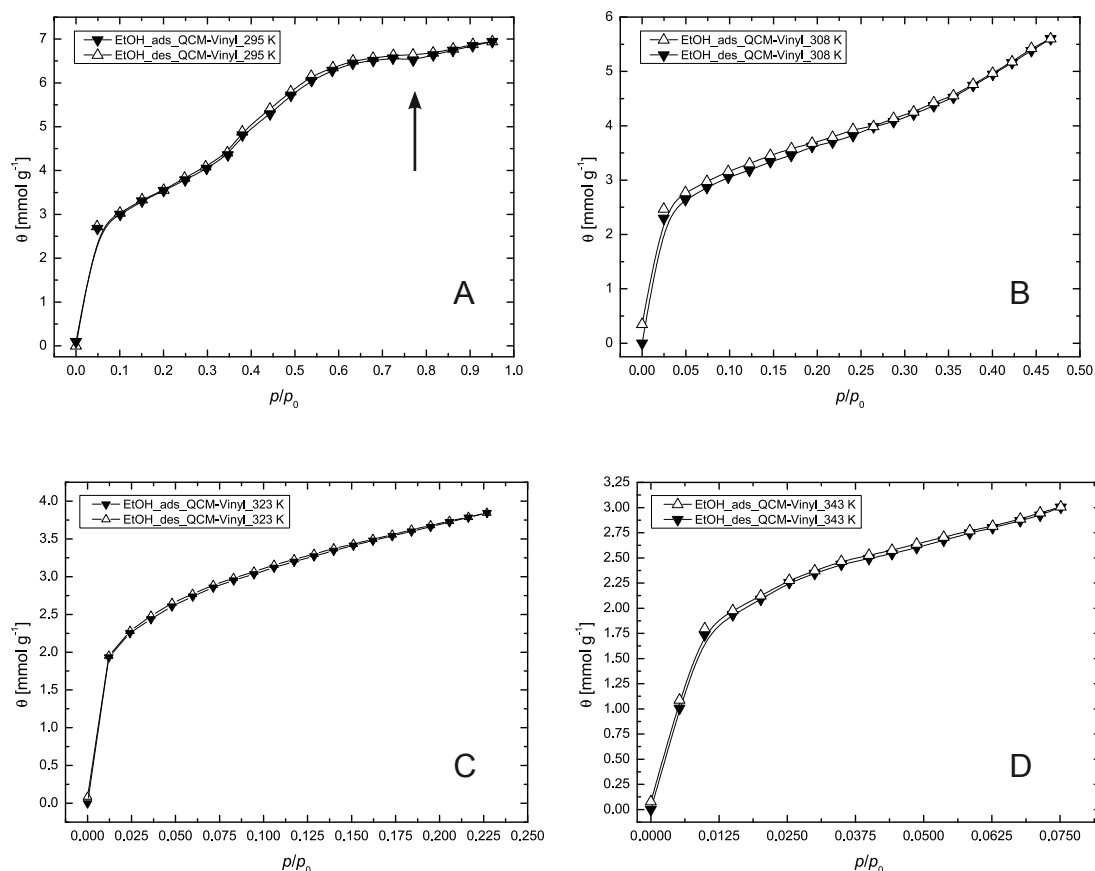


Fig. 103: Sorption isotherm of ethanol on QCM-Vinyl at 295 K (A) 308 K (B), 323 K (C) and 343 K (D)

g<sup>-1</sup>) and the phenyl modified sample QCM-Ph (about 5.5 mmol g<sup>-1</sup>). In figure 104 all previously recorded isotherms are plotted together with the one of QCM-Vinyl. Graph A states the coverage  $\theta$  in mmol g<sup>-1</sup> versus  $p/p_0$  and part B of figure 104 the degree of coverage  $\theta$  in mmol m<sup>-2</sup>.

Up to  $p/p_0 = 0.05$  the isotherm for sample QCM-Vinyl is almost similar to the one of QCM-CN and exhibits a very steep initial slope. In the course of the graph the isotherm behaves more similar to the one determined with sample QCM-Ph.

At identical partial pressures sample QCM-Vinyl offers an approximated 2 mmol g<sup>-1</sup> higher sorption capacity compared to sample QCM-Ph. This superior sorption capacity is present and relatively constant over the whole partial pressure range. Attention has to be drawn to the room temperature isotherm of sample QCM-Vinyl which has been recorded at 295 K (compared to 296 K for sample QCM-E, QCM-Ph).

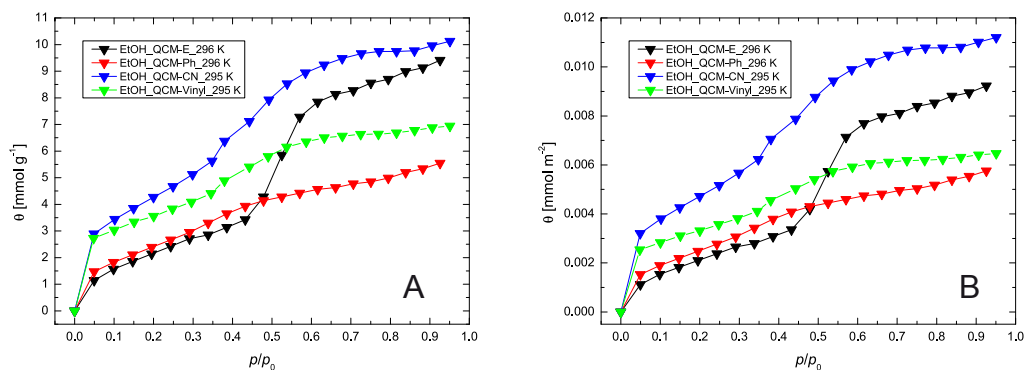


Fig. 104: Adsorption isotherm of ethanol on QCM-E (black), QCM-Ph (red), QCM-CN (blue) and QCM-Vinyl (green) plotted as a function of  $\text{mmol g}^{-1}$  (A) and  $\text{mmol m}^{-2}$  (B)

#### 6.1.4.1 Heat of adsorption

The isosteric heat of adsorption of ethanol adsorbing on the vinyl functionalized sample QCM-Vinyl is listed in table 26.

The averaged isosteric heat of adsorption at the coverage between  $\theta = 2.75 \text{ mmol g}^{-1}$  and  $\theta = 3.0 \text{ mmol g}^{-1}$  for sample QCM-Vinyl is  $-39.1 \pm 4.1 \text{ kJ mol}^{-1}$  in average and thus about  $21.7 \text{ kJ mol}^{-1}$  higher compared to the non-functionalized sample. Calculating the isosteric heat of adsorption without the data obtained from the isotherm at 343 K at 3.5 and  $3.75 \text{ mmol g}^{-1}$  (pressure range experimentally not accessible), the average isosteric heat of coverage between 2.75 and  $3.75 \text{ mmol g}^{-1}$  is  $36.9 \pm 3.5 \text{ kJ mol}^{-1}$ .

EtOH@QCM-Vinyl	
$\theta \text{ [mmol g}^{-1}\text{]}$	$-\Delta H_{\text{ads.}} \text{ [kJ mol}^{-1}\text{]}$
2.75	$39.4 \pm 3.8$
3.0	$38.7 \pm 4.4$
$3.5^{33}$	$35.0 \pm 1.9$
$3.75^{33}$	$34.3 \pm 3.7$

Tab. 26: Heat of adsorption of ethanol adsorbing on QCM-Vinyl

<sup>33</sup> The value for  $\Delta H_{\text{ads.}}$  was determined without the data from the isotherm at 343 K



## 6.1.5 Sorption on mercapto-functionalized mesoporous material: QCM-SH

Sorption isotherms of ethanol on mercapto-modified mesoporous nanosized silica particles are shown in figure 105. The maximum sorption capacity for ethanol sorbing on the QCM-SH sample is approximately  $7.5 \text{ mmol g}^{-1}$ . As expected, the isotherm can be attributed to the IUPAC classification type IV. At higher temperatures small gaps between adsorption and desorption coverage become apparent. A possible explanation are specific equilibria detection duration parameters which could be not suitable for the desorption branch. In other words, the time delay between single decreasing partial pressure steps was too short to allow the system to equilibrate. On the other hand, the differences are within experimental accuracy limits.

During the desorption process all experimental parameters, e.g. MFC step-sizes and time constants to accept equilibria were identical to the adsorption process.

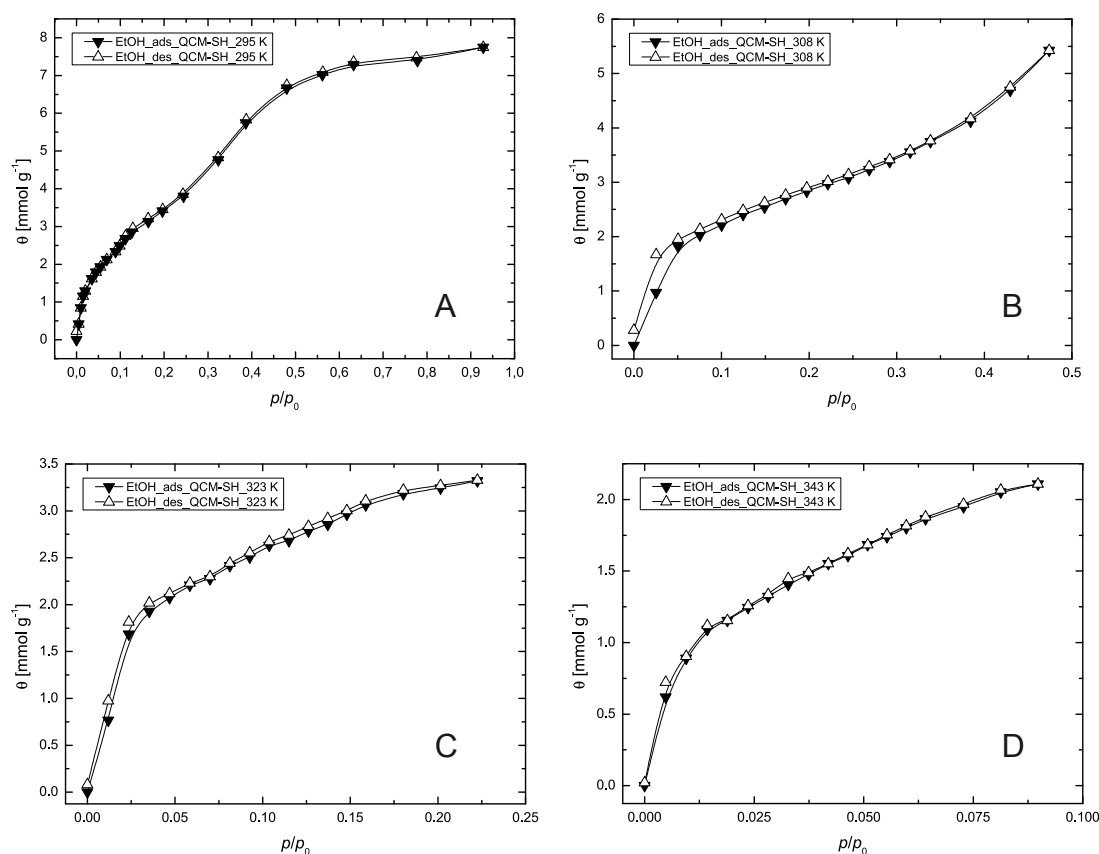


Fig. 105: Sorption isotherm of ethanol on sample QCM-SH at 295 K (A) 308 K (B), 323 K (C) and 343 K (D)

Recapitulating the sorption behavior of all previously investigated pure and modified mesoporous silica nano-particles, the corresponding room temperature isotherms are plotted into one single graph, displayed in figure 106.

In part A  $\text{mmol g}^{-1}$  vs.  $p/p_0$  is plotted whereas part B demonstrates isotherms normalized to  $\text{mmol m}^{-2}$ . The course of the ethanol isotherm of QCM-SH is quite similar to the one of sample QCM-Vinyl but exceeds its sorption capacity from  $p/p_0 = 0.2$  on.

From the displayed isotherms it is evident that a discrimination of the investigated mesoporous sample materials by means of their specific degree of coverage, respectively their shapes of isotherms in the low partial pressure regime is not possible. Assuming a desired sensitivity below 100 ppm which corresponds to partial pressures  $p/p_0 < 0.0013$  ( $T = 298 \text{ K}$ ,  $p = 101300 \text{ Pa}$ ,  $p_0(\text{EtOH}) = 7523 \text{ Pa}$ ), the five isotherms are barely distinguishable with the experimental equipment. Furthermore, the maximum sorption capacity of the investigated samples ranges from 5 - 10  $\text{mmol g}^{-1}$  which is not proportional to the affinity ( $\Delta H_{\text{ads.}}$ ) towards the solvent vapor ethanol. Comparing the recorded isotherms at a higher partial pressure of  $p/p_0 = 0.05$  shows that the investigated samples are capable of discriminating the sorbent molecule EtOH (see details on page 138).

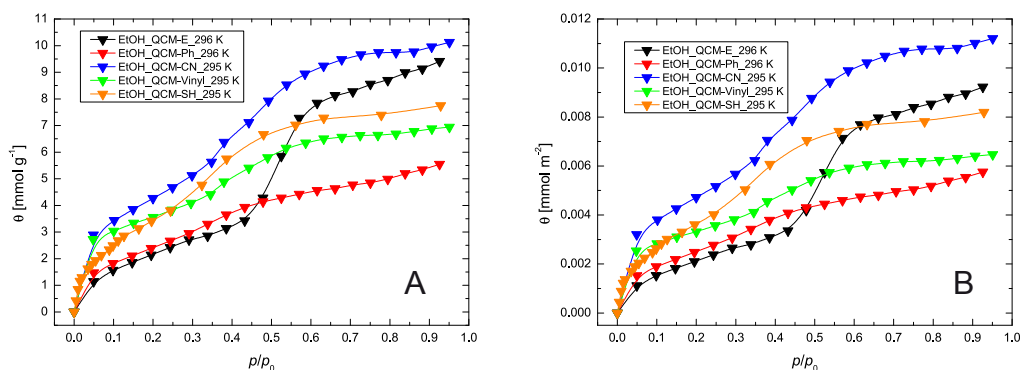


Fig. 106: Adsorption isotherm of ethanol on QCM-E (black), QCM-Ph (red), QCM-CN (blue), QCM-Vinyl (green) and QCM-SH (orange) plotted as function of  $\text{mmol g}^{-1}$  (left) and  $\text{mmol m}^{-2}$  (right)

### 6.1.5.1 Heat of adsorption

The isosteric heat of adsorption of sample QCM-SH calculated at several degrees of coverage is listed in table 27. The average value between the coverages of 1.0 mmol<sup>-1</sup> up to 2.0 mmol<sup>-1</sup> is determined as  $-41.4 \pm 7.3$  kJ mol<sup>-1</sup>. Due to the fact that at 343 K the isotherm does not reach a coverage of 2.0 mmol<sup>-1</sup> in minimum, the value  $\Delta H_{\text{ads}}$  determined at  $\theta = 3.0$  mmol<sup>-1</sup> was calculated without the data available from the isotherm at 343 K.

EtOH@QCM-SH	
$\theta$ [mmol g <sup>-1</sup> ]	$-\Delta H_{\text{ads}}$ [kJ mol <sup>-1</sup> ]
1.0	$39.9 \pm 6.5$
1.5	$40.7 \pm 6.9$
2.0	$43.7 \pm 10.1$
3.0 <sup>34</sup>	$40.2 \pm 8.7$

Tab. 27: Heat of adsorption of ethanol adsorbing on QCM-SH

### 6.1.6 Conclusion mesoporous samples QCM-R

The introduction of organic fragments, like phenyl-, cyano-, vinyl and mercapto-groups (-R) into siliceous mesoporous nanoparticles strongly influences their surfaces properties. Table 28 lists the physical features of the investigated samples as overview.

BET surfaces, maximum sorption capacity for ethanol ( $\theta_{\text{max.EtOH}}$ ), calculated pore sizes and pore volumes, the corresponding heats of adsorption  $-\Delta H_{\text{ads.mean}}$  (the mean value for each individual sample) and the corresponding calculated substitutional polarity of the introduced organic fragments are outlined.

The determination of the polarity of the mesoporous silica sample surfaces, either pure or modified is not trivial because no specific suitable values are published in the literature. Furthermore, no polarity data are available about the synthesis templates RTES. Thus, the desired dipole moments were determined with rudimentary model calcula-

<sup>34</sup> The isosteric heat  $\Delta H_{\text{ads}}$  was calculated without taking into account the isotherm at 343 K

sample ID	BET surface [m <sup>2</sup> g <sup>-1</sup> ]	pore size [nm]	pore volume [cm <sup>3</sup> g <sup>-1</sup> ]	$\theta_{\text{max, EtOH}}$ [mmol g <sup>-1</sup> ]	$-\Delta H_{\text{ads, mean}}$ [kJ mol <sup>-1</sup> ]	dipole moments of organic fragments [Debye] <sup>35</sup>
QCM-E	1020	3.5	0.89	10	17.4 ± 5.6	1.65
QCM-Ph	963	3.2	0.61	5	27.7 ± 4.5	1.77
QCM-CN	904	2.2	0.71	10	22.8 ± 6.2	5.3
QCM-Vinyl	1073	2.6	0.66	6.5	36.9 ± 3.5	1.44
QCM-SH	946	2.3	0.62	7.5	41.4 ± 1.9	4.12

Tab. 28: Sorption data sets for investigated mesoporous samples and adsorption heats for ethanol adsorption (mean values for each individual sample material)

tions<sup>35</sup>, being aware of potential errors due to non appropriately adjusted simulation software preferences. On the other hand, all values obtained were calculated with identical and standard options of the modelling software Cambridgesoft Chem3D<sup>[88]</sup>. It is not intended to present a completely sophisticated simulation of the RTES polarity values but attention is drawn on the general tendency in polarity of the organic moieties. According to the obtained heats of adsorption, the vaporized fluid ethanol with a polarity value of 1.54 Debye adsorbs preferentially on the mercapto functionalized mesoporous silica particles followed by the vinyl-modified sample. The mercapto modified sample QCM-SH offers the highest isosteric heat of adsorption and reveals the second highest polarity (4.12 Debye). Besides the non-functionalized sample QCM-E, sample QCM-SH is capable of forming hydrogen bonds. The isosteric heat of adsorption for ethanol adsorbing on sample QCM-Vinyl ( $\Delta H_{\text{ads}} \approx 37 \text{ kJ mol}^{-1}$ ) is almost doubled compared to the value obtained during adsorption on the non-modified sample QCM-E. The organic molecule vinyltriethoxysilane features a dipole moment of 1.44 Debye. The introduction of the polar cyano functionality results in an approximately 5-6 kJ mol<sup>-1</sup> higher heat of adsorption ( $\Delta H_{\text{ads}} = 22.8 \pm 6.2 \text{ kJ mol}^{-1}$ ) compared to the non-functionalized sample QCM-E. The phenyl-modified sample features a relatively low dipole moment (1.77 Debye) which is reflected in an approximately 10 kJ mol<sup>-1</sup> higher heat of adsorption compared to sample QCM-E.

The relatively low heat of adsorption of  $17.4 \pm 5.6 \text{ kJ mol}^{-1}$  for sample QCM-E is not expected. Furthermore, the possibility of forming hydrogen bonds between silanol groups of the internal surface and the solvent vapor ethanol should result in a higher

<sup>35</sup> calculated with cyano- and mercaptopropyltriethoxysilane, phenyltriethoxysilane, vinyltriethoxysilane and hydroxyltriethoxysilane using reference [88] for calculations (MoPac interface)

heat of adsorption. The most likely interpretation is a small concentration of silanol groups and a large fraction of siloxane bridges at the interface due to condensation reactions at the elevated temperature (350 °C) used for template removal.<sup>[94], [95]</sup>

The difference in surface polarity between a silanol rich and siloxane rich surface was estimated by comparing the theoretical polarity of hydroxysilane and disiloxane. For example, the molecule hydroxysilane offers a dipole moment of 1.22 Debye whereas the disiloxane offers 0.34 Debye.<sup>[88]</sup>

Further detailed investigations including model calculations and solid state NMR experiments are necessary to clarify the relatively low heat of adsorption for ethanol adsorbing on sample QCM-E. Those surface specific research projects were not topic of this work.

As soon as an interpretation of nitrogen sorption data obtained with surface modified samples comes into play a certain uncertainty remains. This is obvious as soon as the maximum sorption capacities of individual samples are compared to each other. The vinyl modified sample represents an even higher surface area compared to the non-modified one although all samples were synthesized under identical conditions. A possible explanation could be surface roughness of the mesoporous sample matrix material or common heterogeneity of the functionalized sample. One has to be additionally aware of model limitations to well known surfaces (Carbon, SiO<sub>2</sub>) and the introduction of organic frameworks into the silica network disturbing the “perfect” silica surface. In the literature, it is well known that the applied BET model is actually not applicable to type IV isotherms, respectively to mesoporous silica materials.<sup>[93]</sup> Nevertheless, the BET model is commonly accepted for general comparison purposes, accepting the limitations of the original infinite multilayer concept. The determined surface areas are hence not absolute values but should be evaluated in the context of the entire set of investigated sample materials.

Additionally, slight variation of synthesis parameters like temperature, pH-value, reactant concentrations, stirring velocity, ambient humidity and post synthesis treatments might contribute to the observed variations.

In summary, the recorded isotherms and their initial slopes are sufficient information to quantify and evaluate the individual sorption affinity of a specific mesoporous sample, either without incorporated organic functionality or with network embedded organic fragments. For example, at relative partial pressures  $p/p_0 = 0.05$  the sorption

capacity for the non-modified sample QCM-E is around  $1.0 \text{ mmol g}^{-1}$ . Compared to the maximum sorption capacity for sample QCM-CN (approximately  $3.0 \text{ mmol g}^{-1}$ ) at this specific relative pressure, a discrimination between those two individual materials is possible. Furthermore, the samples QCM-Ph, QCM-Vinyl and QCM-SH exhibit a higher maximum sorption capacity at  $p/p_0 = 0.05$  compared to sample QCM-E. Sample QCM-Ph shows a 0.5 times higher sorption capacity, sample QCM-Vinyl approximately a 2.5 times higher capacity and sample QCM-SH offers roughly a 2.0 times higher sorption capacity. The introduction of small organic moieties dramatically influences the sorption behavior at low partial pressures.

#### 6.1.7 Sorption on zeolite ZSM-5: sample ZSM-5

In order to prove the reliability of the developed QCM equipment, the well known zeolites ZSM-5 and silicalite-1 were investigated as spincoated colloidal suspension on QCM devices. In contrast to earlier publications<sup>[96],[97]</sup> the zeolite particles deposited onto the QCM chips were nanosized (80 - 130 nm) and the total amount of investigated individual sample material was about  $10^6$  lower compared to mentioned literature data. In addition, the coated zeolite “membranes” offer roughly a 140 times shorter barrier for ethanol molecules (compare reference [96]) to diffuse through the entire silica particle layer.

The sorption isotherm of ethanol vapor adsorbing on thin layers (sample amounts range from  $9.7 - 13.5 \mu\text{g cm}^{-2}$ ) of sample ZSM-5 is illustrated in figure 107. The isotherm is classified as type I (IUPAC) typical for microporous zeolite materials. The recorded room temperature isotherm is consistent with literature data<sup>[98]</sup>. *Nomura et al.*<sup>[96]</sup> reported a saturation amount of  $1.5 - 1.8 \text{ mmol g}^{-1}$ , whereas *Travis et al.*<sup>[97]</sup> determined a maximum sorption capacity of  $2 \text{ mmol g}^{-1}$ . Both authors investigated either binary or ternary liquid mixtures of ethanol, water and acetic acid.

The presented isotherm in figure 107 represents exclusively the adsorption of the vaporized liquid ethanol on the ZSM-5 zeolite.

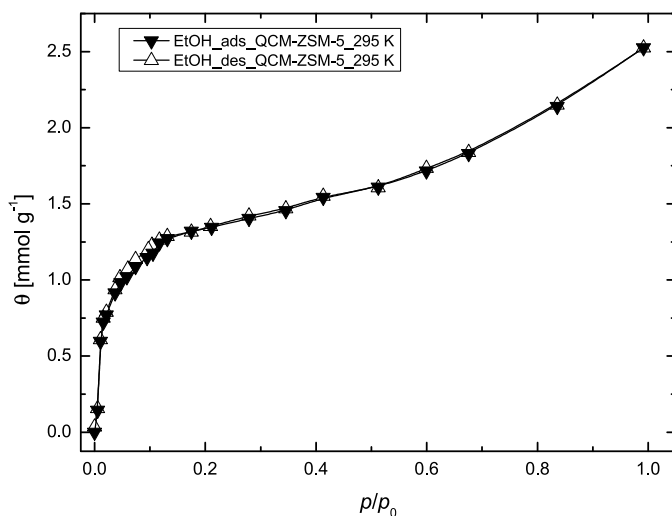


Fig. 107: Sorption isotherm of ethanol adsorbing on zeolite ZSM-5

#### 6.1.7.1 Heat of adsorption of sample ZSM-5

The isosteric heat of adsorption was determined to quantify the reliability and performance of the enhanced QCM setup. The results were compared with available literature data. Gravimetrically acquired temperature dependent isotherms of ethanol adsorbing on the zeolite ZSM-5 are plotted in figure 108.

Table 29 lists the calculated isosteric heat of adsorption at the corresponding degrees of coverage. At the coverage of  $\theta = 1.0 \text{ mmol g}^{-1}$  the value for  $\Delta H_{\text{ads}}$  was calculated

EtOH@ZSM-5	
$\theta \text{ [mmol g}^{-1}\text{]}$	$-\Delta H_{\text{ads}} \text{ [kJ mol}^{-1}\text{]}$
0.25	$43.9 \pm 1.5$
0.5	$44.7 \pm 1.7$
0.75	$44.9 \pm 1.3$
1.0 <sup>a</sup>	$45.3 \pm 1.1$

<sup>a</sup> calculated without the value at 343 K

Tab. 29: Isosteric heat of adsorption of ethanol adsorbing on sample QCM-ZSM-5

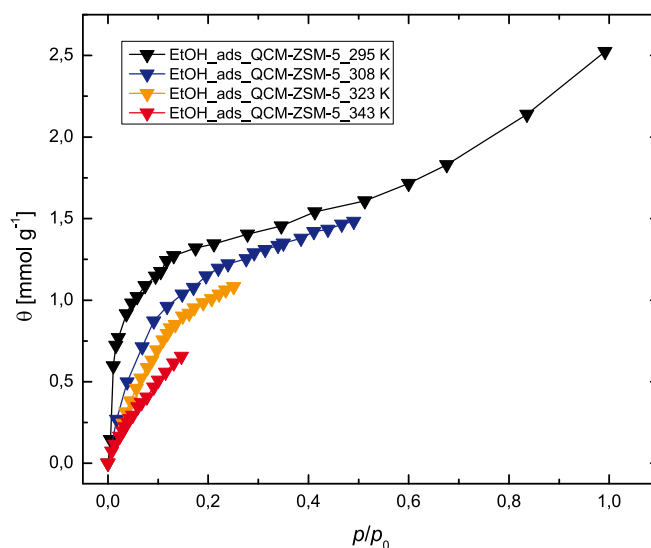


Fig. 108: Adsorption isotherms of ethanol adsorbing on sample ZSM-5 at 295 K (black), 308 K (blue), 323 K (orange) and 343 K (red)

without the isosteric data obtained at 343 K due to the decreased maximum sorption capacity. The average value for the heat of adsorption is  $-44.7 \pm 1.4 \text{ kJ mol}^{-1}$ . The determined sorption heat is in good agreement with very rarely available literature data. *Nayak et al.*<sup>[99]</sup> investigated the sorption and diffusion properties of aliphatic alcohols including ethanol in heteropoly oxometalates (e.g.  $\text{SiW}_{12}\text{O}_{40}^{4-}$ ) and ZSM-5 zeolite. The experiments were carried out with commercially available gravimetric electro-balan-ces (Cahn instruments<sup>36</sup>). The determined heat of adsorption is  $-46 \text{ kJ mol}^{-1}$ , which is in the region of the value for EtOH adsorbing on zeolite ZSM-5.

The maximum sorption capacity for ZSM-5 crystals is stated as  $2.7 \text{ mmol g}^{-1}$ , thus competing with the results of reference [96] and [97]. On the other hand the value of *Nayak et al.* is in good agreement with the results of *Cartón et al.*<sup>[98]</sup> ( $\theta_{\text{EtOH,max}} = 2.6 \text{ mmol g}^{-1}$ ) and *Bowen et al.*<sup>[97]</sup> ( $\theta_{\text{EtOH,max}} = 2.7 \text{ mmol g}^{-1}$ ). The experimental data in this work is  $\theta_{\text{EtOH,max}} = 1.3 - 1.4 \text{ mmol g}^{-1}$ . A possible explanation could be the investigation of micro-sized crystals in reference [97] and [98], which usually leads to textural porosity and might influence the maximum sorption capacity.

A remarkable divergent value for  $\Delta_{\text{Hads}}$  can be found in reference [100] cited as  $\Delta_{\text{Hads}} =$

<sup>36</sup> Cahn Instruments (ATI Cahn), 1000 Fourier Drive, Madison, WI 53717, USA.



-60 kJ mol<sup>-1</sup> although the experimental data reveal no significant different maximum sorption capacity.

### 6.1.8 Sorption on zeolite silicalite-1: sample Sil-1

The alumina free zeolite related to ZSM-5 zeolite silicalite-1 was chosen because both zeolites are of MFI structure and subject to numerous research projects. Hence, those materials are supposed to be reference materials in terms of sorption experiments with the described gravimetric QCM setup.

The adsorption isotherms of vaporized pure ethanol are depicted in figure 109. As obvious, the maximum sorption capacity is comparable to the one of sample ZSM-5. It has to be mentioned that a drastic increase in the degree of coverage  $\theta$  at relative partial pressures  $p/p_0 > 0.85$  is detectable. This behavior is very likely related to inter-particle ethanol condensation due to textural porosity. As expected, the overall shape of the room temperature isotherm follows a type I isotherm. Due to very slow diffusion rates inside the microporous silica network, the ethanol reservoir was exhausted before subsequent desorption steps could be initialized.

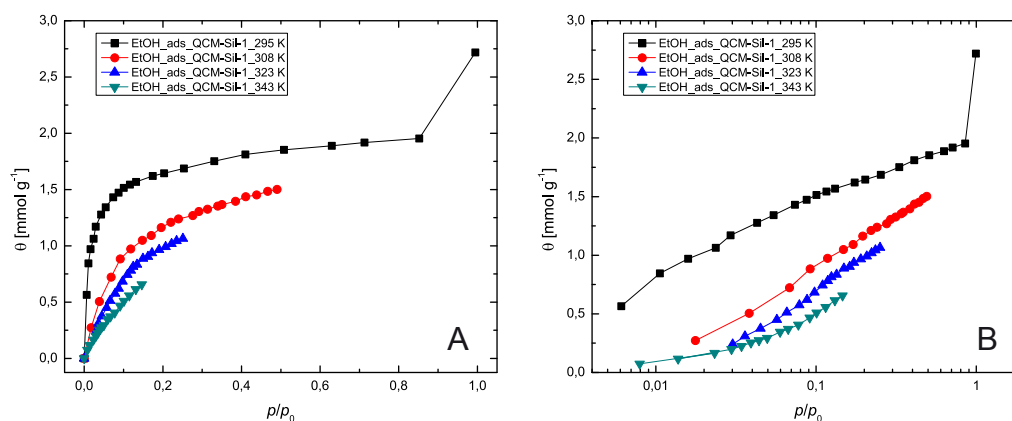


Fig. 109: Adsorption isotherms of ethanol adsorbing on sample Sil-1 at 295 K (black), 308 K (blue), 323 K (orange) and 343 K (red) at linear scale (A) and logarithmic scale (B)

### 6.1.8.1 Heat of adsorption of sample Sil-1

The calculated isosteric heats of adsorption for vaporized ethanol adsorbing on the microporous sample Sil-1 for 4 degrees of coverage are separately listed in table 30. The average isosteric heat of adsorption between  $\theta = 0.25 - 1.0 \text{ mmol}^{-1}$  was determined to be as  $\Delta H_{\text{ads.}} = -44 \pm 1.4 \text{ kJ mol}^{-1}$ .

EtOH@QCM-Sil-1	
$\theta \text{ [mmol g}^{-1}\text{]}$	$-\Delta H_{\text{ads.}} \text{ [kJ mol}^{-1}\text{]}$
0.25	$45.4 \pm 1.6$
0.5	$42.3 \pm 1.2$
0.75	$43.2 \pm 1.3$
1.0	$44.8^{\text{a}} \pm 1.4$

<sup>a</sup> calculated without the value at 343 K

Tab. 30: Isosteric heat of adsorption of ethanol adsorbing on sample QCM-Sil-1

*Thamm*<sup>[101]</sup> intensely investigated the molar sorption heats of various alcohols adsorbing on micro-scaled zeolite silicalite-1. In contrast to the microbalance approach in this work, the author applied the *Calvet* micro-calorimetry (principle setup see on page 109) using vaporized liquid ethanol as sorbate molecules. Experimental setup parameters are not cited except that equilibrium conditions after each dosing step were usually reached within 2 hours.

The author reports a heat of adsorption between ca.  $-44 \text{ kJ mol}^{-1}$  at  $\theta = 0.5 \text{ mmol g}^{-1}$  and approximated  $-58 \text{ kJ mol}^{-1}$  at  $\theta = 2.0 \text{ mmol g}^{-1}$  for pure ethanol adsorbing on silicalite-1.

*Akhmedov et al.*<sup>[102]</sup> reported differential heats of adsorption of ethanolic vapor adsorbing on pure silicalite-1 zeolite. The values for  $\Delta H_{\text{ads.}}$  vary from around  $-42 \text{ kJ mol}^{-1}$  at a low degree of coverage ( $\theta = 0.5 \text{ mmol g}^{-1}$ ) up to  $-45 \text{ kJ mol}^{-1}$  ( $\theta = 2.0 \text{ mmol g}^{-1}$ ) estimated from the printed graph. *Boddenberg et al.*<sup>[103]</sup> could confirm the experimentally obtained data of reference [102] with thermodynamic model calculations. Both authors emphasize the dependence of  $\Delta H_{\text{ads.}}$  on the degree of coverage related to the

adsorption mechanism of ethanol molecules onto the silica surface. For example, ethanol molecules initially interact either with counter ions or surface hydroxyl groups, followed by adjacent ethanol molecules. Subsequently, the alcohol molecules occupy free adsorption sites finally forming tetrahedral complexes at the intersections of the zig-zag channels.<sup>[100]</sup>

Figure 110, taken from reference [100], demonstrates the impressive correlation between degree of coverage and the released heat of adsorption. Note the step-like correlation of the adsorption enthalpy in context with sorption on ZSM-5 zeolite material having  $\text{Na}^+$  counter ions. During sorption experiments with ethanol a stepwise correlation between coverage  $\theta$  and enthalpy  $\Delta H_{\text{ads}}$  is evident. *Thamm* emphasizes the importance of dispersion forces of additional  $\text{CH}_2$ -groups, which contribute with ca. 10 kJ to the total heat of adsorption.

Compared to the literature data discussed above, the experimentally determined values presented in this work (average value:  $\Delta H_{\text{ads}} = -44 \pm 1.4 \text{ kJ mol}^{-1}$ ) are in good agreement.

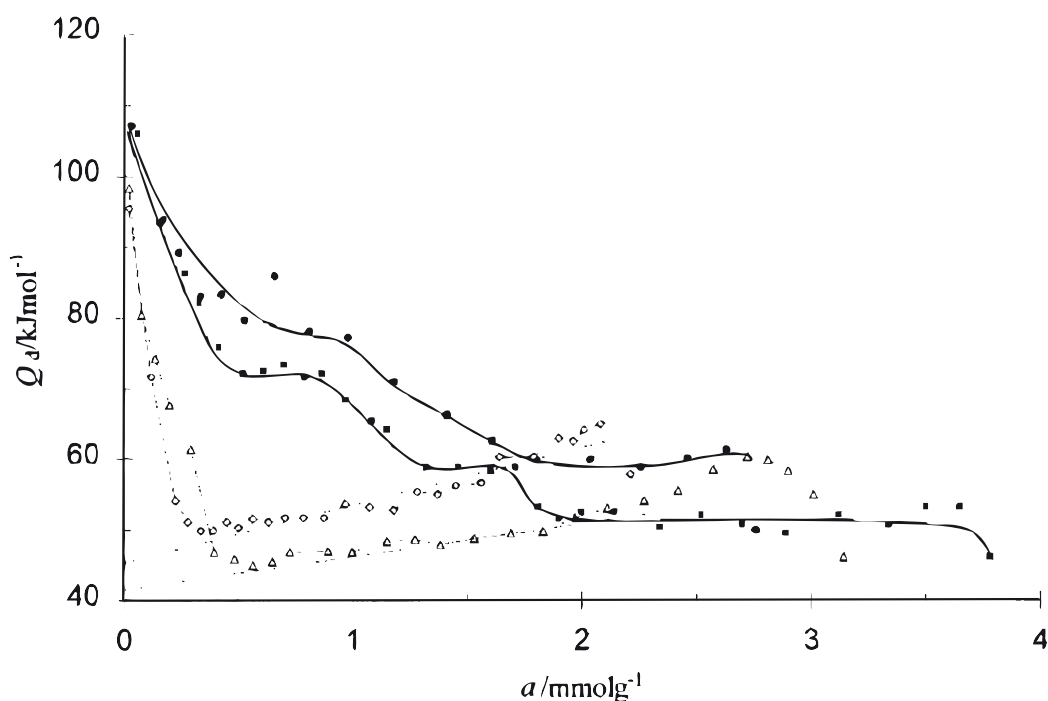
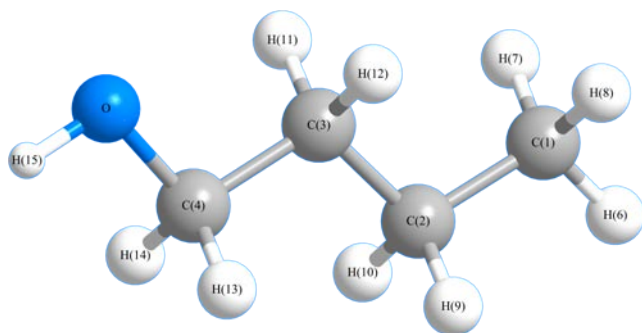


Fig. 110: Dependence of  $\Delta H_{\text{ads}}$  from the degree of coverage of ethanol adsorbing on Na-ZSM-5 (■) and silicalite-1 (△) and methanol adsorbing on Na-ZMS-5 (●) and silicalite-1 (○)<sup>[103]</sup>

6.2 Sorption of 1-butanol

The solvent molecule 1-butanol ( $C_4H_{10}O$ , n-BuOH) can be classified as non-polar with a distinctive  $C_4$ -hydrocarbon molecule fragment which is reflected in the molecular di-



atoms	distance [ $\text{\AA}$ ]
H(15)-H(6)	6.55
O-C(1)	4.86
O-H(6)	5.80
O-H(8)	5.01
H(9)-H(11)	3.10

Fig. 111: Ball and stick model of 1-butanol with labeled atoms

Tab. 31 : Inter-atomic distances of 1-butanol

mensions. Relevant inter-atomic distances are listed in table 31. Figure 111 illustrates the corresponding labeled atoms. The related dipole moment of  $1.66 \pm 0.03$  Debye and relevant physical data of liquid n-BuOH (listed in table 32) where taken from refer-

physical data of 1-butanol				
molar mass [ $\text{g mol}^{-1}$ ]	74.12			
density [ $\text{g cm}^{-3}$ ] (at 293.15 K)	793.5			
vapor pressure [Pa]	295 K	308 K	323 K	343 K
	730	1797	4547	13470
heat of vaporization [ $\text{kJ mol}^{-1}$ ] (at 295 K)	47.13			
boiling point [K]	390.9			
Van-der-Waals parameter				
a	20.94			
b	0.1326			

Tab. 32: Physical data and Van-der-Waals parameter of 1-butanol

ence [72]. In comparison to ethanol, the lower vapor pressure of n-BuOH required the adjustment of flow parameters, especially the nitrogen carrier flow in order to be able to measure frequency changes at relative pressures up to  $p/p_0 = 1$ .

### 6.2.1 Sorption on non-modified mesoporous material: QCM-E

Sorption isotherms at various temperatures (296 K, 311 K, 326 K and 341 K) are printed in figure 112. The room temperature isotherm can be classified as type IV isotherm (IUPAC). Isotherms at higher temperatures exhibit a more distinctive discrepancy be-

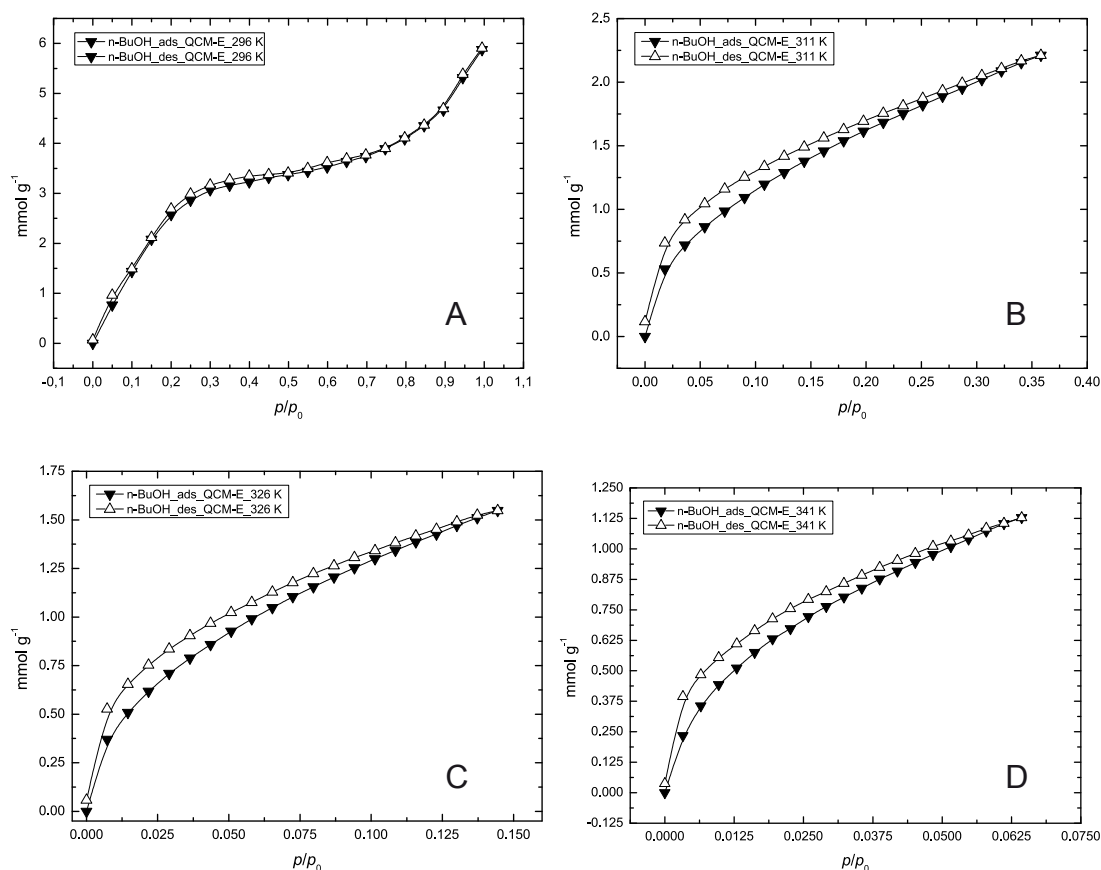


Fig. 112: Sorption isotherms of 1-butanol on non-functionalized sample QCM-E recorded at 296 K (A), 311 K (B), 326 K (C) and 341 K (D)

tween adsorption and desorption branches at identical relative pressures  $p/p_0$ . This behavior is related to the fact that the time delay between partial pressure changes, in detail discussed on page 93, might not be sufficiently extended during the desorption processes in order to record thermodynamically correct identical values. On the other hand, a closer look at isotherms at temperatures above 296 K shows that the differences are not large, for example, at  $T= 341$  K and  $p/p_0= 0.0375$  the difference between the adsorption and desorption branch is less than  $0.125 \text{ mmol g}^{-1}$ .

### 6.2.1.1 Heat of adsorption of sample QCM-E

Table 33 presents the calculated isosteric sorption heats evaluated with the described gravimetric QCM method. At low loadings of 1.0, 1.25, 1.5 and 1.56  $\text{mmol g}^{-1}$  the heat of adsorption was determined. The averaged isosteric heat of adsorption  $\Delta H_{\text{ads}}$  is  $-50.3 \pm 7.5 \text{ kJ mol}^{-1}$ . The rapid increase between  $\theta= 1.0 \text{ mmol g}^{-1}$  and  $1.25 \text{ mmol g}^{-1}$  might be related to the formation of butanol molecule clusters on the internal surface of the silica network as proposed for ethanol and methanol adsorption on silicalite-1.<sup>[101]</sup> In order to verify this theory it is necessary to collect sorption data at higher relative pressures and to compare obtained experimental data with molecular simulations. Unfortunately, the designed setup does not yet allow to measure frequency above ambient pressures (ca. 95000 - 98000 Pa).

In the literature, data about sorption of vaporized n-BuOH on mesoporous silica has

n-BuOH@QCM-E	
$\theta$ [ $\text{mmol g}^{-1}$ ]	$-\Delta H_{\text{ads}}$ [ $\text{kJ mol}^{-1}$ ]
1.0	$41.5 \pm 3.1$
1.25	$55.5 \pm 6.3$
1.5 <sup>37</sup>	$55.9 \pm 9.9$
1.56 <sup>37</sup>	$48.4 \pm 10.6$

Tab. 33: Heat of adsorption of n-BuOH adsorbing on sample QCM-E

<sup>37</sup> calculated without the experimental data from the isotherm at 341 K

rarely been published. *Branton et al.*<sup>[104]</sup> reported in 1995 sorption isotherms of short chain liquid alcohols adsorbing on MCM-41. In the gravimetric approach, sample amounts of  $200 \times 10^{-3}$  g were applied, which implies a limited resolution of  $0.15 \times 10^{-3}$  g. The reported resolution is ca. 6000 times worse and the necessary sample amount is ca. 15000 times higher (estimated from an average value of  $f_0 - f_0^* = 3000$  Hz; for definition see page 93) in comparison to the QCM approach in this work.

As discussed in the publication, the authors had severe problems to collect room temperature (298 K) isotherms of 1-butanol due to its low partial pressure and diffusion limitations. Figure 113, taken from reference [104] depicts the isotherm of 1-propanol at 298 K which is quite similar to the one of 1-butanol as reported by the authors. Compared to experimental data in this work, the main difference is apparent in the relative partial pressure region for intra-pore condensation:

In this work, pore condensation of n-BuOH is considered to be present starting at a relative pressure of  $p/p_0 = 0.3$ . *Branton et al.*<sup>[104]</sup> in contrast suggest pore condensation of 1-butanol in MCM-41 type material arising at a remarkable higher relative partial pressure ( $p/p_0 = 0.4$ ). The MCM-41 type material is considered as comparable to sample QCM-E in terms of elemental composition (silica network) and molecular surface composition. However in the publication of 1995 no explicit isotherm is shown and the suggested shape of the 1-propanol isotherm (see figure 113) is assumed to be valid for

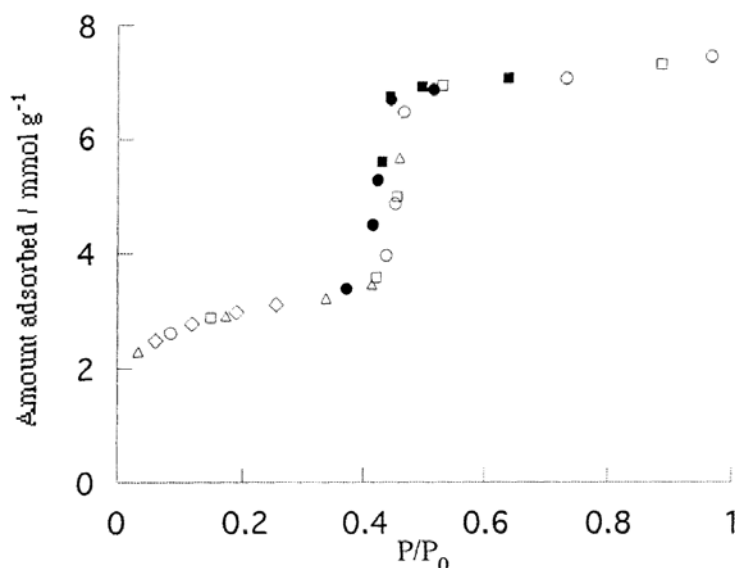


Fig. 113: Sorption isotherm of 1-propanol adsorbing on MCM-41<sup>[104]</sup>

an experimental temperature of 314 K. As mentioned previously, the MCM-41 material is not 100% identical to sample QCM-E. At the temperature of 314 K, the measured room temperature isotherm (296 K) in this work and proposed in the publication are identical up to  $p/p_0 = 0.3$ .

A comparison of calculated isosteric adsorption heats with literature data is hardly possible because no data concerning n-BuOH sorption on wormlike pure mesoporous nanosized silica has been published so far. *Bambrough et al.*<sup>[105]</sup> reported sorption data of liquid n-butanol and tert-butanol on phenyl modified mesoporous silica. According to reference [106] the sample material is more likely, with respect to the introduced phenyl group, comparable to sample QCM-Ph in terms of molar composition. Reliable values for the heat of adsorption of 1-butanol adsorbing on mesoporous nanosized silica material like MCM-41 are not presently available in the literature.

### 6.2.2 Sorption on cyano-modified mesoporous material: QCM-CN

Gravimetrically determined isotherms of 1-butanol adsorbing on sample QCM-CN were recorded at various temperatures and are plotted in figure 114. The room temperature isotherm can be classified as IUPAC type IV isotherm. Especially the recorded isotherm at 311 K shows a tendency of forming a typical plateau and an increasingly pronounced mesopore condensation step around  $p/p_0 = 0.15$ . The total sorption capacity at 296 K (ca. 4.75 mmol g<sup>-1</sup>) is slightly lower compared to the one of sample QCM-E (ca. 6 mmol g<sup>-1</sup>), which is reflected in the available surface areas of 904 m<sup>2</sup> g<sup>-1</sup> and 1020 m<sup>2</sup> g<sup>-1</sup>, respectively (see table 28). All these isotherms show that equilibrium has been reached at the experimental conditions (reached within the predefined time interval of 900 seconds to acquire data points; compare page 100).



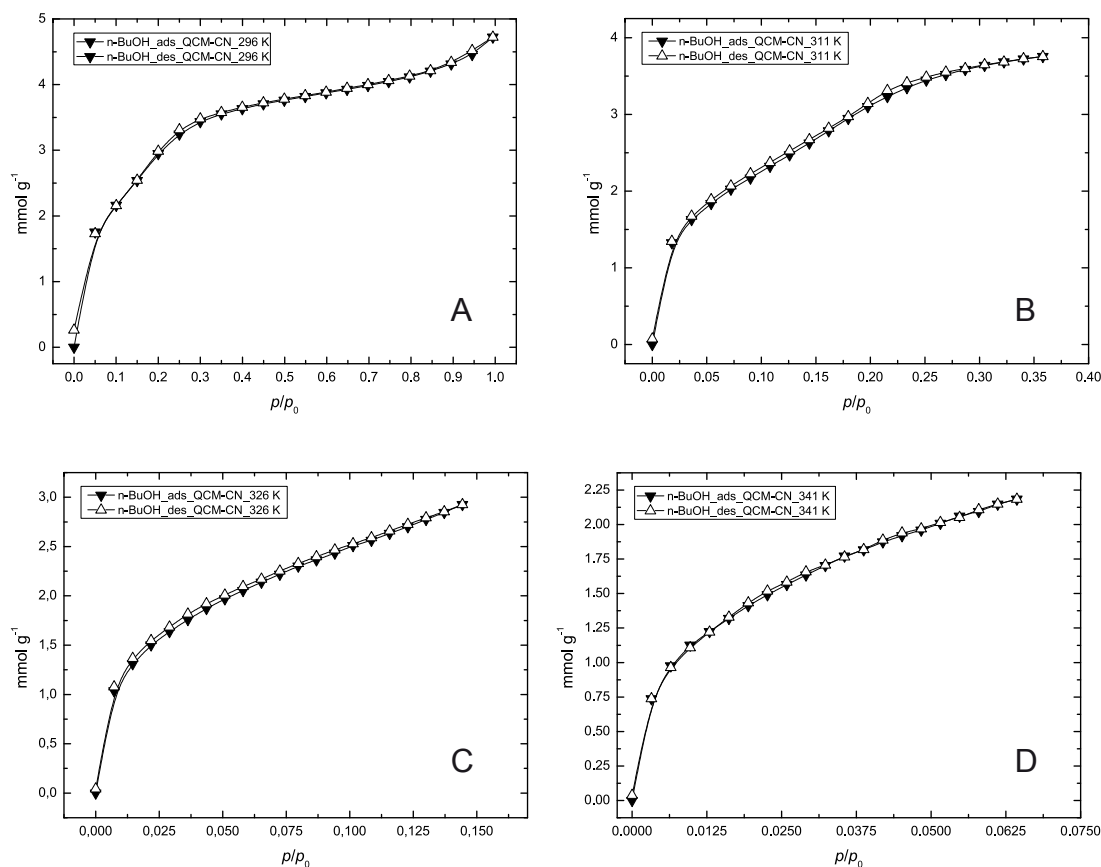


Fig. 114: Sorption isotherms of n-butanol sorbing on sample QCM-CN at 296 K (A), 311 K (B), 326 K (C) and 341 K (D)

### 6.2.2.1 Heat of adsorption of sample QCM-CN

Table 34 lists the acquired isosteric heats of adsorption for sample QCM-CN and the corresponding degrees of coverages. Obviously, the introduction of cyano groups into the pure siliceous surface has a dramatic influence on the heat of adsorption. In comparison to the non-modified sample QCM-E, the average value  $\Delta H_{\text{ads}} = -35.6 \pm 2.4 \text{ kJ mol}^{-1}$  is approximately  $15 \text{ kJ mol}^{-1}$  lower. The difference between sample QCM-E and QCM-CN might be related to deviations in the individual polarity of corresponding sample surfaces. According to table 28, sample QCM-E and QCM-CN exhibit calculated polarities of 1.65 Debye (for silanols) and 5.3 Debye, respectively.

The relative increase in the isosteric heat of adsorption for n-BuOH adsorbing on sample QCM-CN with increasing coverage could be explained by attraction forces

between already adsorbed solvent molecules and gaseous n-BuOH molecules.

n-BuOH@QCM-CN	
$\theta$ [mmol g <sup>-1</sup> ]	$-\Delta H_{\text{ads.}}$ [kJ mol <sup>-1</sup> ]
1.5	28.7 ± 4.5
1.75	33.5 ± 2.2
2.0	39.0 ± 1.2
2.5	41.0 ± 1.8

<sup>a</sup> calculated without the data obtained from the isotherm at 341 K  
 Tab. 34: Heat of adsorption of n-BuOH adsorbing on sample QCM-CN

### 6.2.3 Sorption on phenyl-modified mesoporous material: QCM-Ph

Figure 115 depicts the isotherms of n-butanol adsorbing on sample QCM-Ph at four different experimental temperatures. The shape of the room temperature isotherm is similar to the one of sample QCM-CN and can be classified as type IV (IUPAC), whereas a hysteresis from  $p/p_0 = 0.7$ -1.0 could be recognized. Isotherms recorded at temperatures  $T > 296$  K confirm the high affinity of n-butanol towards the phenyl-modified mesoporous silica framework: An initial very steep increase in the degree of coverage is typical for mesoporous systems and high affinity sorbents. It is worth to mention that the temperature step from 311 K to 326 K entails no significant decrease in sorption capacity of the sample material. However, the maximum sorption capacity at room temperature is remarkably reduced to ca. 2.5 mmol g<sup>-1</sup> which is in good agreement to reference [105]. However, the different sample synthesis, especially the mesitylen-swollen sample of reference [105], which is not exactly similar to sample QCM-Ph has to be taken into consideration. The authors of reference [105] stated that their n-butanol sorption experiment yielded a BET surface area of 461 m<sup>2</sup> g<sup>-1</sup> which is much lower than the BET surface area determined with nitrogen.

Based on the fact that n-butanol differs in molecular dimensions from nitrogen, the authors assume that pore blocking of n-butanol accounts for questionable surface areas

and the erroneous sorption capacity in maximum.

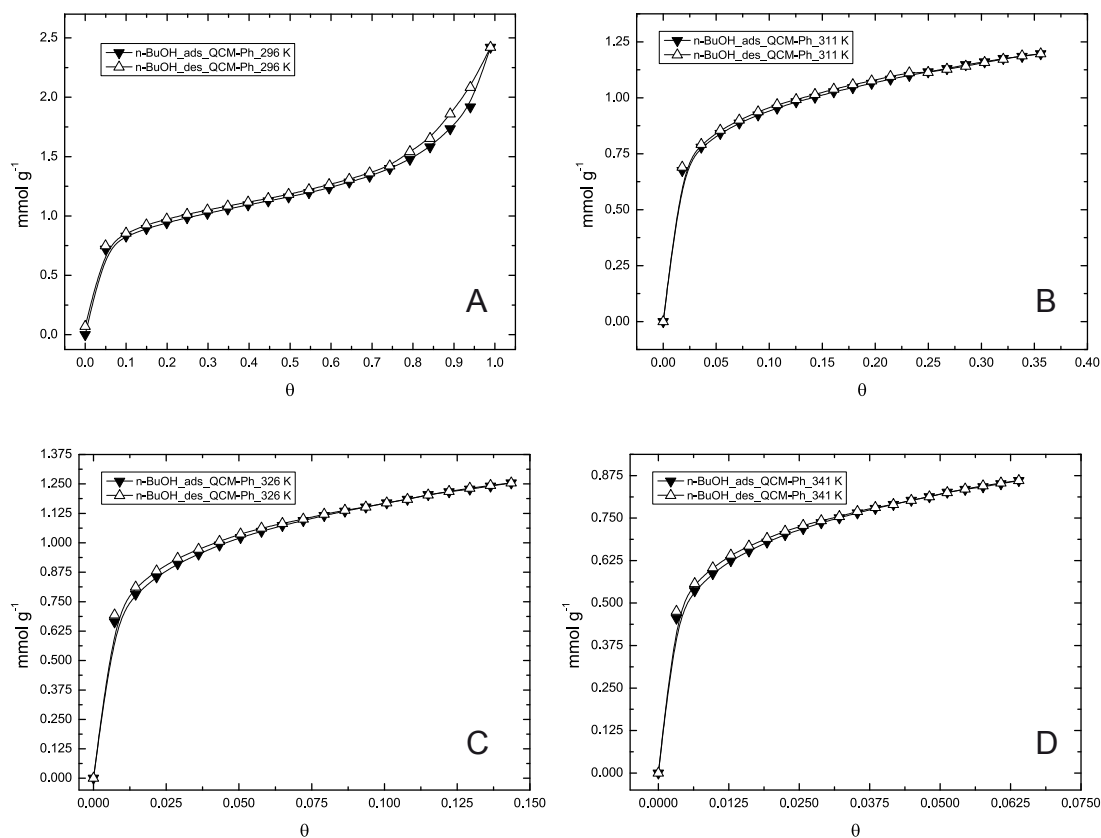


Fig. 115: Sorption isotherms of n-butanol sorbing on sample QCM-Ph at 296 K (A), 311 K (B), 326 K (C) and 341 K (D)

### 6.2.3.1 Heat of adsorption of sample QCM-Ph

The isosteric heat of adsorption was calculated according to the previously explained *Clausius-Clapeyron* method (see equation (28)).

In table 35 the determined values are listed. The average value between  $q = 0.75 - 1.2$  mmol g<sup>-1</sup> is  $-27.1 \pm 5.9$  kJ mol<sup>-1</sup>. The values are in the same range as the values obtained for adsorption of ethanol on phenyl-modified sample QCM-Ph ( $\Delta_{\text{Hads.EtoH}} = -27.7 \pm 4.5$  kJ mol<sup>-1</sup>). Considering the calculated polarity value of 2.64 Debye of the organic

n-BuOH@QCM-Ph		
$\theta$ [mmol g <sup>-1</sup> ]	$-\Delta H_{\text{ads.}}$ [kJ mol <sup>-1</sup> ]	
0.75	33.3	$\pm 15.8$
1.0 <sup>a</sup>	25.8	$\pm 3.0$
1.1 <sup>a</sup>	21.4	$\pm 2.5$
1.2 <sup>a</sup>	27.8	$\pm 2.2$

<sup>a</sup> calculated without the data obtained from the isotherm at 341 K

Tab. 35: Heat of adsorption of n-BuOH adsorbing on sample QCM-Ph

phenyl moiety, the calculated isosteric heats of adsorption seem to be realistic and consistent with the value for ethanol sorption. In this case, the additional -CH<sub>2</sub>-CH<sub>2</sub>- fragment of n-butanol obviously does not significantly increase the non-polar character of the vaporized solvent molecule.

Additionally, the elongated hydrocarbon chain may prevent higher degrees of coverage due to an increased surface space requirement per molecule or, as discussed elsewhere<sup>[105]</sup>, pore blocking may already occur.

#### 6.2.4 Sorption on vinyl-modified mesoporous material: QCM-Vinyl

The following figure 116 depicts the isotherms of n-BuOH adsorbing on the vinyl-modified sample QCM-Vinyl recorded at 296 K, 311 K, 326 K and 341 K. The room temperature isotherm can be classified as IUPAC type IV which represents sorption in mesopores.<sup>[107]</sup> However, the shape of the room temperature isotherm is not typical of type IV compared to nitrogen sorption isotherms. This behavior was previously observed with sample QCM-E and QCM-CN. On the other hand, the adsorptive nitrogen vastly differs in its physical specific parameters, e.g. the nitrogen molecule is considered to be of near-spherical shape and an expected space requirement at the adsorbent surface of 16.2 Å<sup>2</sup> is valid for a wide range of surfaces. A more complex situation arises from physisorption of long alkyl-chain alcohols like n-butanol. So far, no reliable data

were published about space requirements of this solvent adsorbing on siliceous sorbents. Furthermore, no suitable predictions about sorption of n-butanol in organically modified mesoporous silica particles are available. Against the background of possible partial pore blocking (compare reference [105]) the observed 1-butanol isotherm is assumed to represent a realistic sorption behavior. In order to validate the experimentally obtained isotherm, additional simulation and model calculations are necessary.

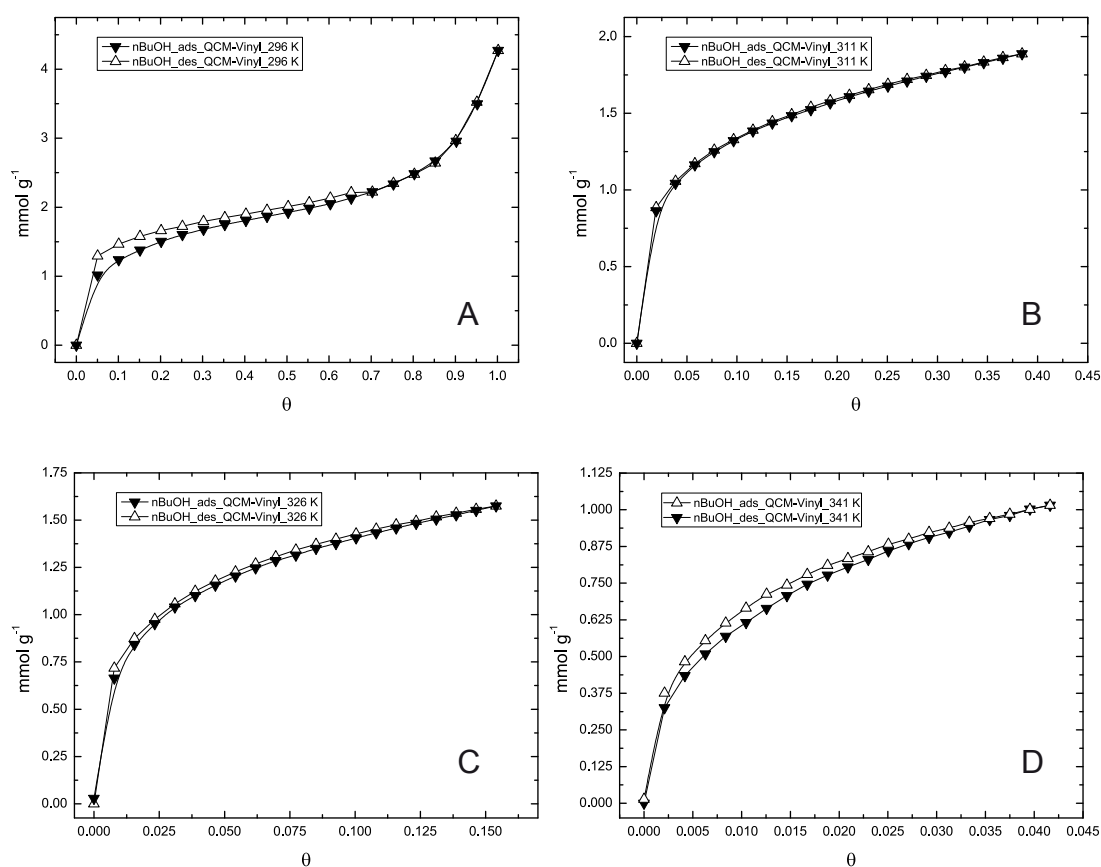


Fig. 116: Sorption isotherms of n-butanol adsorbing on sample QCM-Vinyl at 296 K (A), 311 K (B), 326 K (C) and 341 K (D)

#### 6.2.4.1 Heat of adsorption of sample QCM-Vinyl

As listed in table 36 the heat of adsorption for n-butanol adsorbing on sample QCM-Vinyl is not proportional to the polarity of the introduced chemical moiety  $-\text{CH}=\text{CH}_2$  (2.58 Debye, see table 28). As one would expect from the relatively low polarity of vinyl-groups, the average heat of adsorption between  $\theta = 0.75 - 1.5 \text{ mmol g}^{-1}$  is  $-36.6 \pm 3.6 \text{ kJ mol}^{-1}$ . Without the value  $\Delta H_{\text{ads}}$  obtained for  $\theta = 0.75 \text{ mmol g}^{-1}$ , the mean value  $\Delta H_{\text{ads,mean}}$  for n-butanol adsorbing on sample QCM-Vinyl is  $-39.3 \pm 2.7 \text{ kJ mol}^{-1}$ . With respect to the obtained heat of adsorption for ethanol ( $-36.9 \pm 3.5 \text{ kJ mol}^{-1}$ ) and the comparable data for n-butanol sorption, it could be concluded that the introduction of an additional  $-\text{CH}_2\text{CH}_2$  fragment into the vaporized solvent molecule does not seem to influence the sorption characteristics.

n-BuOH@QCM-Vinyl	
$\theta \text{ [mmol g}^{-1}\text{]}$	$-\Delta H_{\text{ads}} \text{ [kJ mol}^{-1}\text{]}$
0.75	$29.7 \pm 6.5$
1.0 <sup>a</sup>	$41.3 \pm 6.7$
1.25 <sup>a</sup>	$36.6 \pm 1.1$
1.5 <sup>a</sup>	$40.1 \pm 0.2$

<sup>a</sup> calculated without the data obtained from the isotherm at 341 K

Tab. 36: Heat of adsorption of n-BuOH adsorbing on sample QCM-Vinyl

#### 6.2.5 Sorption on mercapto-modified mesoporous material: QCM-SH

The sorption isotherms for n-butanol sorbing on sample QCM-SH at various temperatures can be found in figure 117. The maximum sorption capacity is around  $3.0 \text{ mmol g}^{-1}$  at  $p/p_0 = 1.0$ . It is comparable to the maximum value for sample QCM-Vinyl. The isotherm can be classified as IUPAC type IV isotherm, although mesopore condensation is not pronounced. Obviously, n-butanol causes no typical mesopore condensation “knee” in the sorption isotherm. More insight into sorption equilibria should be

obtained by supporting simulation data.

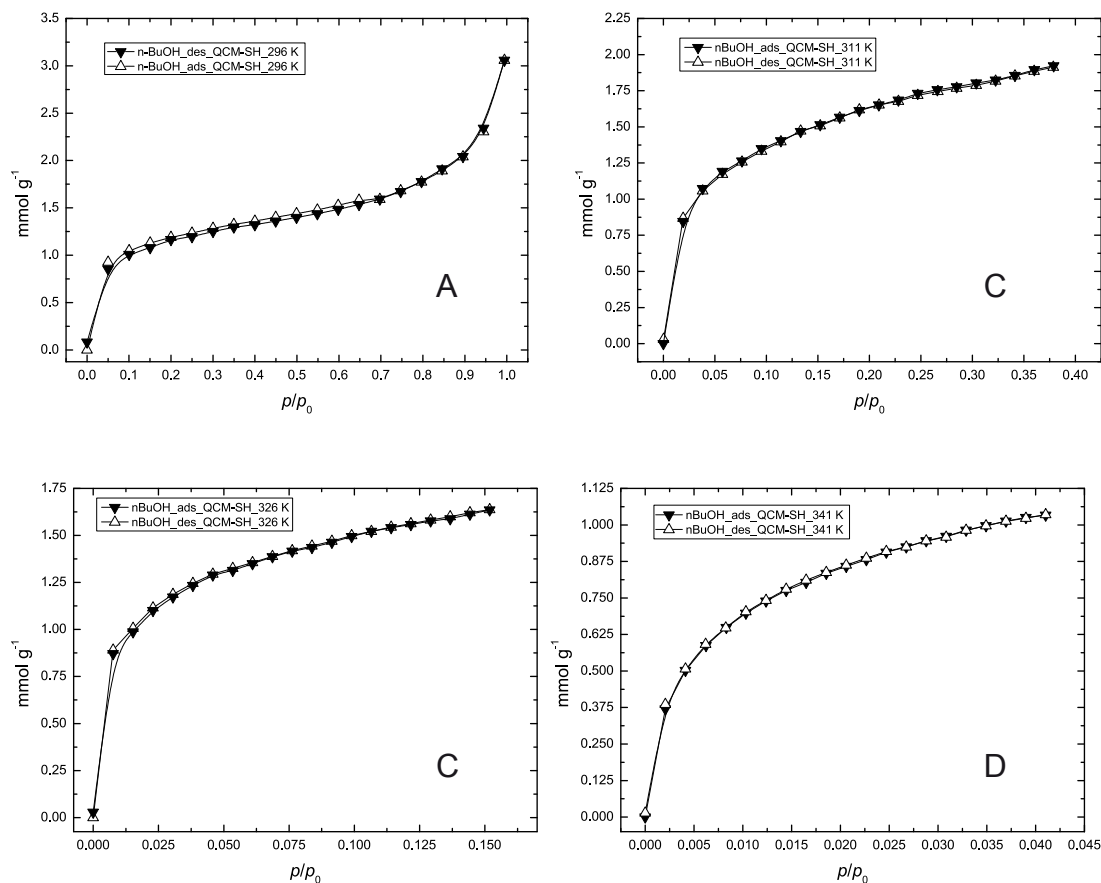


Fig. 117: Sorption isotherms of n-butanol adsorbing on sample QCM-SH at 296 K (A), 311 K (B), 326 K (C) and 341 K (D)

### 6.2.5.1 Heat of adsorption of sample QCM-SH

The isosteric heat of adsorption of n-butanol adsorbing on sample QCM-SH is of special interest due to the ability of forming hydrogen bonds between hydroxyl and mercapto groups. The averaged value for the isosteric heat of adsorption for n-butanol adsorbing on sample QCM-SH is  $-30.7 \pm 4.4$  kJ mol<sup>-1</sup> (table 37).

The determination was performed at four isosteric conditions ( $\theta = 1.0, 1.25, 1.5$  and  $1.63$  mmol g<sup>-1</sup>) with one explicit exception: at  $\theta = 1.25 - 1.63$  mmol g<sup>-1</sup> the data range

n-BuOH@QCM-SH	
$\theta$ [mmol g <sup>-1</sup> ]	$-\Delta H_{\text{ads.}}$ [kJ mol <sup>-1</sup> ]
1.0	32.4 ± 8.6
1.25 <sup>a</sup>	31.1 ± 3.8
1.5 <sup>a</sup>	26.6 ± 3.0
1.63 <sup>a</sup>	27.3 ± 2.2

<sup>a</sup> calculated without the data obtained from the isotherm at 341 K

Tab. 37: Heat of adsorption of n-BuOH adsorbing on sample QCM-SH

from the isotherm at  $T=341$  K was not sufficient. Compared to ethanol sorption experiments, the calculated enthalpy is approximately  $11 \text{ kJ mol}^{-1}$  decreased, which could be attributed to the hydrophobic alkyl chain of n-butanol. As listed in table 28, the heat of adsorption for ethanol sorption could be calculated to  $-41.4 \pm 1.9 \text{ kJ mol}^{-1}$ .

### 6.2.6 Conclusion mesoporous samples QCM-R

Concerning n-butanol sorption experiments on mesoporous nanoscaled non-modified and modified silica particles it can be concluded that two main aspects are considerable. As experimentally determined, all room temperature isotherms of n-butanol differ from the ethanol counterpart in terms of shape and suggested IUPAC classification. The room temperature isotherms of all investigated samples reveal a high affinity towards the vaporized solvent n-butanol, represented by rapidly increasing coverages at relatively low partial pressures ( $p/p_0 < 0.1$ ). According to IUPAC conventions, the isotherms are best described as type IV isotherms without the typical distinctive mesopore condensation “knee”. This observation is yet not fully understood but may be related to potential pore blocking phenomena by some alcohol molecules inhibiting further adsorption as suggested by reference [105].

As listed in table 38, sorption capacities are approximately half the amount of the ethanol sorption capacity with exception of sample QCM-Vinyl. This observation is



sample ID	$\theta_{\max, \text{EtOH}}$ [mmol g <sup>-1</sup> ]	$-\Delta H_{\text{ads, EtOH}}$ [kJ mol <sup>-1</sup> ]	$\theta_{\max, \text{nBuOH}}$ [mmol g <sup>-1</sup> ]	$-\Delta H_{\text{ads, nBuOH}}$ [kJ mol <sup>-1</sup> ]	dipole moments of organic fragments [Debye] <sup>38</sup>
QCM-E	10	17.4 ± 5.6	6	50.3 ± 7.5	1.65
QCM-Ph	5	27.7 ± 4.5	2.5	27.1 ± 5.9	1.77
QCM-CN	10	22.8 ± 6.2	4.75	35.6 ± 2.4	5.3
QCM-Vinyl	6.5	36.9 ± 3.5	4.5	39.3 ± 2.7	1.44
QCM-SH	7.5	41.4 ± 1.9	3	30.7 ± 4.4	4.12

Tab. 38: Comparison of ethanol and n-butanol sorption data obtained from the investigated nanoscale mesoporous samples

consistent with increased space requirements of n-butanol molecules adsorbed on the sample surface. Model calculations (COSMO surface of MoPAC interface of reference [88]) of one single n-butanol molecule show that a single n-BuOH molecule occupies 127 Å<sup>2</sup> at maximum. In contrast, the space requirements of one single ethanol molecule could be calculated to 87 Å<sup>2</sup>. To evaluate the real situation at specific adsorption sites, extended model calculations are highly desirable.

Regarding the evaluated heats of adsorption, two main trends could be observed. Increasing values are detected for adsorption of n-BuOH on the non-modified sample QCM-E in comparison to ethanol sorption. A dramatic increase of nearly  $\Delta H_{\text{total}} = 33 \text{ kJ mol}^{-1}$ , whereas  $\Delta H_{\text{total}} = |-\Delta H_{\text{ads, nBuOH}}| - |-\Delta H_{\text{ads, EtOH}}|$  could be observed on sample QCM-E. The averaged values for the isosteric heat of adsorption are defined as averaged data over all determined isosteric heat values (compare table 33) concerning the specific sample. It turns out that the intermediate surface polarity of sample QCM-E provokes a quite high affinity of the surface towards the ambivalent C<sub>4</sub>-alcohol n-BuOH with relatively polar hydroxyl groups and distinctive non-polar hydrocarbon tail fragments. The heats of evaporation<sup>[72]</sup> for EtOH (42.32 kJ mol<sup>-1</sup>, T= 298K)<sup>[72]</sup> and n-BuOH (52.35 kJ mol<sup>-1</sup>, T= 298K)<sup>[72]</sup> may additionally play an important role for the higher heats of adsorption for the C<sub>4</sub>-alcohol butanol. Higher dispersion forces for n-BuOH are very likely. Furthermore, as already mentioned, dehydroxylation could also contribute to a more non-polar surface of sample QCM-E. It can be stated that the nature of the surface of the nanosized siliceous material QCM-E causes the highest increase of the heat of adsorption in combination with n-butanol sorption when the vaporized adsorbent

<sup>38</sup> calculated with cyano- and mercaptopropyltriethoxysilane, phenyltriethoxysilane, vinyltriethoxysilane and hydroxyltriethoxysilane using reference [88] for calculations (MoPac interface)

material is switched from EtOH to n-BuOH.

Regarding absolute values, sample QCM-Ph offers the lowest surface polarity which is not proportionally reflected in the isosteric heat of adsorption. Both vaporized solvent molecules provoke a comparable heat of adsorption of approximately  $-27$  to  $28$   $\text{kJ mol}^{-1}$ . This might be related to a surface saturation with phenyl groups preventing interactions between the alkyl chain of n-BuOH and the mesoporous surface.

A quite similar observation was made together with sample QCM-Vinyl. Both isosteric heats for EtOH ( $\approx -37$   $\text{kJ mol}^{-1}$ ) and n-BuOH adsorption ( $\approx -39$   $\text{kJ mol}^{-1}$ ) are comparable. This observation could be related to the interaction between the non-polar fragments of the alcohols whereas the additional  $\text{C}_2\text{H}_4$ -olefin fragment does not dramatically influence the isosteric heat of adsorption. The higher space requirements of n-BuOH molecules (lowered sorption capacity in maximum) may also contribute to the observed moderately increased value.

In contrast, the released heat of adsorption of the cyano-modified sample QCM-CN is strongly dependent on the adsorbent molecule. Ethanol sorption is associated with a moderate heat of adsorption of roughly  $-23$   $\text{kJ mol}^{-1}$  and n-BuOH adsorption around  $-35$   $\text{kJ mol}^{-1}$ . The increase of ca.  $12$   $\text{kJ mol}^{-1}$  could be related to more intense interactions between the relatively polar cyano moiety and the hydroxyl head group of the  $\text{C}_4$ -alcohol. This assumption may be supported by the fact, that the maximum sorption capacity is reduced from  $\sim 10$   $\text{mmol g}^{-1}$  (EtOH) to  $4.5$   $\text{mmol g}^{-1}$  (n-BuOH). In this context, the orientation of adsorbed alcohol molecules on the mesoporous silica surface could also play an important role for the increased heat of adsorption together with sample QCM-CN. Spectroscopic investigation of the internal adsorbed species should discover the real situation on the porous surface.

A different situation arises concerning adsorption of EtOH and n-BuOH on sample QCM-SH, which is capable of forming hydrogen bonds between mercapto and hydroxyl groups. The heat of adsorption for EtOH sorption was determined to be approximately  $-41$   $\text{kJ mol}^{-1}$  whereas n-BuOH adsorption shows a decreased value of around  $-31$   $\text{kJ mol}^{-1}$ . This observed decrease of  $10$   $\text{kJ mol}^{-1}$  might be explained by additional repulsion forces between the alkyl chain of n-BuOH and the polar mercapto group. The maximum sorption capacity for ethanol ( $7.5$   $\text{mmol g}^{-1}$ ) is decreased for n-butanol sorption ( $3$   $\text{mmol g}^{-1}$ ) which illustrates the higher space requirements of adsorbed n-BuOH molecules. Furthermore, the orientation of adsorbed n-BuOH molecules (closely packed or tilted) could also contribute to the reduced sorption capacity.

The discovery of specific local orientations of adsorbed molecules was not the goal of this thesis but should be considered as one of the challenges to fully understand the varying isosteric heats of adsorption of modified mesoporous samples.

The determination of the heat of adsorption involves an ongoing discussion: as previously demonstrated on page 108, currently three main techniques are involved in the determination of adsorption heats or desorption heats, respectively. *D. Shen et al.*<sup>[108]</sup> systematically investigated the variation of obtained heats of adsorption by different techniques. Their motivation was driven by the following awareness: “Experimental measurements of heats of adsorption published in the literature are often in disagreement; differences of 10–20% are common.”<sup>[108]</sup>

The authors experimentally investigated the heats of adsorption of pure nitrogen on CaA, oxygen on CaA, and carbon dioxide on NaX zeolites by means of differentiation of adsorption isotherms at constant loading, measurement of adsorption isosteres and finally classic calorimetric experiments. They conclude that the obtained values are not in perfect agreement due to a rather constant 2 kJ mol<sup>-1</sup> discrepancy between the isosteric concepts and the calorimetric approach. The reason for this difference is still not understood.

As a general rule, measured heats of adsorption should always be considered as dependent on sample material or even sample ID. Without 100% identical sample material synthesis, post synthesis treatments and measurement preparation steps, the available literature data can only give an approximate overview of material sorption properties (compare table 44).

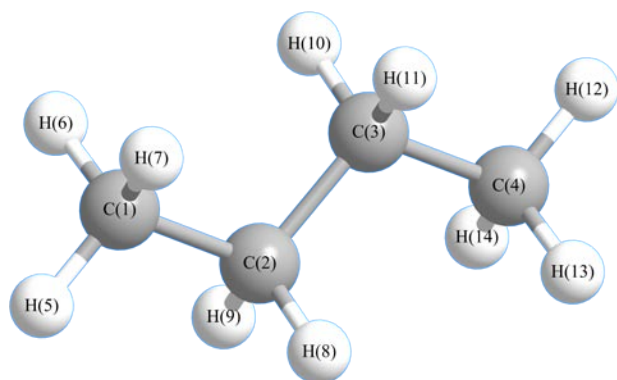
The applied gravimetric quartz crystal balance technique represents a relatively accurate method to determine mass changes related to mass increases, respectively adsorption of volatile molecules on sample surfaces. The determination of isosteric adsorption heats is closely connected to the quality of temperature and ambient pressure control during the experiments. Furthermore, as discussed in reference [108] the influence of temperature on the isosteric heat itself, the heat capacity at constant loading  $\Delta C_0 = \left( \frac{\partial q_{st}}{\partial T} \right)_0$ , was not yet taken into consideration as a possible origin of errors.

#### 6.4 Sorption of n-butane on sample Sil-1

In order to validate results obtained from SAW measurements (available on page 204) the sorption properties of n-butane on sample Sil-1 were investigated using the developed gravimetric experimental QCM setup. Due to the very high partial pressure of n-butane at 296 K (228100 Pa) the basic QCM setup was extended with a cooling aggregate, which allowed us to record frequency changes at the temperature of 272 K. Hence, the relative pressures of  $p/p_0 \approx 1$  could be reached. The cooling system consist of a cooling liquid that circulates through a closed system thus cooling a glycol containing volume down to the desired temperature of 272 K. The QCM measurement cell was thoroughly sealed with Parafilm® and additionally covered and sealed with a polypropylene foil and subsequently immersed into the cooling liquid. Related to the sample cell design, the dosed amounts of n-butane were additionally cooled to 272 K prior releasing the gas into the measurement chamber. The cooling of the gaseous species was performed by immersing roughly 2 metres of the inlet hose into the liquid nitrogen and the measurement cell design itself. The gas is additionally led several times around the 272 K cold metal cell simultaneously equalizing temperature prior it is released into the measurement chamber.

A disadvantage of this modified setup is is the difficulty to make use of the automated loop algorithm in order to detect equilibrium frequency conditions. That problem is related to a different kinetic situation at 272 K which requires an increased time interval before the sorption process reaches equilibrium. At 272 K, after a typical partial pressure step ( $\pm 5\%$  valve opening in maximum) it takes 45 - 60 minutes for one single data point to be recorded. Furthermore, frequency fluctuations are much higher ( $\pm 15\text{-}30$  Hz) due to apparent temperature gradients and the subsequent temperature equilibrating within the surrounding cooling fluid inside the Dewar vessel.

By manually controlling and operation of n-butane sorption experiments these obstacles are present. The measurements at the 272 K were performed by manually increasing partial pressures. At constant frequency values over a certain period of time (usually  $\pm 15\text{-}30$  Hz within 60 minutes) the data point was taken. The desired automated recording of sorption isotherms at temperatures below 295 K can only be performed by a radical redesign of the QCM-setup including the sample cell, e.g. equipped with a Peltier element in order to minimize temperature fluctuations and to be able to record isotherms at constant low temperatures.



atom	distance [ $\text{\AA}$ ]
C(1)-C(4)	3.9095
H(5)-H(12)	5.6577
H(9)-H(11)	3.1048
H(6)-H(13)	4.8102

Fig. 118: Ball and stick model of n-butane

Tab. 39: Inter-atomic distances of n-butane

The sorptive n-butane can be classified as non-polar according to its polarity value of 0 Debye. Figure 118 depicts a ball and stick model of n-butane with labeled atoms which are used to highlight interatomic distances listed in table 39. The maximum dimension can be stated as 5.66  $\text{\AA}$ . Compared to the pore openings of silicalite-1 (5.1  $\text{\AA}$  x 5.5  $\text{\AA}$  [100] and 5.3  $\text{\AA}$  x 5.6  $\text{\AA}$  [010])<sup>[109]</sup> the adsorptive molecule just fits into the entrance of the internal pore system. However, this conclusion is only valid for the linear conformation of n-butane.

The results of n-butane sorption experiments performed by gravimetric measurements are given in figure 119. As expected, the acquired isotherm is typical for a microporous material with an initial very steep increase in coverage at relatively low coverages  $\theta < 0.05$  and the typical asymptotic approach at higher relative partial pressures. It is commonly accepted that micropore filling occurs already at very low partial pressures.

The maximum sorption capacity at 272 K is approximately 1.6 mmol g<sup>-1</sup>. The maximum sorption capacity obtained from SAW measurements is ca. 1.55 mmol g<sup>-1</sup> at 295 K and  $p = 20000$  Pascal or  $p/p_0 = 0.09$  (compare page 208), respectively, which is furthermore in good agreement with available literature data.<sup>[110]</sup>

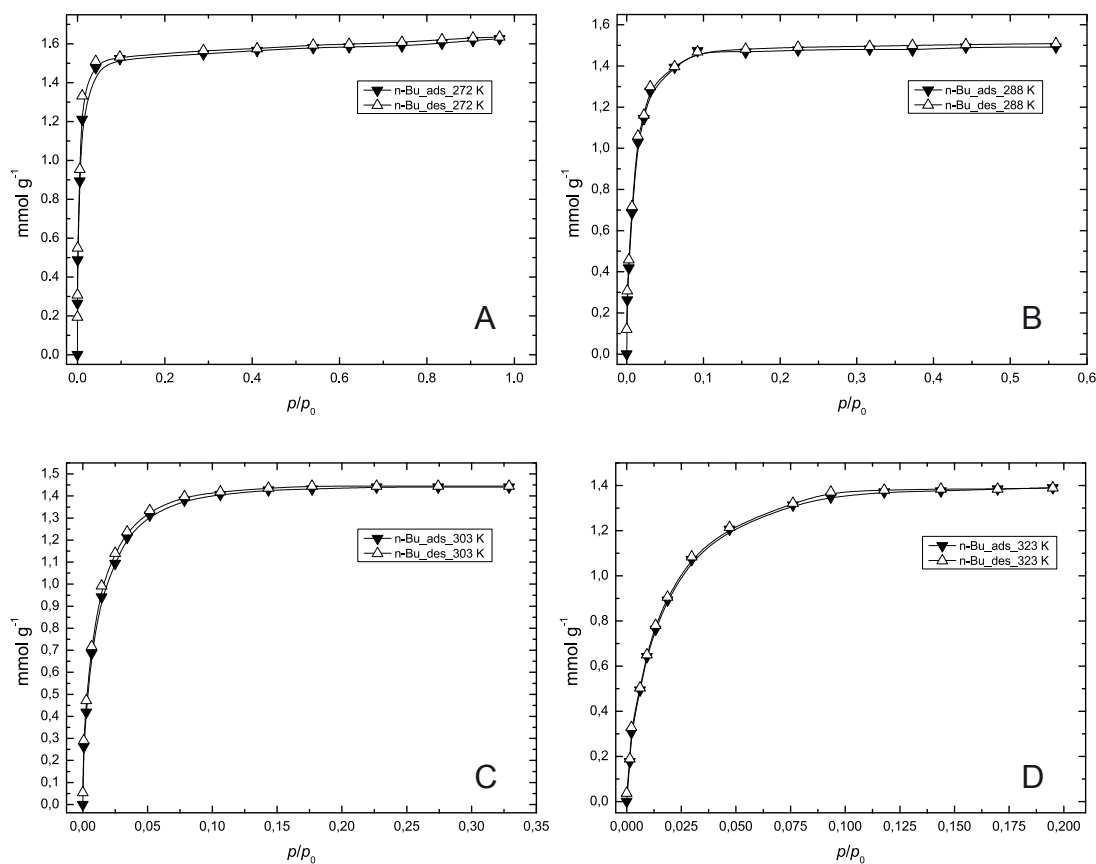


Fig. 119: Temperature dependent sorption isotherms of n-butane on sample Sil-1 at 272 K (A), 288 K (B), 303 K (C) and 323 K (D)

#### 6.4.1 Heat of adsorption of sample Sil-1

The isosteric heat of adsorption was determined as in previous experiments. Table 40 lists the calculated adsorption enthalpies at various isosteric conditions confirming the results obtained from SAW experiments (compare page 208). In order to evaluate both techniques, the isosteric heats were determined at identical values ( $\theta = 0.25, 0.5$  and  $1.0 \text{ mmol g}^{-1}$ ). At  $\theta = 0.75 \text{ mmol g}^{-1}$  an additional value was calculated. The average heat of adsorption of n-butane adsorbing on the microporous zeolite sili-calite-1 is  $-50.5 \pm 1.2 \text{ kJ mol}^{-1}$  which is comparable to literature data.<sup>[111], [112], [113], [114], [115], [116], [117], [118], [119]</sup>

n-Bu@Sil-1	
$\theta$ [mmol g <sup>-1</sup> ]	$-\Delta H_{\text{ads.}}$ [kJ mol <sup>-1</sup> ]
0.25	49.6 ± 1.1
0.5	50.0 ± 0.8
0.75	51.3 ± 1.3
1.0	51.0 ± 1.5

Tab. 40: Heat of adsorption of n-butane adsorbing on silicalite-1

## 7 **Special issue I: QCM measurements as advanced tool to investigate sorption and surface properties of porous materials**

In the following next two special issues the developed automated QCM measurement setup was applied as advanced research tool in order to investigate sorption properties of various porous samples and to obtain the thermodynamic parameter, the isosteric heat of adsorption. Furthermore, the gravimetric approach supported the investigation of surface connectivity of several different synthesized organically modified mesoporous particle surfaces.

Both projects were cooperations with collaborators in the working group of Prof. Bein (LMU Munich). The first project were carried out together with Johann Kecht who did the synthesis of mesoporous samples and parts of spectroscopic characterisation. The second project was a collaboration with Enrica Biemmi, who was responsible for the synthesis of the metal organic framework samples and the corresponding traditional material characterisation.

### 7.1 Probing the intrapore surface of phenyl-substituted nanoscale mesoporous silica

The incorporation of organic moieties into siliceous frameworks leads to a wide variety of adsorbate–adsorbent interactions including weak Van-der-Waals attractions as well as strong interactions such as Coulomb forces. Depending on the desired properties of such substituted highly porous matrix materials, optimized synthesis routes can be established to enhance the desired internal pore surface–affinity towards certain volatile compounds. Based on a fundamental knowledge of the host–guest system, sorption related applications may benefit from individually fine-tuned and modified sample materials. The sorption isotherms of vaporized toluene on non-modified and phenyl-functionalized mesoporous silica samples were determined using the gravimetric QCM technique at different temperatures. The mesoporous silica was modified by in situ co-condensation and post-synthesis grafting approaches, respectively. All samples were thoroughly characterized by nitrogen sorption, thermogravimetric



analysis, scanning and transmission electron microscopy, solid state nuclear magnetic resonance ( $^{29}\text{Si}$ -NMR), dynamic light scattering, Raman spectroscopy and toluene adsorption on the automated QCM setup. The different heats of adsorption of toluene on the various modified silica surfaces obtained by the sorption data made it possible to gain additional information about the degree and type of surface functionalization. It is thus demonstrated that QCM studies can be a powerful and convenient tool for efficient investigations of functionalized mesoporous silica particles that yield valuable quantitative information on molecule-surface interactions.

### 7.1.1 *Introduction and motivation*

The present work utilizes the previously introduced and advanced QCM technique to determine sorption isotherms of unfunctionalized and phenyl-functionalized periodic mesoporous silica. The thin mesoporous films used in this study fulfill the preconditions of the *Sauerbrey* equation<sup>[61]</sup> of limited thickness and homogeneity of the deposited material. Although some alternative techniques including the functionalization by metalorganic reagents<sup>[120]</sup> and by silazanes<sup>[121]</sup> have been reported recently, the two common primary methods for functionalization of mesoporous silica materials are the grafting and co-condensation approaches. In the former method, trialkoxy- or trichlorosilanes bearing the desired functionalities are attached to the surface silanol groups of the mesoporous structure by a post-synthesis treatment step. In the co-condensation approach, the functionalization takes place in situ by adding the appropriate amount of functionalized trialkoxysilanes to the reaction mixture as already utilized for synthesis of samples QCM-R. While both methods are adequate to introduce high amounts of organic moieties into the material, they can result in significantly different surface properties.

In this special issue, both functionalization approaches, the co-condensation and grafting of phenyltriethoxysilane, are applied in the synthesis of colloidal suspensions of non-functionalized and phenyl-containing mesoporous silica nanoparticles (MSN in the sample codes). The materials are thoroughly characterized by various standard techniques and subsequently applied in the preparation of homogeneous layers on the

surface of QCM devices via spin-coating. For each sample, toluene sorption isotherms were recorded at four different temperatures, thus allowing the calculation of the respective heats of adsorption via the *Clausius-Clapyron* equation (see equation (28)). The relevant data were taken at isosteric conditions from the adsorption branch of the corresponding isotherms.<sup>[93]</sup> The resulting heats of adsorption yield information about the affinity of the adsorbate towards the modified mesoporous materials. It is thus demonstrated that QCM measurements can be applied for the efficient characterization of mesoporous silica materials, which is a valuable approach due to the rapidly achieved equilibrium conditions and short diffusion times obtained by using small amounts of sample in thin films.

### 7.1.2 Synthesis of mesoporous samples MSN

Tetraethyl orthosilicate (TEOS, Fluka, >98%), phenyltriethoxysilane (PTES, Aldrich, 98%), cetyltrimethylammonium chloride (CTAC, Fluka, 25% in H<sub>2</sub>O) and triethanolamine (TEA, Aldrich, 98%) were used as received without further purification. Doubly distilled water from a Millipore system (Milli-Q Academic A10) was used for all synthesis and purification steps. Unfunctionalized mesoporous silica nanoparticles were prepared according to reference<sup>[32]</sup> from reaction mixtures with a molar composition of 1 TEOS : 9.6 TEA : 0.22 CTAC : 145 H<sub>2</sub>O (sample MSN-I). TEOS (10.4 g) and TEA (71.5 g) were heated for 25 minutes at 363 K without stirring in a 250 mL polypropylene reactor. An aqueous CTAC-solution (133.6 g, 2.58 %wt) preheated to 333 K was added and the resulting mixture stirred at room temperature for 3 hours. After addition of 100 ml ethanol, the mesoporous silica nanoparticles were separated by centrifugation and redispersed in ethanol. Extraction of the organic template was performed by heating under reflux at 368 K for 30 minutes in two solutions containing 2 g ammonium nitrate in 100 ml ethanol and 4 g concentrated hydrochloric acid in 100 ml ethanol, respectively. The nanoparticles were washed by centrifugation after each extraction step, resulting in clear ethanolic suspensions.

For preparation of phenyl-grafted material (sample MSN-II), 400 mg PTES were added to 6.5 g of an ethanolic suspension containing 3.0 wt% unfunctionalized extracted

nanoparticles. The suspension was heated under reflux for 3 hours and purified by two steps of centrifugation and redispersion in ethanol.

For the preparation of phenyl-containing samples by the co-condensation route, the synthesis for mesoporous silica nanoparticles was performed starting from a reaction mixture with a molar composition of 0.9 TEOS : 0.1 PTES : 9.6 TEA : 0.22 CTAC : 145 H<sub>2</sub>O (sample MSN III).

All samples were stabilized as ethanolic suspensions with a solid concentration of about 3 wt% and repeatedly spin-coated (3000 rpm) onto a QCM device, thus obtaining deposited sample amounts on the electrodes varying from 14.6 g cm<sup>-2</sup> up to 36.2 μg cm<sup>-2</sup>. The resulting QCM devices were heated in a furnace at 623 K in air for 10 hours with a prior heating ramp of 0.5 K min<sup>-1</sup> in order to decompose any residual template molecules inside the silica mesopores.

Prior to any recording of isotherms the QCM device was heated up to 403 K inside the measurement cell in a nitrogen atmosphere at a constant flow of 2000 ml min<sup>-1</sup> for at least 20 minutes until frequency stability was reached. After the heating and purging period at 403 K, a deviation of less than ± 10 Hz within a 240 seconds period was accepted as sufficiently stable to indicate the absence of water in the mesopores, subsequently enabling the next temperature step.

### 7.1.3 *Characterization of mesoporous samples MSN*

Dynamic light scattering measurements to determine the hydrodynamic particle diameter in colloidal suspensions were performed with a Malvern Zetasizer-Nano instrument equipped with a 4 mW He-Ne laser (633 nm) and avalanche photodiode detector. Thermogravimetric analyses of the bulk samples were performed on a Netzsch STA 440 C TG/DSC (heating rate of 10 K min<sup>-1</sup> in a stream of synthetic air of about 25 ml min<sup>-1</sup>). Solid state <sup>29</sup>Si-CP-NMR measurements were performed on a Bruker DSX Avance 500 FT. Raman spectra of the coated QCM devices were recorded on a Jobin Yvon Horiba HR800 UV Raman microscope using a HeNe laser emitting at 632.8 nm. Transmission electron microscope images were taken with a JEOL JEM 2011 microscope operating at 200 kV, by drying the diluted colloidal suspensions on a carbon-

coated copper grid.

In order to evaluate the smoothness and overall sample thickness and to validate the applicability of the *Sauerbrey* equation, the mesoporous silica layer on top of the quartz

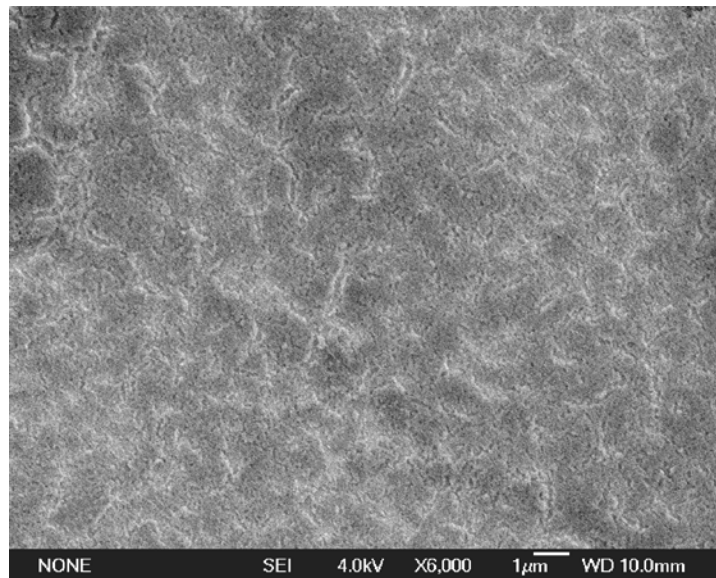


Fig. 120: SEM image of sample MSN-III

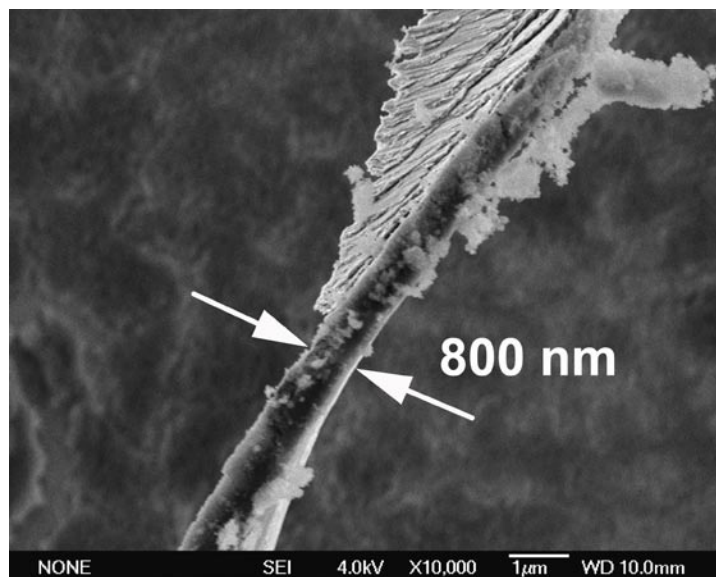


Fig. 121: SEM image of scratched sample MSN-III, demonstrating the low thickness

crystal was investigated with a JEOL JSM 6500F scanning electron microscope. As an example, figure 120 shows the surface of the QCM device spin-coated with sample MSN-III, which does not contain any large agglomerations. figure 121 also demonstrates the low thickness of about 800 nm of the removed particle layer observed after scratching the silica surface with a scalpel.

Nitrogen sorption measurements were performed on a Quantachrome Instruments NOVA 4000e at 77 K. For calculations of pore sizes and volumes a NLDFT equilibrium model of N<sub>2</sub> on silica was used. Pore diameters based on the BJH model are also given for better comparison with literature data. A BET model was applied to evaluate the surface areas.

The recording of isotherms was performed on the QCM experimental setup described in detail starting on page 89. A 10 MHz QCM device was used to measure frequency changes due to additional adsorbed mass. The data sheet of the QCM chip can be found on page 239. The common relationship between frequency and mass changes as described on page 93 was set for granted and valid.

The overall frequency fluctuation of the system was  $\pm 1\text{--}2$  Hz at room temperature. Concerning the sorption of the vaporized liquid toluene, partial pressures were calculated using the Van-der-Waals equation (see equation (14)) with real gas state assumptions. Van-der-Waals parameters for toluene ( $a = 24.86$ ,  $b = 0.1497$ ) were taken from reference 72.

#### 7.1.4 *Dynamic light scattering*

DLS measurements reveal that all samples possess narrow particle size distributions with hydrodynamic diameters in the range of 100–200 nm (see figure 122 part I.). Corresponding TEM investigations show round and elongated mesoporous particles (sample MSN-I) with diameters below 100 nm as shown in part II. of figure 122.

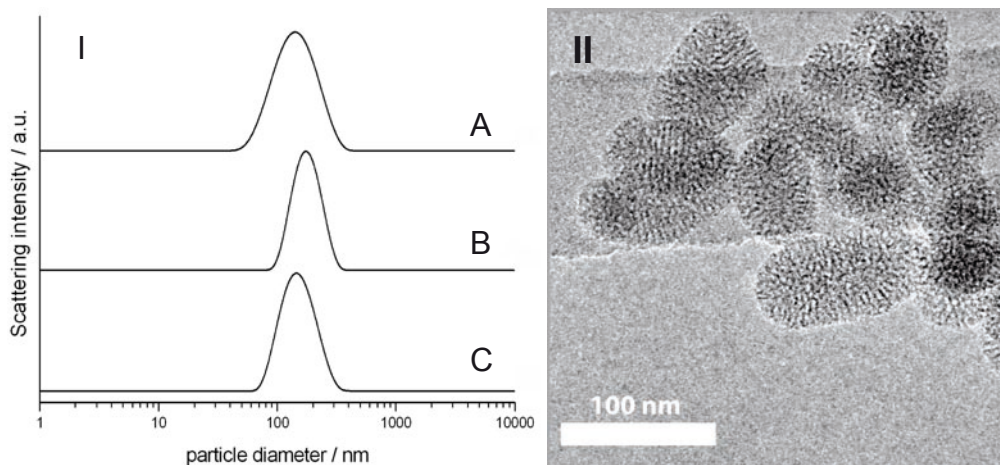


Fig. 122: DLS data (I) of sample MSN-I (A), MSN-II (B) and MSN-III (C) and TEM image of sample MSN-I (II). Data recorded by J. Kecht.

### 7.1.5 Nitrogen sorption characterisation

Parts of the solutions were dried for further characterization of powder samples. Ni-

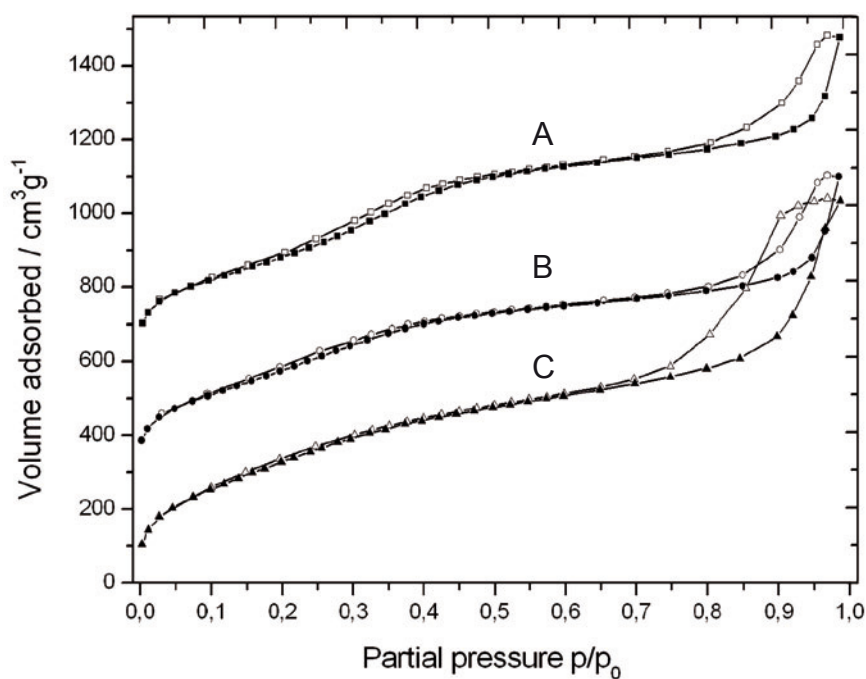


Fig. 123: Nitrogen sorption data of sample MSN-I (A), MSN-II (B) and MSN-III (C). Data recorded by J. Kecht.

trogen sorption measurements were applied to investigate the porous nature of the products (figure 123). All samples show the expected IUPAC classified type IV shape isotherm, typical for mesoporous systems, indicating mesopore filling as well as a pronounced hysteresis loop at higher  $p/p_0$ -values due to external textural porosity of the nanoparticles. BET calculations reveal high surface areas for all three samples due to the large internal surface of the mesoporous channel system. NLDFT calculations show that the pore diameter of 3.7 nm in the unfunctionalized material is decreased by about 0.3 nm by incorporation of phenyl groups (figure 124) which is less than twice the molecular dimension ( $2 \times 0.3$  nm for two single phenyl groups), thus suggesting a tilted arrangement and/or a low density of the phenyl groups coating the silica network walls.<sup>[88]</sup> The reduced pore diameter is also reflected in the decreased pore volume (see table 41). A complete coverage of the silica surface with densely packed and vertical oriented phenyl groups would result in a decrease of the pore diameter by about 0.6 nm, by assuming a layer of phenyl groups facing each other on both sides of a pore wall. However, such a scenario would be highly unlikely considering the respective mechanisms of phenyl incorporation. During grafting, the density of the phenyl groups

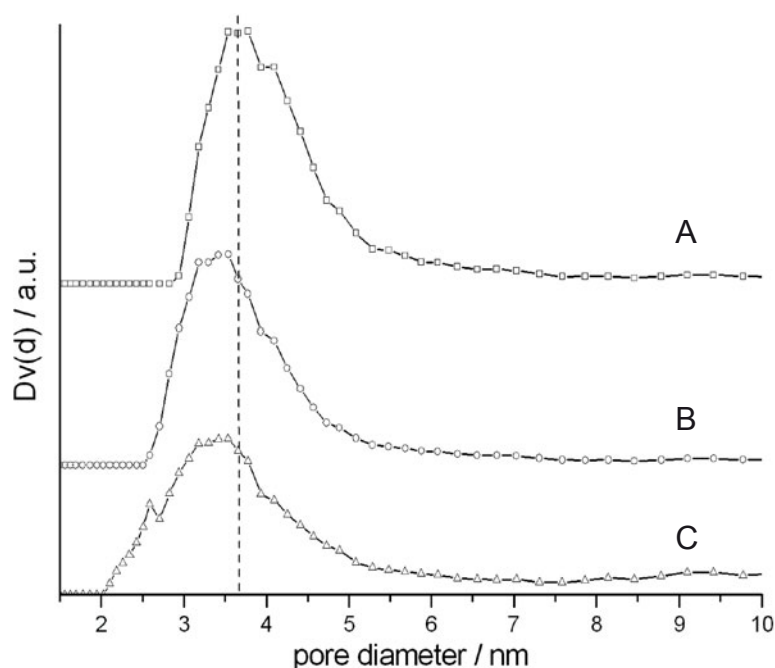


Fig. 124: Pore size distribution of sample MSN-I (A), MSN-II (B) and MSN-III (C). Data recorded by J. Kecht.

on the silica surface is determined by the availability of binding sites and remaining free space between previously grafted molecules, which will prevent a close packing of the phenyl groups. During co-condensation, the relevant phenyl groups are placed on the hydrophilic–hydrophobic interface of the micelles and will arrange themselves in such a way that they are pointing inside the hydrophobic part of the micelles during self-assembly. Since the pore walls can therefore only be partially functionalized, the observed pore size reduction is smaller than expected from a densely packed monolayer of phenyl groups.

sample	functionalization method	BJH pore diameter [nm]	DFT pore diameter [nm]	DFT pore volume <sup>a</sup> [cm <sup>3</sup> g <sup>-1</sup> ]	BET surface area [m <sup>2</sup> g <sup>-1</sup> ]
MSN-I	unfunctionalized	2.6	3.7	0.82	1187
MSN-II	grafting	2.2	3.4	0.62	1104
MSN-III	co-condensation	2.1	3.4	0.61	1275

<sup>a</sup> for pores under 8 nm

Tab. 41: Nitrogen sorption data

### 7.1.6 Thermogravimetric analysis

In order to determine the extent of phenyl functionalization, thermogravimetric analysis was performed on all samples (figure 125). It is assumed that the thermal decomposition of the template in the MSN-samples is similar to the mechanism reported for CTAB-containing MCM-41 described in the literature.<sup>[122]</sup>

In the temperature range up to 383 K, physisorbed water is released from the pores. From 383 K to about 668 K, remaining cetyltrimethylammonium template is decomposed by first undergoing Hoffmann elimination followed by oxidation to CO<sub>2</sub>.<sup>[122]</sup> In the range of about 668 K to 1173 K, three reactions can take place. In all three samples, water is released by condensation of framework silanol groups, and small amounts of carbonaceous residues from incomplete template combustion are oxidized. In the case of phenyl containing samples, the aromatic groups are also decomposed within this temperature range. While the thermogravimetric graphs of all samples are similar for



temperatures up to 668 K, the extent of functionalization is clearly evident by comparison of the weight loss between 668 and 1173 K for sample MSN-I (2.6 %) in contrast to samples MSN-II (11.3 %) and MSN-III (13.7 %).

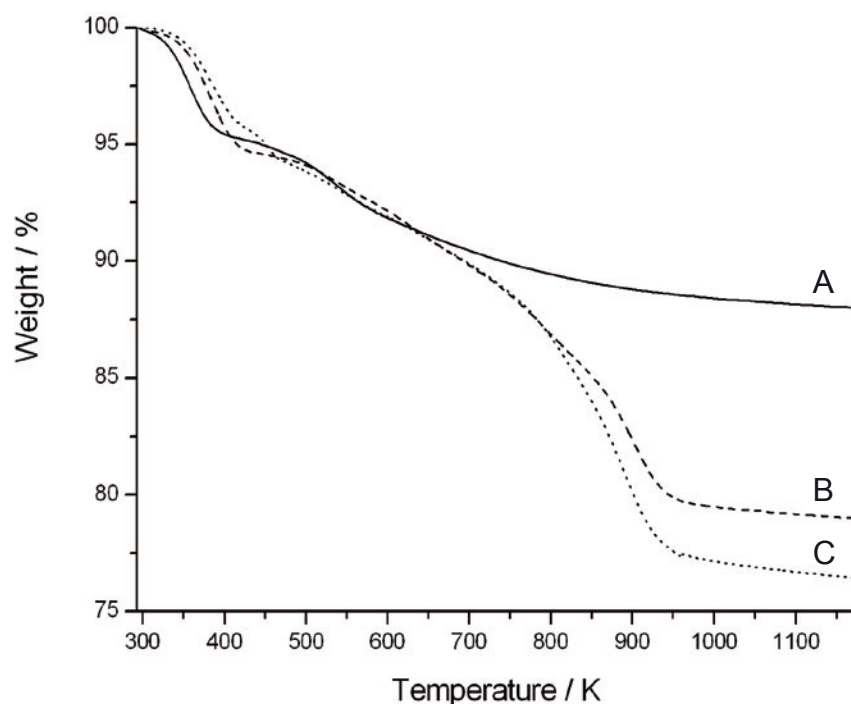


Fig. 125: Thermogravimetric analysis data of sample MSN-I (A), MSN-II (B) and MSN-III (C). Data recorded by J. Kecht.

### 7.1.7 *Solid state $^{29}\text{Si}$ -CP-MAS-NMR experiments*

While both samples MSN-II and MSN-III contain comparable mass loadings of phenyl groups, there should be major differences in the degree of framework attachment.  $^{29}\text{Si}$ -CP-MAS-NMR was used to investigate the different connectivity of the functionalized silicon atoms to the mesoporous framework prior to the calcination step at 623 K in air (see figure 126). All three samples show  $\text{Q}^4$ ,  $\text{Q}^3$  and to less extent  $\text{Q}^2$  resonances at -110, -100 and -90 ppm, respectively, arising from the incompletely condensed silica framework ( $\text{Q}^4 = \text{Si}(\text{OSi})_4$ ,  $\text{Q}^3 = \text{Si}(\text{OSi})_3\text{OH}$ ,  $\text{Q}^2 = \text{Si}(\text{OSi})_2(\text{OH})_2$ ). However, the  $\text{Q}^2$  spe-

cies seem to be reduced in sample MSN-II due to further condensation at higher temperatures during the grafting treatment. For the co-condensed sample MSN-III, signals corresponding to  $T^3$  and  $T^2$  sites can be found at -80 and -70 ppm, respectively. They are related to the phenyl-bearing silicon atoms that were co-condensed into the mesoporous silica framework ( $T^3 = \text{Si}(\text{OSi})_3\text{R}$ ,  $T^2 = \text{Si}(\text{OSi})_2(\text{OH})\text{R}$ ,  $T^1 = \text{Si}(\text{OSi})(\text{OH})_2\text{R}$ ). In contrast, the phenyl groups in sample MSN-II were grafted onto the silica surface of the sample by a post-synthesis treatment. Existing  $T^3$  sites are less prominent compared to the co-condensed sample. However, a higher concentration of  $T^2$  sites and a signal corresponding to  $T^1$  sites at about -63 ppm is detected. This indicates that the grafted silyl species bearing phenyl groups are mainly connected to the silica framework by two siloxane bonds. As the framework is already pre-formed, phenyltriethoxysilane moieties attaching to the surface are not always able to find silanol groups in suitable locations for further condensation reactions. After attachment of two groups, as is the case at a  $T^2$  site, the flexibility and rotation of the group is hindered, thereby reducing

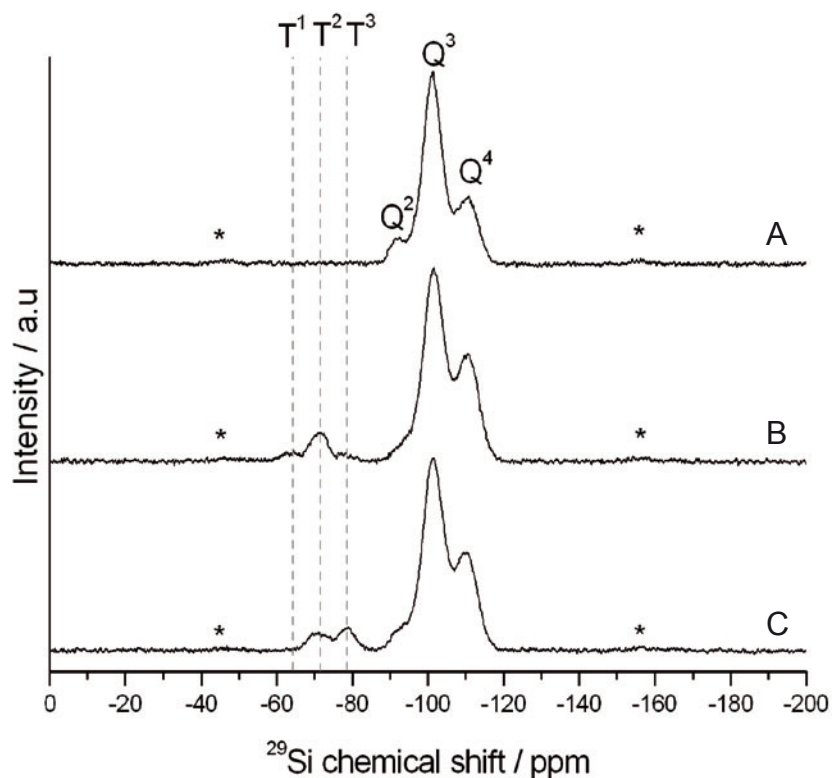


Fig. 126:  $^{29}\text{Si}$ -MAS-NMR data of sample MSN-I (A), MSN-II (B) and MSN-III (C) before calcination. Data recorded by J. Kecht.

the possibility of finding a third opportunity for condensation and thus explaining the prominence of T<sup>2</sup> sites in sample MSN-II.

A different picture is obtained after heating treatment. In order to evaluate the influence of the calcination step at 623K on the degree of silanol condensation and connectivity of the phenyl groups, the solid state NMR measurements were repeated on calcined samples (figure 127). As expected, framework condensation is significantly increased during heating, resulting in a higher degree of Q<sup>4</sup> species by annealing of free silanol groups in the material.

In all three samples the relative intensity of the Q<sup>4</sup> signals versus Q<sup>3</sup> signals is increased, and similar observations can be made for signals corresponding to T<sup>3</sup> and T<sup>2</sup> species. It should also be noted that the high degree of T<sup>2</sup> sites detected earlier in grafted sample MSN-II was drastically lowered by the calcination treatment. This was probably caused by the increased mobility of the phenyl-bearing silyl groups at higher temperatures, thus enabling the final condensation step of the remaining silanol group

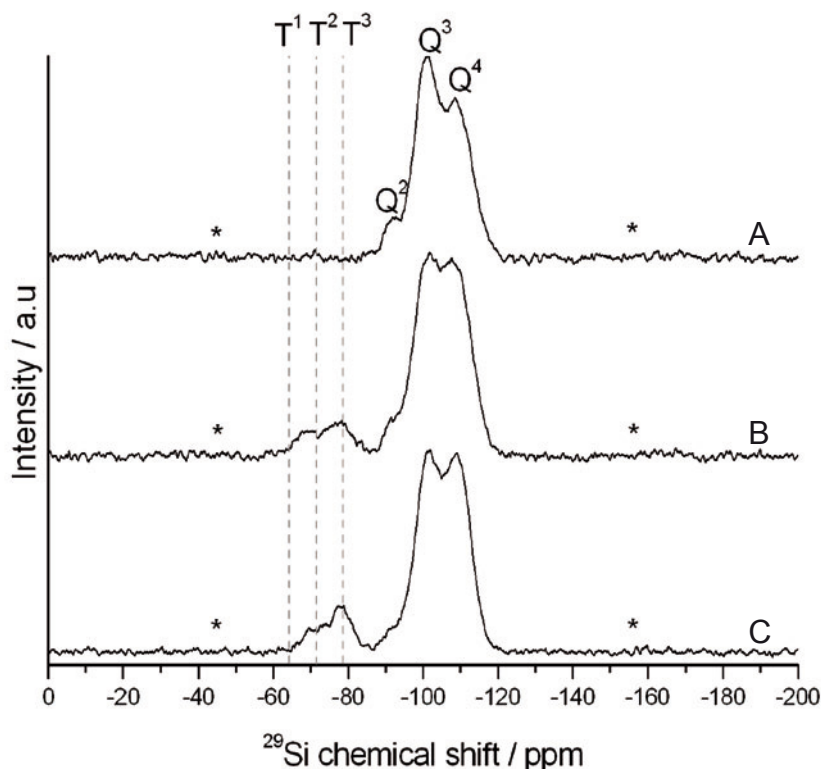


Fig. 127: <sup>29</sup>Si-MAS-NMR data of sample MSN-I (A), MSN-II (B) and MSN-III (C) after calcination. Data recorded by J. Kecht.

on the T<sup>2</sup> species to the framework surface. It can therefore be stated that based on NMR analysis the connectivity of phenyl-bearing silyl groups in the grafted and co-condensed samples after calcination are rather similar.

### 7.1.8 Raman spectroscopy

Raman spectroscopic studies on the QCM device were performed in order to elucidate the fate of the attached phenyl groups after heating the film at 623 K (figure 128). Samples MSN-II and MSN-III show three additional bands emerging at  $\tilde{\nu} = 622, 1002$  and  $1032 \text{ cm}^{-1}$ , which can be assigned to the in-plane ring deformation, C-H-in-plane and C=C- stretching vibrations of the phenyl group, respectively. The other bands belong to vibrations of the quartz plate, as can be seen by comparison with an uncoated

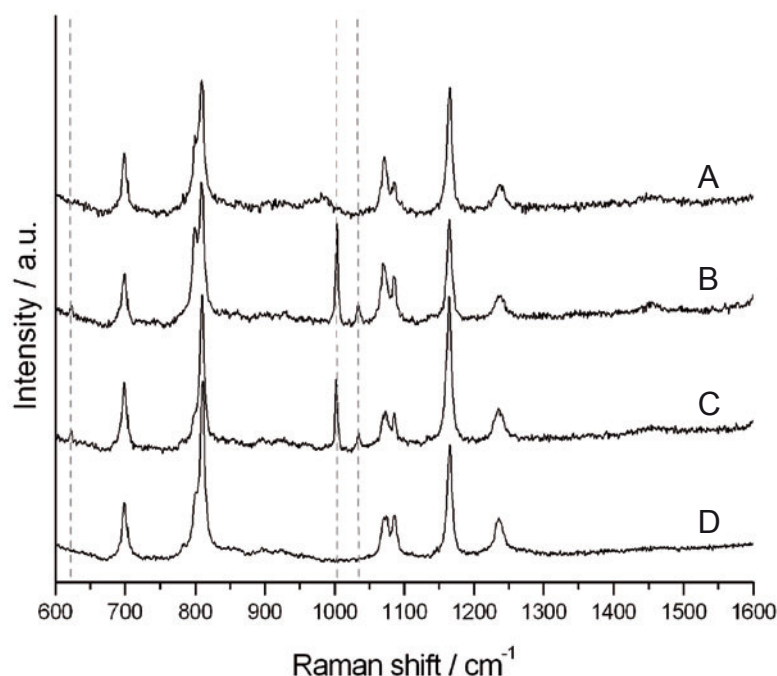


Fig. 128: Raman spectroscopic data of sample MSN-I (A), MSN-II (B), MSN-III (C) and empty reference QCM-chip (D). Data recorded by J. Kecht.

QCM-chip. It is therefore concluded that the phenyl groups remain intact in the calcined films, which is also to be expected based on the thermal stability shown during TG analysis. The observed Raman bands are in good agreement with the previously investigated phenyl substituted sample QCM-Ph (compare figure 23) whereas the region =C-H- with vibrations around  $\tilde{\nu} = 3000 - 3100 \text{ cm}^{-1}$  was not explicitly examined with MSN samples.

### *7.1.9 Toluene sorption experiments and determination of isosteric heats of adsorption*

Toluene sorption isotherms at 298 K recorded with QCM-devices coated with the 3 samples are illustrated in figure 129. The sorption of toluene on MSN-I shows a steep Type IV isotherm, and samples MSN-II and MSN-III exhibit Type IV isotherms as well. Type IV classified isotherms represent a high affinity of the gaseous molecules towards the adsorbent which is shown by the steep increase of toluene-loading at low relative pressures in all three samples. Nevertheless, the typical mesopore condensation step is not clearly perceptible. The determination of the heat of adsorption based upon sorption isotherms provides a quantitative refinement of the affinity of toluene during physisorption towards the three different types of sample surfaces.

Table 42 illustrates the isosteric heats of adsorption calculated at different degrees of coverage for all three samples. It should be mentioned that the determination of the adsorption enthalpy at isosteric conditions is not recommended in the isotherm region of adsorbate–adsorbate adsorption as it would generate erroneous values which would be influenced by the adsorption of toluene on toluene. To overcome that problem the heats of adsorption were calculated according to the individual break point at which sub-monolayer coverage of toluene adsorbing on each individual sample can still be assumed. Therefore, the heat of adsorption on sample MSN-III was evaluated at coverages of 0.75, 1.0 and 1.5 mmol g<sup>-1</sup> (table 42). The lowest expected monolayer coverage of toluene is calculated assuming a space requirement of 116 Å<sup>2</sup> per molecule toluene (COSMO surface in the MoPac package of reference [88]) occupying all sorption sites with the  $\pi$ -electron system parallel to the surface (which is unlikely). In this case, a

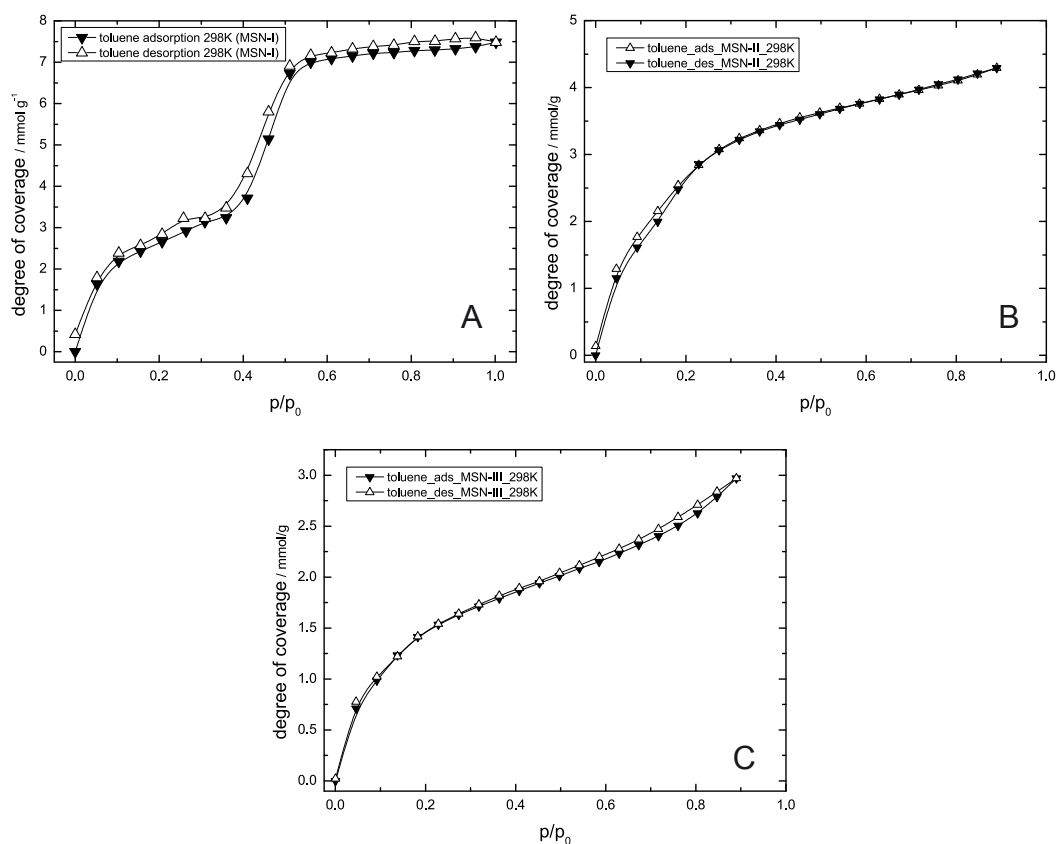


Fig. 129: Toluene sorption isotherms for sample MSN-I (A), MSN-II (B) and MSN-III (C) recorded at 298 K and ambient pressure

monolayer of toluene molecules would be present at a coverage of about  $1.7 \text{ mmol g}^{-1}$  (MSN-I),  $1.7 \text{ mmol g}^{-1}$  (MSN-II) and  $1.8 \text{ mmol g}^{-1}$  (MSN-III) (these values vary because of the different surface areas of the samples). Thus, determining the heats of adsorption at loadings below these values will ensure the desired sub-monolayer coverages. A closer look at the sorption isotherms of sample MSN-I and MSN-II shows, that an almost linear correlation of relative pressure and coverage can be observed up to  $2.5 \text{ mmol g}^{-1}$  and  $3.0 \text{ mmol g}^{-1}$ , respectively. It is therefore assumed that toluene–toluene adsorption will only have a minor influence on the results within this data range. This is further supported by the fact that all variations of the loading parameter in this data range lead only to minimal variations in the calculated heat of adsorption.

The unfunctionalized silica sample MSN-I exhibits the lowest heat of adsorption for toluene. This is attributed to the relatively small affinity of the non-polar solvent vapor of toluene ( $0.375 \pm 0.01 \text{ Debye}$ )<sup>[72]</sup> to the relatively polar, silanol rich internal surface

$\theta$ [mmol g <sup>-1</sup> ]	MSN-I	MSN-II	MSN-III
0.75	-	-	23.9 ± 1.4
1.0	-	-	24.2 ± 0.6
1.5	17.8 ± 1.6	28.1 ± 1.2	24.1 ± 0.8
2.0	17.9 ± 1.6	32.2 ± 1.1	-
2.5	18.3 ± 1.5	31.6 ± 1.2	-
3.0	-	30.3 ± 1.2	-
<i>average</i>	<i>18.0 ± 1.6</i>	<i>30.5 ± 1.2</i>	<i>24.1 ± 1.0</i>

Tab. 42: Isothermic heats of adsorption of sampel MSN-I, MSN-II and MSN-III

of the silica material. This behavior is also reflected in the higher heats of adsorption of the samples bearing a phenyl-substituted surface. The post-synthesis grafted sample MSN-II shows a distinctive high affinity to toluene vapor which results in an average value for the heat of adsorption of  $30.5 \pm 1.2$  kJ mol<sup>-1</sup> calculated from four different loadings (1.5, 2.0, 2.5 and 3.0 mmol g<sup>-1</sup>). The heat of adsorption for the phenyl-grafted sample MSN-II is the highest of all three, but still noticeably lower than the heat of vaporization of toluene (38.01 kJ mol<sup>-1</sup> at 298 K).<sup>[72]</sup>

In contrast, the sample MSN-III which was phenyl-functionalized via co-condensation, only reveals an average isothermic heat of adsorption of  $24.1 \pm 1.0$  kJ mol<sup>-1</sup>, indicating a lower affinity of toluene molecules towards the co-condensed surface, although TGA data indicate a higher concentration of phenyl groups (by 2.5 %wt).

Reproducibility of the measurements was confirmed by a second set of samples prepared at identical conditions. The obtained values for the toluene heat of adsorption were  $18.6 \pm 1.4$  kJ mol<sup>-1</sup>,  $30.8 \pm 1.1$  kJ mol<sup>-1</sup> and  $24.5 \pm 1.2$  kJ mol<sup>-1</sup> for the unmodified, grafted and co-condensed sample, respectively. The heat of adsorption on these samples is thus matching the values obtained for MSN-I, MSN-II and MSN-III within the calculated error limits.

The observed differences between samples MSN-II and MSN-III regarding their heats of adsorption can be explained by taking into account the different localization of phenyl groups at the internal pore surface. The grafted sample offers the highest amount of freely available phenyl groups that are accessible at the internal pore sur-

face. By nature of the grafting procedure, all phenylsilane groups are concentrated at the internal and external sample surface where they replace up to three hydroxyl groups by condensation reactions (compare figure 130).

Even though the co-condensed sample MSN-III contains somewhat more phenyl

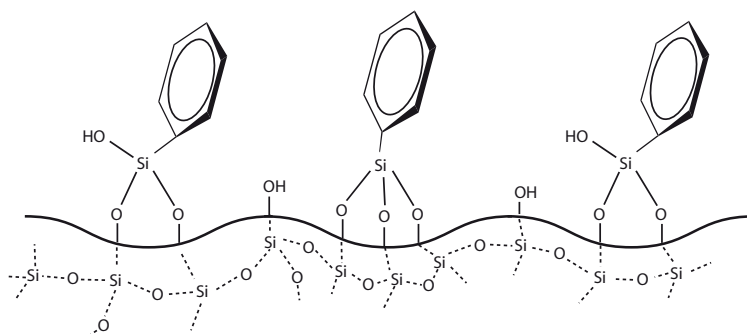


Fig. 130: Schematic illustration of phenyl-grafted surface of sample MSN-II

groups according to TGA data, this attachment scheme will not result in a significant capping of silanols, due to steric requirements, and possible incorporation of phenyl groups in the silica walls. This would lead to a surface that could be considered, in terms of interaction forces, as an intermediate between the unfunctionalized and the grafted surface with respect to silanol concentration. The outer surface therefore still bears a high amount of free hydroxyl groups and less phenyl groups than the grafted

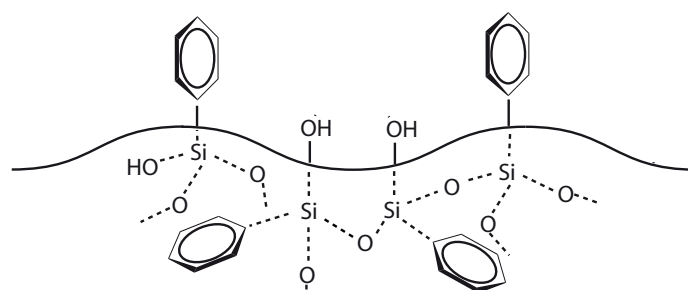


Fig. 131: Schematic illustration of phenyl co-condensed surface of sample MSN-III



sample (figure 131). This results in a lower affinity and decreased heat of adsorption for the non-polar toluene molecules.

According to figure 132, the isotherms of sample MSN-II confirm the good reversibility of the adsorption at 298 K, 313 K, 328 K and 343 K. Minor differences between the adsorption and desorption branches in terms of sorption capacity at identical relative pressures are attributed to the much slower desorption kinetics and to a possible drift of the experimental system. The isotherms at higher temperatures for samples MSN-I and MSN-III are available as supplemental information (appendix D).

In order to demonstrate equilibration behavior of the system, one raw data set is illustrated in figure 133 showing the decrease in frequency caused by increasing relative pressure (adsorption) and vice versa (desorption). The automated experimental setup records frequency changes at 4 temperatures, including a purging and heating step at a nitrogen flow of 2000 ml min<sup>-1</sup> at 403 K before adjusting each new experimental tem-

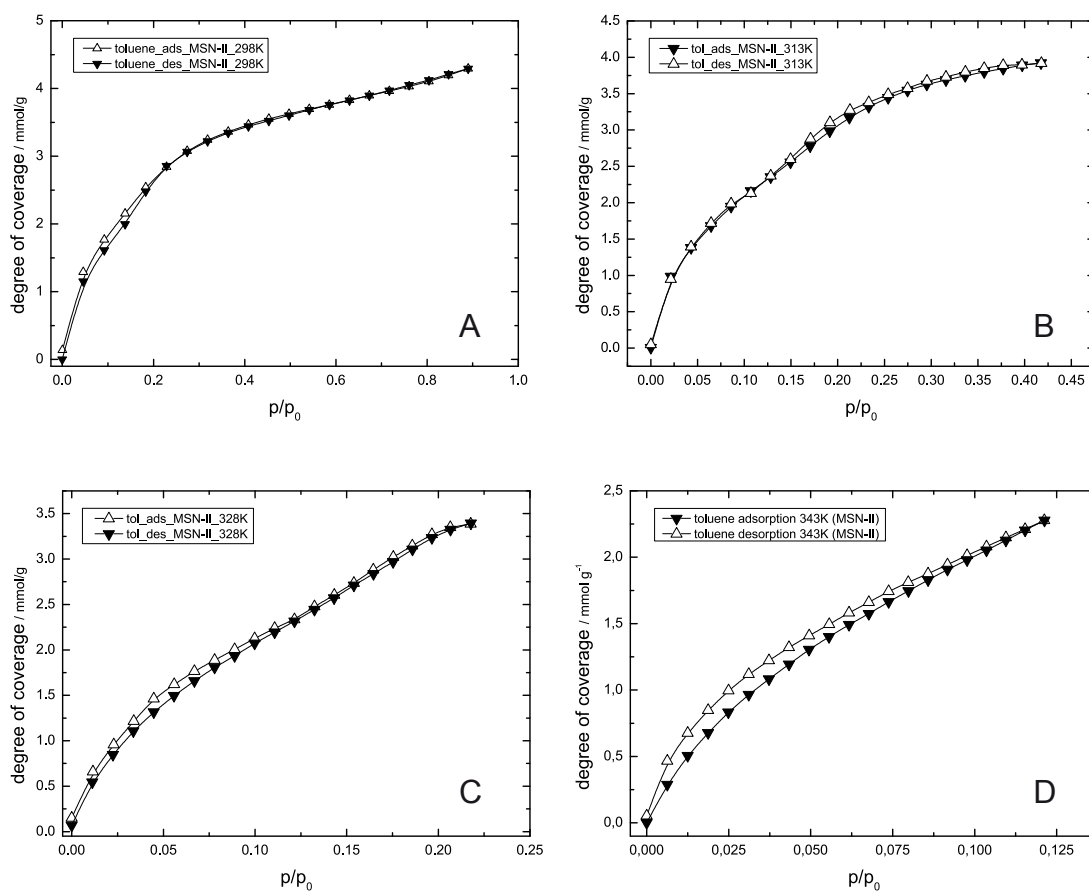


Fig. 132: Toluene isotherms for sample MSN-II at 298 K (A), 313 K (B), 328 K (C) and 343 K (D)

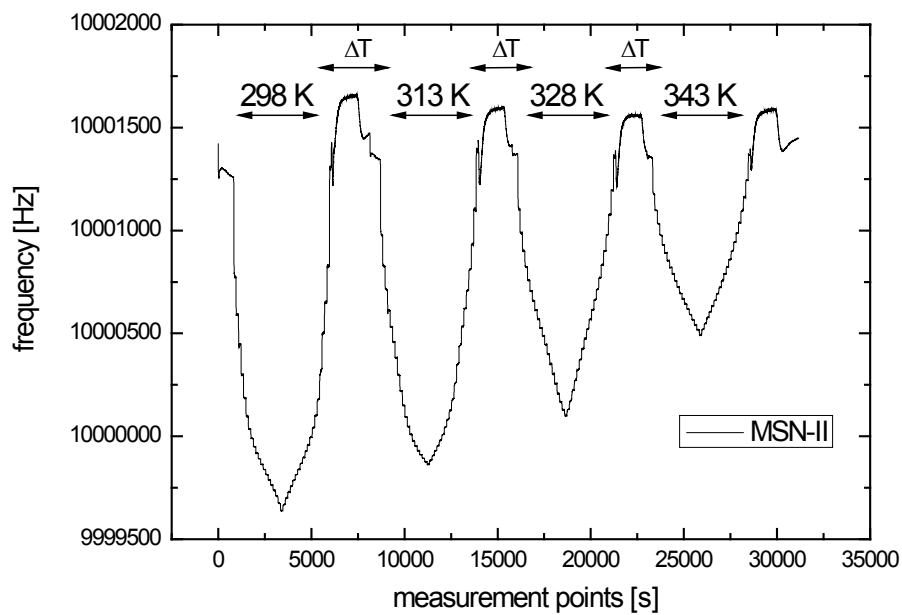


Fig. 133: QCM raw data set for sample MSN-II acquired at 298 K, 313 K, 328 K and 343 K. The  $\Delta T$  label indicates the heating and  $N_2$  purging period at 403 K

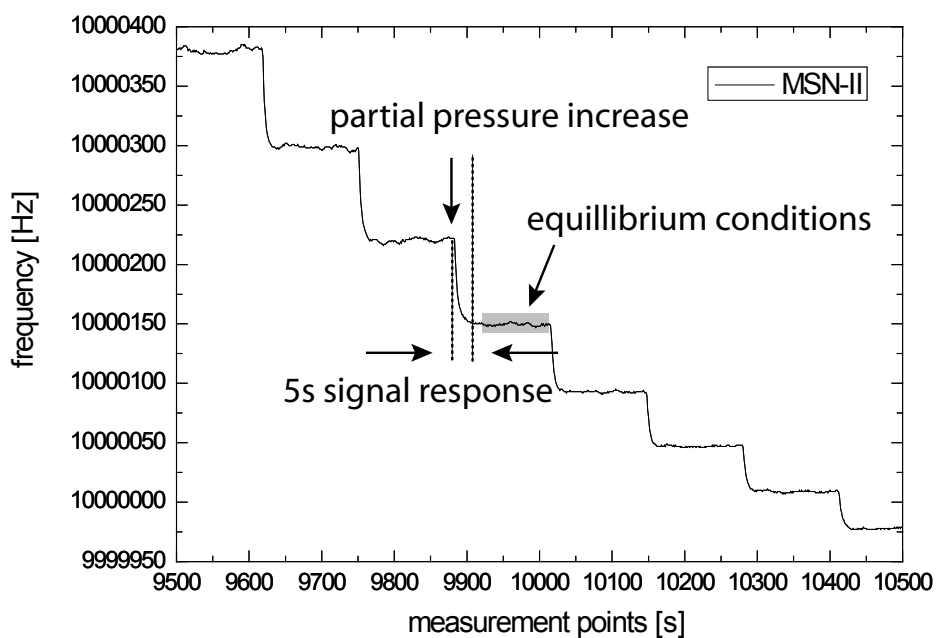


Fig. 134: Magnified raw data set of the measurement for sample MSN-II recorded at 313 K

perature, to ensure the complete removal of residual toluene molecules.

A magnified graph (see figure 134) shows that equilibrium is reached during the experimental conditions for adsorption: within 100 s no measurable frequency changes are observed, while the initial partial pressure increase step (or decrease step) is very fast and completed within 5 seconds.

## 7.2 Conclusion phenyl-substituted nanoscaled mesoporous silica

A convenient and fast method for determining heats of adsorption in porous nanoparticles was demonstrated for the case of unfunctionalized and phenyl-functionalized mesoporous silica synthesized by co-condensation and grafting routes. Although both samples incorporate comparable amounts of phenyl groups, the resulting surface functionalization differs significantly with respect to the affinity of the pores' surface towards toluene. The effect of surface functionalization on the heat of adsorption of toluene has been quantified using QCM measurements at different temperatures. While co-condensed material shows only a 33 % increase of the heat of adsorption, with respect to the unfunctionalized host, the increase is more than doubled for grafted material.

The QCM-based sorption method offers the capability to acquire isotherms of volatile vapors and the corresponding heats of adsorption at the same time, while using very small sample amounts in the range of about 5 to 30  $\mu\text{g}$ . The small amounts of sample, presented in the form of a thin film, additionally result in a very fast signal response due to the short diffusion times, thus allowing standard measurements to be completed in 4–6 hours. On the other hand, standard gravimetric determination of sorption isotherms utilizes sample masses in the range of milligrams, thus requiring significantly more time to reach equilibrium conditions.<sup>[123]</sup> Even multiple samples could be measured at once if the system is parallelized with several QCM devices. Possible applications of such QCM-based techniques include the screening of potential catalytic active materials in terms of affinity for different gaseous species, development of sensors for volatile compounds, and evaluation of membrane materials. The method is capable, with statistical significance because it averages over the entire sample, of giving more insights into the nature of surface modifications and their influence on sorption proper-

ties.

Considering the characterization of functionalized mesoporous materials, this study shows that even with seemingly similar samples (based on loading levels with the same functional groups), the adsorbate-surface interactions can still differ significantly due to subtle differences in local surface structure. This was demonstrated by comparing two phenyl-functionalized mesoporous silica materials with comparable amounts of functional groups but prepared by different functionalization routes. It was shown that QCM sorption studies could distinguish and quantify the differences between a sample where most phenyl groups are placed on the silica surface by post-synthesis treatment and a sample where phenyl groups are partially dispersed in the silica framework during synthesis.

## 8 **Special issue II: Direct-growth of $\text{Cu}_3(\text{BTC})_2(\text{H}_2\text{O})_3 \cdot x\text{H}_2\text{O}$ thin films on modified QCM-gold electrodes: Water vapor sorption measurements and determination of the heat of adsorption**

### 8.1 Introduction to metal organic frameworks and motivation of the study

Metal organic frameworks (MOFs) have been the subject of intensive investigation due to their unusual properties and their high potential as a new class of crystalline porous materials. These materials, resulting from the combination of metal-cations and organic linkers, often present well-defined accessible microporosity, large pore volume, and adjustable chemical functionality.<sup>[124]</sup> Many new structures have been synthesized, based mainly on the combination of metals and carboxylates.<sup>[125]</sup> MOFs as bulk materials have been investigated with respect to their sorption properties concerning gas storage, separation and purification.<sup>[126], [127]</sup>

The production of thin porous films opens new perspectives for potential applications of those materials, for example in the context of optical coatings, catalysts, or for sensor applications. Several synthetic schemes have been developed for the preparation of thin films, including the post-synthetic attachment of crystals to surfaces as a method to organise compact monolayers on a substrate, for example with zeolite crystals.<sup>[128], [129], [130], [131]</sup> On the other hand, biomineralisation<sup>[132], [133], [134]</sup> has inspired the direct growth of zeolite-type materials on self-assembled molecular layers thus offering the opportunity to control the orientation of the grown crystals.<sup>[135], [136]</sup> Recently thin, patterned films of MOF-5 on gold substrates were prepared on COOH-terminated self assembled monolayers (SAMs).<sup>[137]</sup>

As the focus of this special issue was the preparation and characterization of thin films of the porous copper 1,3,5-benzentricarboxylate open-framework  $\text{Cu}_3(\text{BTC})_2(\text{H}_2\text{O})_3 \cdot x\text{H}_2\text{O}$  (HKUST-1)<sup>[138]</sup> the synthesis and mainly the characterisation was done by my colleague Enrica Biemmi. Therefore the detailed synthesis route, formation of thin films as well as extended information about the structure of the HKUST material can be found in Mrs. *E. Biemmi* PhD thesis.<sup>[139]</sup>

The structural features of HKUST-1 make this material an attractive candidate for the design of chemically selective sensors. Furthermore, this unique structure features available coordination sites on the constituent Cu(II) centers which offer the potential

for selective adsorption of certain molecules. In the as-synthesized material, these sites are occupied by removable water molecules, and they can work as binding sites for the growth/attachment of the crystals on a SAM-modified surface. Therefore a larger variety of SAM's functionalities can be explored to prepare thin-films of the porous framework on gold surfaces.

## 8.2 Sample preparation

As the synthesis was performed by *E. Biemmi* only a brief overview about the sample preparation is given. The detailed bottom-up approach is described in reference [139]. A thin opaque layer of  $\text{Cu}_3(\text{BTC})_2$  was obtained by a self assembled layer of nanocrystals grown from a mother solution and deposited on a 11-mercaptoundecanol functionalized Au-electrode of a QCM-chip. Initially the chip was plasma cleaned (air oxygen plasma) followed by a treatment with 11-mercaptoundecanol ( $\text{HS}(\text{CH}_2)_{10}\text{CH}_2\text{OH}$ ). During the crystal growth from a separately prepared mother solution containing the precursor molecules ( $\text{Cu}(\text{NO}_3)_2 \cdot 2.5 \text{H}_2\text{O}$ ,  $\text{C}_6\text{H}_3(\text{COOH})_3$ ) the self assembly synthesis yielded a homogenous covered gold electrode. In figure 135 the proof is given that the non pre-treated reference QCM-chip did not show the formation of any crystalline  $\text{Cu}_3(\text{BTC})_2(\text{H}_2\text{O})_3$ . The morphology and the thickness of the grown film is displayed in figure 136.

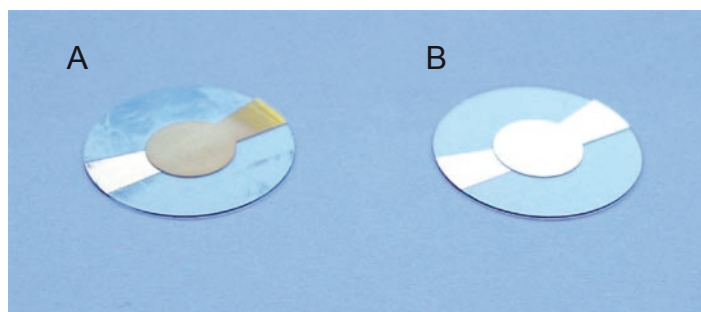


Fig. 135: QCM-devices after the layer growing step: opaque layer on the SAM-modified gold electrode (A) and empty reference chip (B). Photograph taken by E. Biemmi.

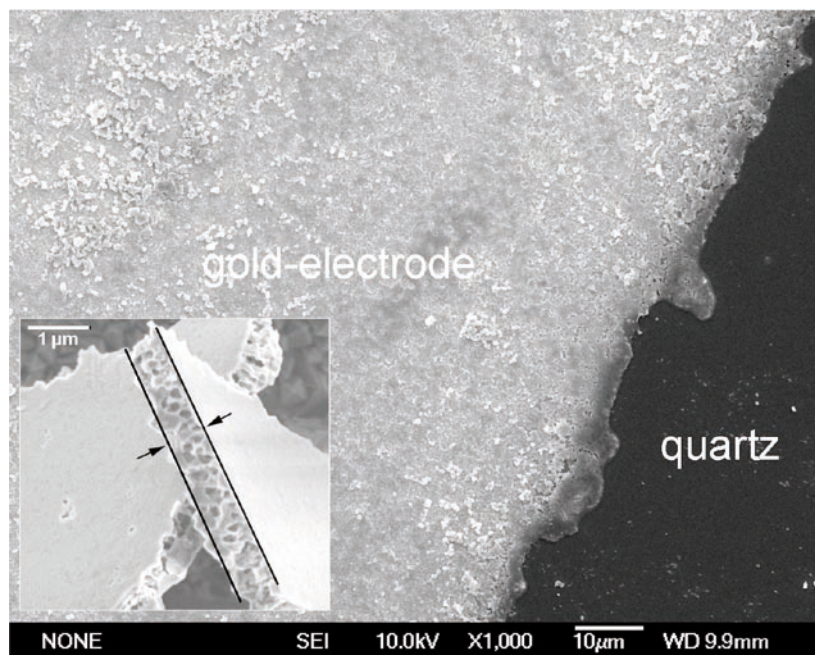


Fig. 136: Scanning-electron micrograph of a thin film of  $\text{Cu}_3(\text{BTC})_2$  on the gold electrode of a QCM-chip. The film thickness (ca. 600 nm) was directly measured on a scratch of the film, as shown in the inset. Image was taken by E. Biemmi.

### 8.3 X-Ray analysis and TGA experiments

The X-ray diffraction pattern (figure 137)<sup>[139]</sup>, compared with a simulated one obtained from the crystallographic data of HKUST-1, confirms the growth of a thin layer of  $\text{Cu}_3(\text{BTC})_2(\text{H}_2\text{O})_3 \cdot x\text{H}_2\text{O}$  on the QCM gold-electrode (see figure 135).

Thermogravimetric analysis was performed on a dried powder sample of  $\text{Cu}_3(\text{BTC})_2$  previously treated in humid atmosphere.<sup>[139]</sup> The thermogravimetric diagram (figure 138) shows a first weight loss of 31 % between room temperature (RT) and 150 °C. This weight loss can be assigned to the removal of the  $\text{H}_2\text{O}$  molecules present in the channels and coordinated to the metal centers of the MOF-structure, which corresponds to ca. 16 mmol  $\text{g}^{-1}$ . The empty framework of  $\text{Cu}_3(\text{BTC})_2$  is thermally stable up to 300 °C in synthetic air. In the next step (300 - 330 °C), a weight loss of 43% (63% referred to dry  $\text{Cu}_3(\text{BTC})_2$ ) is detectable that corresponds to the oxidative degradation of the two organic linker molecules per formula unit (theoretical weight loss from dry  $\text{Cu}_3(\text{BTC})_2$  of 64.6 %). A further increase of the temperature, above 350 °C, leads to the formation of  $\text{Cu}_2\text{O}$ .<sup>[139]</sup>

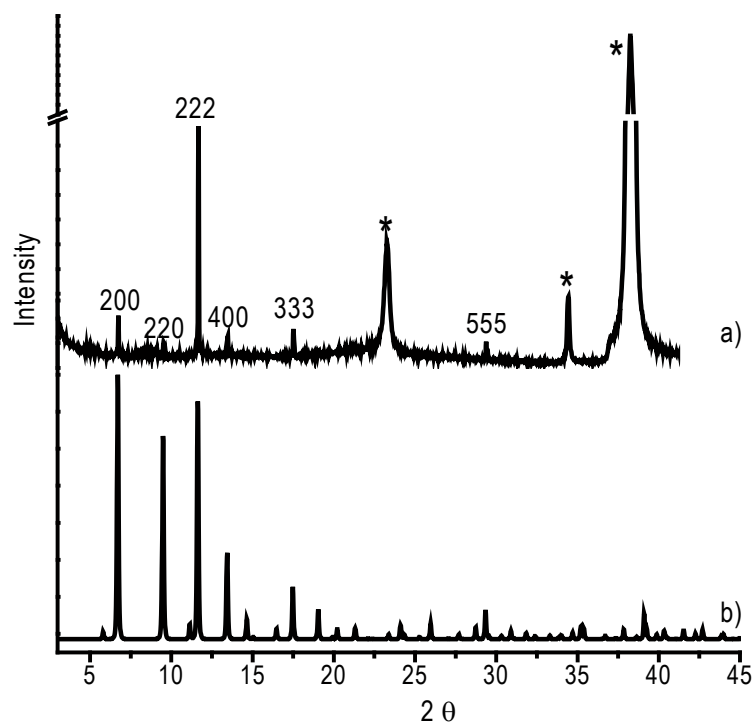


Fig. 137: X-Ray pattern of of sample  $\text{Cu}_3(\text{BTC})_2$  (A) and as simulated (B). Data recorded by E. Biemmi.

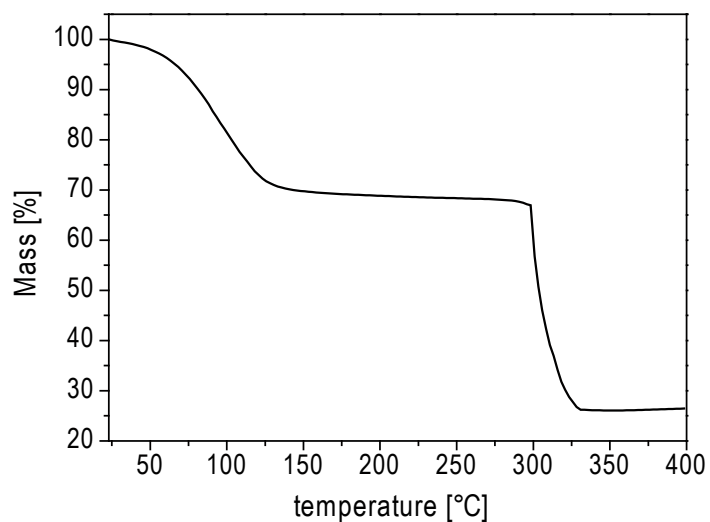


Fig. 138: Thermogravimetric data of sample  $\text{Cu}_3(\text{BTC})_2$ . Data recorded by E. Biemmi.



Raman spectroscopic investigations support the existence of a HKUST-1 structure. The detailed discussion of the experimental results can be found in reference [139].

#### 8.4 QCM sorption experiments with vaporized water

The QCM experiment was carried out analogous to previously investigated mesoporous and microporous siliceous samples as described in details on page 89 and following.

Figure 139 demonstrates the raw data obtained for water adsorption on  $\text{Cu}_3(\text{BTC})_2$ . As obvious, frequency fluctuations are apparent which are related to the higher measurement temperature of 328 K (heater fluctuations) and controller flow fluctuations ( $< 0.1\%$ ) of the corresponding MFC. The graph represents three adsorption steps with increasing partial pressures of toluene. It is worth to mention that the frequency equilibrates and is constant over a time period of 16.000 measurement points in maximum, respectively more than four hours. The desorption of toluene takes even longer compared to the adsorption process which is reflected in the observed shape of isotherms of non-closing adsorption and desorption branches.

At measurement temperatures above 328 K differences in specific values for the degree of coverage are diminishing at identical partial pressure for adsorption and desorption

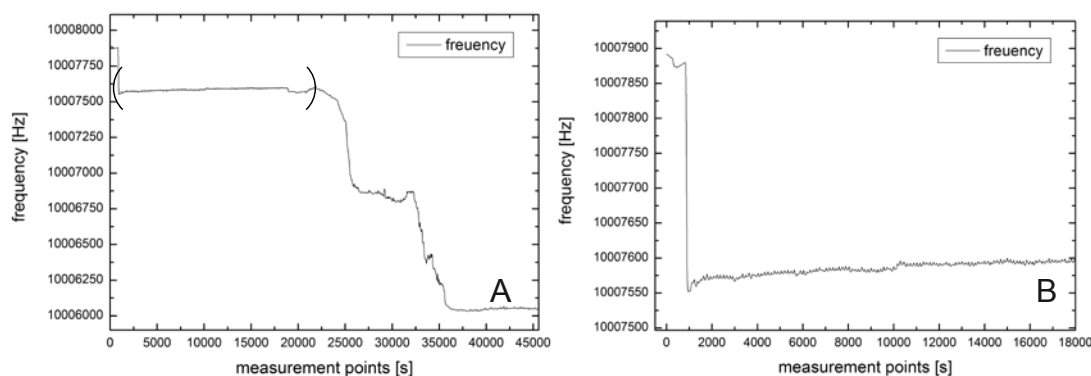


Fig. 139: QCM frequency raw data (cutout of three steps, A) of water adsorbing on  $\text{Cu}_3(\text{BTC})_2$  recorded at 328 K and magnified frequency deviation (B)

which corresponds to an increased kinetic energy thus reaching state of equilibrium within the preset time interval. In order to evaluate time constants which allow a complete thermodynamic reversibility the MOF coated chip was measured with extended time delays between each step. As figure 140 clearly delineates, time periods > 4 hours for each single step provoke redox reactions on the chip surface. It is assumed that elemental iron of the chip-holder clamp reacts with the copper rich MOF layer at hydrothermal conditions. Although there is no direct contact of the chip-holder and the coated gold electrode (borderline is emphasized in red) the redox reaction takes likely place making succeeding measurement impossible due to a destroyed MOF network. The partial pressure of the analyte was increased in sequential steps while the frequency shifts were recorded according to the procedure described starting on page 89. Considering the non-ideality of the adsorptive water vapor, the partial pressures were corrected considering Van-der-Waals behavior. The characteristic parameters  $a$  and  $b$  were taken from available literature data.<sup>[72]</sup>

In figure 141 the room temperature (294 K) isotherm collected with the QCM setup is compared to a reference measurement of a bulk sample synthesized at identical conditions as those used for the thin film, and recorded on an AUTOSORB-1 analyzer (Quantachrome Instruments). The isotherm shape can be classified as type II in the IUPAC classification. A comparison of the two measurements indicates a difference in

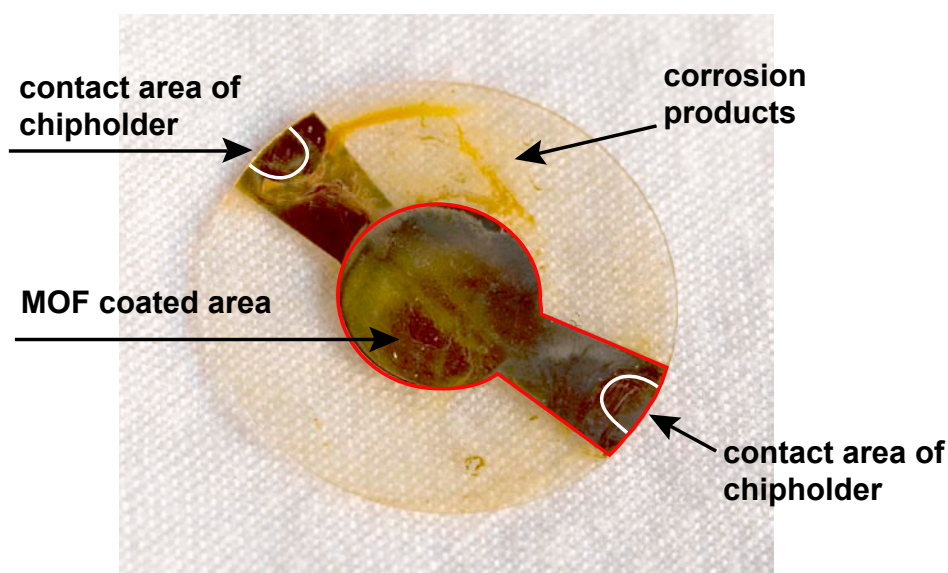


Fig. 140: Corroded MOF layer and redox reaction products after extended measurements at hydrothermal conditions

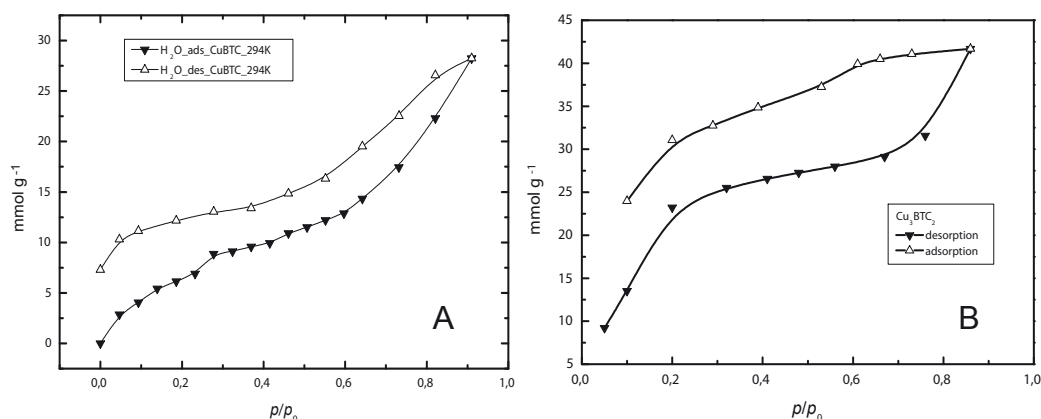


Fig. 141: Water sorption isotherms on  $\text{Cu}_3(\text{BTC})_2$  recorded at 294 K on a thin film with the QCM setup (A), and isotherm of a bulk sample measured with Autosorb-1 analyzer. Data (B) recorded by E. Biemmi.

the adsorbed amount  $\theta$  ( $\text{mmol g}^{-1}$ ). At a partial pressure of  $p/p_0 = 0.2$  during adsorption a loading of  $6.4 \text{ mmol g}^{-1}$  is observed, whereas at identical partial pressure the bulk measurement reveals a value of  $21.6 \text{ mmol g}^{-1}$ . The difference in sorption capacity is constant throughout the entire sorption isotherm. This discrepancy could be explained considering the difference in the two measurement principles (gravimetric and volumetric) and the fact that the calculations relative to the volumetric measurement are mainly based on ideal behavior of the water-vapor. Furthermore, no detailed information is available about the specific calculation steps and assumptions of the bulk measurements, e.g. amount of water film adsorbed on valves and tubes. However, these large discrepancies need to be addressed in additional investigations.

The sorption data collected on the QCM setup at room temperature are confirmed with results from the TGA measurement (compare figure 138). The amount of water adsorbed at  $p/p_0 = 0.8$  is approximately  $16 \text{ mmol g}^{-1}$ , whereas from the TGA data around  $16 \text{ mmol g}^{-1}$  of water (weight-loss 31%) are desorbed between RT and  $130^\circ\text{C}$ . Considering that the bulk sample used for the thermogravimetric analysis was pretreated under an atmosphere of about 80% relative humidity ( $p/p_0 = 0.8$  at  $T = 294 \text{ K}$ ), the two results are consistent.

The isotherm shows a distinctive increase in coverage in the adsorption branch up to  $p/p_0 = 0.2$ . This behavior could be explained considering the water molecules coordinated to the metal-cation that are energetically different from the physisorbed ones.

## 9 Adsorption of organic vapors in thin films of nanosized microporous and mesoporous materials measured with surface acoustic waves

A very important factor regarding any potential sensor application is the knowledge about the characteristic adsorption isotherm of the analyte gas or vapor.

Several techniques were developed, for example nitrogen sorption apparatus, calorimetric and gravimetric analysis, temperature-programmed desorption (TPD) and micro balance sorption measurements to characterize the materials with regards to their sorption properties.<sup>[112], [140], [141]</sup> In recent experiments it has been demonstrated that the QCM technique is also an appropriate tool to investigate sorption properties of porous materials. In typical experiments, gram or milligram amounts of the sample material are usually used and as a result the measurement takes several minutes or even days due to diffusion limitations. The aim of this work was to develop a new experimental method based on surface acoustic wave (SAW) devices to determine the sorption isotherms of porous materials at a very low degree of material loading down to the low  $\mu\text{g}$  range. Besides small sample amounts used, nanosized crystals of the sensing porous materials were employed to avoid any diffusion limitations.<sup>[142]</sup>

The project was carried out as collaboration with the physics department of the LMU Munich (Prof. Kotthaus) and funded by the Bayerische Forschungstiftung (ForNano<sup>[143]</sup> project).

### 9.1 Generation of surface acoustic waves

Surface acoustic waves were systematically described for the first time by Lord Rayleigh in 1885.<sup>[144]</sup>

Elastic acoustic waves are commonly transversal waves (pressure waves) or longitudinal waves (shear waves) whereas both types can be simultaneously observed. Figure 142 schematically depicts those two types of acoustic waves. Transversal waves are best described with density fluctuations of the materials surface, illustrated with dark (high density) and bright (low density) areas. Longitudinal waves in contrast, are shear waves evoked by dislocations of surface material.

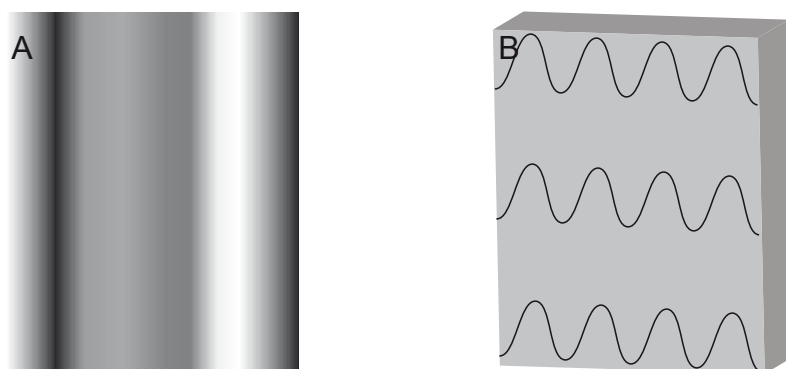


Fig. 142: Scheme of transversal (left) and longitudinal acoustic wave

The stimulus of acoustic waves occurs with an appropriate deformation of the piezoelectric material, the precondition of SAW active materials (compare piezoelectricity on page 79). As basically explained in previous chapters, so called interdigital transducers (IDT) are necessary to provoke an elastic surface acoustic wave. In figure 143 the SEM image and a schematic illustration of the experimentally used surface acoustic wave IDTs is shown. The dimension of the finger period is usually settled in the range of 5 - 100  $\mu\text{m}$  for commercially available SAW devices. In this work the distance between IDT fingers was even lowered down to 2  $\mu\text{m}$  in order to enable resonance frequencies  $>110$  MHz (basic vibrational mode of the used SAW prototype chip). At

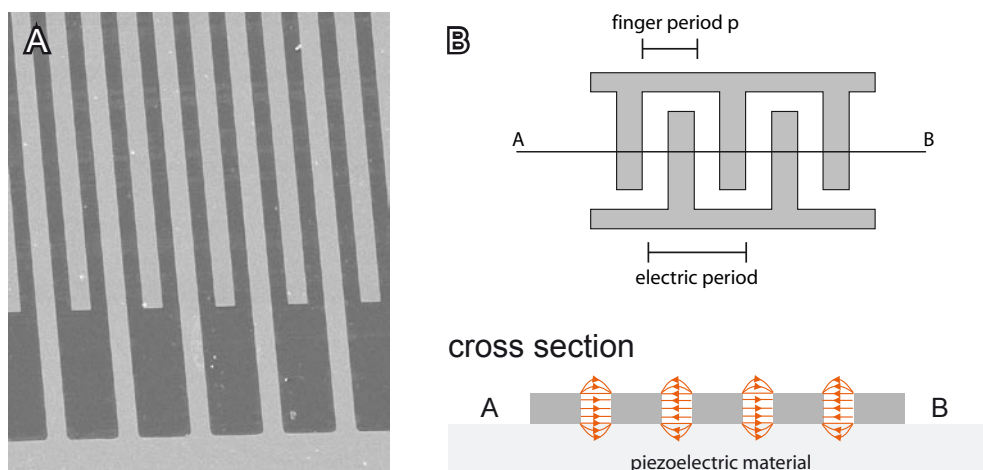


Fig. 143: SEM image of IDT (A) and sketch with cross section of a metallic IDT (B)

higher frequencies a smaller acoustic wave front is expected to be generated thus in principle offering the possibility to decrease the size of the chip design and the area of the sensitive coatings. The finger period of the IDT design determines the resonance frequency of the SAW according to equation (29), whereas  $f_0$  is the fundamental operating frequency,  $m$  the number of the stimulated overtone,  $v_m$  the phase velocity and  $p$  the mentioned periodicity of the IDT fingers.

$$f_0 = m \frac{v_m}{p} \quad (29)$$

In figure 144 a typical SAW signal is displayed. The fundamental operating frequency is 110 MHz. Additional “side” signals are related to several also provoked but unspecified wave modes, distinguishable from the SAW signal. The elastic surface wave penetrates the bulk material only for one wavelength, roughly. For a 110 MHz SAW chip ( $\text{LiNbO}_3$ ,  $128^\circ$  rot cut) the wavelength and the surface penetration depth can be estimated to  $31 \mu\text{m}$ , approximately.

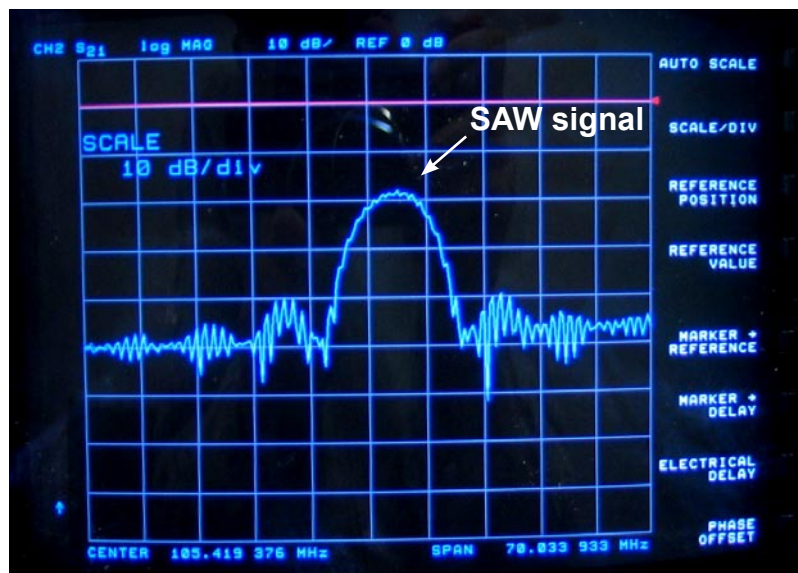


Fig. 144: Surface acoustic wave signal

## 9.2 SAW device and sample deposition

The SAW technique was utilized to realize measurements with small sample amounts. The SAWs velocity strongly depends on the adsorbed mass on the surface where the wave propagates (figure 145). The 1.8 mm<sup>2</sup> delay line sensing area was coated with the colloidal sample material. The sensing material, e.g. silicalite-1 nanocrystals, covers a square area of 600 μm by 3000 μm. The colloidal nanoparticles were spin-coated onto the sensor delay line on a lithographically opened small window of the delay line, resulting in a thin layer of porous particles and subsequently heated at 673 K for 24 h (0.5 °C min<sup>-1</sup>) to remove organic molecules from the synthesis route.

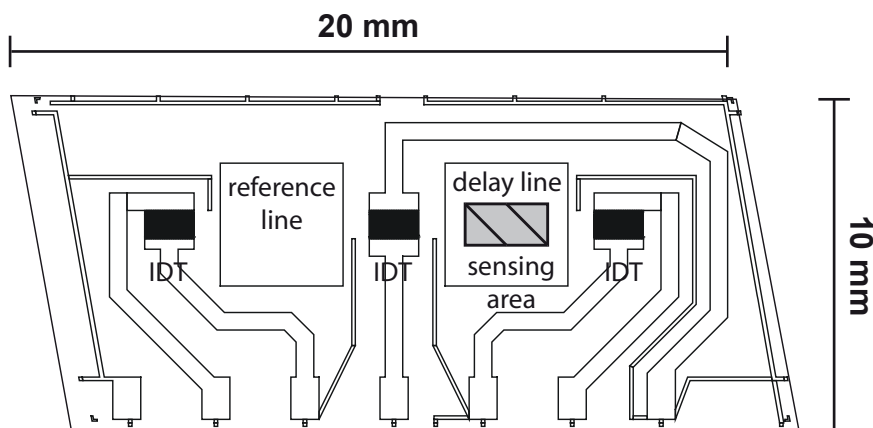


Fig. 145: Schematic sketch of the used prototype SAW-chip

In contrast to earlier publications, the phase shift of the reference delay line with respect to the covered sensor delay line rather than frequency changes were recorded.<sup>[145]</sup>

The additional mass of the adsorbed gas molecules causes a slight change in velocity of the delay line SAW, which is monitored as phase shift between the empty reference line and the coated and sensing delay line. It was shown that the chip design with fan-type IDTs is capable of generating a SAW at different vertical positions, thus addressing certain lines of the coated material.<sup>[146]</sup> The constructed sample-chip holder was heated up to 200 °C to degas the porous material before and after the measurement to ensure complete adsorption and desorption processes. Additionally, the ability of measuring at different temperatures is required to obtain thermodynamic values for

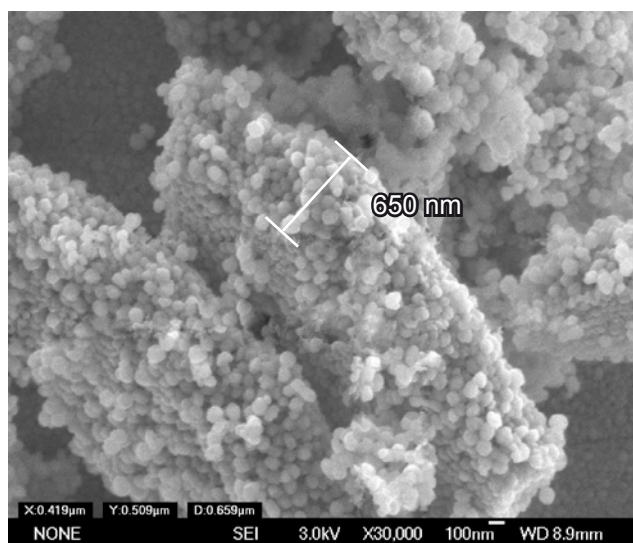


Fig. 146: SEM image of silicalite-1 crystals, taken after scratching the sensing layer

the subsequent determination of the heat of adsorption. The SAW chip<sup>39</sup> runs at the fundamental operating frequency of 110 MHz but the functionality has also been demonstrated at the 3rd overtone at around 330 MHz, depending on the chip individually used in the experiment.

The adsorption properties are strongly influenced by the deposited nanosized particles,

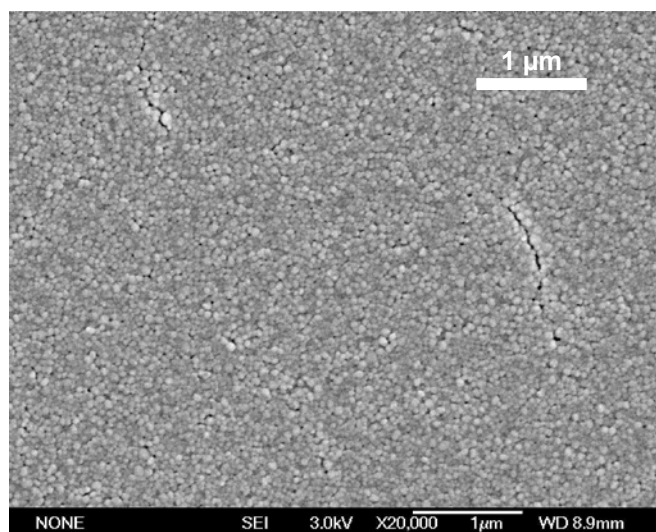


Fig. 147: SEM image of sample Sil-1 layer

<sup>39</sup> Developed by Alexander Müller and produced by the Advalytix AG, Eugen-Sänger-Ring 4, 85649 Brunnthal, Germany.





#### 9.4 Measurement chamber

One of the challenges of the experimental setup design was to construct a measurement chamber with minimal dead volume and suppression of turbulent flows which are contra productive in terms of phase stability. As illustrated in figure 149 the whole measurement cell is made of inert material Teflon (light blue). To contact the golden contact pads of the SAW-chip (green colored), spring-loaded pins are used. Figure 150 shows the high temperature resisting circuit board<sup>40</sup> with Au coated spring loaded contact pins and the pathway to the high frequency external connectors. The inner aluminium block ensures fast heat transfer and can be additionally heated ( $T_{\max} = 185\text{ °C}$ ) and cooled ( $T_{\min} = 15\text{ °C}$ ) with heating and water-cooling cartridges. The total dead volume inside the chamber is  $10.5\text{ cm}^3$ . The gas-flow system and the measurement setup are schematically displayed in figure 151. Several pre-dried gases can be connected to digital mass flow controllers (MFC). A digital control unit operated by a computer via RS232 bus controls the MFCs themselves (details on page 98).

In every experiment evaporated liquid nitrogen was used as pure carrier gas. The radio frequency was applied time triggered and pulsed in order to avoid recognition of false signals due to crosstalk of the electromagnetic wave which is transmitted at about  $3 \cdot 10^8\text{ m s}^{-1}$ . The acoustic wave instead propagates with a velocity depending on the crystal cut in the range between  $3500 - 4000\text{ m s}^{-1}$ . For example, a Y-cut ( $128^\circ$ )

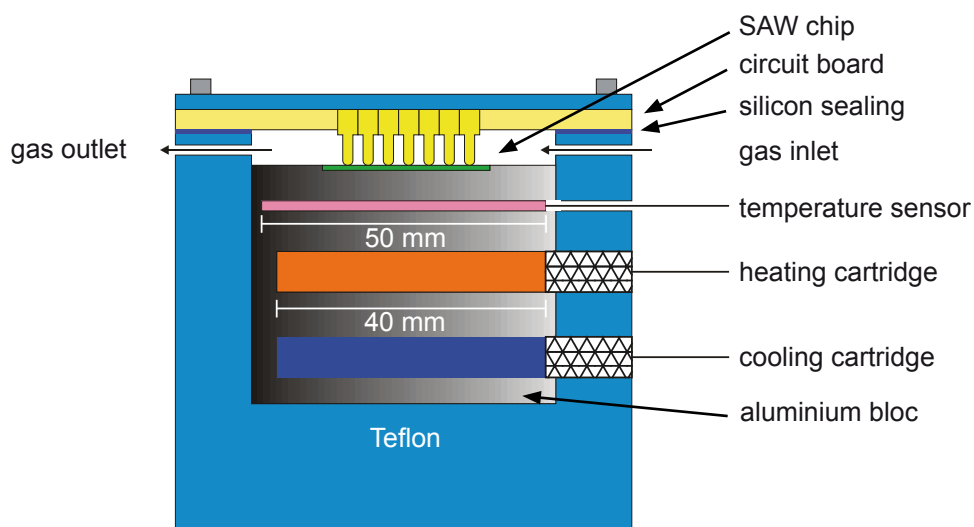


Fig. 149: Scheme of sorption measurement cell (sideview)

<sup>40</sup> Advanced Dielectric Division, 136 Coonbrook Road, Petersburg, NY 12138, USA.

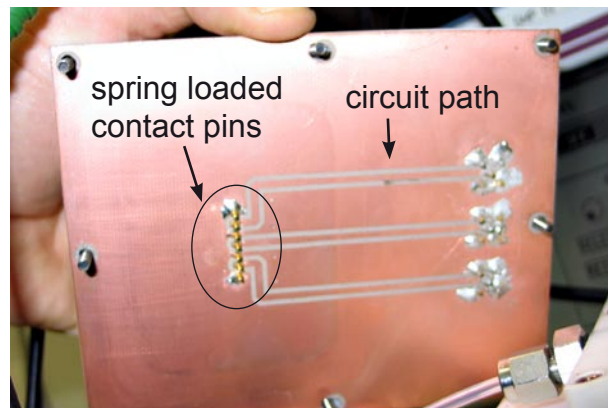
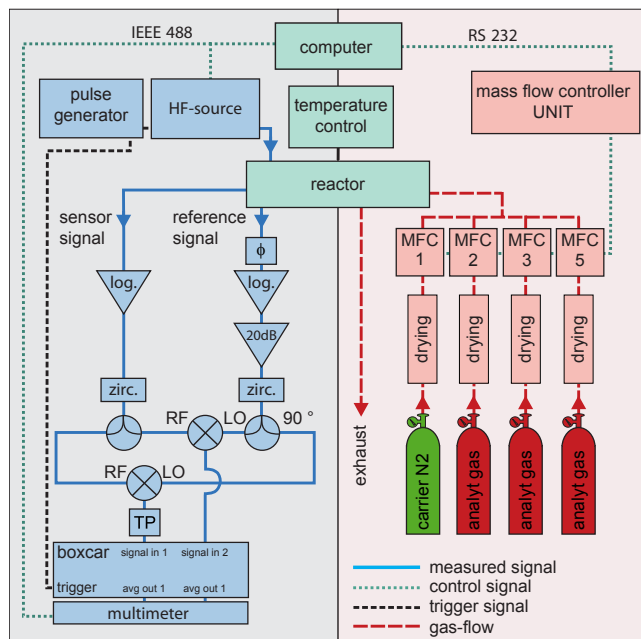


Fig. 150: High temperature resistant circuit board

LiNbO<sub>3</sub> SAW device excites surface acoustic waves with a velocity of 3490 m s<sup>-1</sup> in z-direction.<sup>[147]</sup> Due to different velocities of the electromagnetic wave and the SAW, the experiment was carried out time-triggered in a way that only the acoustic wave signal was recorded. The radio frequency is applied at  $f_0 = 110$  MHz, the fundamental vibration of the LiNbO<sub>3</sub> chip. The SAW is evoked from the median IDT to the reference line and the sensing delay line.

Fig. 151: Measurement setup displayed as flow-chart<sup>[146]</sup>

The effective relative phase shift  $\Delta\phi/\phi$  between the mentioned reference and delay line SAW signals due to mass adsorption is proportional to the relative change in velocity  $\Delta v/v$ , which itself is proportional to the additional surface mass density  $\rho_m$  (see equation (30)).

$$\frac{\Delta\phi}{\phi} = \frac{\Delta v}{v} = c_m f_0 \rho_m \quad (30)$$

In order to calculate the additional mass density  $\rho_m$  the total phase for the delay line has to be determined. By applying equation (31) the desired phase  $\phi$  is obtained.

$$\phi = 2\pi \frac{l}{\lambda} \quad (31)$$

The desired value mmol analyte gas per gram adsorbent material ( $\theta$  in mmol g<sup>-1</sup>) is calculated with equation (32), whereas  $M_a$  is the molar weight of the analyte and  $m_{sub}$  the mass in g cm<sup>-2</sup> of the substrate material deposited on the delay line. The deposited

$$\theta = \frac{\Delta\phi}{2\pi \frac{l}{\lambda} c_m M_a m_{sub}} \quad (32)$$

mass per cm<sup>-2</sup> was obtained from the thickness of the applied layer (650 nm, see figure 147) multiplied by the estimated overall density of the deposited zeolite layer. This specific density was estimated from the density of silicalite-1 (1,76 g cm<sup>-3</sup>)<sup>[169]</sup> and an assumed closed sphere packing factor of 0.74. The material sensing parameter of the piezo-electric substrate  $c_m$  is 10<sup>-6</sup> s cm<sup>2</sup> g<sup>-1</sup>.

The isotherms could be obtained by applying the parameters given in table 43. With

the described method and the designed chip, velocity changes of the SAW in the range of  $\Delta v/v \approx 0.3 \cdot 10^{-6}$  could be monitored, resulting in a sensitivity of  $1 \cdot 10^{-9} \text{ g cm}^{-2}$ .

frequency [Hz]	$110 \cdot 10^6$
thickness of material layer [m]	$6.5 \cdot 10^{-7}$
density of silicalite-1 layer [ $\text{g cm}^{-3}$ ] ( $\rho_{\text{silicalite}} = 1.76 \text{ g cm}^{-3}$ ) x 0,74 (sphere packing assumed)	1.30
surface mass density [ $\text{g cm}^{-2}$ ]	$7.55 \cdot 10^{-5}$
material constant $c_m$ [ $10^{-6} \text{ s cm}^2 \text{ g}^{-1}$ ]	$1 \cdot 10^{-6}$
molar weight butane [ $\text{g mol}^{-1}$ ]	58.12
molar weight propane [ $\text{g mol}^{-1}$ ]	44.09
molar weight propene [ $\text{g mol}^{-1}$ ]	42.08
molar weight 1-butene [ $\text{g mol}^{-1}$ ]	56.11

Tab. 43: Parameters used for the determination of isotherms

The raw data recorded, the relative phase shift  $\Delta\phi/\phi$  versus time, is exemplarily shown in figure 152. The graph illustrates the adsorption of iso-butane on sample Sil-1 deposited as thin film on the SAW chip. The zero-line corresponds to the undisturbed system with an exclusive carrier gas flow of nitrogen at a flow rate of  $1000 \text{ ml min}^{-1}$ . At certain points (15 s, 40 s, 70 s, 90 s and 120 s) iso-butane is released into the measurement chamber with increasing partial pressures at each dosing step. Therefore, the amount of adsorbed gas molecules in equilibrium increases. With increased mass loading the velocity of the SAW decreases and a phase shift between the delay line (covered with sample Sil-1) and the reference delay line (empty) is observed. It was experimentally proven that there is no significant adsorption on an empty sensor delay line.

According to figure 148, the measurement principle is based on the following equations in order to monitor the desired  $\Delta\phi/\phi$  signal.

The mixer device multiplies both the reference delay line and the delay line signals (equation (33)).

The radio frequency is applied on the transmitting central IDT. Both  $t_1$  and  $t_2$  are equal.

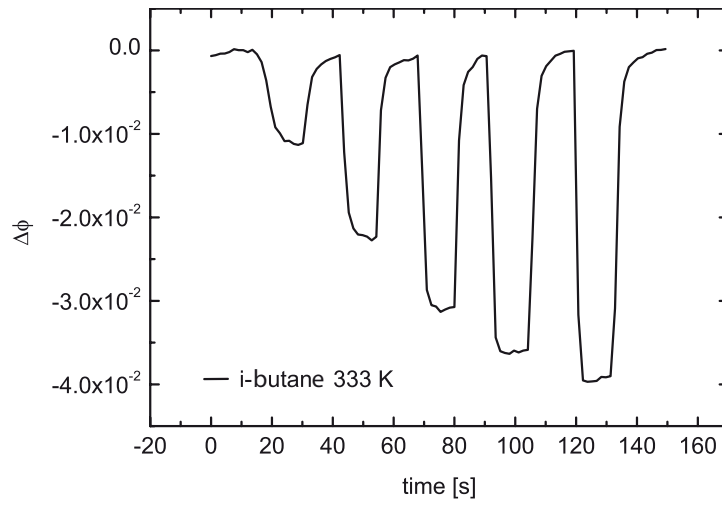


Fig. 152: Relative phase shift of iso-butane adsorbing on sample Sil-1

$$\begin{aligned} \sin A(\omega_1 t_1 + \varphi_1) \cdot \sin B(\omega_2 t_2 + \varphi_2) = \\ \frac{1}{2} AB [\cos(\omega_1 t_1 + \varphi_1 - \omega_2 t_2 + \varphi_2)] - \frac{1}{2} \cos[\omega_1 t_1 + \varphi_1, \omega_2 t_2 + \varphi_2] \end{aligned} \quad (33)$$

The high frequency part  $\varphi_1 + \varphi_2$  in equation (34) is filtered out by a low-pass filter. In equation (34) it is also valid  $\omega_1 = \omega_2$ .

$$\begin{aligned} \stackrel{t_1=t_2}{=} \frac{1}{2} AB [\cos(\omega_1 - \omega_2)t + \varphi_1 - \varphi_2] - \frac{1}{2} \cos[(\omega_1 + \omega_2)t + \varphi_1 + \varphi_2] \end{aligned} \quad (34)$$

According to equation (35) the recorded signal is proportional to  $\cos \Delta\varphi$ .

$$\stackrel{\omega_1=\omega_2}{=} \frac{1}{2} AB \cos \Delta\varphi \quad (35)$$

## 9.5 Sorption of gaseous C<sub>4</sub>-hydrocarbons

According to the described method, isotherms of n-butane, iso-butane and 1-butene were recorded. Due to the limited capability of the flow system, it was not possible to record data sets beyond partial pressures of 10 kPa. Additionally, it has to be mentioned that below a nitrogen flow rate of 500 ml min<sup>-1</sup> phase shift fluctuations became apparent and the gained data could not be used for further calculations.<sup>[146]</sup> After each single measurement the whole gas flow system including the measurement cell was purged with pure evaporated liquid nitrogen for a minimum of 4 h at a flow rate of 2000 ml min<sup>-1</sup> and additionally the chip was heated on a external hotplate at 300 °C under nitrogen flow. This procedure is valid for all adsorption measurements of hydrocarbons.

### 9.5.1 Sorption of n-butane on sample Sil-1

On the right part of figure 153 the partial pressure is logarithmically scaled to demonstrate the recorded measurement points in the pressure range from 0.01 kPa to 10 kPa. The data points were taken at different temperatures to obtain the values for the heat of adsorption. As one would expect from the micro porous sample material Sil-1 (zeolite silicalite-1), a type I isotherm is observed, which can be described with the *Langmuir*

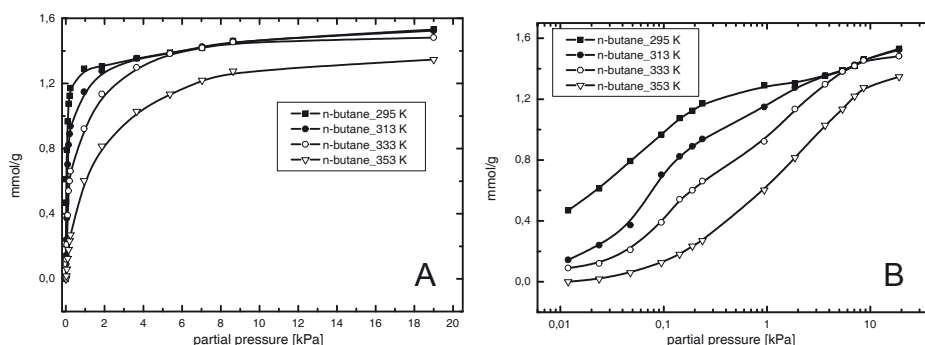


Fig. 153: Sorption isotherm of n-butane on silicalite-1 at linear (A) and logarithmic scale (B)

model (equation (36)). The recorded isotherm is in good agreement with literature data.<sup>[110], [111]</sup>

$$\theta = \frac{Kp}{1 + Kp} \quad (36)$$

Due to the narrow pore opening of 5.1 Å x 5.5 Å [100] and 5.3 Å x 5.6 Å [010] the silicalite-1 zeolite<sup>[109]</sup> adsorbs 1.3 - 1.4 mmol n-butane per gram in the low pressure regime up to 6 kPa, respectively  $p/p_0 = 0.03$  at  $T = 293$  K and the micropores are filled. Higher partial pressures  $> 20$  kPa ( $p/p_0 > 0.1$ ) are not reachable due to technical limitations of the flow system to ambient pressure (100 kPa in maximum). As stated in earlier publications, n-butane is preferentially adsorbed in the channel system, not in the intersections and the amount of adsorbed molecules is strongly dependent on the length of the zeolite channels and adsorbent molecular size.<sup>[112], [113], [148], [149]</sup>

As presented on page 161 the isotherm of n-butane adsorbing on nanosized silicalite-1 (sample Sil-1) was confirmed by QCM measurements. The maximum sorption capacity as well as the thermodynamic value of the heat of adsorption match the results obtained from gravimetric sorption experiments performed with the QCM system.

### 9.5.2 Sorption of iso-butane on sample Sil-1

A different situation arises from the sorption of iso-butane. The isotherm, displayed in figure 154, can best be described with a dual-site Langmuir model.<sup>[150]</sup>

To take into account the dimple in the isotherm, several approaches demonstrate the dual-site adsorption behavior.<sup>[149]</sup> Related to two distinguishable adsorption coordinates, the zigzag and the straight channels and the intersections in between, iso-butane can adsorb on energetically distinguishable sites. *Zhu et al*<sup>[151]</sup> propose that the differences between the zigzag and the straight channels is negligible. In contrast, the enthalpy difference between the channels and the intersections is obviously detectable.



Referring to figure 154, at low  $p/p_0$  values, mainly the four intersections per unit cell are occupied. While increasing the partial pressure of the branched alkane the isotherm reaches a plateau indicating that all intersections are filled. Above that critical  $p/p_0$  value the two channel systems are filled. Significant less heat of adsorption is released by filling the channel system indicated by a step in the isotherm.<sup>[148]</sup>

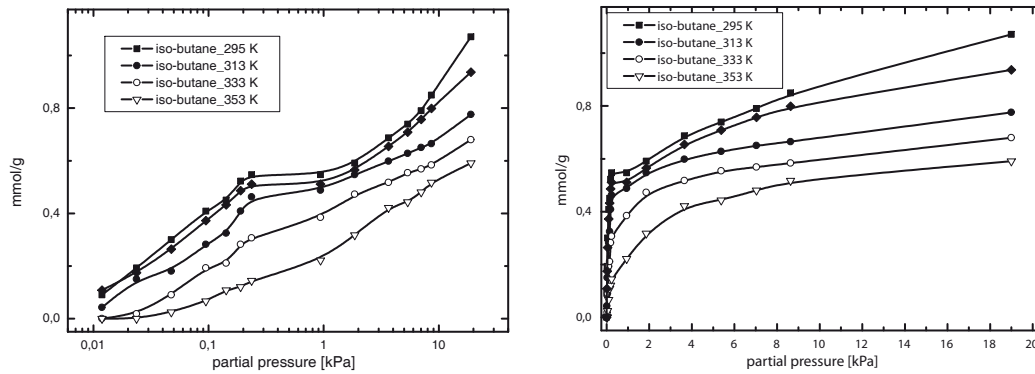


Fig. 154: Adsorption isotherms of iso-butane on silicalite-1

According to reference [148], iso-butane isotherm on silicalite-1 can be described with equation (37).<sup>[150]</sup>

$$\theta = \theta_c^{sat} \frac{K_c p}{1 + K_c p} + \theta_i^{sat} \frac{K_i p}{1 + K_i p} \quad (37)$$

According to that relationship,  $\theta$  is the amount of adsorbed molecules per unit cell,  $K_c$  and  $K_i$  the equilibrium constants for the adsorption in the intersections and channels, respectively. The parameters  $\theta_c^{sat}$  and  $\theta_i^{sat}$  correspond to the maximal possible loading of the sorbent molecules.

Further details of theoretical investigation on sorption of hydrocarbons on zeolites can be found in the literature.<sup>[152], [153], [154]</sup>

### 9.5.3 Signal answer time

A magnified graph of the raw data (see figure 155) shows a rapid response to concentration changes (purging with nitrogen or increasing partial pressure of the analyte gas) within 5-15 seconds due to the very thin layer of silicalite-1 and the nanosized crystals itself. Therefore diffusion limitations of mass transport are of minor priority compared to former experiments.<sup>[111]</sup>

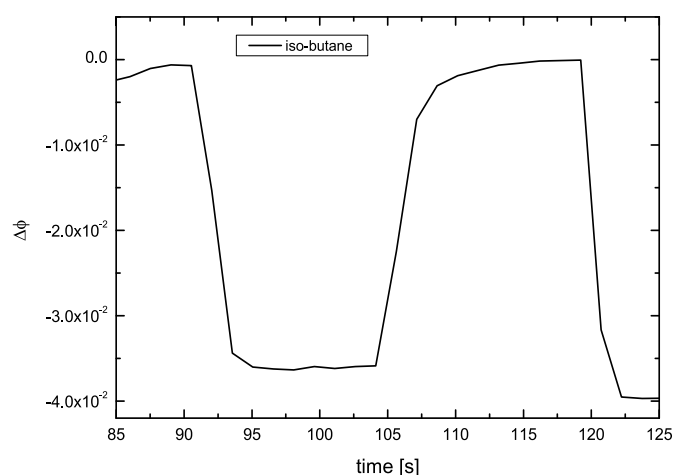


Fig. 155: Magnified graph of raw data  $\Delta\phi$  vs. time in seconds

### 9.5.4 Heat of adsorption

The measurements were performed at different temperatures to determine the isosteric heat of adsorption (compare figure 153). At specific coverages of 0.25 mmol g<sup>-1</sup>, 0.5 mmol g<sup>-1</sup> and 1.0 mmol g<sup>-1</sup> of the analyte gases,  $\ln p$  versus  $T^{-1}$  was plotted.

According to equation (28), the isosteric heat of adsorption for n-butane and iso-butane adsorbing on silicalite-1 could be acquired. Table 44 exhibits the heat of adsorption data from this work and an extensive comparison with available literature data. The obtained values of -52 kJ mol<sup>-1</sup> for n-butane and -49 kJ mol<sup>-1</sup> for iso-butane are in good agreement with literature data.

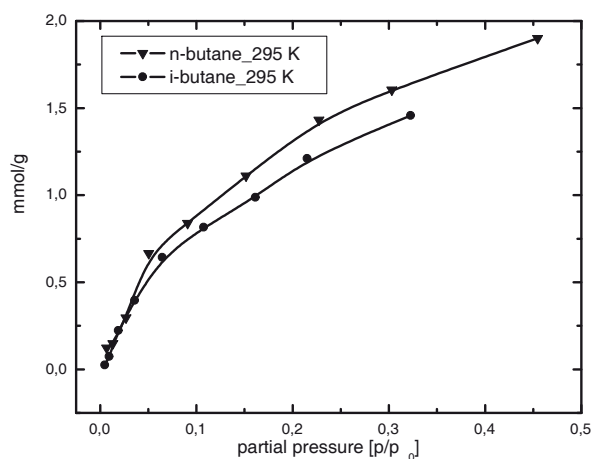
[kJ mol <sup>-1</sup> ] $-\Delta H_{ads}^0$	this work	literature data <sup>[106], [107], [108], [109], [110], [111], [112], [113], [114]</sup>
n-butane	52	48 - 58
i-butane	49	47.5 - 54.8

Tab. 44: Heat of adsorption of n- and iso-butane adsorbing on sample Sil-1

### 9.5.5 Sorption of n-butane and iso-butane on sample QCM-E

Isotherms of n-butane and iso-butane on mesoporous sample material QCM-E were recorded with the described experimental setup. In figure 156 the adsorption of n-butane and iso-butane on sample QCM-E material are displayed. Related to the vapor pressure of n-butane (222 kPa) and iso-butane (319 kPa) at 295 K it was not possible to measure beyond relative pressures  $p/p_0 = 0.45$ , respectively 0.33. The graph represents typical type IV isotherms for mesoporous materials in the pressure range up to  $p/p_0 = 0.45$ .

The high internal surface of sample QCM-E is not capable to distinguish between the linear and the branched alkane like the zeolite silicalite-1. This strongly indicates that the adsorption sites are randomly occupied inside the pores.

Fig. 156: Adsorption isotherms of C<sub>4</sub>-alkanes adsorbing on QCM-E

### 9.5.6 Sorption of 1-butene on sample Sil-1

Besides sorption experiments with n-butane and iso-butane adsorbing on sample Sil-1, the adsorption behavior of 1-butene was investigated to evaluate the reproducibility and reliability of the surface acoustic wave technique.

Figure 157 displays the adsorption branch of the isotherm at 295 K. No remarkable differences are detectable between the alkene and the alkane (compare figure 153 and 157). The additional  $\pi$ -electron system of the alkene has no impact on the maximum sorption capacity of the internal surface of the matrix material. At a partial pressure of 5 kPa and a coverage of  $1.6 \text{ mmol g}^{-1}$  of 1-butene one can assume that all micropores are filled.

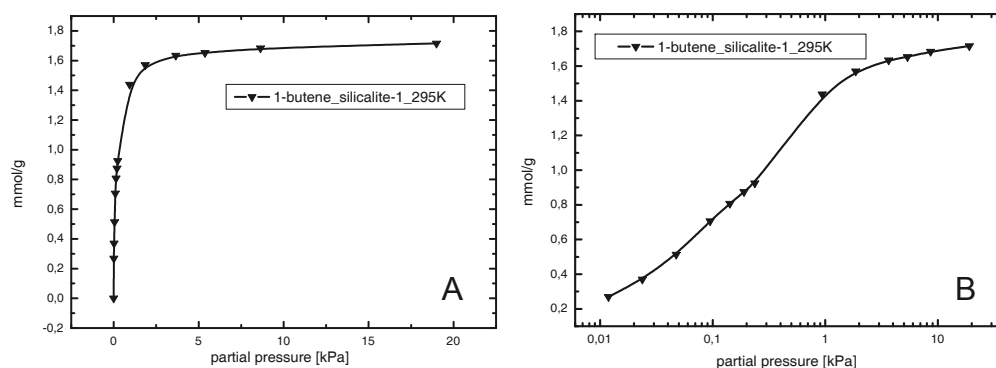


Fig. 157: Sorption of 1-butene on silicalite-1 at linear scale (A) and log scale (B)

### 9.5.7 Conclusion sorption of $C_4$ -alkanes

In good agreement with literature data<sup>[150]</sup>, the maximum amount of adsorbed n-butane ( $1.3 - 1.4 \text{ mmol g}^{-1}$ ) is already reached at a partial pressures around 20 kPa. Based on the parameters and assumptions made as listed in table 43, the volume of  $1.17 \mu\text{m}^3$ , respectively a layer of  $1.36 \mu\text{g}$  zeolite is sufficient to record sorption isotherms and determine the isosteric heat of adsorption of n-butane and iso-butane.

The amount of used coating material thus is a factor of  $10^5$  lower compared to the tapered element oscillating micro balance (TEOM) technique, in details described elsewhere.<sup>[151]</sup> In terms of time constants, the crystal size differences play a major role.

Diffusion takes place at a time scale of seconds compared to 1-5 min together with the TEOM technique with an average crystal size of  $100 \cdot 50 \cdot 50 \mu\text{m}$ . Furthermore, the TEOM method utilizes a relatively high total amount of 47 mg per individual sample.

## 9.6 Sorption of gaseous $\text{C}_3$ -hydrocarbons

At identical experimental parameters the isotherms of certain gaseous  $\text{C}_3$ -hydrocarbons were recorded. Thereby, the same SAW-devices were applied as used during investigations of  $\text{C}_4$ -hydrocarbons. Prior to any sorption experiment the coated  $\text{LiNbO}_3$  chip was heated and simultaneously purged with nitrogen to get rid of adherent volatile compounds (details on page 204).

### 9.6.1 Sorption of propane on sample Sil-1

The reliability of the developed SAW sensor design was also demonstrated by sorption experiments with the analyte gas propane. In figure 158 the adsorption isotherm of n-propane up to a partial pressure  $p = 0.3 \text{ kPa}$ , respectively  $p/p_0 = 0.11$  obtained with the SAW technique is shown.

To compare the experimental data with literature data<sup>[111]</sup>, the values of the isotherms given in molecules per unit cell were converted into mmol propane per gram sample material Sil-1. In order to calculate these values, the parameters given in table 45 were

density [ $\text{g cm}^{-3}$ ]	1.76 <sup>[163]</sup>
unit cell parameters [ $\text{m}$ ] <sup>[94]</sup>	$a = 20.09 \cdot 10^{-10}$ $b = 19.738 \cdot 10^{-10}$ $c = 13.142 \cdot 10^{-10}$
volume [ $\text{m}^3$ ]	$5.211 \cdot 10^{-27}$

Tab. 45: Physical and crystallographic data of silicalite-1

applied.

In figure 159 the comparison between the amount of adsorbed propane per gram silicalite-1 and literature data is displayed.<sup>[151]</sup> Due to the limitations of an open experimental system, it was not possible to record data points beyond a partial pressure of 0.3 kPa. At a partial pressure of 0.01 kPa, respectively 100 ppm of propane, a phase shift signal of  $\Delta\phi = 1.23 \cdot 10^{-3}$  is observed.

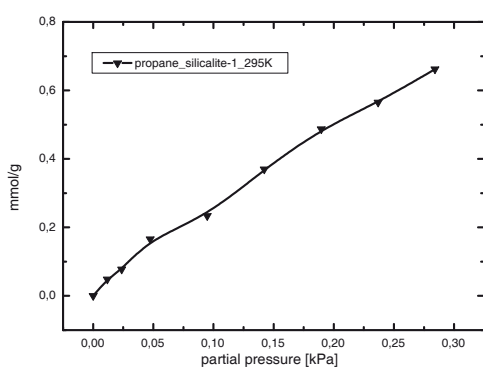


Fig. 158: Adsorption of propane on sample Sil-1

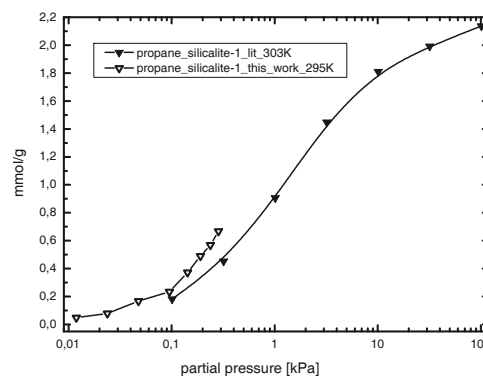


Fig. 159: Adsorption of propane on sample Sil-1 (open triangles) and literature data (closed triangles)<sup>[151]</sup>

It is obvious, that the data in this work reveals a slightly higher loading of propane compared to the literature data taken from *Zhu et al.*<sup>[151]</sup> However, the sorption investigations at room temperature were carried out at a 8 K lower temperature which is very likely responsible for higher coverages at identical partial pressures.

### 9.7 Conclusion of sorption experiments carried out with the developed SAW device

In previous chapters sorption isotherms were obtained with the gravimetric QCM technique. The demands of an ongoing miniaturization and the ability to establish a wireless read out procedure lead to the development of surface acoustic wave sensor systems. In this work, proof of concept with a prototype SAW chip design based on phase shift changes due to additional adsorbed mass was provided. During measurements no environmental influences on the surface acoustic wave like temperature, pressure changes or electromagnetic interferences were observed. With sample amounts in the low  $\mu\text{g}$  range (e.g. 1.36  $\mu\text{g}$  for sample Sil-1) adsorption isotherms for light alkanes and alkenes adsorbing on pure siliceous zeolite silicalite-1 within ambient pressure parameters were obtained and validated by comparison with literature data and QCM sorption experiments. The recently discovered dual-site *Langmuir* model for iso-butane adsorbing on silicalite-1 was likewise experimentally confirmed.

Evaluating thermodynamical data as the isosteric heat of adsorption, determined by the application of *Clausius-Clapeyrons* equation, yield comparable results for n-butane (52  $\text{kJ mol}^{-1}$ ) and iso-butane (49  $\text{kJ mol}^{-1}$ ) sorbing on silicalite-1 in consistence with literature data. Furthermore, it could be shown, that the nanosized porous sample material and the small sample amount is advantageous in terms of adsorption kinetics, as proven with raw data obtained. The relative phase shift (between empty reference delay line and covered sensing delay line) versus time was printed and evaluated. Within less than 5 seconds it can be assumed that the entire adsorption process on the internal surface of the microporous material is completed.

Compared to traditional methods, like volumetric determination of isotherms or calorimetric evaluation of the heat of adsorption the experimental time consumption is reduced by a factor of 10 - 1000. Valuable sample amounts could be reduced to less than 2  $\mu\text{g}$  covering a sensitive area of 1.8  $\text{mm}^2$ .

Related to the possibility to enhance the parallel IDT to a fan type design<sup>[146]</sup> to evoke SAWs at different horizontal positions a potential sensor application based on size selective microporous materials or in combination with mesoporous materials, possibly functionalized with organic moieties may extend the application of SAW devices in the near future.

Beside the fact that individual functionalized pixel may act as individual sensor ele-

ments the developed method principally offers a fast and convenient method to sequentially scan and evaluate new candidates for catalysts and appropriate materials for artificial noses.



**10 Literature**

- [1] [http://www.aro.army.mil/arowash/rt/awards/cbd\\_fy011\\_phasei\\_company.html](http://www.aro.army.mil/arowash/rt/awards/cbd_fy011_phasei_company.html), **2006**.
- [2] M. O. Adebajo, R. L. Frost, J. T. Kloprogge, O. Carmody, S. Kokot, *Journal of Porous Materials*, 10, **2003**, 159.
- [3] J. M. Balbus, K. Florini, R. A. Denison, S. A. Walsh, *Journal of Nanoparticle Research*, 9, **2007**, 11.
- [4] K. S. W. Sing, R. T. Williams, *Part. Part. Syst. Charact.* 21, **2004**, 71.
- [5] N. Kubicek, F. Vaudry, B. H. Chiche, P. Hudec, F. Di Renzo, P. Schulz, F. Fajula, *Applied Catalysis A: General*, 175, **1998**, 159.
- [6] <http://www.iza-structure.org/databases>, **2007**.
- [7] Y. K. Kim, H. B. Park, Y. M. Lee, *Journal of Membrane Science*, 251, **2005**, 159.
- [8] S. Manocha, *Sadhana*, 28, **2003**, 335.
- [9] K. S. W. Sing, D. H. Everett, R. A. W. Haul, L. Moscou, R. A. Pierotti, J. Rouquerol, T. Siemieniewska, *Pure & Appl. Chem.*, 57, 4, **1985**, 603.
- [10] <http://www.MarketResearch.com>, 2007.
- [11] B.A. Snopok, I. V. Kruglenko, *Thin Solid Films*, 418, **2002**, 21.
- [12] E. J. Staples, *The Industrial Physicist*, 10, 3, 2004.
- [13] W. A. Groves, E. T. Zellers, *Ann. occup. Hyg.*, 45, 8, **2001**, 609.
- [14] H. Huang, J. Zhou, S. Chen, L. Zeng, Y. Huang, *Sensors and Actuators B*, 101, **2004**, 316.
- [15] C. K. Ho, A. Robinson, D. R. Miller, M. J. Davis, *Sensors*, 5, **2005**, 4.
- [16] D. W. M. Arrigan, *Analyst*, 129, **2004**, 1157.
- [17] R. V. Matalucci, C. Esparza-Baca, R. D. Jimenez, *Characterization, monitoring, and sensor technology catalogue*. SAND95-3062, Sandia National Laboratories, Albuquerque, NM, **1995**.

- [18] R. S. Harmon, F. C. De Lucia, A. W. Miziolek, K. L. McNesby, R. A. Walters, P. D. French, *Geochemistry: Exploration, Environment, Analysis*, 5, **2005**, 21.
- [19] R. S. Harmon, F. C. DeLucia Jr., A. LaPointe, R. J. Winkel Jr., A. W. Miziolek, *Anal. Bioanal. Chem.*, 385, **2006**, 1140.
- [20] D. S. Blair, *Evaluation of an evanescent fiber optic chemical sensor for monitoring aqueous volatile organic compounds*. SAND97-0782, Sandia National Laboratories, Albuquerque, NM, **1997**.
- [21] G. Eranna, B. C. Joshi, D. P. Runthala, R. P. Gupta, *Critical Reviews in Solid State and Materials Sciences*, 29, **2004**, 111.
- [22] R. Rella et al., *Sensors and Actuators B*, 58, **1999**, 283.
- [23] G. S. Korotchenkov, S. V. Dmitriev, V. I. Brynzari, *Sensors and Actuators B*, 54, **1999**, 202.
- [24] <http://www.sandia.gov/media/acoustic.htm>, 2007.
- [25] G.-Z. Zhang, E. T. Zellers, *Anal. Chem.*, 65, **1993**, 1340.
- [26] A. D'Amico, *Sensors and Actuators*, 3, **1982**, 31.
- [27] B.-S. Joo, J.-S. Huhb, D.-D. Lee, *Sensors and Actuators B*, 121, **2007**, 47.
- [28] M. Penza, V. I. Anisimkin, *Sensors and Actuators*, 76, **1999**, 162.
- [29] M. Plötner, O. Berger, H. Stab, W.-J. Fischer, P. König, D. Beyerlein, A. Schwarz, *IEEE International Frequency Control Symposium and PDA Exhibition*, 2001.
- [30] E. J. Cho, F. V. Bright, *Analytica Chimica Acta*, 470, **2002**, 101.
- [31] A. Müller, A. Darga, A. Wixforth, R. Gross et al. (eds.), *Nanoscale devices - Fundamentals and applications*, **2006**, 3, Springer.
- [32] K. Möller, J. Kobler, T. Bein, *J. Mater. Chem.*, **2007**, DOI: 10.1039/b611931j.
- [33] A. Darga, J. Kecht, T. Bein, *Langmuir*, 23, **2007**, 12915.
- [34] E. P. Barrett, L. G. Joyner, P. P. Halenda, *J. Am. Chem. Soc.*, 73, **1951**, 373.
- [35] P. I. Ravikovitch, G. L. Haller, A. V. Neimark, *Adv. Colloid Interface Sci.*,

- 76–77, **1998**, 203.
- [36] P. I. Ravikovitch, A. V. Neimark, *Langmuir*, 16, **2000**, 2419.
- [37] S. Brunauer, T. H. Emmett, E. Teller, *J. Am. Chem. Soc.*, 60, **1938**, 309.
- [38] M. W. Maddox, J. P. Olivier, K. E. Gubbins, *Langmuir*, 13, **1997**, 1737.
- [39] M. Grün, K. K. Unger, A. Matsumoto, K. Tsutsumi, *Microporous and Mesoporous Materials*, 27, 1999, 207.
- [40] R. Ryoo, J. M. Kim, C. H. Ko, C. H. Shin, *J. Phys. Chem.*, 100, **1996**, 17718.
- [41] A.S. M. Chong, X.S. Zhao, A. T. Kustedjo, S.Z. Qiao, *Microporous and Mesoporous Materials*, 72, **2004**, 33.
- [42] F. Babonneau, L. Leite, S. Fontlupt, *J. Mater. Chem.*, 9, **1999**, 175.
- [43] M. Thommes, R. Köhn, M. Fröba, *J. Phys. Chem. B.*, 104, **2000**, 7932.
- [44] P. Van Der Voort, P. I. Ravikovitch, K. P. De Jong, A. V. Neimark, A. H. Janssen, M. Benjelloun, E. Van Bavel, P. Cool, B. M. Weckhuysenc, E. F. Vansan, *Chem. Commun.*, **2002**, 1010.
- [45] R. L. McCreery, *Raman Spectroscopy for Chemical Analysis*, The Ohio State University, Columbus, Ohio, Wiley Interscience. 2000, 264.
- [46] D. W. Mayo, F. A. Miller, R. W. Hannah, *Course Notes on the Interpretation of Infrared and Raman Spectra*, Wiley Interscience. 2003.
- [47] K. Moeller, J. Kobler, T. Bein; *J. Mater. Chem.*, 17, **2007**, 624.
- [48] S. Mintova, V. Valtchev, *Microporous and Mesoporous Materials*, 55, 2002, 171.
- [49] G. M. Murray, G. E Southard, *Instrumentation & Measurement Magazine*, 5, **2002**, 12.
- [50] N. Rupcich, A. Goldstein, J. D. Brennan, *Chem. Mater.*, 15, **2003**, 1803.
- [51] E. J. Cho, Z. Tao, E. C. Tehan, F. V. Bright, *Anal. Chem.*, 74, **2002**, 6177.
- [52] International Human Genome Sequencing Consortium, *Nature*, 431, 2004, 931.
- [53] <http://www.genome.org>, **2007**.

- [54] J. L. DeRisi, L. Penland, P.O. Brown, M. L. Bittner, P. S. Meltzer, M. Ray, Y. Chen, Y. A. Su, J. M. Trent, *Nature Genetics*, 14, **1996**, 457.
- [55] J. L. DeRisi, V. R. Iyer, P. O. Brown, *Science*, 278, **1997**, 680.
- [56] D. Rose, *Microarray Printing Technologies*, Cartesian Technologies, Inc., 1096 E. Highway 54, Suite 200A, Durham, NC 27713, USA.
- [57] M. Schena, R.A. Heller, T. P Theriault, K. Konrad, E. Lachenmeier, R.W. Davis, *Trends in Biotechnology*, 16, **1998**, 301.
- [58] R. Duggal, F. Hussain, M. Pasquali, *Adv. Mater.*, 18, **2006**, 34.
- [59] Y. Y. Tarasevich, *Phys. Rev. E*, 71, **2005**, 27301.
- [60] S. Mintova, J. Hedlund, B. Schoeman, V. Valtchev, J. Sterte, *Chem. Commun.*, **1997**, 15.
- [61] G. Sauerbrey; *Zeitschrift für Physik*, 155; **1959**; 206.
- [62] C. K. O'Sullivan, G.G. Guilbault, *Biosens. Bioelectron.* 14, **1999**, 663.
- [63] I. I. Postinkov, *Acoustical Physics*, 40, **1994**, 586.
- [64] M. D. Ward, E. J. Delawski, *Anal. Chem.*, 63, **1991**, 886.
- [65] K. K. Kanazawa, G.J. Gordon II, *Anal. Chem.*, 57, **1985**, 1770.
- [66] R. Borngräber, Dissertation, *Quarzresonanzsensoren für flüssige Medien – Systemdesign und Anwendung* –, Dissertation, Otto-von-Guericke-Universität Magdeburg, **2001**.
- [67] Z. A. Talib, Z. Baba , S. Kurosawa , H. A. A. Sidek, A. Kassimb, W. M. M. Yunus, *American Journal of Applied Sciences*, 3, 5, **2006** 1853.
- [68] M. Rodahl, F. Höök, B. Kasemo, *Anal. Chem.*, 68 (13), **1996**, 2219.
- [69] Y. Yin, R. E. Collins, *Thin Solid Films*, 257, **1995**, 139.
- [70] V. Mecca, R. V. Bucur, *Thin Solid Films*, 60, **1979**, 73.
- [71] J. Krim, A. Widom. *Phys. Rev. B*, 38, **1988**, 12184.
- [72] D. R. Lide; *Handbook of Chemistry and Physics*; CRC Press; 2004 - 2005; 43.
- [73] P.-G. Jonsson, *Acta Cryst.*, B32, **1976**, 232.

- [74] K. N. Marsh, *Recommended Reference Materials for the Realization of Physicochemical Properties*, Blackwell, Oxford, **1987**.
- [75] A. L. Smith, S. R. B. Mulligan, H. M. Shirazi, *Journal of Polymer Science: Part B: Polymer Physics*, **42**, **2004**, 3893.
- [76] A. Saitoh, Y. Asari, T. Nomura, *Proceedings of IEEE: Sensors*, **1**, **2002**, 435.
- [77] J. Pruski, A. Pekediz, H. de Lasa, *Chem. Eng. Sci.*, **51**, **1996**, 1799.
- [78] A. Gianetto, H. I. Farag, A. P. Blasetti, H. de Lasa, *Ind. Eng. Chem. Res.*, **33**, **1994**, 3053.
- [79] J. A. van Bokhoven, M. Tromp, D. C. Koningsberger, J. T. Miller, J. A. Z. Pieterse, J. A. Lercher, B. A. Williams, H. H. Kung, *J. Catal.*, **202**, **2001**, 129.
- [80] T. F. Narbeshuber, H. Vinek, J. A. Lercher, *J. Catal.*, **157**, **1995**, 388.
- [81] W. Haag, *Adv. Catal.* **27**, **1977**, 247.
- [82] Mingshi Li, Jianyi Shen, *J. Catal.*, **205**, **2002**, 248.
- [83] <http://www.fluidat.com>, Bronkhorst High-Tech, BV Nijverheidsstraat 1A, 7261 AK Ruurlo.
- [84] D. P. Serrano, G. Calleja, J. A. Botas, F. J. Gutierrez, *Ind. Eng. Chem. Res.*, **43**, **2004**, 7010.
- [85] J. P. Fox, S. P. Bates, *Langmuir*, **21**, **2005**, 4746.
- [86] C. Nguyen, C. G. Sonwane, S. K. Bhatia, D. D. Do, *Langmuir*, **14**, **1998**, 4950.
- [87] S. Z. Qiao, S. K. Bhatia, *Microporous and Mesoporous Materials*, **2005**, 112.
- [88] CambridgeSoft, 100 Cambridge Park Drive, Cambridge, MA 02140, USA.
- [89] Y. He, N. A. Seaton, *Langmuir*, **22**, **2006**, 1150.
- [90] D. Caputo, F. Iucolano, F. Pepe, C. Colell, *Microporous and Mesoporous Materials*, **105**, **2007**, 260.
- [91] D. G. Hartzog, S. Sircar, *Adsorption*, **1**, **1995**, 133.
- [92] S. Sircar, *Applied Surface Science*, **252**, **2005**, 647.

- [93] D. D. Do, *Adsorption Analysis: Equilibria And Kinetics*, Imperial College Press, **1998**, 17 et sqq.
- [94] E. Geidel, H. Lechert, J. Döbler, H. Jobic, G. Calzaferri, F. Bauer, *Microporous and Mesoporous Materials*, **65**, **2003**, 31.
- [95] L. L. Hench, J. K. West, *Chem. Rev.*, **90**, **1990**, 33.
- [96] M. Nomura, T. Yamaguchi, S. Nakao, *Journal of Membrane Science*, **144**, **1998**, 161.
- [97] T. C. Bowen, L. M. Vane, *Langmuir*, **22**, **2006**, 3721.
- [98] A. Cartón, G. Gonzalez Benito, J. A. Rey, M. de la Fuente, *Bioresource Technology*, **66**, **1998**, 75.
- [99] V. S. Nayak, J. B. Moffat, *J. Phys. Chem.*, **92**, **1988**, 7097.
- [100] M. M. Dubinin, G. D. Rakhmatkariev, A. A. Isirikyan, *Russian Chemical Bulletin*, **38**, **1989**, 2419.
- [101] H. Thamm, *J. Chem. Soc., Faraday Trans. 1*, **85**(1), **1989**, 1.
- [102] K. S. Akhmedov, G. U. Rakhmatkariev, M. M. Dubinin, A. A. Isirikyan, *IzV. AN SSSR, Ser. Khim.*, **8**, **1987**, 1717.
- [103] B. Boddenberg, G. U. Rakhmatkariev, R. Greth, *J. Phys. Chem. B*, **101**, **1997**, 1634.
- [104] P. J. Branton, P. G. Hall, K. S. W. Sing, *Adsorption*, **1**, **1995**, 77.
- [105] C. M. Bambrough, R. C. T. Slade, R. T. Williams, *Phys. Chem. Chem. Phys.*, **2**, **2000**, 3499.
- [106] C. M. Bambrough, R. C. T. Slade, R. T. Williams, *J. Mater. Chem.*, **8**, **1998**, 569.
- [107] K. S. W. Sing, *Journal of Porous Materials*, **2**, **1995**, 5.
- [108] D. Shen, M. Bülow, F. Siperstein, M. Engelhard, A. L. Myers, *Adsorption* **6**, **2000**, 275.
- [109] G. T. Kokotailo, S. L. Lawton, D. H. Olson, W. M. Meier, *Nature*, **272**, **1978**, 437.
- [110] M. S. Sun, D. B. Shah, H. H. Xu, O. Talu, *J. Phys. Chem. B*, **1998**, **102**, 1466.

- [111] W. Zhu, J. M. van de Graaf, L. J. P. van den Broeke, F. Kapteijn, J.A. Moulijn, *Ind. Eng. Chem.Res.*, **1998**, 37, 1934.
- [112] T. J. H. Vlugt, R. Krishna, , B. Smit, *J. Phys. Chem. B*, **1999**, 103, 1102.
- [113] R. L. June, A. T. Bell, D. N. Theodorou, *J. Phys. Chem.*, 94, **1990**, 1508.
- [114] F. Eder, M. Stockenhuber, J. A. Lercher, *J. Phys. Chem B*, **1997**, 101, 5414.
- [115] E. J. Maginn, A.T. Bell, D. N. Theodorou, *J. Phys. Chem.*, **1995**, 99, 2057.
- [116] B. Millot, A. M'ethivier, H. Jobic, I. Clemençent, B. Re-bours, *Langmuir* , **1999**, 15, 2534.
- [117] R. E. Richards, L.V. C. Rees, *Langmuir*, 3 **1987**, 335.
- [118] H. Stach, U. Lohse, H. Thamm, W. Schirmer, *Zeolites*, 6, **1986**, 74.
- [119] H. Thamm, *Zeolites*, 7, **1987**, 341.
- [120] S. Angloher, J. Kecht, T. Bein, *Chem. Mater.*, 2007, in press, cm0608387.
- [121] C. Zapilko, M. Widenmeyer, I. Nagl, F. Estler, R. Anwander, G. Raudaschl-Sieber, O. Groeger, G. Engelhardt, *J. Am. Chem. Soc.*, 128, **2006**, 16266.
- [122] F. Kleitz, W. Schmidt, F. Schüth, *Micropor. Mesopor. Mater.*, 65, **2003**, 1.
- [123] H. Huang, Q. h, H. Xiao, M. Eic', *Micropor. Mesopor. Mater.*, 98, **2007**, 330.
- [124] S. Kitagawa, R. Kitaura, S.-i. Noro, *Angew. Chem. Int. Ed.*, 43, **2004**, 2338.
- [125] C. N. R. Rao, S. Natarajan, R. Vaidhyanathan, *Angew. Chem. Int. Ed.*, 43, **2004**, 1466.
- [126] A. I. Skoulidas, D. S. Sholl, *J. Phys. Chem. B*, 109, **2005**, 15760.
- [127] B. Panella, M. Hirscher, *Adv. Mater.*, 17, **2005**, 538.
- [128] S. Y. Choi, Y.-J. Lee, Y. S. Park, K. Ha, K. B. Yoon, *J. Am. Chem. Soc.*, 122, **2000**, 5201.
- [129] A. Kulak, Y.-J. Lee, Y. S. Park, K. B. Yoon, *Angew. Chem. Int. Ed.*, 39, **2000**, 950.
- [130] J. Lee, J. Li, J. Jagiello, *J. Solid State Chem.*, 178, **2005**, 2527.
- [131] J. L. C. Rowsell, A. R. Millward, K. S. Park, O. M. Yaghi, *J. Am. Chem. Soc.*,

- 126, **2004**, 5666.
- [132] D. Braga, *Angew. Chem. Int. Ed.*, **42**, **2003**, 5544.
- [133] E. Dujardin, S. Mann, *Adv. Eng. Mater.*, **4**, **2002**, 461.
- [134] S. Weiner, L. Addadi, *J. Mater. Chem.*, **7**, **1997**, 689.
- [135] J. S. Lee, Y.-J. Lee, E. L. Tae, Y. S. Park, K. B. Yoon, *Science*, **301**, **2003**, 818.
- [136] M.-H. Zeng, X.-L. Feng, X.-M. Chen, *Dalton Transactions*, **2004**, 2217.
- [137] S. Hermes, F. Schroeder, R. Chelmoski, C. Woell, R. A. Fischer, *J. Am. Chem. Soc.*, **127**, **2005**, 13744.
- [138] S. S. Y. Chui, S. M. F. Lo, J. P. H. Charmant, A. G. Orpen, I. D. Williams, *Science*, **283**, **1999**, 1148.
- [139] E. Biemmi, Dissertation, **2007**.
- [140] Célio L. Cavacante, Jr., Douglas M. Ruthven, *Ind. Eng. Chem. Res.*, **1995**, **34**, 177.
- [141] M. S. Sun, D.B.Shah, Heather H. Xu, Orhan Talu, *J. Phys. Chem. B*, **1998**, **102**, 1466.
- [142] W. Song, V. H. Grassian, S. C Larsen, *Chemical Communications*, **23**, **2005**, 2951-2953.
- [143] <http://www.abayfor.de/fornano/index.php>, **2008**.
- [144] Lord Raleigh, *Proc. London Math. Soc.*, **7**, **1885**, 4.
- [145] D.J. Tylor, P.F. Fleig, S.L. Hietala, *Thin solid films*, **1998**, **332**, 257.
- [146] A. Müller, Dissertation, Sensorische Anwendungen mit akustischen Oberflächenwellen, **2004**.
- [147] J. Temmyo, I. Kotaka, T. Inamura and S. Yoshikawa, *IEEE Transactions on Sonics and Ultrasonics*, **27**, **4**, **1980**, 218.
- [148] T. J. H. Vlugt, W. Zhu, F. Kapteijn, J. A. Moulijn, B. Smit and R. Krishna, *J. Am. Chem. Soc.*, **120**, **1998**, 5599.
- [149] B. Smit, L. D. J. C. Loyens, G. L. M. M. Verbist, *Faraday Discuss.*, **106**, **1997**, 93.



- [150] W. Zhu, F. Kapteijn, J. A. Moulijn, *Phys. Chem. Chem. Phys.*, **2**, **2000**, 1989.
- [151] W. Zhu, F. Kapteijn, J. A. Moulijn, *Adsorption* **6**, **2000**, 159.
- [152] F. Leroy, B. Rousseau, A. H. Fuchs, *Phys. Chem. Chem. Phys.*, **6**, **2004**, 775.
- [153] W. Zhua, A. Malekian, M. Eić, F. Kapteijn, J.A. Moulijn, *Chemical Engineering Science*, **2004**, *59*, 3827.
- [154] T. Q. Gardner, J. B. Lee, Richard D. Noble, J. L. Falconer, *Ind. Eng. Chem. Res.*, **41**, **2002**, 4094.
- [155] B. A. Williams, S.M. Babitz, J. T. Miller, R.Q. Snurr, H. H. Kung, *Appl. Catal. A.*, **177**, **1999**, 161.
- [156] J. F. Denayer, G. V. Baron, W. Souverijns, J. A Martens, P. A. Jacobs, *Ind. Eng. Chem. Res.*, **36** (8), **1997**, 3242.
- [157] A. Van De Runstraat, P. J. Stobbelaar, J. Van Grondelle, B. G. Anderson, L. J. Van Ijzendoorn, R. A. Van Santen, *Stud. Surf. Sci. Catal.*, **105B**, **1997**, 1253.
- [158] H. Vinh-Thang, Q. Huang, M. Eić, D. Trong-On, S. Kaliaguine, *Langmuir*, **21**, **2005**, 5094.
- [159] R. Schumacher, *Angew. Chem.* **102**, **1990**, 347.
- [160] K. A Marx, *Biomacromolecules*, **4**, **2003**, 1099.
- [161] D. Ramirez, Shaoying Qi, M.J. Rood, *Environ. Sci. Technol.*, **39**, **2005**, 5864.
- [162] A. I. Skoulidas, *J. Am. Chem. Soc.* **9**, **126**, **5**, **2004**, 1357.
- [163] Q. M. Wang, D. Shen, M. Bülow, M. L. Lau, S. Deng, F. R. Fitch, N. O. Lemcoff, J. Semanscin, *Microporous and Mesoporous Materials*, **55**, **2002**, 217.
- [164] K. Schlichte, T. Kratzke, S. Kaskel, *Microporous and Mesoporous Materials*, **73**, **2004**, 81.
- [165] F. Iucolano, F. Pepe, C. Colell, *Microporous and Mesoporous Materials*, **2007**, **105**, 260.
- [166] Chih-Shun Lu, O. Lewis, *J. Appl. Phys.*, **43**, **1972**, 4385.
- [167] S. L. Burkett, S. D. Sims, S. Mann, *Chem. Commun.*, **1996**, 1367.
- [168] P. I. Ravikovitch, A. Vishnyakov, A. V. Neimark, M. M. L. Ribeiro Carrott, P.

- A. Russo, P. J. Carrott, *Langmuir*, 22, 2, **2006**, 513.
- [169] E. M. Flanigen, J. M. Bennett, R. W. Grose, J. P. Cohen, R. L. Patton, R. M. Kirchner, J. V. Smith, *Nature*, 271, **1978**, 512.
- [170] C. Hardacre, S. P. Katdare, D. Milroy, P. Nancarrow, D. W. Rooney, J. M. Thompson, *Journal of Catalysis*, 227(1), **2004**, 44.
- [171] M. Vilaseca, J. Coronas, A. Cirera, A. Cornet, J. R. Morante, J. Santamaria, *Catalysis Today*, 82, **2003**, 179.
- [172] J. S. Beck, J. C. Vartuli, W. J. Roth, M. E. Leonowicz, C. T. Kresge, K. D. Schmitt, C. T-W. Chu, D. H. Olson, E. W. Sheppard, S. B. McCullen, J. B. Higgins, J. L. Schlenkert, *J. Am. Chem. Soc.*, 114, **1992**, 10834.
- [173] S. Mintova, V. Valtchev; *Microporous and Mesoporous Materials*, 55, **2002**, 171.
- [174] C. Nguyen, C. G. Sonwane, S. K. Bhatia, D. D. Do, *Langmuir*, 14, **1998**, 4950.
- [175] M. E. Davis, *Nature*, 417, **2002**, 813.

## 11 Acknowledgement

I would like to express my gratitude to all those who gave me the possibility to complete this thesis. I want to thank the Department of Physical Chemistry and Biochemistry for giving me permission to commence this thesis in the first instance, to do the necessary research work and to use departmental data. I have furthermore to thank all the people who stand by me during the last often very stressful and exhausting years. I am deeply indebted to my supervisor Prof. Dr. Thomas Bein for stimulating suggestions and encouragement during the research period and the interesting and substantial discussion of gained results.

I would like to thank Dr. Alexander Müller, my former colleague at the Physics department of the LMU University for the inspiring time, the discussions about our research together in the lab and the relaxing lunch times. I'm very grateful for the help of Dipl. Ing. Stephan Manus to develop the necessary equipment for the SAW measurements at the physical department of the LMU. I would like to thank Prof. Dr. Jörg. P. Kotthaus for giving Alexander Müller and me the opportunity to perform our experiments in his labs.

Furthermore I want to thank the F-practicant students Philip Severin and Johannes Büttnner for their support in programming the automated QCM based analytical system. Especially I'm obliged to my colleagues Enrica Biemmi, Johannes Kobler and Johann Kecht for the cooperation and their support with sample materials. Dr. Ralf Köhn for the discussions about isotherms and reversibility and the "Subway sandwich" adventures.

All the members of the Prof. Dr. Thomas Bein group I would like to say "Thank you" for the pleasant atmosphere, the Chinese food session every Tuesday and our legendary barbecue events, even in winter.

I want to thank my beloved girl friend Sonja for her patience, her understanding and trust in my "dancing on a razors edge" - the PhD thesis and labor at the company.

My parents, who encouraged me not to give up and giving me the opportunity to write the thesis at their home.

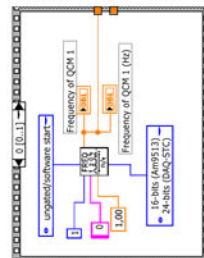
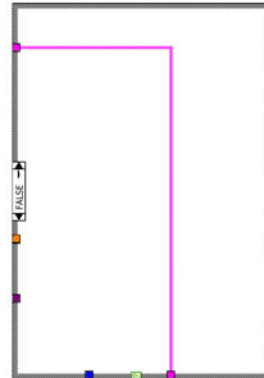
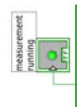
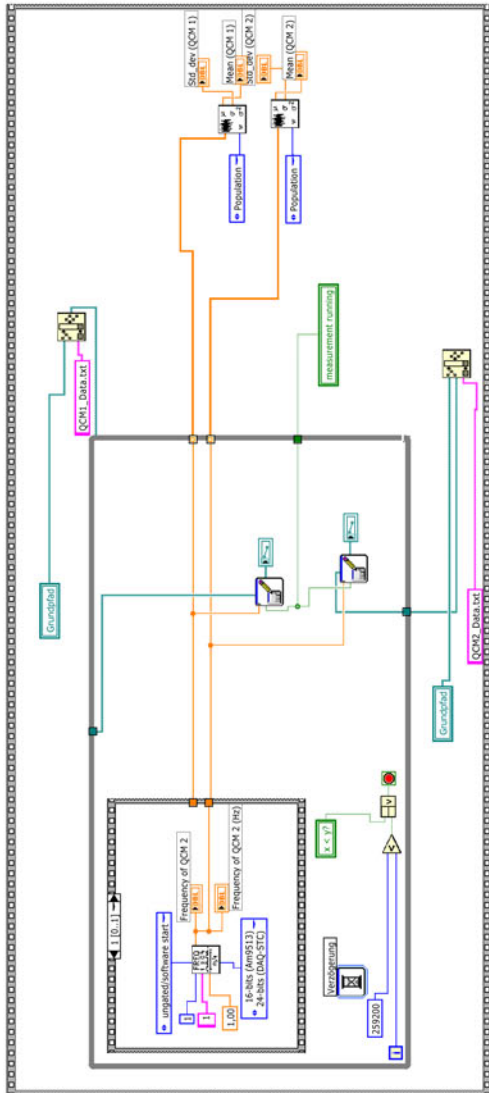
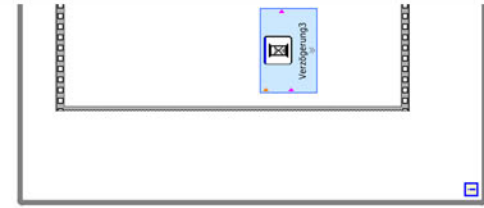
Last but not least, I want to thank all persons who supported and helped me to achieve the final goal.

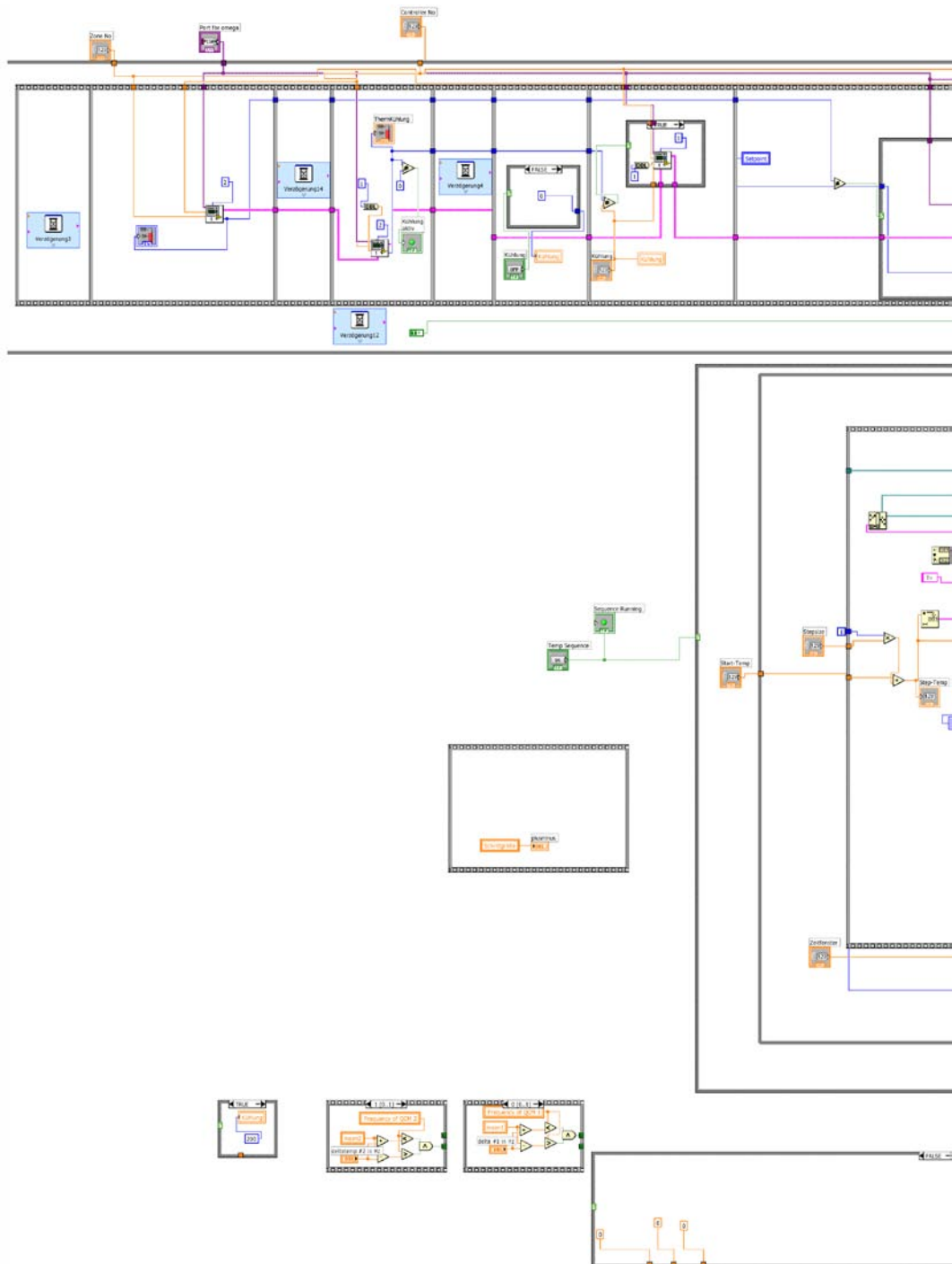
## **12 Appendix**

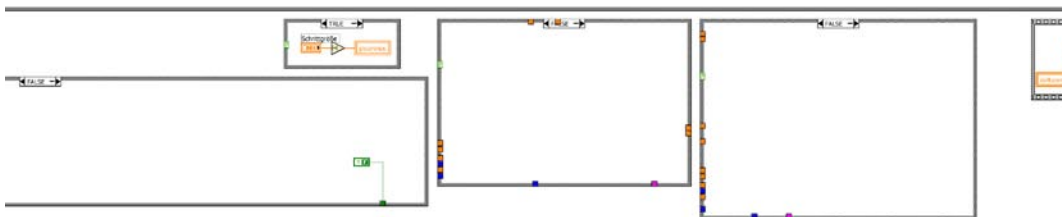
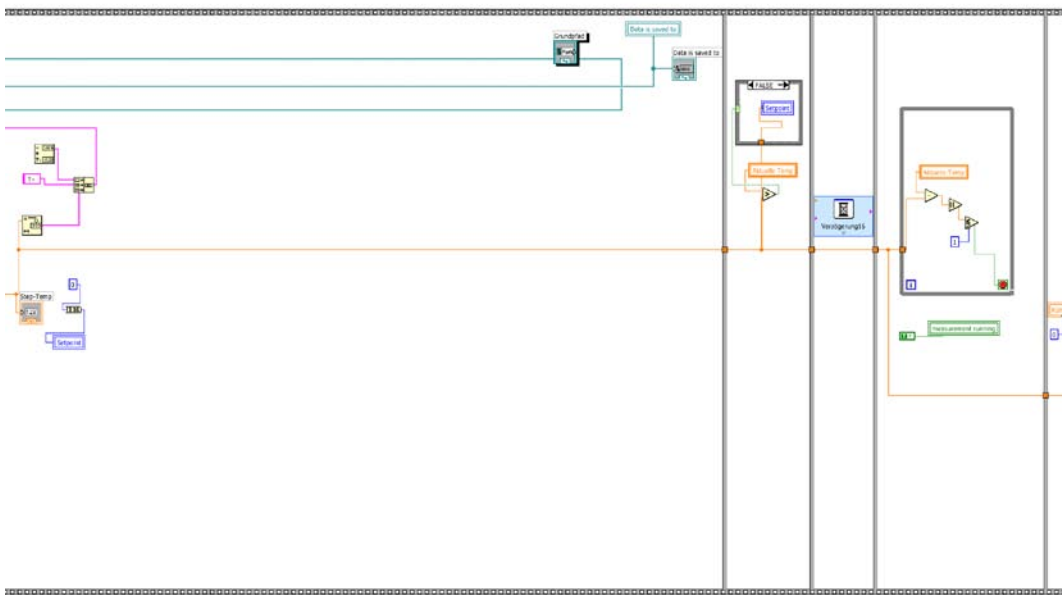
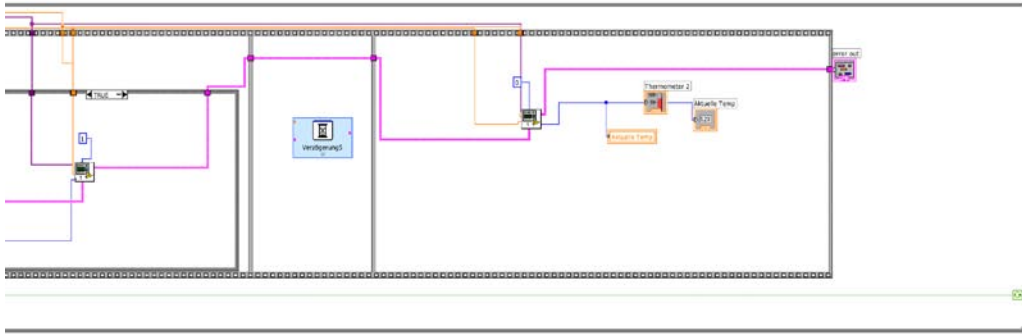
### 12.1 Labview controlling and regulation program

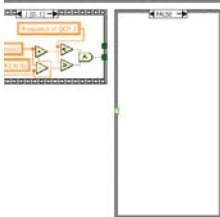
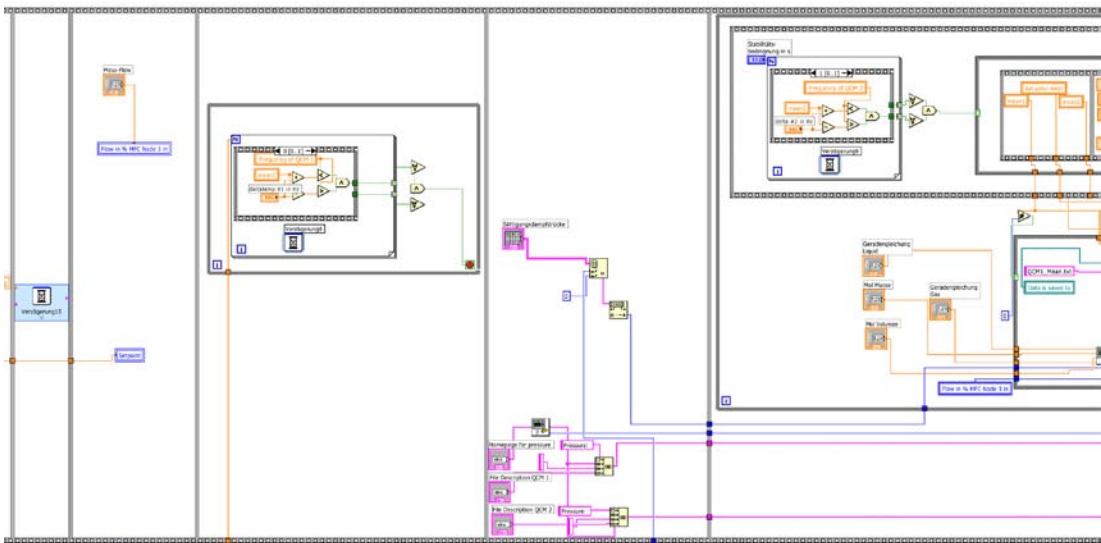
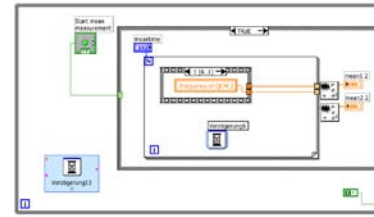
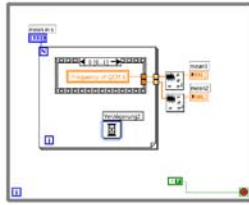
The Labview program has been printed as a big PDF file and separated into smaller pictures and picked up into this document to guarantee the clarity. The program was taken with it's originally state from the year 1992 and dramatically enhanced. The only original part is the frequency measuring part.

Due to the graphical interface of Labview, the whole program can not be printed as code lines but is divided into several sub windows, containing some parts of the program. To "read" the Labview program, it is recommended to combine each single numbered page into one complete page by printing the following pages.



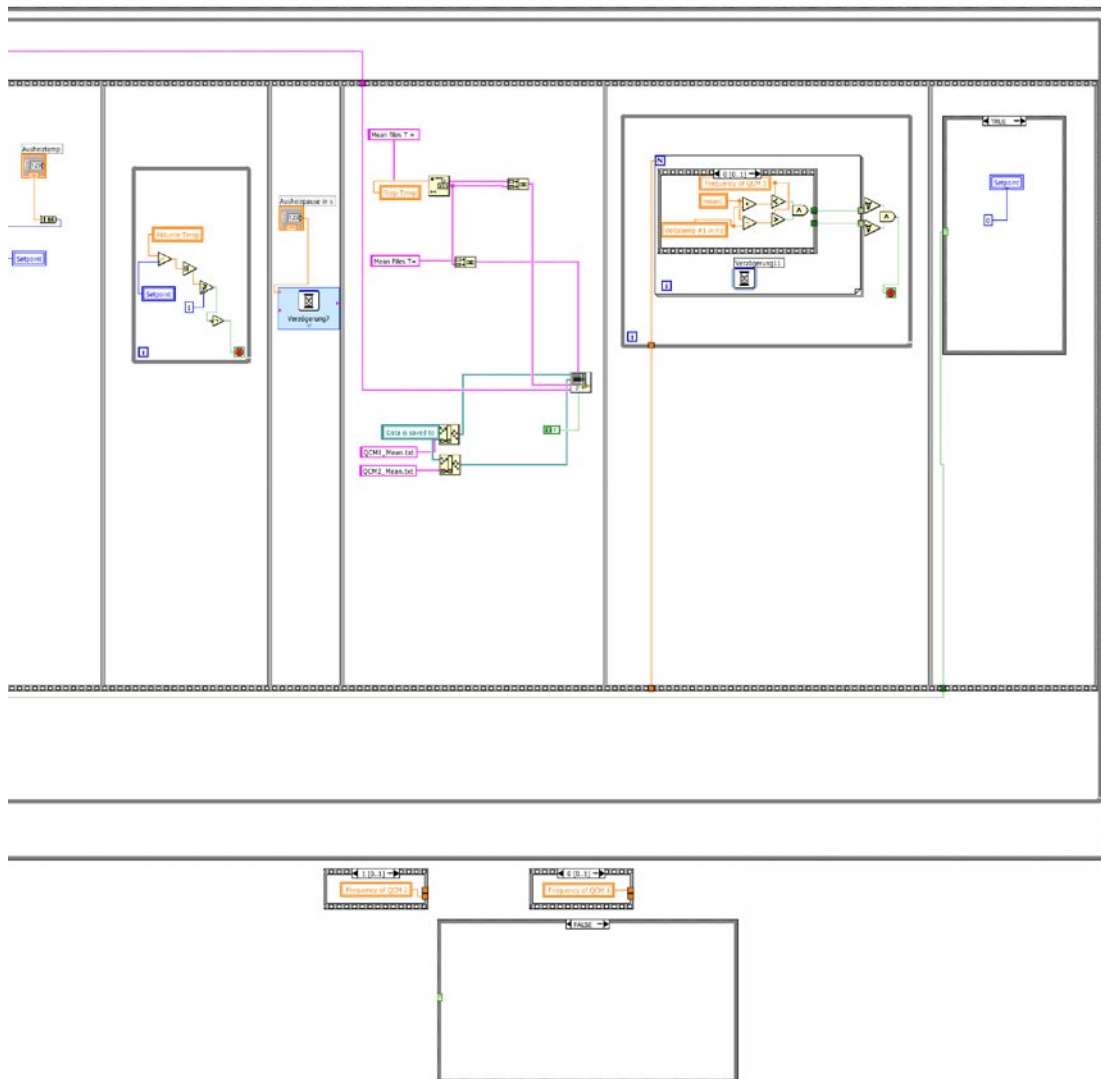












## 12.2 Calibration certificates of Bronkhorst mass flow controllers




---



---

**CALIBRATION CERTIFICATE**


---



---

We herewith certify that the instrument mentioned below has been calibrated in accordance with the stated values and conditions. The calibration standards used are traceable to national standards of the Dutch Weights & Measures (NMI).

---

**Identifications**


---

	<u>Calibrated Instrument</u>	<u>Calibration Standard</u>
Type :	Flow controller(D)	Piston Prover
Serial number :	M1207898A	INM0205301A
Model number :	F-200D-RBA-11-V	FPP T-005-TD
Certificate no. :	BHTG28/209643	BHTG09/184123

---

**Conditions**


---

	<u>Customer</u>		<u>Calibration</u>
Fluid :	CO	Fluid :	AiR
Pressure :	5 bar (g)	Pressure :	6.0 bar (a)
Temperature :	20 °C	Temperature :	23.1 °C
Flow (*) :	10 mln/min	Room temperature :	23.1 °C
Output range :	0 - 100 %	Atm. pressure :	1012 hPa

---

**Results**


---

Nominal Flow Setting	Calibrated Output Signal	Customer Flow(*)	
0.0 %	-0.04 %	0.0000	mln/min
10.0 %	9.44 %	0.9486	mln/min
20.0 %	19.04 %	1.897	mln/min
40.0 %	38.30 %	3.830	mln/min
60.0 %	58.06 %	5.815	mln/min
80.0 %	78.85 %	7.876	mln/min
100.0 %	101.17 %	10.12	mln/min

---

**Notes**


---

- \* Reference conditions of flow units: 0.00 °C, 1013.25 hPa (a).
- \* The conversion of calibration conditions to customer flow is done by using Bronkhorst HI-TEC FLUIDAT software.

Calibrator : H.M.

Date : 15-01-2002

Signed : QC : 




---



---

**CALIBRATION CERTIFICATE**


---



---

We herewith certify that the instrument mentioned below has been calibrated in accordance with the stated values and conditions. The calibration standards used are traceable to national standards of the Dutch Weights & Measures (NMI).

---

**Identifications**


---

	<u>Calibrated Instrument</u>	<u>Calibration Standard</u>
Type :	Flow controller(D)	Piston Prover
Serial number :	M1207898B	INM0205301A
Model number :	F-200D-RBA-11-V	FPP T-005-TD
Certificate no. :	BHTG28/209640	BHTG09/184123

---

**Conditions**


---

	<u>Customer</u>		<u>Calibration</u>
Fluid :	CO	Fluid :	AiR
Pressure :	5 bar (g)	Pressure :	6.0 bar (a)
Temperature :	20 °C	Temperature :	23.3 °C
Flow (*) :	10 mln/min	Room temperature :	23.3 °C
Output range :	0 - 100 %	Atm. pressure :	1012 hPa

---

**Results**


---

Nominal Flow Setting	Calibrated Output Signal	Customer Flow(*)	
0.0 %	0.16 %	0.0000	mln/min
10.0 %	9.50 %	0.9493	mln/min
20.0 %	19.01 %	1.902	mln/min
40.0 %	38.27 %	3.825	mln/min
60.0 %	58.12 %	5.815	mln/min
80.0 %	78.97 %	7.894	mln/min
100.0 %	101.19 %	10.12	mln/min

---

**Notes**


---

- \* Reference conditions of flow units: 0.00 °C, 1013.25 hPa (a).
- \* The conversion of calibration conditions to customer flow is done by using Bronkhorst HI-TEC FLUIDAT software.

Calibrator : H.M.

Date : 15-01-2002

Signed : 

QC : 




---



---

**CALIBRATION CERTIFICATE**


---



---

We herewith certify that the instrument mentioned below has been calibrated in accordance with the stated values and conditions. The calibration standards used are traceable to national standards of the Dutch Weights & Measures (NMI).

---

**Identifications**


---

	<u>Calibrated Instrument</u>	<u>Calibration Standard</u>
Type :	Flow controller(D)	Piston Prover
Serial number :	M1207898C	INM0205301B
Model number :	F-201C-RBA-33-V	FPP T-016-TD
Certificate no. :	BHTG28/209641	BHTG09/184175

---

**Conditions**


---

<u>Customer</u>		<u>Calibration</u>	
Fluid :	O <sub>2</sub>	Fluid :	AiR
Pressure :	5 bar (g)	Pressure :	6.0 bar (a)
Temperature :	20 °C	Temperature :	20.7 °C
Flow (*) :	400 mln/min	Room temperature :	20.7 °C
Output range :	0 - 100 %	Atm. pressure :	1018 hPa

---

**Results**


---

<u>Nominal Flow Setting</u>	<u>Calibrated Output Signal</u>	<u>Customer Flow(*)</u>	
0.0 %	-0.28 %	0.0000	mln/min
10.0 %	9.32 %	37.39	mln/min
20.0 %	18.95 %	75.64	mln/min
40.0 %	38.03 %	152.1	mln/min
60.0 %	57.56 %	230.5	mln/min
80.0 %	78.29 %	312.9	mln/min
100.0 %	100.96 %	403.9	mln/min

---

**Notes**


---

- \* Reference conditions of flow units: 0.00 °C, 1013.25 hPa (a).
- \* The conversion of calibration conditions to customer flow is done by using Bronkhorst HI-TEC FLUIDAT software.

Calibrator : H.M.

Date : 16-01-2002

Signed :

QC :

# BRONKHORST HI-TEC

## CALIBRATION CERTIFICATE

We herewith certify that the instrument mentioned below has been calibrated in accordance with the stated values and conditions. The calibration standards used are traceable to national standards of the Dutch Weights & Measures (NMI).

### Identifications

	Calibrated Instrument	Calibration Standard
Type :	Flow controller(D)	Piston Prover
Serial number :	M1207898D	INM0205301C
Model number :	F-201C-RBA-33-V	FPP T-050-TD
Certificate no. :	BHTG28/209642	BHTG09/184249

### Conditions

Customer		Calibration	
Fluid :	N2	Fluid :	AiR
Pressure :	5 bar (g)	Pressure :	6.0 bar (a)
Temperature :	20 °C	Temperature :	21.3 °C
Flow (*) :	2000 mln/min	Room temperature :	21.3 °C
Output range :	0 - 100 %	Atm. pressure :	1018 hPa

### Results

Nominal Flow Setting	Calibrated Output Signal	Customer Flow(*)	
0.0 %	-0.25 %	0.0000	mln/min
10.0 %	9.58 %	192.2	mln/min
20.0 %	19.41 %	387.0	mln/min
40.0 %	38.80 %	776.0	mln/min
60.0 %	58.39 %	1169	mln/min
80.0 %	78.81 %	1575	mln/min
100.0 %	100.73 %	2015	mln/min

### Notes

- \* Reference conditions of flow units: 0.00 °C, 1013.25 hPa (a).
- \* The conversion of calibration conditions to customer flow is done by using Bronkhorst HI-TEC FLUIDAT software.

Calibrator : H.M.

Date : 16-01-2002

Signed : 

QC : 



**CALIBRATION CERTIFICATE**

We herewith certify that the instrument mentioned below has been calibrated in accordance with the stated values and conditions. The calibration standards used are traceable to national standards of the Dutch Weights & Measures (NMI).

== Identifications ==

	<u>Calibrated Instrument</u>	<u>Calibration Standard</u>
Type :	Flow controller(D)	Piston Prover
Serial number :	M1207898E	80362
Model number :	F-201C-RBA-33-V	FPP T-050-TD
Certificate no. :	BHTG28/209637	BHTG09/185547

== Conditions ==

	<u>Customer</u>		<u>Calibration</u>
Fluid :	H2	Fluid :	H2
Pressure :	5 bar (g)	Pressure :	6.0 bar (a)
Temperature :	20 °C	Temperature :	23.4 °C
Flow (*) :	2000 mln/min	Room temperature :	23.4 °C
Output range :	0 - 100 %	Atm. pressure :	1020 hPa

== Results ==

Nominal Flow Setting	Calibrated Output Signal	Customer Flow(*)	
0.0 %	-0.06 %	0.0000	mln/min
10.0 %	9.49 %	189.8	mln/min
20.0 %	19.23 %	384.6	mln/min
40.0 %	38.84 %	776.6	mln/min
60.0 %	58.80 %	1176	mln/min
80.0 %	79.35 %	1587	mln/min
100.0 %	100.76 %	2015	mln/min

== Notes ==

\* Reference conditions of flow units: 0.00 °C, 1013.25 hPa (a).

Calibrator : H.H.H.

Date : 16-01-2002

Signed : 

QC : 

# BRONKHORST

## HI-TEC

### CALIBRATION CERTIFICATE

We herewith certify that the instrument mentioned below has been calibrated in accordance with the stated values and conditions. The calibration standards used are traceable to national standards of the Dutch Weights & Measures (NMI).

#### Identifications

	Calibrated Instrument	Calibration Standard
Type :	Flow meter(D)	Piston Prover
Serial number :	M1208230A	80254
Model number :	F-111C-RBA-11-V	FPP T-016-TD
Certificate no. :	BHTG01/209432	BHTG09/165805

#### Conditions

	Customer		Calibration
Fluid :	AiR	Fluid :	AiR
Pressure :	2 bar (g)	Pressure :	0.0 bar (g)
Temperature :	20 °C	Temperature :	24.3 °C
Flow (*) :	200 mln/min	Room temperature :	24.3 °C
Output range :	0 - 10 V	Atm. pressure :	1024 hPa

#### Results

Nominal Flow Setting	Calibrated Output Signal	Customer Flow(*)	
0.0 %	-0.017 V	0.0000	mln/min
10.0 %	0.907 V	18.18	mln/min
20.0 %	1.832 V	36.58	mln/min
40.0 %	3.676 V	73.55	mln/min
60.0 %	5.598 V	112.0	mln/min
80.0 %	7.702 V	154.0	mln/min
100.0 %	10.090 V	201.8	mln/min

#### Notes

\* Reference conditions of flow units: 0.00 °C, 1013.25 hPa (a).

Calibrator : D.W.

Date : 14-01-2002

Signed : 

QC : 





CALIBRATION CERTIFICATE

We herewith certify that the instrument mentioned below has been calibrated in accordance with the stated values and conditions. The calibration standards used are traceable to national standards of the Dutch Weights & Measures (NMI).

== Identifications ==

	Calibrated Instrument	Calibration Standard
Type :	Flow meter (D)	Reference meter
Serial number :	M4208464A	M3207010A
Model number :	L01-RBA-11-0	L01-AAA-99-0-80S
Certificate no. :	BHTL64/298479	BHTL48/296291

== Conditions ==

Customer		Calibration	
Fluid :	H2O	Fluid :	H2O
Pressure :	0.5..1 bar (g)	Pressure :	2.0 bar (a)
Temperature :	20 °C	Temperature :	22.0 °C
Flow :	1 g/h	Room temperature :	22.0 °C
Output range :	0 - 100 %	Atm. pressure :	1010 hPa

== Results ==

Nominal Flow Setting	Calibrated Output Signal	Customer Flow	
0.0 %	0.00 %	0.0000	g/h
25.0 %	25.00 %	0.2497	g/h
50.0 %	50.00 %	0.4995	g/h
75.0 %	75.00 %	0.7493	g/h
100.0 %	100.00 %	1.002	g/h

== Notes ==


Calibrator : W.K.

Date : 19-11-2004

Signed : 

QC : 

12.3 Data sheet XA1600 QCM chip

		<h1>XA 1600</h1>																								
<small>TAR010</small>																										
<p><b>Specification:</b></p> <table border="0"> <tr> <td>Package:</td> <td>BLANK</td> </tr> <tr> <td>Frequency:</td> <td>10.000.015 Hz</td> </tr> <tr> <td>Mode of vibration:</td> <td>1</td> </tr> <tr> <td>Temperature stability</td> <td>from 0°C to 70 °C max ± 10 ppm</td> </tr> <tr> <td>Reference temperature:</td> <td>25 °C</td> </tr> <tr> <td>Adjustment tolerance at 25 °C</td> <td>max ± 1000 ppm</td> </tr> <tr> <td>Load capacity:</td> <td>serie</td> </tr> <tr> <td>Equivalent parameters:</td> <td>C0: 7,2 pF ± ,1 pF</td> </tr> <tr> <td>Equivalent series resistance R1max:</td> <td>120 ohms</td> </tr> <tr> <td>Level of drive:</td> <td>1 mW</td> </tr> <tr> <td>(Standard: IEC 444, transmission line method)</td> <td></td> </tr> <tr> <td>Operable temperature range:</td> <td>0 °C to 70 °C</td> </tr> </table>			Package:	BLANK	Frequency:	10.000.015 Hz	Mode of vibration:	1	Temperature stability	from 0°C to 70 °C max ± 10 ppm	Reference temperature:	25 °C	Adjustment tolerance at 25 °C	max ± 1000 ppm	Load capacity:	serie	Equivalent parameters:	C0: 7,2 pF ± ,1 pF	Equivalent series resistance R1max:	120 ohms	Level of drive:	1 mW	(Standard: IEC 444, transmission line method)		Operable temperature range:	0 °C to 70 °C
Package:	BLANK																									
Frequency:	10.000.015 Hz																									
Mode of vibration:	1																									
Temperature stability	from 0°C to 70 °C max ± 10 ppm																									
Reference temperature:	25 °C																									
Adjustment tolerance at 25 °C	max ± 1000 ppm																									
Load capacity:	serie																									
Equivalent parameters:	C0: 7,2 pF ± ,1 pF																									
Equivalent series resistance R1max:	120 ohms																									
Level of drive:	1 mW																									
(Standard: IEC 444, transmission line method)																										
Operable temperature range:	0 °C to 70 °C																									
<p><b>Additional data</b></p>																										
		<p><b>Marking:</b></p> <p>Mon/KVG/Jahr 10000,0KHZ XA 1600</p>																								
Teile-Nr:	326984	<b>KVG Quartz Crystal Technology GmbH</b> P.O.B 61 74922 Neckarbischofsheim																								
Originator:	LS      EC																									
Edition-Date:	26-09-05      07-10-04	Page 1 of 1																								

12.4 Microarray program

The following screenshots demonstrate the developed  $n$  times 3x3 microarray whereas in most printing scenarios only a 3x3 array was printed.

Part I



Part II

max Dichte dist.175 µm STEALTH 140704 Enrica Test\* - Cartesian AxSys

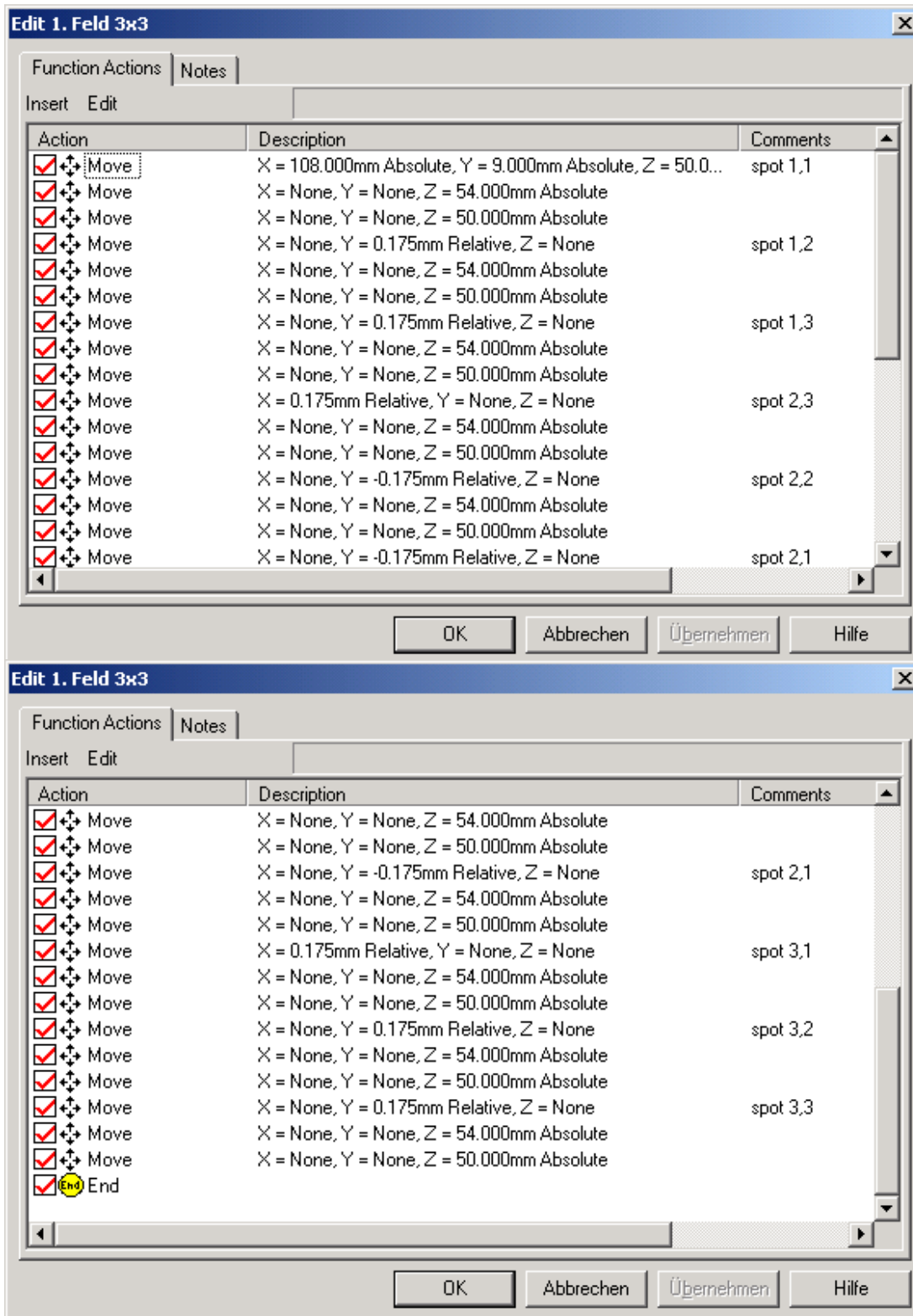
File Edit Insert View Run Tools Help

Action	Description	Comments
	X = None, Y = None, Z = 36.000mm Absolute	
	X = 0.175mm Relative, Y = None, Z = 36.000mm Absolute	spot 2,3
	X = None, Y = None, Z = 38.500mm Absolute	
	X = None, Y = None, Z = 36.000mm Absolute	
	X = None, Y = -0.175mm Relative, Z = 36.000mm Absolute	spot 2,2
	X = None, Y = None, Z = 38.500mm Absolute	
	X = None, Y = None, Z = 36.000mm Absolute	
	X = None, Y = -0.175mm Relative, Z = 36.000mm Absolute	spot 2,1
	X = None, Y = None, Z = 38.500mm Absolute	
	X = 0.175mm Relative, Y = None, Z = 36.000mm Absolute	spot 3,1
	X = None, Y = None, Z = 38.500mm Absolute	
	X = None, Y = None, Z = 36.000mm Absolute	
	X = None, Y = 0.175mm Relative, Z = 36.000mm Absolute	spot 3,2
	X = None, Y = None, Z = 38.500mm Absolute	
	X = None, Y = None, Z = 36.000mm Absolute	
	X = None, Y = 0.175mm Relative, Z = 36.000mm Absolute	spot 3,3
	X = None, Y = None, Z = 38.500mm Absolute	
	X = None, Y = None, Z = 36.000mm Absolute	
	Set XY plane & Z axis	
	X = None, Y = None, Z = Home	
	X = Home, Y = Home, Z = None	

Off Line

For Help, press F1

## Part III - subroutine



12.5 Maple program for the determination of  $V_{\text{real}}$ 

```

<Van der Waal real gas equation for water
12.05.06
> R:=8.341:      universal gas constant
> T:=294:       temperature [Kelvin]
> P:=95200:     pressure [Pascal]
> a:=5.537:    Van der Waal coefficient. a
> b:=.0305:    Van der Waal coefficient. b
> n:=9.25925926E-04:  molar amount of dosed liquid

> van_der_waal_eq:= P/1E5*v^3-(P/1E5*n*b+n*R*T)*v^2+a*n^2*v+a*n^3*b=0;      pressure normalized to bar (p/1E5)
van_der_waal_eq := 0.95200 v^3 - 2.270632441 v^2 + 0.000004747085049 v + 1.340611982 10^-10 = 0

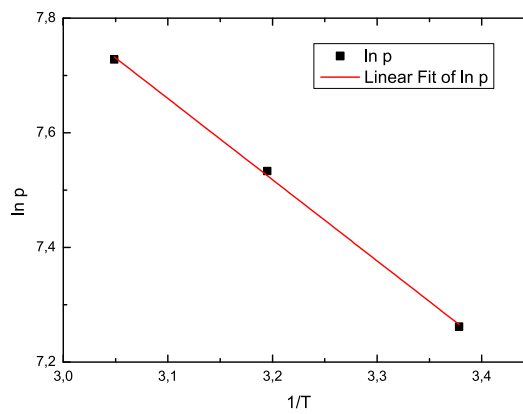
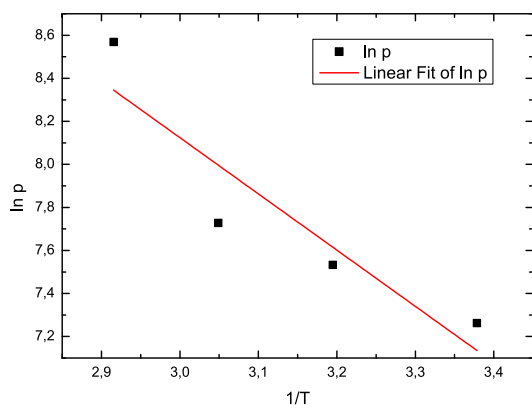
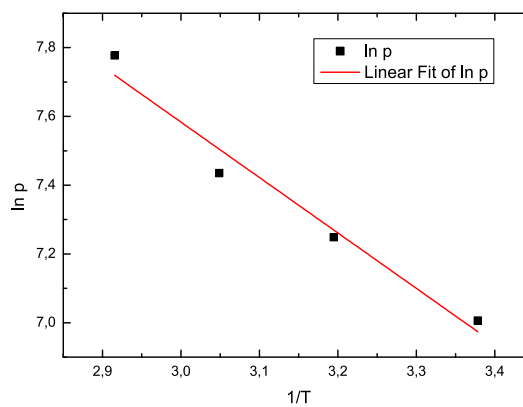
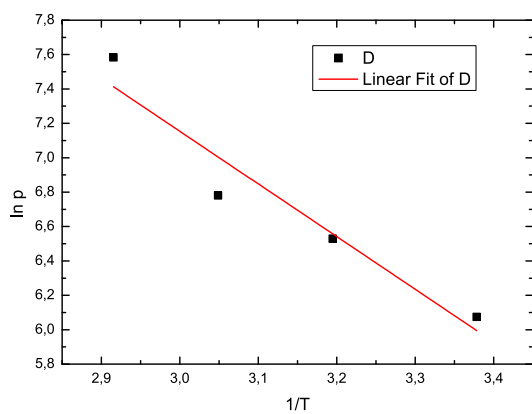
Van der Waal molar volume
> Van_Vol:=(solve(van_der_waal_eq,v))/100;      normalized to [L]
Van_Vol := 8.799955110 10^-8, 0.02385116020, -6.709284100 10^-8

Ideal gas molar volume
> Ideal_Vol:=n*22.4;
Ideal_Vol := 0.02074074074

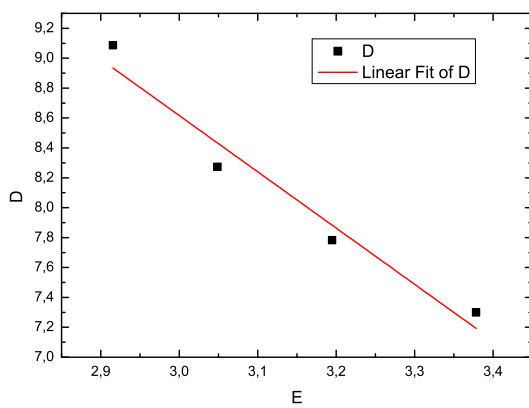
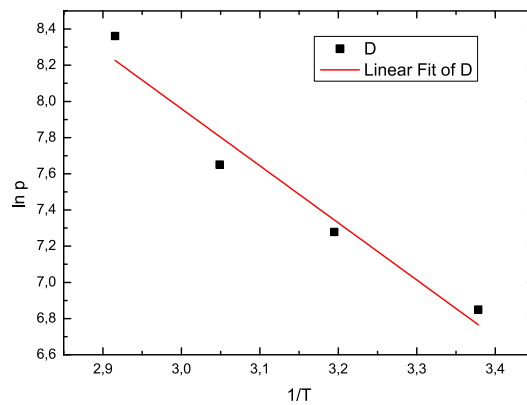
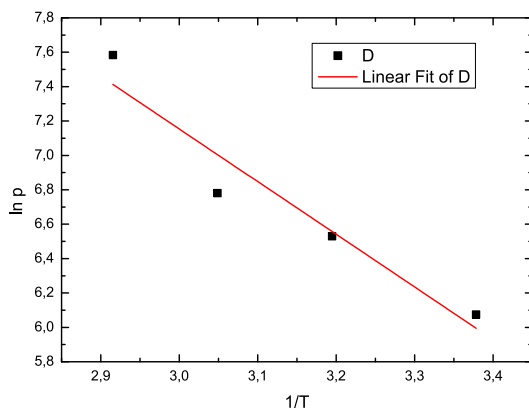
```

## 12.6 Linear regression plots of QCM sorption experiments

EtOH@QCM-E

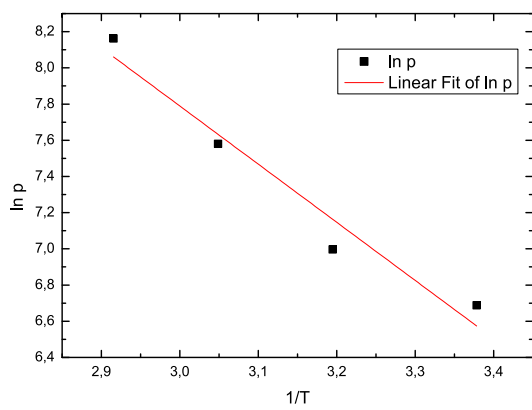
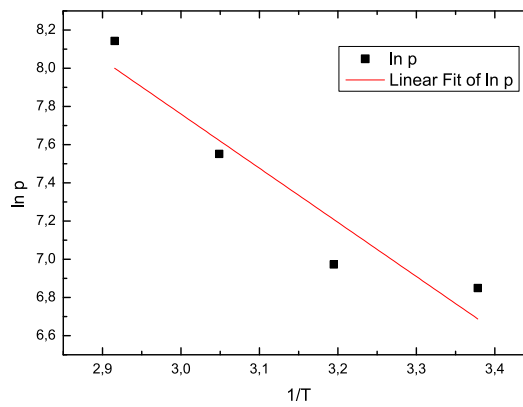
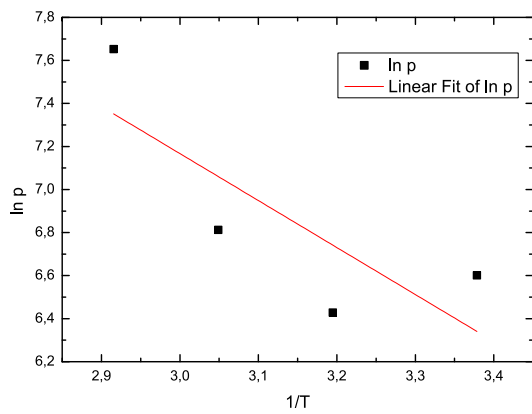


EtOH@QCM-Ph

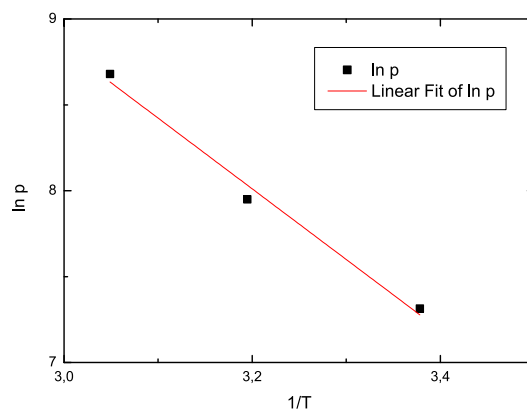
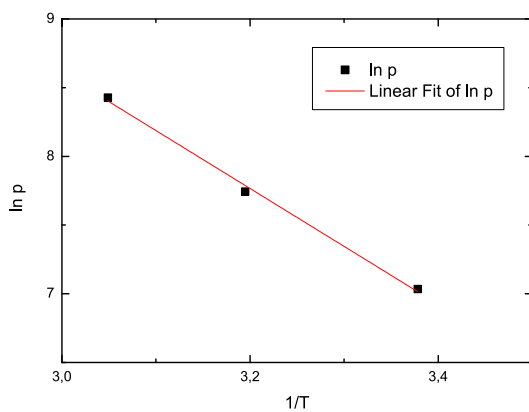
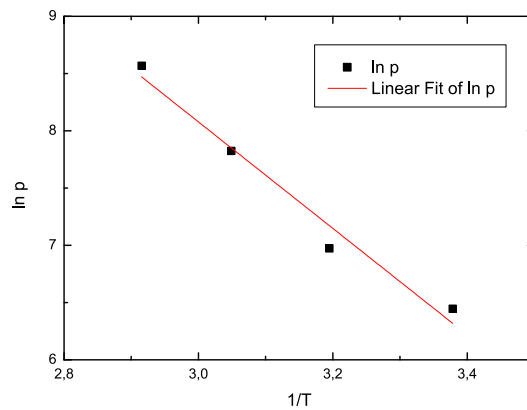
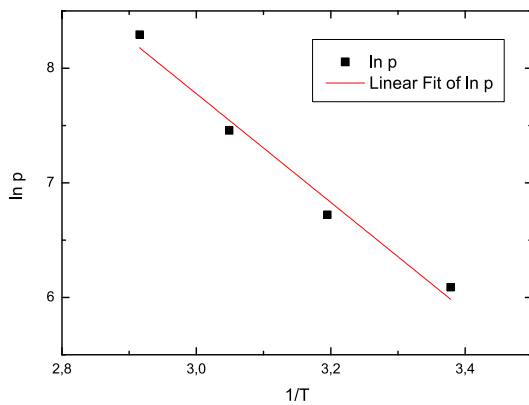




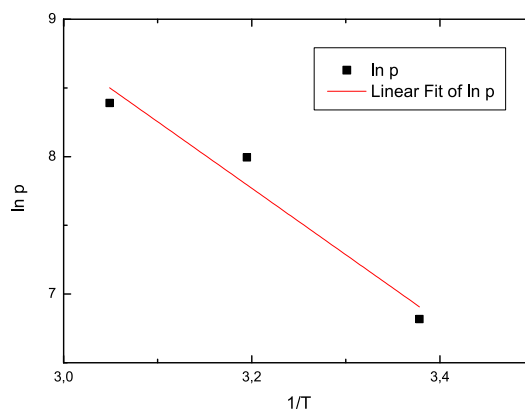
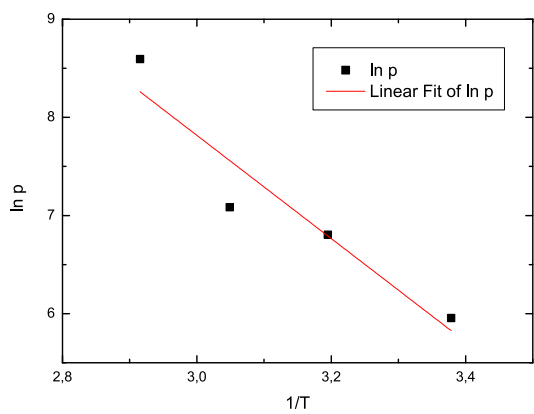
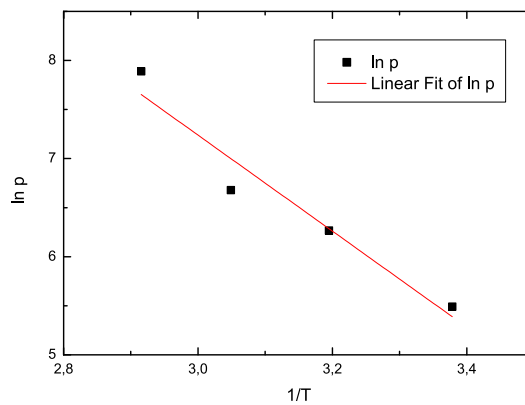
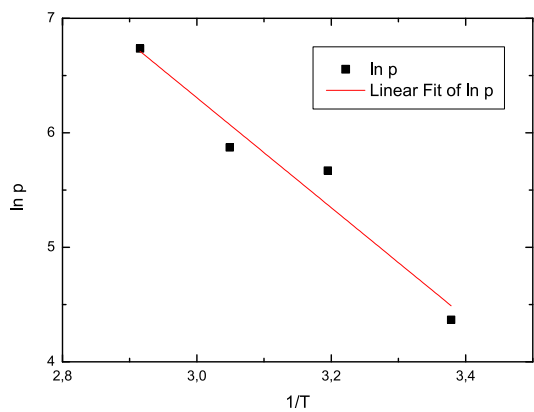
## EtOH@QCM-CN



EtOH@QCM-Vinyl

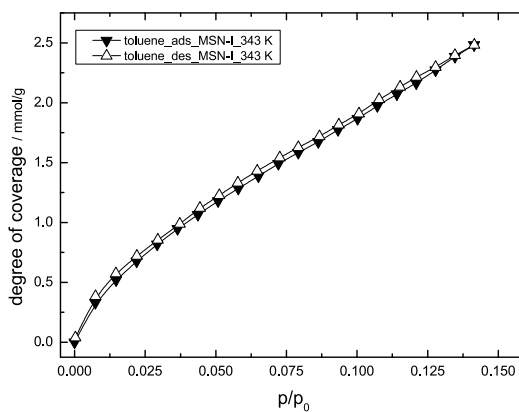
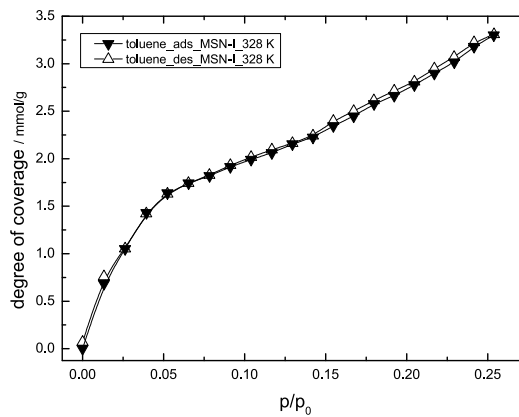
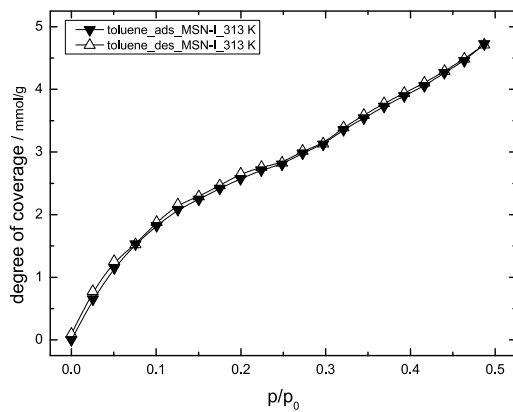


EtOH@QCM-SH

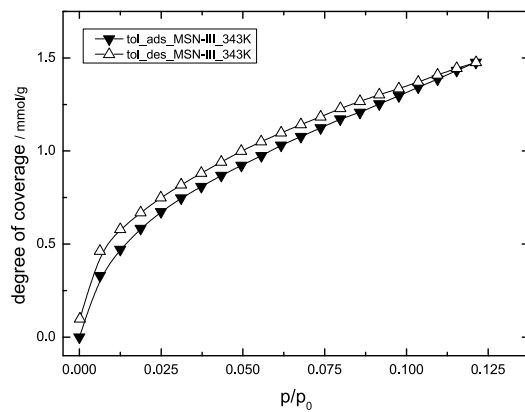
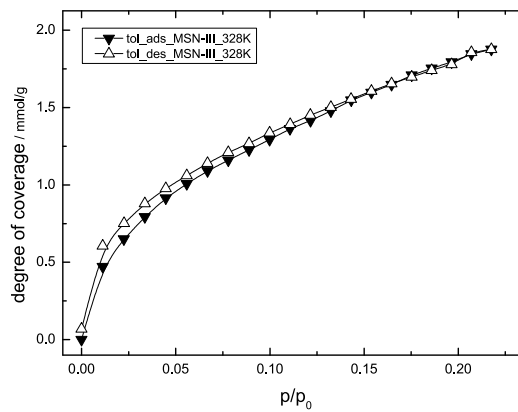
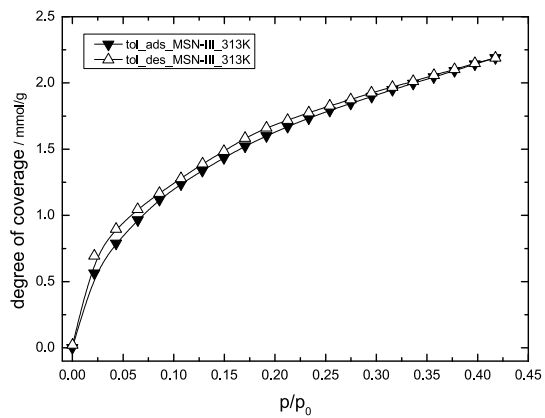


## 12.7 Supplementary toluene isotherms

## MSN-I



## MSN-III



## 12.8 Equipment used for SAW experiments

LiNbO <sub>3</sub> SAW chip:	Advantix AG
chemicals:	Sigma-Aldrich
boxcar:	Stanford Research Systems SRS SR250
voltage readout:	Keithley 199
function generator:	Toellner Toe 7708
power supply phase shifter 1: Delta	Elektronika E030-1
power supply logarithmic amplifier: Delta	Elektronika E18-0.6D
logarithmic amplifier:	in house workshop
damping element:	Mini Circuits ZHL-2-S-SMA
mixer:	Mini Circuits ZFM-2B
splitter:	Mini Circuits ZFSC-2-4
variable damping element:	Wavetek 5010A
low-pass filter (10 MHz):	in house workshop
90° power divider (at 110 MHz):	in house workshop
frequency generator:	Rhode & Schwarz SMP02
temperature control:	Jumo , Watlow and in house workshop
digital mass flow controllers:	Bronkhorst
controller unit:	Bronkhorst
PC control unit:	GPIB bus, Labview
high temperature circuit board:	Taconic RF-35-0300-C1/C1
high frequency generator:	Stanford Research DG535 and Phillips PM579113

## 13 Curriculum Vitae

### Alexander Darga

\* 18.10.1975 in Rosenheim

### Familienstand

verheiratet, ein Kind

### Schulbildung

1982-1986 Grund- und Hauptschule Bad Feilnbach

1986-1995 Gymnasium Bad Aibling, Abschluß Abitur

### Studium

1995-2001

Diplom-Chemie an der LMU München

26.11.2001 - 10.06.2002

Anfertigung der Diplomarbeit am Lehrstuhl Physikalische Chemie, Prof. Thomas Bein

Thema der Diplomarbeit:

„Lithographische Verfahren zur Strukturierung mesoporöser Dünnschichtfilme“

01.11.2002 - 03.07.08

Promotion an der Ludwig-Maximilians-Universität München im Arbeitskreis Prof. Thomas Bein, Physikalische Chemie

### Beruflicher Werdegang

Sep. 2000 - Okt. 2004

freiberuflicher EDV- und Netzwerktechniker, IT-Consultant

seit Februar 2004

Geschäftsführer der Dantotec GmbH